NATIVE IN-TISSUE STRUCTURES OF AMYLOID-β PLAQUES IN A MOUSE MODEL OF ALZHEIMER'S DISEASE BY CRYOGENIC ELECTRON TOMOGRAPHY

CONNY LEISTNER

Submitted in accordance with the requirements for the degree of

DOCTOR OF PHILOSOPHY

University of Leeds

Faculty of Biological Sciences

School of Biomedical Sciences

September 2022

Intellectual property rights

The candidate confirms that the work submitted is her own and that appropriate credit has been given where reference has been made to the work of others.

This copy has been supplied on the understanding that it is copyright material and that no quotation from the thesis may be published without proper acknowledgement.

The right of Conny Leistner to be identified as Author of this work has been asserted by her in accordance with the Copyright, Designs and Patents Act 1988.

Abstract

Senile plaques composed of amyloid-β (Aβ) are a major pathological hallmark of Alzheimer's disease (AD). Aβ fibrils prepared *in-vitro* or purified from post-mortem tissue have been investigated extensively revealing their atomic structure. However, the native architecture of Aβ plaques and the organisation of Aβ fibrils within the brain itself is currently unknown.

Here, we developed a workflow to determine the in-tissue architecture of Aβ plaques using cryogenic correlative light and electron tomography (cryo-CLET) in the brain of a knock-in mouse model of AD (1 year old male *App*$^{NL\text{-}G\text{-}F}$, n=2). After injecting mice with Methoxy-X04, a fluorescent dye that labels Aβ plaques, fresh cortical tissue biopsies were vitrified by high-pressure freezing. Next, tissue cryo-sections were collected on cryo-EM grids and Methoxy-X04 stained plaques were mapped by correlative imaging to direct the collection of cryo-electron tomographic data.

3D reconstructions revealed the in-tissue molecular architecture of Aβ plaques. Aβ fibrils were organised within multiple distinct domains of varying densities, including a meshwork and parallel bundles. Numerous other macromolecular features were observed within the plaque, including liquid-like droplets. Subcellular compartments interdigitated the pathology, within and between Aβ parallel bundles. These included membranes containing higher-order protein networks, c-shaped membrane, and membrane nanopedia. The boundary of Aβ plaques was characterised by cells in close proximity to Aβ fibrils that contained

an abundance of mitochondria, endoplasmic reticulum, ribosomes and microtubules. Overall, these results reveal the molecular heterogeneity of Aβ plaques and the rich diversity of cellular constituents that define the amyloid pathology of AD.

Table of contents

List of Figures

List Of Tables

Abbreviations

2PM	Two Photon Microscopy
3D	Three Dimensional
A.U.	arbitrary units
ACSF	Artificial Cerebrospinal Fluid
AD	Alzheimer’s disease
AMPA-R	α-Amino-3-Hydroxy-5-Methyl-4-Isoxazole Propionic Acid Receptor
APP	Amyloid Precursor Protein
Aβ	Amyloid Beta
BSA	Bovine Albumin Serum
C100	100 µm condenser lens
CCD	Charge-coupled Device
CEMOVIS	Cryogenic Electron Microscopy of Vitreous Specimens
CNS	Central Nervous System
cryo-CLEM	Cryogenic Correlated Light and Electron Microscopy
cryo-EM	Cryogenic Electron Microscopy
cryo-ET	Cryogenic Electron Tomography
cryo-FIBSEM	Cryogenic Focussed Ion Beam Scanning Electron Microscopy
cryo-FM	Cryogenic Fluorescence Microscopy
CTF	Contrast Transfer Function
DMSO	Dimethyl Sulfoxide
dSTORM	Direct Stochastic Optical Reconstruction Microscopy
EM	Electron Microscopy
ER	Endoplasmic Reticulum

EV	Extracellular Vesicles
FFT	Fast Fourier Transformation
FIB	Focussed Ion Beam
HACSF	HEPES-buffered Artificial Cerebrospinal Fluid
HPF	High Pressure Freezing
i.p.	Intraperitoneal
MT	microtubule
MVB	Multivesicular Body
MX04	Methoxy-X04
NA	Numerical Aperture
NMDA-R	N-Methyl-D-Aspartate Receptor
NMDG	N-Methyl-D-Glucamine
PALM	Photoactivated Localisation Microscopy
PBS	Phosphate Buffered Saline
PFA	Paraformaldehyde
PM	Plasma Membrane
PSD	Postsynaptic Density
PSF	Point Spread Function
RT	Room Temperature
SEM	Scanning Electron Microscopy
SPA	Single Particle Analysis
STED	Stimulated Emission Depletion
STORM	Stochastic Optical Reconstruction Microscopy
TBS	Tris Buffered Saline
TEM	Transmission Electron Microscope
VPP	Volta phase plate

WT	Wild type

Table 1: Abbreviations

1. Introduction

1.1. Alzheimer's Disease

1.1.1. From a macroscopic to microscopic scale

Alzheimer's disease (AD) is the leading cause of death in the UK, 850,000 people in the UK and 50 million people worldwide suffer from dementia. By 2050 it is expected that about 70 million people will suffer from dementia worldwide. The most common cause of dementia is Alzheimer's disease (AD). At the preclinical stage, AD pathology starts to form without any cognitive impairment (Dubois *et al.*, 2016). Early symptoms are cognitive decline, followed by changes in behaviour, disorientation, and disturbances in motor functions in later stages (Kyle, 2001; Alzheimer's Association, 2016). Different treatments for these symptoms are available (Chen *et al.*, 2017; Yiannopoulou and Papageorgiou, 2020), although disease onset and progression currently cannot be delayed or stopped. Post mortem observations of brains from patients in late stages of AD show severe atrophy, due to neuronal and synapse loss (Dickson and Vickers, 2001).

The cause of AD remains unknown, although a high variety of risk factors and gene mutations associated with the disease have been identified (Reitz and Mayeux, 2014). Furthermore, chronic inflammation due to reactive gliosis has been observed in studies of Alzheimer's disease brains. Two of the major pathological hallmarks in Alzheimer’s disease are senile plaques and neurofibrillary tangles. Neurofibrillary tangles are intracellular aggregates of the microtubule associated protein tau, whereas senile plaques are extracellular aggregates of the amyloid beta (Aβ) protein. Alois Alzheimer first identified Aβ plaques and neurofibrillary tangles by silver stain in 1907 (Alzhelmer, 1907; Stelzmann, Norman Schnitzlein and Reed Murtagh, 1995). The term amyloid was first introduced by Rudolf Virchow who had mistakenly described the protein as a starch (Latin word amylum and Greek: ἄμυλον amylon; Kyle, 2001). To date, the term amyloid refers to abnormal, typically extracellular aggregates of proteins, which can be detected with dyes, including Thioflavine and Congo red. After Congo red staining, aggregates show green birefringence under polarised light. Moreover, amyloid fibrils show a generic cross-β structure (Benson *et al.*, 2020). Interestingly, the amyloid state of a protein is thermodynamically often the most stable form (Baldwin *et al.*, 2011). Although, the formation of amyloid is prevented by quality control mechanisms which seem to fail in diseases like AD (Knowles, Vendruscolo and Dobson, 2014).

Aβ plaques are derived from small Aβ-peptides. The amyloid precursor protein (APP), an integral membrane protein, is cleaved into small peptides intracellularly by β-secretase and intramembranously by γ-secretase. Two isoforms of Aβ that have been discovered to aggregate in AD are produced upon cleavage, a 42 and a 40 amino acid long isoform (Vassar *et al.*, 1999; Vassar, 2013). Aβ(42) is considered to be the more toxic isoform (Younkin, 1995; Cole and Vassar, 2007; Lambert *et al.*, 1998; Duff *et al.*, 1996; Mucke *et al.*, 2000). Aβ is released into the extracellular space where it forms Aβ plaques through multiple steps. The amyloid hypothesis proposes that oligomers or Aβ protofibrils are the toxic species that trigger a cascade of pathogenic events that leads to neurodegeneration (Selkoe, 1998), including synaptic loss around the plaques (Spires-Jones *et al.*, 2007), neuritic malfunction and reactive gliosis (Serrano-Pozo *et al.*, 2011). Other studies suggest that activated microglia and activated astrocytes which are found in close contact to the plaque, have a neurotoxic effect by releasing proinflammatory substances which trigger a series of events that ultimately leads to cell death (Garwood *et al.*, 2017; Schwabe, Srinivasan and Rhinn, 2020).

1.1.2. The structure of Aβ

After cleavage of APP, plaques are formed in several steps. Monomeric subunits may be stacked to form oligomers or protofilaments. In amyloid fibrils, every subunit contributes at least one β-strand. This cross-β is stabilised by backbone hydrogen bonds (Figure 1 A). Hydrogen bonds are the most stable interactions that hold the cross-β structure together (Fitzpatrick *et al.*, 2011). Oligomers are very heterogeneous and do not always show the typical cross-β structures of amyloid (Chen *et al.*, 2017); Figure 1 B). Multiple monomeric subunits form protofilaments (Figure 1 C). Two or more protofilaments wrap around each other and form helical twisted fibrils that deposit to form plaques (Figure 1 D and E). Different types of plaques are found, including diffuse plaques, dense cored plaques and burned-out plaques. It has been proposed that loosely packed diffuse plaques are the most primitive form which matures into dense-cored plaques and further into burned-out plaques ((Wisniewski *et* *al.*, 1989; Serrano-Pozo *et al.*, 2011). Dense cored plaques are surrounded by a diffuse corona of fibrils whilst burned-out plaques only consist of a tightly packed plaque core (Wisniewski *et al.*, 1989; Serrano-Pozo *et al.*, 2011).

A great variety of amyloid-β polymorphism has been identified, in which the same polypeptide sequence results in different protein folding patterns. Strands are most commonly parallel in register where the strand direction is the same and identical amino acids are stacked on top of one another. These are stabilised by π–stacking of aromatic amino acids and hydrogen bonds between amidic amino acids. In contrast, antiparallel out of register strands have an altered strand direction in each layer and amino acids stacked on top of one another are not identical. However, antiparallel out of register strands have not been observed in nature, yet. Short side chains like Glycine or Proline introduce turns to the strands. Some structures show in-register parallel β-sheets in the fibril core, however N-terminus and C-terminus can be disordered (Figure 1 C; (Ghosh *et al.*, 2021).

Complementary side chains from adjacent strands interdigitate and form steric zippers which are stabilised by van der Waals forces. These occur most commonly between hydrophobic side chains. Typically, two Aβ protofilaments form fibrils with a helical twist stabilised by salt bridges or hydrogen bonding and C_2 symmetry (Yang *et al.*, 2022) or pseudo-2_1 symmetry (Gremer *et al.*, 2017; Kollmer *et al.*, 2019; Yang *et al.*, 2022). C_2 symmetry occurs when subunits are packed in-register with a 180° helical twist. The pseudo-2_1 screw symmetry is observed more commonly (Figure 1 E). Here, strands are staggered and one subunit is shifted ~2.4 Å further along the fibril axis (Taylor and Staniforth, 2022). The helical twist is typically left-handed for fibrils derived from the brain (Yang *et al.*, 2022; Gremer *et al.*, 2017; Kollmer *et al.*, 2019; Yang *et al.*, 2022), but a right handed twist has been observed in Aβ(40) purified from meninges of AD patients. Interestingly, these structures had a 2_1 screw symmetry with parallel in-register sheets (Gremer *et al.*, 2017; Kollmer *et al.*, 2019; Yang *et al.*, 2022). Table 2 summariases fibril structures from three different models.

Recently, the first structure from Aβ fibrils purified from human brain tissue was compared to fibrils purified from a humanised mouse model of AD. The human tissue type II structure is similar to the mouse model *App*$^{NL\text{-}F}$ structure (mouse model will be described in 1.1.3 Mouse models of AD). The human type I structure is formed by two identical S-shaped protofilaments (residues 19-42) with an ordered core (G9 - A42). The human type II structure has an ordered core from V12 - A42 and the S-shape is formed by residues 20-42 (Figure 2 A). Both structures have a disordered N-terminus. Figure 2 B shows that the S-shaped protofilaments of both human structures are very similar (Gremer *et al.*, 2017; Kollmer *et al.*, 2019; Yang *et al.*, 2022). The structures were resolved with a maximum of 2.5 Å resolution.

Recombinantly expressed Aβ(42) fibrils, studied by NMR and cryo-EM showed two protofilaments with an LS-shaped structure, where the N terminus is L shaped and the C-terminus is S-shaped with a left handed twist (Gremer *et al.*, 2017). Overall this structure is very different to the cryo-EM structures of Aβ(42) purified from human brain tissue (Figure 2 C). Importantly, fibrils were grown in pH2 which could explain these differences in structure.

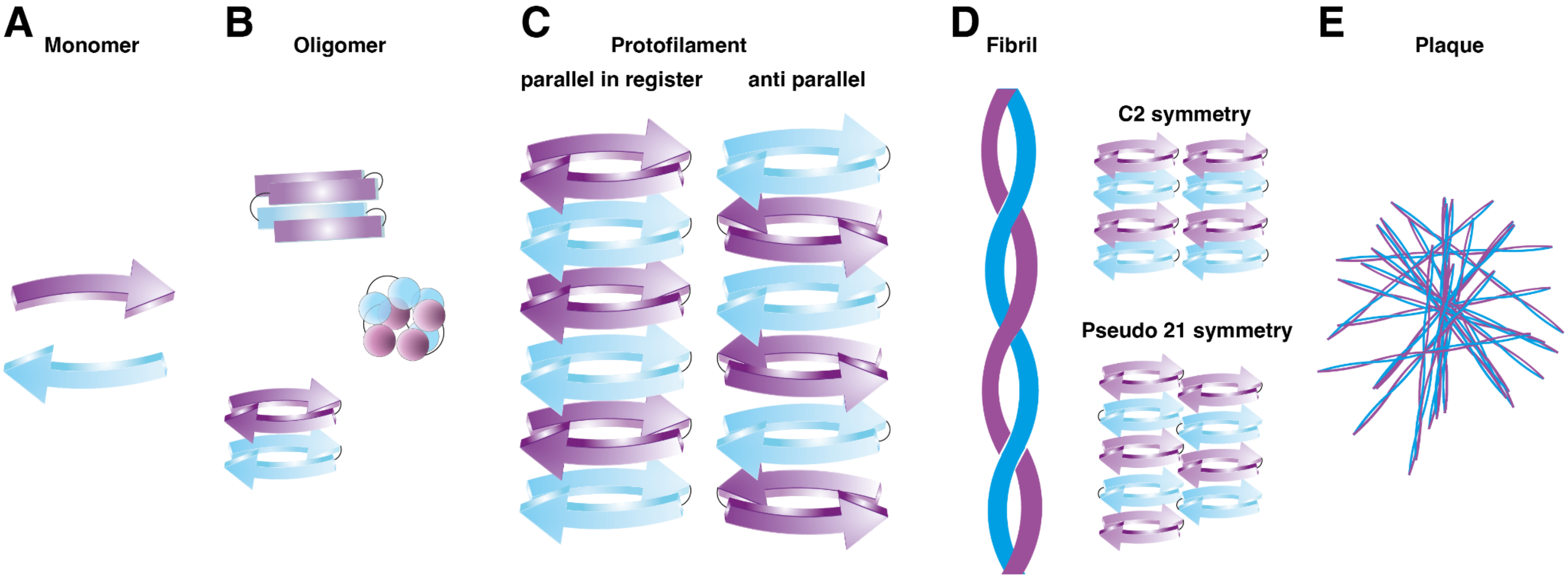

Figure 1: Schematic of Aβ organisation from monomers to plaques. Monomers consist of β-sheet (A) which can assemble into oligomers. These can be disorganised, organised into spheres or form typical cross-β structures (B). Monomers are stacked into protofilaments. These can be organised parallel in-register or antiparallel out of register (C). Typically fibrils are composed of two or more

protofilaments. Fibrils can be arranged parallel forming a C2 symmetry or pseudo 21 screw symmetry. Antiparallel symmetry has been proposed, although it has not been observed in nature (D). Fibrils aggregate i*n-vivo* and *in-vitro* and form plaques (E).

Publication	Type	Handedness	Symmetry	Diameter	Features	Technique	Resolution
(Gremer *et al.*, 2017)	*in-vitro* Aβ(42)	left handed twist	2_1 screw symmetry	7 nm	2 LS-shaped protofilaments	cryo-EM, NMR	4.0 Å
(Kollmer *et al.*, 2019)	human AD meninges Aβ(40)	right handed twist	pseudo 2_1 screw symmetry	7.4 ± 0.4 nm	2 U-shapes peptides peptides form ordered core	cryo-EM	4.4 Å
(Yang *et al.*, 2022)	human AD brain Aβ(42) type I	left handed twist	pseudo 2_1 screw symmetry	[1]	2 S-shaped protofilaments, ordered core	cryo-EM	2.5 Å
(Yang *et al.*, 2022)	human AD brain Aβ(42) type I	left handed twist	C_2 symmetry	[1]	2 S-shaped protofilaments, ordered core	cryo-EM	2.8 Å

Table 2: Comparison of four different Aβ fibril structures. First studies derived structures from *in-vitro* prepared Aβ(42) fibrils and later from Aβ(40) fibrils purified from meninges from AD cases. A recent study showed two different types of Aβ(42) fibrils derived from AD patients.

---

[1] this parameter was not measured by the authors

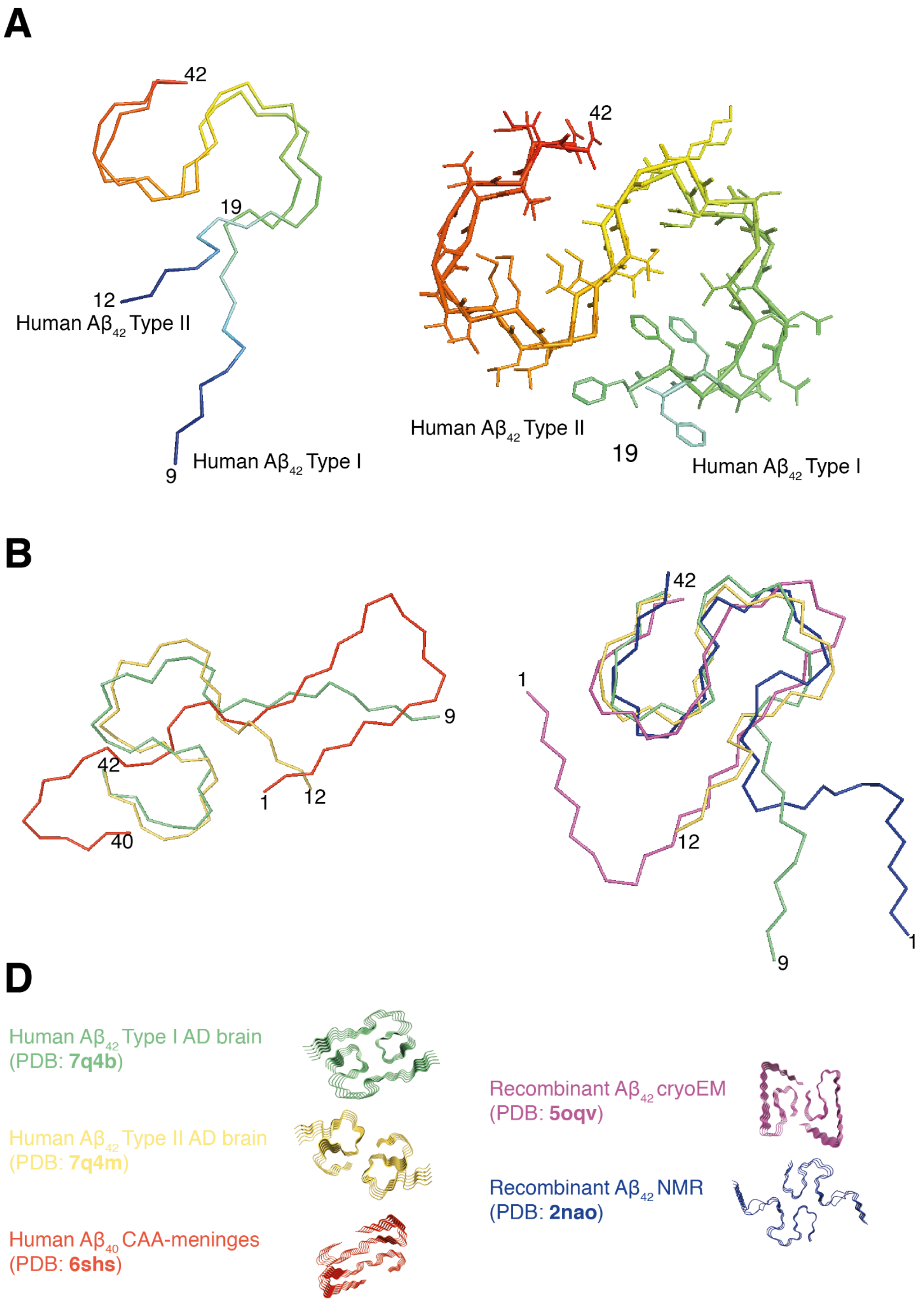

Figure 2: Comparison of Aβ structures from different models. Comparison of human type I and human type II Aβ(42) structures purified from brain tissue. S shaped fold is conserved in both, but N terminal tails differ (Yang et al. 2022, A). Comparison of

human Aβ(40) purified from meninges of AD patients (red, Kollmer et al. 2019) and human type I (green), type II (yellow). Human Aβ(40) structures from meninges fold into a U shape and strongly differ from structures of human brain type I and II (B). S shape is conserved in the core region of recombinantly expressed Aβ(42) with C and N terminal anchors (cryo-EM structure - magenta, NMR structure - blue, Gremer et al. 2017, C). Fibril structures and PDB IDs are shown (D).

Moreover, in structures of Aβ(40) purified from AD meninges, two protofilaments form an ordered U-shaped core and the C- and N-termini form arches. (Figure 2 D; (Kollmer *et al.*, 2019). This structure has a very different conformation to the human Aβ(42) brain structures.

In conclusion, fibril structures can adapt to a very diverse range of conformations. The studies compared here were from different AD tissues, namely brain parenchyma and meninges. They used samples from multiple patients and showed different types of Aß fibril structures within those. However, the samples used to determine all of these structures were purified and thus not in their natural environment. Purification can introduce artefacts (Laverty *et al.*, 2019) and it remains unclear if all of the native forms of Aβ were purified or only the most stable forms. Hence, I established a workflow to study the native in-tissue structure of Aβ and compared these results with the structures from single particle analysis (SPA) cryo-EM data.

1.1.3. Mouse models of AD

A great variety of AD mouse models are available and each of them shows differences in phenotypes. Most transgenic mouse models overexpress mutant

APP or APP/presenilin cDNA which can introduce artificial phenotypes. Additionally, these mice overexpress not only the Aβ but also other fragments of APP (Sasaguri *et al.*, 2017).

Plaques	Aggressive amyloidosis; plaques develop in homozygous mice starting at 2 months with near saturation by 7 months. Aβ deposition at 4 months in heterozygous mice. Cortical and subcortical amyloidosis present.
Tangles	Absent; although phosphorylated tau is elevated in dystrophic neurites around plaques.
Neuronal Loss	Absent.
Gliosis	Microglia and activated astrocytes accumulate with age starting around 2 months, especially around plaques in a manner concurrent with plaque formation.
Synaptic Loss	Reduction of synaptophysin and PSD95 immunoreactivities associated with Aβ plaques in both cortical and hippocampal areas.
Changes in LTP/LTD	Unknown.
Cognitive Impairment	Memory impairment in homozygous mice by 6 months of age as measured by the Y maze.

Figure 3: Phenotypes of *App*$^{NL\text{-}G\text{-}F}$ mice (taken from Alzforum: APP NL-G-F Knock-in, 2012).

Therefore, more recently humanised APP knock-in models were established as an alternative. *App*$^{NL\text{-}F}$ and *App*$^{NL\text{-}G\text{-}F}$ are humanised knock-in mice which express APP on a wild type level under its endogenous promoter (Saito *et al.*, 2014a). These mice harbour the Swedish (KM670/671NL, “NL”), Iberian mutation

(I716F, “F”) and in the case of the $App^{NL\text{-}G\text{-}F}$ knock-in mouse an Arctic mutation (E693G , “G”). These mutations cause an increase in total Aβ production (Swedish mutation “NL”), increase in cleavage of *App* and increase in the ratio of Aβ 42 to Aβ 40 levels (Iberian mutation “F”). The $App^{NL\text{-}G\text{-}F}$ knock-in mouse has an additional third mutation that enhances aggregation of Aβ (Arctic mutation “G”). The mice express *App* at wildtype levels under an endogenous promoter and thus show a normal expression pattern. $App^{NL\text{-}F}$ mice develop Aβ pathology after 6 months, memory loss after 18 months. $App^{NL\text{-}G\text{-}F}$ mice develop cortical amyloidosis after 2 months which reaches saturation after 9 months. Subcortical amyloidosis started after 4 months in these mice. Additionally, 9 months old $App^{NL\text{-}G\text{-}F}$ mice had greater gliosis compared to $App^{NL\text{-}F}$ mice. $App^{NL\text{-}G\text{-}F}$ mice showed memory impairment after 6 months. Both mouse models showed synaptic alterations. Aggregates of the microtubule associated protein tau and neurodegeneration were not detected in these mice (Figure 3; Saito *et al.*, 2014a).

1.2. Techniques to see into the brain

1.2.1. Length scales

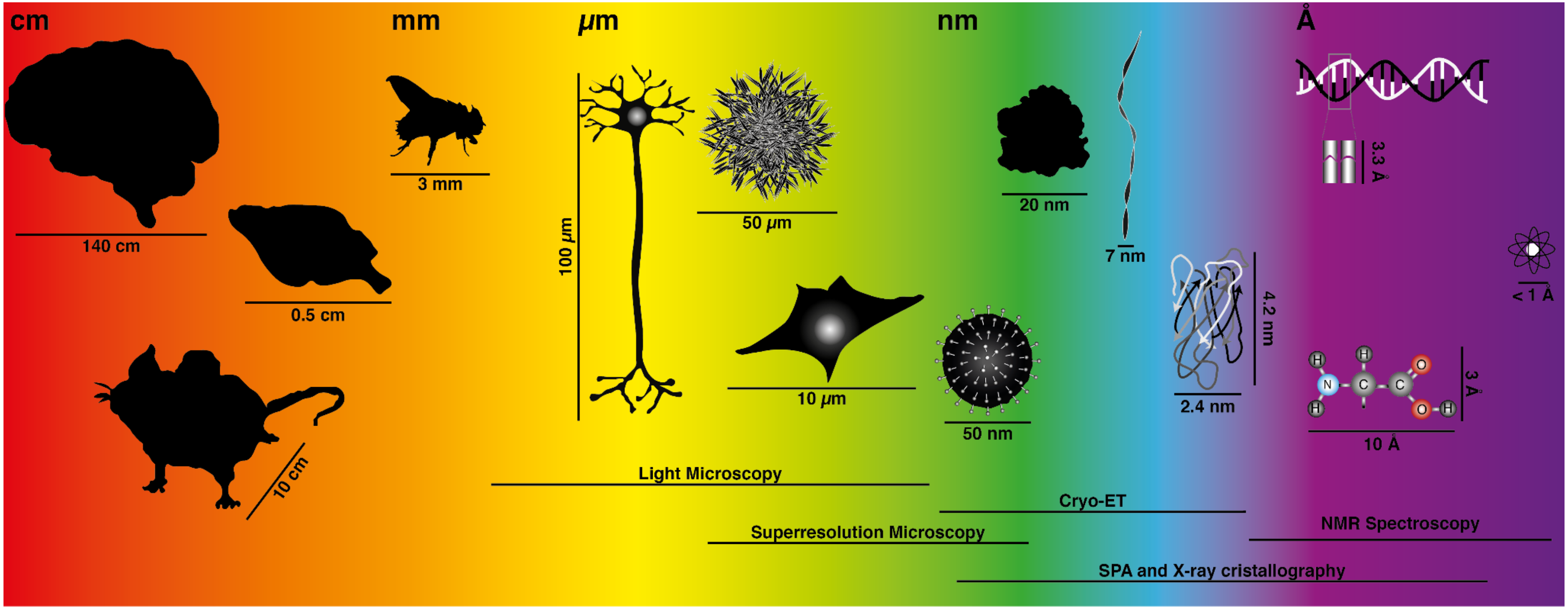

Figure 4: Different length scales and techniques to solve biological structures. In neuroscience, behavioural and cognitive studies are carried out on model organisms for example mice or flies. The anatomy of their brains can be studied by eye. We need light microscopy to visualise individual cells, superresolution techniques enable us to resolve proteins down to 20 nm in size. To solve structures of cell organelles like ribosomes or viruses, cryoET, SPA and X-ray crystallography are used. SPA and X-ray crystallography have the power to solve individual amino acids in a protein. Moreover, NMR spectroscopy allows us to see single atoms. Every single one of these techniques has its strengths and limitations. To understand structures involved in complex biological processes, it is important to use a combination of all of these techniques.

On a systems level, complex behaviour and cognitive features are studied in human subjects and animal models (Figure 4). In order to understand these often complex phenotypes, connections and signal transductions among individual neurons across the central nervous system (CNS), several molecular approaches have been developed which can link structural and functional aspects. Calcium imaging is performed to analyse gene expression and neurotransmitter release. In electrophysiology electrical activity of cells is measured. Light microscopy and electron microscopy reveal the architecture of cells, organelles, arrangement of proteins and single neurons can be classified. These approaches can be integrated to solve fundamental questions in neuroscience, like learning, memory formation and language on different length scales (Table 3). Moreover, alterations and malfunctions in the brain can be studied. In 1873, Camillo Golgi first visualised individual neurons of the CNS by silver staining (Golgi, 1873). Santiago Ramon y Cajal then applied this method to describe different neuronal cell types and synaptic buttons in 1894 (Cajal, 1894). In 1931, nanometer scale transmission electron microscopy (TEM; (Knoll and Ruska, 1932) was established to visualise synapses, differentiate between inhibitory and excitatory synapses and identify synaptic buttons, active zones and the postsynaptic density (PSD; (Gray, 1959). Different length scales within the nervous system, namely neuronal circuits, morphology of single cells, ultrastructure of subcellular compartments and individual proteins are examined using light and electron microscopy (Figure 4).

in-situ structure	a biological specimen in its native biological state
in-vitro structure	structure of cells in a dish outside their natural environment
ex-vivo structure	structure obtained from tissue outside an organism
morphology	shape and structure of cells and cellular organelles
ultrastructure	architecture of cells in subnanometer range that is only visible with an electron microscope
clusters	formation of macromolecules of the same type, for example synaptic receptor cluster
nanodomains	set of proteins bound together within nanometer range

Table 3: Definition of length scales in neuroscience.

1.2.2. Labelling of specimens for light and electron microscopy

In fluorescence light microscopy, individual proteins are labelled using chemical dyes or fluorescent proteins which are genetically expressed and then imaged to qualitatively and quantitatively investigate an individual protein, its location and dynamics (Thorn, 2016).

For EM, cell types and cellular compartments are classified according to known criteria (White et al., 1986; Helmstaedter et al., 2013), such as morphology, cellular compartments are determined and cellular organelles are distinguished. In order to automate cell classification, diverse software tools have been developed (Kasthuri et al., 2015; Zheng et al., 2018).

Furthermore, multiple different labelling techniques have been established. For example, genetically encoded tracers expressing enzymes that label a certain population of cells can be expressed (Joesch et al., 2016). This method allows one to directly identify labelled cells in EM without correlation to light microscopy. Immunogold labelling where colloidal gold particles are attached to secondary antibodies are often used in classical EM (Hermann, Walther and Müller, 1996).

1.2.3. Advances in light microscopy

To visualise features of cells and cell organelles, light microscopy is required where structures bigger than ~20 nm can be resolved using fluorophores (Figure 4). The first improvement to a classical fluorescent microscope was a confocal microscope which visualises individual cells and protein distribution across the cell with a lateral resolution of about 200 nm (Webb, 1996). Confocal microscopy is typically performed on post-fixed tissue and *in-vitro* on live or fixed cells; it is not suitable for studies on living animals, because it induces photodamage and scattering. Therefore, 2 photon microscopy (2PM) has been developed where fluorophores are only excited upon stimulation with 2 photons with lower intensity, hence bleaching, tissue damage and scattering are decreased. 2PM reaches an imaging depth up to ~1 mm (Theer, Hasan and Denk, 2003). However, the lateral resolution remains around 200 nm (Hell and Stelzer, 1992). *In-vivo* imaging and imaging of acute brain slices is possible using 2PM, which can reveal the activity of labelled molecules. To interrogate the composition of synapses and protein dynamics, superresolution techniques, for instance stimulated emission depletion (STED; Hell and Wichmann, 1994), stochastic optical reconstruction microscopy (STORM; Rust, Bates and Zhuang, 2006) and photoactivated localisation microscopy (PALM; Betzig *et al.*, 2006) have been developed.

Various imaging techniques have been developed, with the decision of which method to use depending strongly on the biological question. For example, investigating the fine morphological details of cells and subcellular compartments, determining activity dependent changes of molecules and observing the organisation of different parts of the cell in the nanometer range, all rely on distinct imaging techniques. To address questions such as these, recent advancements in light microscopy with a resolution below diffraction limit have been developed. Superresolution, such as STED, PALM or STORM is required to examine the morphology of small neuronal structures (less than ~200 nm).

Using STED microscopy for example it is possible to reconstruct 3D models of dendritic structures with a lateral resolution of about 60-80 nm (Horisberger, 1981; Nägerl *et al.*, 2008; Urban *et al.*, 2011) which is obtained by a red shifted depletion beam outside detection range and thus it shapes the point spread function (PSF[2]; Hell and Wichmann, 1994). Due to its high imaging depth, STED microscopy is suitable for imaging inside the brain of living mice which makes it a useful tool to interrogate the dynamics and structures *in-situ*. In

---

[2] PSF: light from the point source is spread by diffraction when it passes through the optics of a microscope which results in diffraction rings surrounding the object and thus the object appears larger than it actually is (Cole, Jinadasa and Brown, 2011).

STED microscopy, the PSF is shaped physically, while in PALM and STORM, resolution below the subdiffraction limit is obtained by photoswitchable labels. In many circumstances it could be essential to perform *in-situ* studies on unfixed tissue to reveal their native structure. Although PALM and direct STORM (dSTORM) are compatible with live cell imaging on neuronal cell cultures (Ries *et al.*, 2012), the imaging depth is not sufficient for *in-vivo* and *ex-vivo* imaging. For dynamic studies, optical labels in a size of 1-25 nm are required. Therefore, different labels, namely organic dyes, quantum dots and gold particles have been developed to track the movement of membrane proteins in cells (Ries *et al.*, 2012; Cognet, Lounis and Choquet, 2014). For STORM and PALM, small photoswitchable dyes and genetically encoded fluorescent proteins are required. Using a combination of fluorescent proteins and nanobodies, high resolution of about 20 nm can be achieved in live cells by PALM and thus dynamic studies on cells can be performed. One of the major limitations in fluorescence microscopy is that labels are imaged and not the molecules themselves. Labelling can cause false positive observations by nonspecific binding, or false negatives due to incomplete binding. Furthermore, only the location and quantity of a protein is observed using fluorescent labels, but not the structure of the protein itself. Multicolour imaging is limited by the overlap of emission and excitation wavelength of fluorophores and thus only a few different proteins can be co-labelled within the same sample. In contrast, in EM it is possible to see the ultrastructure of whole cells without labelling individual proteins.

1.2.4. Advances in electron microscopy

Electron microscopy provides insight into membrane architecture with a subnanometer resolution and therefore is used to resolve ultrastructures of subcellular compartments down to single molecules. In conventional electron microscopy, samples are fixed, dehydrated and can be labelled with markers, for example immunogold (Horisberger, 1981), the contrast is generated by heavy metal staining. The first staining in EM that was developed used phosphotungstic acid, followed by development of heavy metal stainings, such as lead hydroxide (Reynolds, 1963) and osmium (Palay *et al.*, 1962; Reynolds, 1963) which enhance the contrast of biological membranes. In first studies using negative stained samples for EM different synapse morphologies, including synaptic connections of the visual cortex (Gray, 1959), and dendritic pathways in the olfactory bulb (Rall *et al.*, 1966), were examined. However, tissue samples have to be fixed, typically using aldehydes followed by embedding in resins, thus dynamic studies cannot be performed (Lockwood, 1964; Glauert, Rogers and Glauert, 1956; Rall *et al.*, 1966; Hündgen, 1968).

Although classical EM solved fundamental biological questions, it is limited by fixation artefacts. Chemical fixatives crosslink proteins and the native structure of the tissue is not well preserved due to tissue shrinkage, embedding artefacts and damage of the proteins (Hopwood, 1969; Kiernan, 2000; Lucˇic´ *et al.*, 2005; Korogod, Petersen and Knott, 2015). Therefore, new methods have been developed to directly investigate tissue in its native state without any fixatives. Moreover, combining the advantages of both methods, electron microscopy and light microscopy, correlative light and electron microscopy (CLEM) has been developed, where the region of interest is selected and mapped. The location and dynamics of single proteins can be identified in light microscopy and subsequent EM imaging allows one to obtain the ultrastructure of the same protein. However, depending on the sample type CLEM is not always accurate enough to resolve individual proteins with subnanometer resolution, especially when working with tissue samples.

1.2.5. Techniques to achieve subnanometer resolution

To determine the structure of individual molecules, X-ray crystallography has been the state-of-the-art technique, because if protein crystals can be obtained atomic resolution can be achieved (Figure 4).

The first 3D structures of a non-fixed native membrane protein was obtained from the purple membrane of Halobacterium halobium at 7 Å resolution by electron crystallography (Henderson and Unwin, 1975). 15 years later, the first high resolution cryo-EM structure was resolved after the development of new electron detectors which replaced CCD cameras and film. Electron detectors improved sensitivity and speed of data collection (Van Drie and Tong, 2020) and thus the native structure of the membrane protein bacteriorhodopsin was resolved showing individual side chains with near atomic resolution of 3.5 Å (Henderson *et al.*, 1990).

Cryo-EM has been employed in single particle analysis (SPA), cryo-electron tomography (cryo-ET) where cells grown on grids and tissue samples are studied. To preserve the native state of biological specimens under cryo-conditions, biological material is vitrified (Chang *et al.*, 1983). Therefore, biological material is frozen rapidly, to -120° to solidify water molecules and prevent formation of ice crystals. To achieve this, cryoprotectants, for example sucrose, are applied to reduce tissue damage during the freezing process (Tokuyasu, 1973). Dubochet *et al.*, 1982 established plunge freezing of biological specimens in liquid ethane for vitrification in 1982. This technique allows to freeze biological samples rapidly and obtain a thin, homogenous layer of samples on an EM grid.

Not only structures of single proteins, but also macromolecular complexes can be revealed by cryo-EM. Lipidprotein interactions can be determined by electron crystallography and the resolution has been improved up to <2 Å (<0.2 nm; Gonen *et al.*, 2005). 3D models of lipid-protein interactions in their native environment can be obtained by cryo-EM with 3.4 Å resolution (Gao *et al.*, 2016). In neuroscience, structures of synaptic protein complexes, such as interactions of α-amino-3-hydroxy-5-methyl-4-isoxazolepropionic acid receptors (AMPA-R) and regulatory molecules can be observed using SPA (Twomey *et al.*, 2016). Typically for single particle cryo-EM, electron micrographs are collected from purified proteins frozen onto an EM grid, followed by various processing steps, including motion correction, alignment and classification. However, in single particle cryo-EM proteins are not preserved inside their native environment. Moreover, purification can modify the native structure of proteins, potentially introducing artefacts. Multidimensional computations for 3D reconstructions from electron micrographs are required on particles. Particles with the same size and shape are imaged from different angles, a model is generated from the data and fit (Klug and Finch, 1968) or if the structure is known a model that has previously been generated is used and fit to the new dataset to improve its resolution (Klug and Finch, 1968; Rosier, de Rosier and Klug, 1968).

Tissue samples are often heterogeneous which makes it harder to study their native 3D structures. New workflows in cryo-EM provide insight into in-situ structures of proteins in vitrified cells and tissue. To resolve 3D structures of vitreous tissue samples, cryo-electron tomography (cryo-ET) has been developed. In cryo-ET the specimen is tilted to view it from different angles (Figure 5 A). After motion correction, the tilt series is aligned to the tilt axis and reconstructed to achieve a 3D view of the specimen (Baumeister, Grimm and Walz, 1999). In order to obtain high resolution by cryo-ET, subtomogram averaging is performed. Therefore, the structures of interest are cropped from a 2D volume of the tomogram, aligned and averaged to obtain a 3D structure (Figure 5 B).

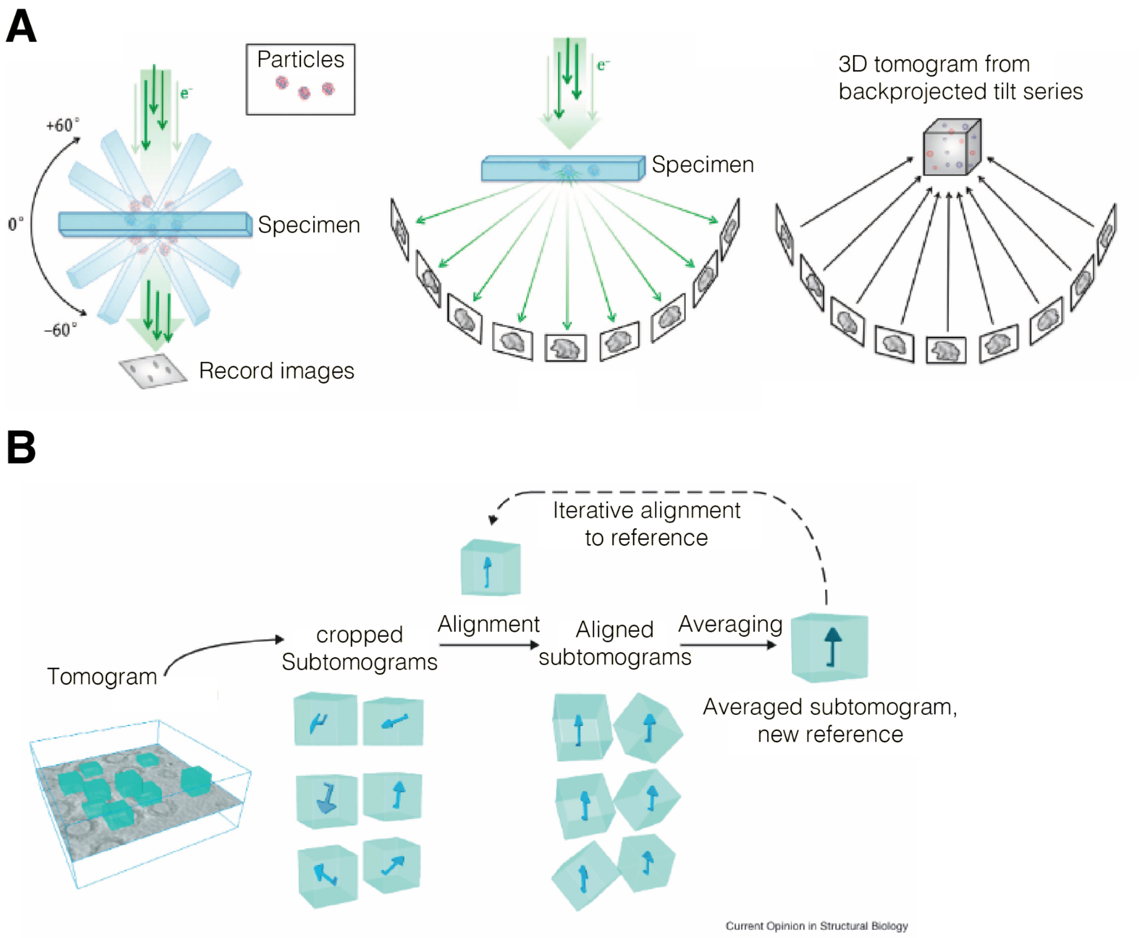

Figure 5: Principles of cryo-ET and subtomogram averaging. The sample is tilted from 60 to -60° and an image is recorded in every tilt (left) which creates a tilt series of images (middle) that is backprojected to create a 3D tomogram (right, A, modified from Galaz-Montoya and Ludtke, 2017). To achieve a higher resolution structure of macromolecular complexes, these are cropped, aligned and averaged to create an initial reference. The particles are then realigned to the reference (B, modified from Briggs, 2013).

Recent advances in cryo-EM can approach a resolution of less than 2 Å (Saibil, 2022). Thus, 3D structures of individual proteins, helices, strands and side chains with a resolution about ~10 Å and amino acid residues with 3.5 Å size (Mandelkern et *al*., 1981) can be achieved. Moreover, recent developments in superresolution microscopy and cryo-EM allow one to resolve 3D structures and localisation of particular proteins in cells and tissues in their native biological state (Jing *et al.*, 2021; Lovatt, Leistner and Frank, 2022).

1.2.6. Cryo-EM to elucidate protein structures in their native environment

In cryo-ET protein structures and protein composition of subcellular compartments can be investigated in ultrathin (50 - 150 nm) sections from cells or tissue. Sample preparation in cryo-ET involves plunge freezing of cells grown on grids followed by cryogenic focussed ion beam (cryo-FIB) milling (Figure 6 A) which produces a thin vitreous layer on EM grids (Schaffer *et al.*, 2015) or plunge freezing of biochemically fractionated tissue homogenates (Figure 6 B). High pressure freezing (Dubochet and McDowall, 1981) and subsequent freeze substitution (Figure 6 C; Simpson, 1941) or sectioning by cryo-ultramicrotomy (Figure 6 C; Al-Amoudi, Norlen and Dubochet, 2004) to perform cryo-EM of vitreous sections (CEMOVIS; Dubochet, 2012) provides an alternative workflow. The theoretical background for HPF was described by Le Chatelier in The Equilibrium Law (Hatta, 1987). The freezing point is lowered which reduces the rate of ice crystal formation.

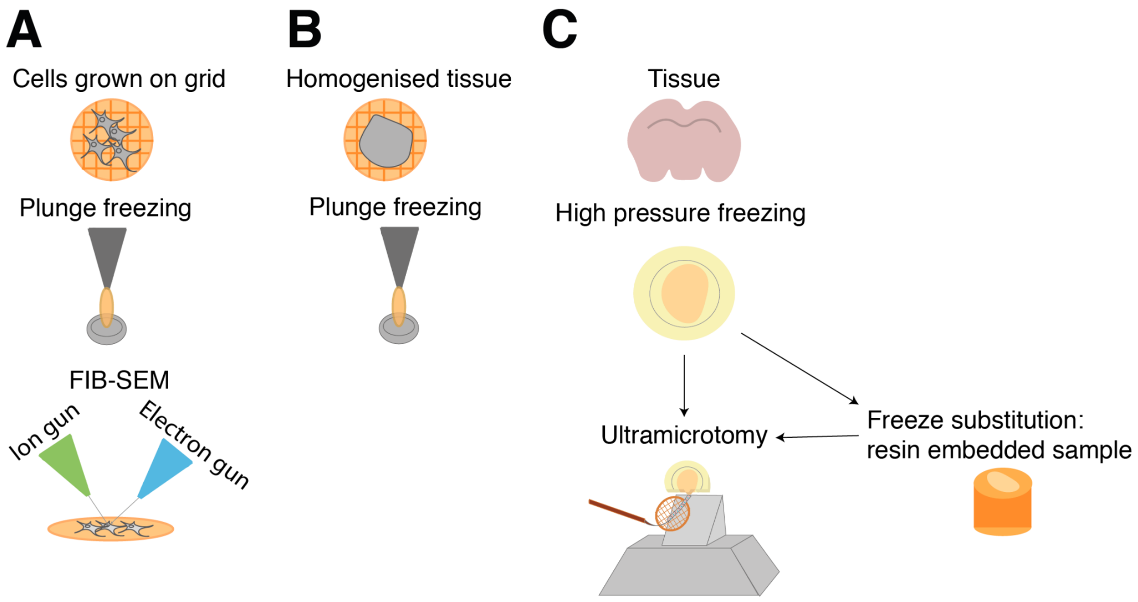

Figure 6: Sample preparation methods to vitrify biological specimens. Cells grown on grids can be plunge frozen followed by milling into a thin layer (A). Alternatively, biochemically fractionated tissue can be applied to the grid and plunge frozen (B) or a tissue biopsy can be high pressure followed by either cryo-ultramicrotomy or freeze substitution where the tissue is slowly warmed up to room temperature and at the same time infiltrated with resin. The resin embedded tissue is then sectioned into ultrathin samples at room temperature.

The advantage of CEMOVIS is that samples are not fixed and do not show any embedding artefacts or dehydration. Hence CEMOVIS reveals the cellular architecture in its native state with a resolution that is much higher than in light microscopy. Moreover, in contrast to light microscopy, no labels are required. To give an example, 3D models of macromolecular complexes and actin filaments of eukaryotic cells have been obtained by CEMOVIS (Hatta, 1987; Medalia *et al.*, 2002). However, cryo-sectioning causes cutting damage (Dubochet, 2012). FIB milling provides an alternative to prevent formation of this cutting damage.

First 3D reconstruction of structures within different cell organelles were obtained by cryo-FIB scanning electron microscopy (SEM) on HPF tissue (Dubochet, 2012; Schertel *et al.*, 2013). Cryo-FIBSEM provides a fast technique to reconstruct a volume of frozen thick specimens, because tissue is preserved in its native biological state. The first study that successfully applied cryo-FIB milling and lift out to tissue was performed on C.elegans tissue (Dubochet, 2012; Schertel *et al.*, 2013; Schaffer *et al.*, 2019). Thus, this could provide a powerful alternative to CEMOVIS in the future.

One major advantage of cryo-ET is that it requires no heavy metal staining for contrast enhancement, instead a low contrast is generated by defocus phase shift. Hence, different methods have been developed to enhance contrast and increase signal-to-noise ratio, including phase plates (Danev *et al.*, 2014; Guerrero-Ferreira and Wright, 2014) and energy filters (Schröder, Hofmann and Ménétret, 1990).

The cryo-EM consists of multiple electromagnetic lenses that focus the electron beam which is generated by an electron gun (field emission gun: FEG). The aperture lens which is located in the back focal plane after the sample eliminates the electrons that scatter at high angles which improves the contrast of the image (Figure 7 A).

The image is recorded by a detector and the contrast is generated by absorption of part of the electron beam by the sample which generates amplitude contrast. However, amplitude contrast is very low in biological samples because they consist of light atoms. Phase contrast is a result of scattering events when the electron beam collides with the sample. Inelastic scattering occurs when the electron beam collides with nuclei or electrons of an atom and energy is lost, these electrons are usually filtered out before the beam hits the detector. Elastic scattered electrons are deflected and the energy is unchanged (Figure 7 B). The variations in phases are encoded into amplitude variations which can be captured by the detector. The phase plate is inserted into the back focal plane to shift the phase of the electrons to introduce a higher phase contrast by generating constructive interference (for review see Orlova and Saibil, 2011).

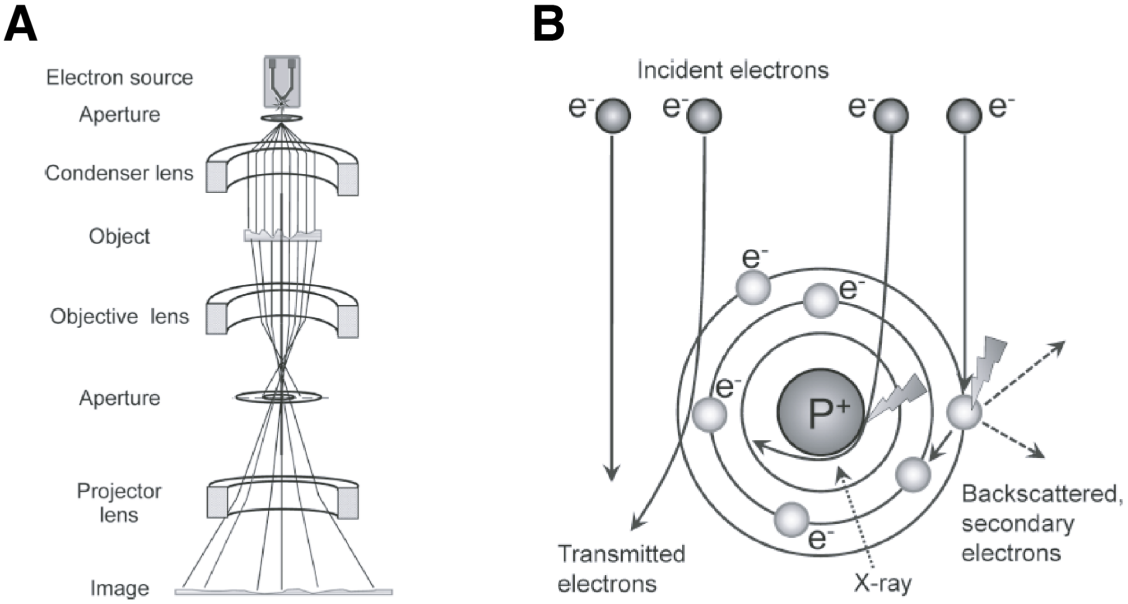

Figure 7: Anatomy of an electron microscope (A) and scattering of electrons (B, taken from Orlova and Saibil, 2011).

One limitation of EM is radiation damage which is introduced when electrons interact with macromolecules of the sample. In classical EM, heavy metals resist the radiation damage. In cryo-EM samples are not stained with heavy metals, thus electron micrographs are collected with low electron dose (Nogales, 2016).

Recent advances in cryo-EM enable investigation of in-situ structure of single proteins in their native environment, such as membrane receptor and receptor complexes. Furthermore, structure and dynamics of synaptic proteins, the organisation of the cytoskeleton, in particular the architecture and dynamics of actin and tubulin filaments and their interaction with motor proteins have been revealed by cryo-EM (Downing and Nogales, 2010). In addition, structures of protein aggregates in neurodegenerative diseases can be observed in order to obtain possible drug targets. Previously, most of these studies have been performed on recombinant proteins or on cell cultures. Localisation and structures of recombinant α-synuclein, synthetic amyloid fibrils, *in-vitro* seeded amyloid fibrils collected from human AD brain tissue and neurofibrillary tangles purified from a post-mortem Alzheimer's disease brain were investigated by EM (Boassa *et al.*, 2013; Lu *et al.*, 2013; Schmidt *et al.*, 2015; Wälti *et al.*, 2016; Fitzpatrick *et al.*, 2017). Cryo-ET has the potential to reveal the in-tissue structure of these aggregates in the brain and their native environment.

1.2.7. Summary of techniques in structural biology

Overall, the various microscopy techniques have different limitations and advantages. Sample preparation is much more time consuming and harsh for electron microscopy, X-ray crystallography and NMR spectroscopy in contrast to fluorescence light microscopy. The latter allows us to study tissue and cells in their native *in-vitro* or *in-vivo* state using a fluorescent marker in cell cultures, acute tissue slices or alive mice. One limitation is the resolution, in light microscopy a dye is imaged, not the structure itself. Similarly, in classical EM the contrast is generated by heavy metals. Cryo-EM on the other hand is a powerful tool to study the native structure of proteins. CEMOVIS enables us to study proteins in their native environment (Table 4). Thus, multiple techniques can be combined using correlated light and electron microscopy.

Technique	Lateral Resolution	Imaging depth	Experimental approach	Resolution enhancement
confocal microscope	200 nm		fixed specimen	pinhole, laser scanning to decrease PSF
2PM	200 nm	1 mm	*in-vivo* imaging	2 photons with low intensity to prevent photobleaching
STED	60-80 nm	120 µm	*in-vitro* imaging	depletion laser to reduce PSF
STORM/ PALM	20-30 nm	50-60 nm	*in-vitro* imaging	genetically encoded photoswitchable fluorophores/small photoswitchable organic dyes
Resin embedded negative stain EM	20 Å (Scarff *et al.*, 2018)	TEM (ultrathin sections	resin embedded tissue or cells	contrast generated by heavy metal staining cryo-EM 1.8 Å vitrified tissue in native state, single particle structure
cryo-ET	5.6 Å (O'Reilly *et al.*, 2020)	TEM (thin layer of ice, ultrathin cryo-sections)	Plunge frozen or high pressure frozen intakt tissue or cells Plunge frozen viral particles	contrast generated by defocus phase shift, phase plate, energy filters, processing: subtomogram averaging
SPA	1.54 Å (Kato *et al.*, 2019)	TEM (thin layer of ice)	Plunge frozen, purified proteins	contrast generated by defocus phase shift, phase plate, energy filters, processing: classification and refinement

X-ray crystallography	0.48 Å (Schmidt *et al.*, 2011)		crystals of protein	measuring angles and intensities of these diffracted beams
NMR spectroscopy	Single molecules		analyte in deuterium lock solvent	Application of strong magnetic field to molecules, measuring resonant frequencies of the nuclei

Table 4: Light microscopy techniques and tools in structural biology to visualise or detect cells, tissue and individual proteins. Their resolutions, limitations, specimens and methods to improve contrast, thus improving resolution are shown.

1.3. Aim

Although much is known about AD, the in-tissue structure of Aβ fibrils and their surrounding tissue architecture remains unknown. Revealing the native structure and most prevalent state of the Aβ fibrils in the brain will contribute to designing new experiments to understanding of the mechanisms underlying AD.

Structure of protein aggregates which cause neurodegenerative diseases have been studied extensively *in-vitro* and *ex-vivo*. In these studies, proteins were purified from their native tissue environment which can cause artefacts and it is unclear whether a fraction of the proteins are lost.

Here, cryo-CLEM in combination with cryo-ET was utilised to elucidate the native in-tissue structures in AD brains. A novel workflow was developed and is described in Chapter 3 (Development of a sample preparation workflow for in-tissue correlated imaging).

High pressure freezing was applied to prevent ice crystal formation and to preserve the native structure of the tissue. Using fluorescent labels, Aβ plaques and their surrounding environment can be studied by cryo-CLEM. Furthermore, in future different markers for astrocytes, microglia, synapses and other cell organelles can be co-labeled to determine alterations in their structure. This workflow can be used to study pathology in post mortem tissue of Alzheimer's disease patients. This new approach can also reveal new insights into possible disease mechanisms and structural alterations and therefore results can help to design new experiments to answer fundamental questions: how does the disease develop and progress? What are possible triggers for onset of AD and what can prevent onset and progression?

Here, this workflow was applied to *App*$^{NL\text{-}G\text{-}F}$ knock-in mice to study the native in-tissue structure of Aβ plaques and the tissue surrounding these plaques in Chapter 4 (Qualitative analysis to determine the in-tissue architecture of amyloid beta plaques and their surrounding environment). These first in-tissue tomograms revealed the diverse composition of Aβ plaques in their native state.

Lastly, these cryo-ET data were analysed to quantify the heterogeneity of Aβ fibrils and other macromolecular features found within plaques as described in Chapter 5 (Quantitative analysis of data).

2. Material and Methods

2.1. Laboratory Animals

Laboratory animals were housed and bred according to British Home Office Regulations, local ethical approval, and NIH guidelines. *App*$^{NL\text{-}G\text{-}F}$ knock-in mice (13 - 14 months) were generated as described previously (Saito *et al.*, 2014a). Oversight and approval was also provided by the University of Leeds Animal Welfare and Ethical Review Board.

2.2. Chemicals

Chemical	Company	Serialnumber
NMDG	Sigma	M2004
NaCl	Fisher Science UK	S312063
KCl	BDH Laboratory Supplies	102104V
NaH2PO4	Sigma-Aldrich	31437
NaHCO3	Sigma	S7778
HEPES	Sigma	H4034
Glucose	Sigma	G8270
sodium ascorbate	Sigma	11140
Thiourea	Sigma-Aldrich	T7875
sodium pyruvate	Sigma	P2256
MgSO4.7H2O	Scientific Laboratory Supplies	CHE2460.00
CaCl2.2H2O	BDH Laboratory Supplies	100704Y
PBS	Gibco	2026-05
Dextran	Sigma	31389
Triton-X-100	Sigma	93443

Chemical	Company	Serialnumber
PFA	Sigma	F1268
BSA	Fisher Chemicals	BPE1605

Table 5: Chemicals used, manufacturers and serial numbers.

2.3. Fluorescence assay

Mice received an intraperitoneal (i.p.) injection of 5 mg/kg Methoxy-X04 in 10% Dimethyl sulfoxide (DMSO) containing PBS (by René Frank) to stain amyloid-β plaques. Twenty-four hours after injection, mice were culled by neck dislocation (Schedule 1). Then, brains were dissected out. Forebrains were homogenised in HEPES buffered artificial cerebrospinal fluid (HACSF, 25 mM HEPES, 120 mM Sodium chloride, 5 mM Potassium chloride, 1.2 mM Magnesium chloride, 2 mM Calcium chloride, 25 mM HEPES, 30 mM Glucose) and fluorescent signal was examined with a plate reader (Tecan Spark) in a 96 well plate at excitation: 350/20nm, emission: 460/20. Statistics were performed in R using a one-way unpaired ANOVA to test for differences between groups (α=0.05). Then, multiple pairwise-comparisons between the means of groups were tested with Tukey post-hoc test (α=0.05).

2.4. Purification of Aβ fibrils

Fibrils were purified from *App*$^{NL\text{-}G\text{-}F}$ knock-in mice by Stanley Goodbody following the protocol from (Yang *et al.*, 2022, no date).

2.5. Staining of recombinantly expressed Aβ fibrils

Recombinantly expressed Aβ fibrils (kindly provided by Sheena Radfords group were stained with 1 mg/ml Methoxy-X04 for 30 min and centrifuged at 100,000 x g. Supernatant was removed and fibrils were resuspended in phosphate buffered saline (PBS, 137 mM Sodium Chloride, 2.7 mM Potassium Chloride, 10 mM Sodium Phosphate Dibasic, 1.8 mM Potassium Dihydrogen Phosphate). These steps were repeated three times.

2.6. Homogenisation of brain tissue

Mice received an intraperitoneal (i.p.) injection of 5 mg/kg Methoxy-X04 in 10% Dimethyl sulfoxide (DMSO) containing PBS. Twenty-four hours after injection, mice were culled by neck dislocation (Schedule 1). Then, brains were dissected out and forebrains were homogenised in ice cold HACSF by applying 12 strokes of a Teflon-glass pestle and mortar.

2.7. Plunge freezing

Mice received an intraperitoneal (i.p.) injection of 5 mg/kg Methoxy-X04 in 10% Dimethyl sulfoxide (DMSO) containing PBS. Twenty-four hours after injection, mice were culled by neck dislocation (Schedule 1). Then, brains were dissected out and homogenised in HACSF. Brain homogenates were diluted in HACSF (1:50) and 10 nm bovine serum albumin (BSA)-gold (5:1, BBI Solutions, EM.BSA10). Then, 5 µl of the homogenate or recombinantly expressed Aβ fibrils were applied to a glow discharged (Cressington glow discharger, 60 s at

10^{-4} mbar, 15 mA) Quantifoil R 1.2/1.3, 300 mesh Au grid (Quantifoil Micro Tools), plotted from the back for 3-9 s with filter paper (Whatman, 1001-090) and plunge-frozen in liquid ethane on a FEI Vitrobot MK IV (Thermo).

2.8. Preparation of acute slices

Mice received an i.p. injection of 5mg/kg Methoxy-X04 in 10% DMSO containing PBS. 24 hours after injection mice were injected with pentobarbital and intracardially perfused with N-methyl-D-glucamine (NMDG)-HEPES solution (93 mM NMDG, 2.5 mM Potassium chloride, 1.2 mM Sodium hydrogen carbonate, 20 mM HEPES, 25 mM Glucose, 5 mM Sodium ascorbate, 2 mM Thiourea, 3 mM Sodium pyruvate, 10 mM Magnesium sulphate heptahydrate, 0.5 mM Calcium chloride dihydrate, Ting et al., 2014, Osmolality = 300 - 315 mOsmol/kg, pH 7.4). Brains were retrieved and 100 µm thick acute slices were prepared using a vibratome (speed 0.26 mm/s, Leica, VT1200S, Campden Instruments Limited blades, J52/11SS blades) in ice-cold carboxynated NMDG-HEPES solution. Additional staining on acute slices for *App*$^{NL-F}$ x *PSD95*$^{eGFP/eGFP}$ mice was performed for 1 h in 24-well plates with FLAG-Cy3 antibody (Sigma, A9594), followed by 3 washes (5 min each) in carboxynated NMDG-HEPES solution.

2.9. Confocal Microscopy and Immunohistochemistry

For immunohistochemistry, acute brain slices were cut and free-floating sections were fixed in 4% Paraformaldehyde (PFA), blocked in 5% BSA, 0.1%

Triton-X100 containing Tris Buffered Saline (TBS, 50 mM Tris-Cl, 150 mM NaCl) and after three washes with TBS incubated with 6E10 anti-amyloid-beta 1-16 mouse IgG1 (1:750, Biolegend, 803001) in 0.1% Triton-X100 containing TBS at 4°C for 24 h. After three washes in TBS, slices were incubated with anti-mouse-IgG1-AF-633 (1:1000, Lifetechnologies, A21126) in 0.1% Triton-X100 in TBS for 48 h at 4°C. After 3 washes, slices were mounted in Vectashield (Vector Laboratories) on superfrost slides (Erpredia, J1810AMNZ) with coverslips (Academy, 0400-8-18). Images were captured with a confocal laser scanning microscope (Zeiss LSM 700) using a 10/0.3 and a 20x/0.5 numerical aperture (NA) air objective lens, with frame size 1024x1024 pixels and 512x512 pixels, respectively.

Fluorophore	Excitation	Emission
Methoxy-X04	405 nm	435 nm
AF-633	639 nm	669 nm

Table 6: Excitation and emission wavelength of different fluorophores.

2.10. High pressure freezing

Acute brain slices were cut on a vibratome (speed 0.26 mm/s, Leica, VT1200S, Campden Instruments Limited blades, J52/11SS blades) and 2 mm diameter cortical tissue biopsies were taken. These were incubated in cryoprotectant (20% 40,000 Dextran +/- 10% Sucrose in NMDG-HEPES solution) adapted from (Zuber *et al.*, 2005) for 30 min - 1 h RT. 100 µm deep wells of the specimen carrier type A (Leica, 16770152) were filled with cryoprotectant, tissue biopsies were carefully placed inside and covered with the flat side of the lipid-coated specimen carrier type B (Leica, 16770153). Carriers were then loaded into the cartridge of the Leica EM ICE and high pressure frozen.

2.11. Cryo-ultramicrotomy

High pressure frozen sample carriers were imaged with a cryo-fluorescence microscope (cryo-FM, Leica EM Thunder) at -180°C to determine the location of Aβ plaques. The brightest fluorescent signal with an excitation of 350/50 nm and emission of 460/50 nm underneath the surface of ice were chosen for cryo-sectioning. Then, the distance from Aβ plaque of interest to the edge of the carrier was measured. All images were captured using a HC PL APO 50/0.9 NA cryo-objective lens with 50x zoom factor and a frame size of 2048x2048 pixels. Based on the orientation of tissue and location of Aβ plaques, carriers were mounted into the specimen holder, so that tissue ribbons could be cut from the target. Cryo-sectioning was performed using a Leica EM FC7. Carriers were trimmed with a diamond knife (Diatome, trim 45, T1865 and trim 20, T399). 70 - 150 nm thin sections were cut at -150°C with a diamond knife (Diatome, cryo immuno, MT12859). Sections were picked up with a gold eyelash and adhered onto a glow discharged (Cressington glow discharger, 60 s, 10^{-4} mbar, 15 mA) 3.5/1, 300 mesh Cu grid (Quantifoil Micro Tools) using an electrostatic gun (Pierson *et al.*, 2010) and micromanipulators (Studer *et al.*, 2014; Nakane *et al.*, 2020).

2.12. Cryogenic fluorescence microscopy

Ultrathin cryo-sections and high pressure frozen tissue inside gold carriers were screened for fluorescence using a cryogenic fluorescence microscope Leica EM Thunder with a HC PL APO 50x/0.9 NA cryo-objective, Orca Flash 4.0 V2 sCMOS camera (Hamamatsu Photonics) and a Solar Light Engine (Lumencor). Filters used: DAPI filter set (excitation 365/50, dichroic 400, emission 460/50) GFP filter set (excitation 470/40, dichroic 495, emission 525/50), Rhodamine filter set (excitation 546/10, dichroic 560, emission 525/50) and Cy5 filter set (excitation 628/40, dichroic 560, emission 628/40). The images were acquired with frame size 2048x2048 pixels. Z-stacks of ultrathin cryo-sections were acquired with 30% intensity and an exposure time of 0.2 s. Tile scans of high-pressure frozen carriers were acquired with 17% laser intensity for 0.1 s. Images were processed using Fiji ImageJ (Schindelin *et al.*, 2012).

2.13. Cryogenic correlated light and electron microscopy (cryo-CLEM)

The location of amyloid plaques in ultrathin cryo-sections was assessed by cryogenic fluorescence microscopy of Methoxy-X04 (excitation 370 nm, emission 460-500 nm). Grid squares that contained a signal for Methoxy-X04 under DAPI filter sets were then selected for electron tomography. Regions that contained bright fluorescence signals, dim fluorescence as well as regions around the plaque without a fluorescent signal, within holes of the carbon were selected for a batch collection of cryo-electron tomographic tilt series. The location of plaques on the EM grid was mapped in the cryo-FM images to guide the tomogram collection. First, an EM atlas (tile scan of the whole EM grid) was collected at 370 x magnification per tile, 0.23 s exposure and an illumination area of 1100 µm (pixel size: 34.97 nm, total dose: 0.01 e/nm^2). Next, an electron micrograph of the grid square that showed a signal in cryo-FM images was captured at 1200 x magnification, 0.21 s exposure and 313 µm illumination (pixel size: 10.59 nm, total dose: 0.02 e/nm^2). A magnification of 15,000 x with 0.68 s exposure time and 10.38 µm illumination (pixel size: 1.7 nm, total dose: 10.4 e/nm^2) was chosen to visualise individual holes in the 3.5 µm holey carbon film of the grid. The correlation between fluorescent images and electron micrographs after tomogram collection was performed using a Matlab script according to previous experiments (Schorb and Briggs, 2014); (Kukulski *et al.*, 2011). The centres of 10 holes in the carbon foil surrounding the region of interest were used as fiducial markers to align the cryo-FM and cryo-EM images.

2.14. Cryo-electron tomography and image reconstruction

Tilt series of locations selected by cryogenic fluorescence microscopy were collected with a FEI Titan Krios G2, X-FEG and autoloader (Camera: Energy filtered Gatan K2 XP summit direct electron detector and FEI Ceta; Voltage: 300 KeV) equipped with BioQuantum energy filter (Gatan Inc.) from +60° to -60° in increments of two using a dose symmetric tilt-shift (Hagen, Wan and Briggs,

2017) in serialEM (Mastronarde, 2005). Two of the datasets were collected with a Volta phase plate (Fukuda *et al.*, 2015) conditioned to 0.4 - 0.7 π rad with a 0.8 to 1.3 μm defocus and two datasets were collected with 5.0 to 6.5 μm defocus and a 100 μm condenser aperture. Each tilt increment received 2 s exposure (fractionated into 8 movie frames) at a 0.5 $e^-/Å^2/s$ dose rate, resulting in a total dose per tilt series of ~61 electrons and pixel size of 3.42 Å. Dose fractions were aligned and tomograms were reconstructed using patch tracking in IMOD (Kremer, Mastronarde and McIntosh, 1996). Contouring of fibrils and membranes was performed in Dynamo (Castaño-Díez *et al.*, 2012), membranes were divided into different categories according to their shape. Fibrils were picked using the filament along axis function and membrane with the membrane by layers in each z position.

2.15. Deconvolution

Gctf (Zhang, 2016) was used for contrast transfer function (CTF) estimation to determine the defocus values for each tomogram. These values were used in a matlab script with a Wiener-like filter (tom_deconv package:https://github.com/dtegunov/tom_deconv) that is part of the software warp (Tegunov and Cramer, 2019, no date) to deconvolve the CTF in tomograms with deconvolution strength of 10.8 snr falloff of 1 and high pass nyquist of 0.05.

2.16. Fourier analysis of fibril architecture

Fourier analysis was performed to quantitatively assess the arrangement of amyloid fibrils in parallel bundles. In Fiji ImageJ, boxes (size 32x32 nm) were drawn along parallel bundles and meshwork to obtain regions of interest (ROIs) from tomograms for further analysis. The in-built fast Fourier transformation (FFT) function was used to generate a power spectrum for each ROI. Images were rotated 180 times by 1° in order to generate circular power spectra for each region. The power spectrum of each ROI was generated and the overall average per parallel bundle/ meshwork was calculated. Line profiles of the power spectra were taken and the distance between the origin and Fourier peaks was measured to determine whether the fibrils were organised parallel or into a meshwork.

2.17. Measurement of fluorescent Intensities

After cryo-FM and cryo-EM images were correlated, boxes in size of tomograms were drawn on cryo-FM images. In Fiji ImageJ, the size of cryo-FM images were adjusted to match the size of tomograms. Then, boxes (size 32x32 nm) were drawn at FFT regions. Fluorescent intensities were measured in cropped images and paired t-test was performed to measure differences between fluorescence of parallel bundles and meshwork.

2.18. Measurements of fibril diameter

To measure diameters of fibrils the coordinates of the outside edges of fibrils were marked in IMOD (Kremer, Mastronarde and McIntosh, 1996). The Euclidean distance between pairs of points on the edges of fibrils was computed in Matlab. Tomograms with low signal to noise, poor reconstructions and without Methoxy-X04 signal in CLEM were excluded. Welch t-test (α = 0.05) was performed using R to compare *ex-vivo* and in-tissue tomograms. One-way ANOVA and Tukey post-hoc test was performed to compare individual in-tissue tomograms.

2.19. Subtomogram averaging

Particles were picked in IMOD. Subtomogram averaging was performed using Peet (Nicastro *et al.*, 2006; Heumann *et al.*, 2011). Initial reference was generated using three tomograms from purified fibrils (pixel size = 11.60 Å) with a box size of 20 voxels, a cylindrical mask (15 voxels) from 125 particles. Particles were aligned to the tomogram Y-axis and reference was refined in every iteration. The reference was scaled to match the pixel size of the in tissue tomograms (13.68 Å) using EMAN2 (Tang *et al.*, 2007). Subtomogram averaging on in-tissue tomograms was performed with a box size of 20 voxels and a cylindrical mask (14 voxels) from 187 particles. Particles were aligned to the tomogram Y-axis and reference was the same in every iteration.

2.20. Software

Software	Version
ChimeraX	1.1.1
EMAN2	2.3
Fiji ImageJ	2.0.0-rc-69/1.52i
Gctf	1.18
IMOD	4.10.30
Peet	1.15.0
R	1.2.5042
SerialEM	3.8
Tom_deconv (warp)	3
Tomography (TOMO)	5.8

Table 7: Software versions used.

3. Development of a sample preparation workflow for in-tissue correlated imaging

3.1. Results

3.1.1. Introduction

New avenues to understand disease mechanisms and structural alterations in the AD brain were explored. The results of this study can help to design new experiments to answer fundamental questions: which structures are found within an Aβ plaque? Which mechanisms are involved in the disease?

To date, the native in-tissue structure of Aβ fibrils and surrounding tissue architecture remains unknown, thus we performed cryo-ET of vitreous specimens. To do so, a humanised mouse model of AD, namely *App*$^{NL\text{-}G\text{-}F}$ knock-in mice (Saito et al., 2014) that has three familial AD mutations was utilised.

This mouse model was chosen in particular because subcortical and cortical amyloidosis starts after 2 months and becomes saturated after 7 months, thus mice do not have to be aged for longer than 7 months.

Here, I established a novel sample preparation workflow using high pressure freezing to vitrify fresh brain tissue from *App*$^{NL\text{-}G\text{-}F}$ knock-in mice and determine the native in-tissue molecular architecture of Aβ plaques. Different approaches for labelling, vitrification, cryo-ET, cryo-CLEM and challenges that had to be overcome will be described in this chapter.

Lastly, I applied my workflow to another AD mouse model with multiple additional knockin mutations, *App*$^{NL\text{-}F}$ *x PSD95*$^{eGFP/ePFP}$ *x GluN1*$^{TAP/TAP}$ triple knock-in (Frank *et al.*, 2016) to test multiple labelling modalities in my new cryo-CLEM workflow. These mice have two mutations associated with AD, namely the Swedish mutation ("NL") and the Iberian mutation ("F"). In addition, mice have an eGFP tag on the postsynaptic density protein 95 (PSD95) which is a marker for mature synapses. PSD95 was shown to be decreased in AD synapses (Shao *et al.*, 2011) and therefore the GluN1 subunit of N-methyl-D-aspartate receptor (NMDA-R) is tagged in these mice to enable us to study synapses in AD. Synaptic loss in transgenic mice has been shown in close vicinity of the plaques (Spires *et al.*, 2005; Koffie *et al.*, 2009). Moreover, changes in expression and unconventional signalling of NMDA-R has been observed in AD models (Liu *et al.*, 2019). The novel workflow I developed was adapted to study synaptic alterations in *App*$^{NL\text{-}F}$ *x PSD95*$^{eGFP/ePFP}$ *x GluN1*$^{TAP/TAP}$ triple knock-in mice.

The workflow that was established allows us to study the native in-tissue molecular architecture of amyloid pathology in the brain for the first time.

3.1.2. Cryo-CLEM labelling of Aβ

In order to label Aβ plaques for cryo-CLEM 13 - 14 months old *App*$^{NL\text{-}G\text{-}F}$ knock-in mice were i.p. injected with 5 mg/kg Methoxy-X04, a small fluorescent dye, that can penetrate the blood brain barrier and binds to dense-core plaques (Klunk *et al.*, 2002). To confirm that Methoxy-X04 labels Aβ plaques within 24 h after intraperitoneal (i.p.) injection of mice, acute slices[3] were fixed and stained for immunofluorescence microscopy. Samples were stained with an anti-amyloid-beta antibody that binds to the N-terminus of Aβ peptides (residues 1-16; Baghallab *et al.*, 2018) and imaged with a confocal microscope. Confocal images showed that Methoxy-X04 and the anti-amyloid-beta antibody colocalised within amyloid deposits that were ~20-25 μm in diameter, indicating that Methoxy-X04 selectively stains plaques (Figure 8 A top panel). Moreover, negative controls without the anti-amyloid antibody that were only incubated with a secondary antibody showed no fluorescence, confirming specificity of this antibody (Figure 8 A bottom panel).

To test the specificity of Methoxy-X04 in live tissue, fresh acute brain slices from Methoxy-X04 injected $App^{NL\text{-}G\text{-}F}$ and wild type mice were imaged under a confocal microscope. A fluorescent signal for Methoxy-X04 was observed in fresh acute slices of $App^{NL\text{-}G\text{-}F}$ knock-in mice, in contrast to wild type tissue (Figure 8 B).

---

[3] "Brain slices are *ex-vivo* preparations obtained by serial sectioning of brain tissue, typically from rats or mice. Acute brain slices are kept vital *in-vitro* for time periods between four and, sometimes, more than twenty-four hours and contain a functional brain cell micro-circuitry *in situ*."(Ballanyi and Ruangkittisakul, 2008)

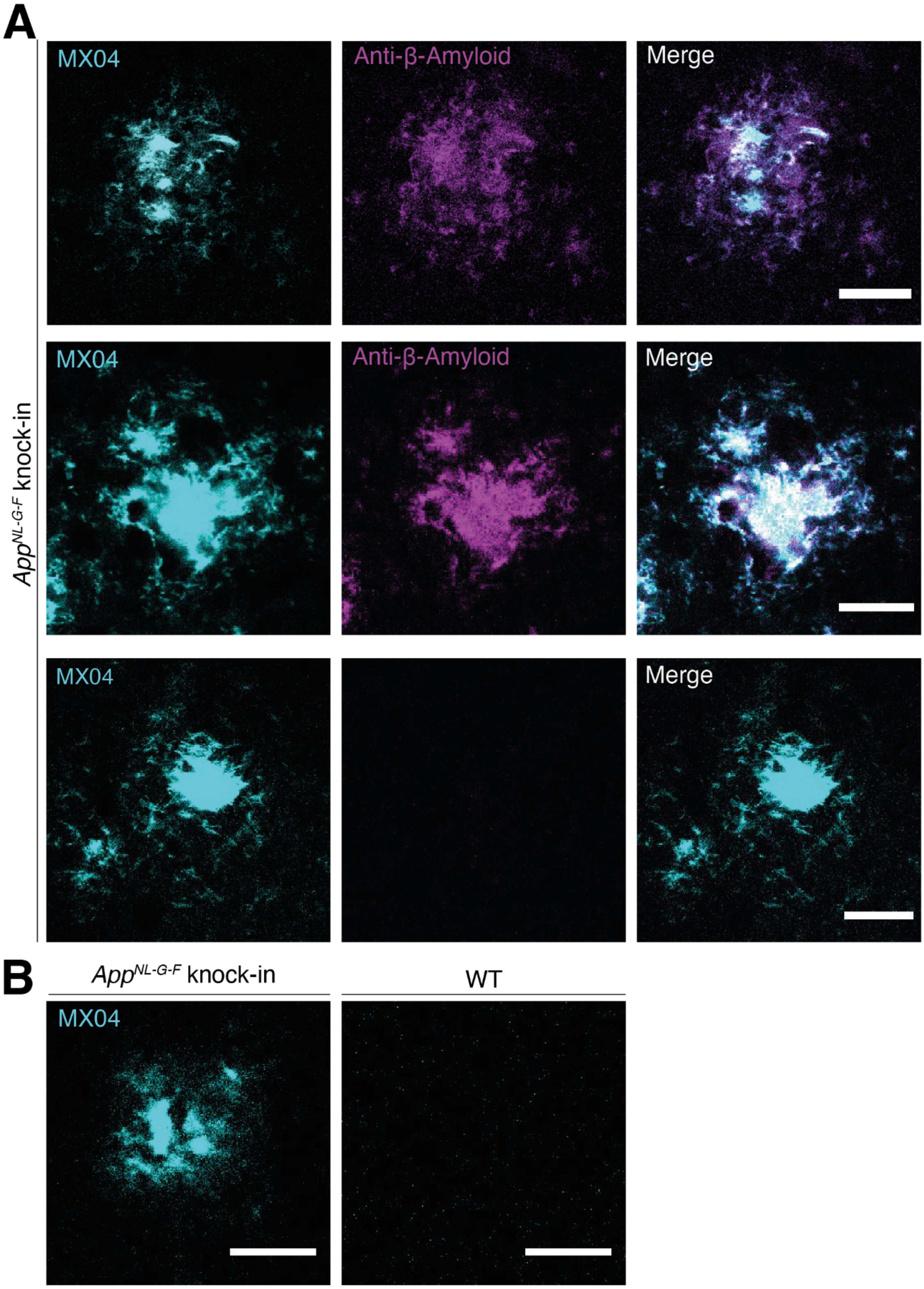

Figure 8: Validation of Methoxy-X04 specificity as a label for Aβ plaques 24 h after injection. Acute brain slices of *App*$^{NL\text{-}G\text{-}F}$ knock-in mice injected with Methoxy-X04

(cyan) and stained with an anti-amyloid-beta antibody (magenta) were imaged at a confocal microscope. Methoxy-X04 and anti-amyloid-beta antibody colocalise (Merge, n=1, top and middle panel, A) which confirmed that Methoxy-X04 specifically stains Aβ plaques. The bottom panel shows negative control, no specific signal was observed without an anti-amyloid-beta antibody (n=1, bottom panel, A). Confocal images of fresh acute brain slices from mice injected with Methoxy-X04. Left image shows a specific signal for Methoxy-X04 labelled plaques in samples from *App*$^{NL\text{-}G\text{-}F}$ knock-in mice (n=1), compared to tissue from wildtype (n=1, B). All scale bars, 20 μm..

3.1.3. Homogenisation of brain tissue and vitrification of Aβ fibrils

In order to perform cryo-EM, samples are frozen in a vitreous state. First, the forebrains from *App*$^{NL\text{-}G\text{-}F}$ knock-in mice were homogenised and plunge-frozen in liquid ethane (Adrian *et al.*, 1984). This method has been developed to preserve native structures of biological specimens without dehydration.

Therefore, 24 h after Methoxy-X04 injection into both *App*$^{NL\text{-}G\text{-}F}$ knock-in mice and wild type mice, forebrain samples were prepared following the ‘ultra-fresh’ method (Peukes *et al.*, Biorxiv). Dissected forebrains were immediately homogenised in ice-cold HEPES-buffered ACSF, applied to EM grids, blotted from the back and plunge-frozen in liquid ethane. Cryo-FM images of plunge-frozen grids from *App*$^{NL\text{-}G\text{-}F}$ knock-in mice revealed no specific amyloid signal, compared to wild type mice (Figure 9 A).

To test whether Methoxy-X04 labelled Aβ can be detected by plunge freezing, recombinantly expressed fibrils (kindly provided by Sheena Radfords group) were plunge-frozen in liquid ethane as positive control, buffer only samples as a negative control. A specific fluorescent signal was detected by cryo-FM in samples containing recombinantly expressed fibrils compared to negative controls (Figure 9 B).

To confirm the presence of Methoxy-X04 in ultrafresh samples, the bulk fluorescence was measured in a fluorometer on brain samples from Methoxy-X04 injected *App*$^{NL\text{-}G\text{-}F}$ knock-in mice and wild type mice. Samples from wild types that were not injected with the fluorescent dye showed a relatively low background fluorescence. Methoxy-X04 injected *App*$^{NL\text{-}G\text{-}F}$ knock-in mice showed a significantly higher fluorescence signal compared to Methoxy-X04 injected wild type and uninjected wild type controls (p-values shown in Table 8, Figure 9 C). This suggests that amyloid is present in the sample.

To further investigate if the amyloid signal can be measured in ultra-fresh samples, homogenates were imaged using a confocal microscope. Aβ fibrils or plaques were not observed in homogenates from Methoxy-X04 injected *App*$^{NL\text{-}G\text{-}F}$ nor wild type mice (Figure 9 D).

Two different mechanisms could explain the outcome of not being able to detect Methoxy-X04 labelled amyloid plaques in homogenised ‘ultra-fresh’ samples when using confocal imaging. Homogenisation may have caused disaggregation of Aβ plaques or fibrils into structures that are too small to be detected by fluorescence light microscopy. The concentration of Aβ plaques may have been too low following the $2.5\text{x}10^5$ dilution factor required to prepare ultra-fresh samples (forebrains homogenised in ~250 µl buffer and diluted 1:50 in immunogold).

In conclusion, the ultra-fresh method was unsuitable for the preparation of tissue samples containing Aβ plaques, since amyloid could not be detected in plunge-frozen homogenates from *App*$^{NL\text{-}G\text{-}F}$ knock-in mice by cryo-FM nor at room temperature by confocal microscopy.

Condition	**Mean Methoxy-X04 Intensity (A.U.)**	**Comparison**	**P-value**
App$^{NL\text{-}G\text{-}F}$ +	48850.5±4022	*App*$^{NL\text{-}G\text{-}F}$ + - WT+	$0.1*10^{-6}$
WT+	27005.5±6271	WT+ - WT-	$0.35*10^{-3}$
WT-	14713.5±5170	*App*$^{NL\text{-}G\text{-}F}$ + - WT-	10^{-7}

Table 8: Comparison of Methoxy-X04 intensities from fluorometer assay. Fluorescence from homogenates of *App*$^{NL\text{-}G\text{-}F}$ knock-in mice injected with Methoxy-X04 (*App*$^{NL\text{-}G\text{-}F}$ +) compared to wild type injected with Methoxy-X04 (WT+) and uninjected (WT-). Means of groups from one-way unpaired ANOVA test (p=6.71*10-11 < α=0.05) were pairwise-compared with Tukey Honest Significant Differences. Conditions that were compared and p-values from the post hoc test are shown. All conditions were significantly different from each other with α=0.05.

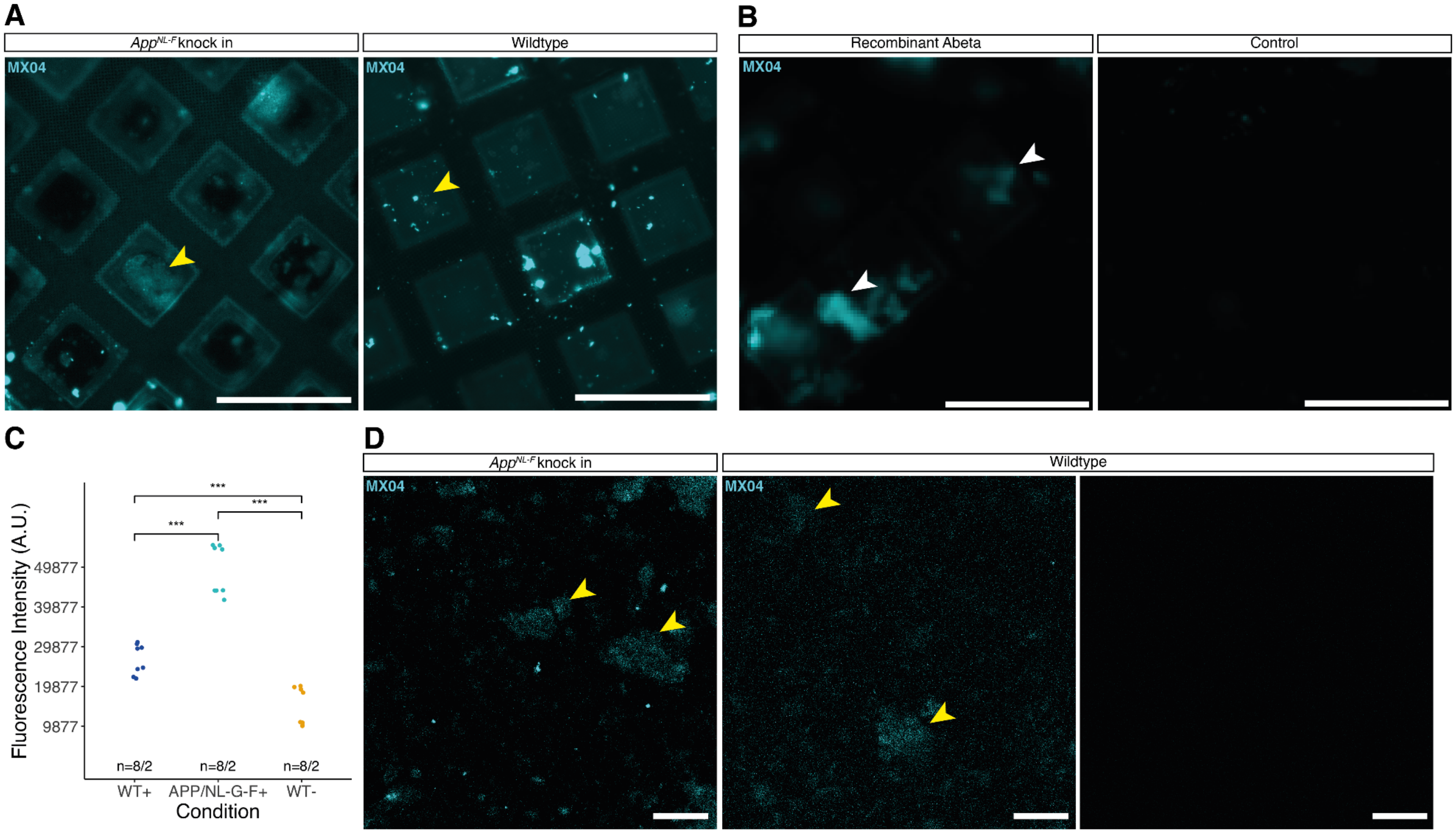
A
App^NL-F knock in
Wildtype
MX04
MX04
B
Recombinant Abeta
Control
MX04
C
***
***
***
Fluorescence Intensity (A.U.)
49877
39877
29877
19877
9877
n=8/2
n=8/2
n=8/2
WT+
APP/NL-G-F+
WT-
Condition
D
App^NL-F knock in
Wildtype
MX04
MX04

Figure 9: Applying the ‘ultra-fresh’ method for the detection of Aβ plaques in homogenised tissue. Ultra-fresh samples from Methoxy-X04 injected *App*$^{NL\text{-}G\text{-}F}$ knock-in mice (left) and Methoxy-X04 injected wild type mice (right) show no specific fluorescent signal (A). Recombinantly expressed Aβ labelled with Methoxy-X04 was plunge-frozen onto an EM grid and a specific amyloid signal was observed, in contrast to negative control where buffer was applied to grid and plunge-frozen (B). Fluorescence was measured with a fluorometer to determine Methoxy-X04 intensity of forebrains from wild type mice injected with Methoxy-X04 (WT+, n=2), *App*$^{NL\text{-}G\text{-}F}$ knock-in mice injected with Methoxy-X04 (APP/NL-G-F+, n=2) and controls (uninjected wild type, WT-, n=2). *App*$^{NL\text{-}G\text{-}F}$ samples showed the highest fluorescent signal. Fluorescence in samples from Methoxy-X04 injected wild types was higher than background fluorescence measured in control (C). Homogenised forebrains from *App*$^{NL\text{-}G\text{-}F}$ (left) and wild type (right) mice injected with Methoxy-X04 were imaged with a confocal microscope. Aβ plaques were not found in homogenates (D). Yellow arrowheads indicate nonspecific signals, white arrowheads indicate specific amyloid signals. All scale bars, 100 μm.

3.1.4. *S*ample preparation for in-tissue structure determination

To determine the native structure of Aβ plaques, its tissue environment and the overall architecture of AD brains, I established a new alternative workflow to vitrify brain tissue for cryogenic correlated light and electron tomography. 24 h after Methoxy-X04 injection, mice were perfused with NMDG-HEPES solution and brains were dissected out. Subsequently, 100 µm thick acute brain slices were cut in NMDG-HEPES solution which has been shown to preserve neurological activity and viability of acute brain slices by limiting excitotoxicity (Ting *et al.*, 2018).

Since the ultra-fresh method is not suitable to detect amyloid plaques, 2 mm tissue biopsies taken from cortex were vitrified by high pressure freezing. High pressure frozen samples were sectioned, but the plaque load of the mice was relatively low considering the size of the block face that was produced for cryo-sectioning which created a needle in the haystack problem. Therefore, the HPF samples were imaged using a cryo-FM (described in more detail in Localisation of fluorescence and cryo-sectioning). Subsequently, the plaque was targeted and ultrathin cryo-sections were cut and attached onto EM grids (Figure 10).

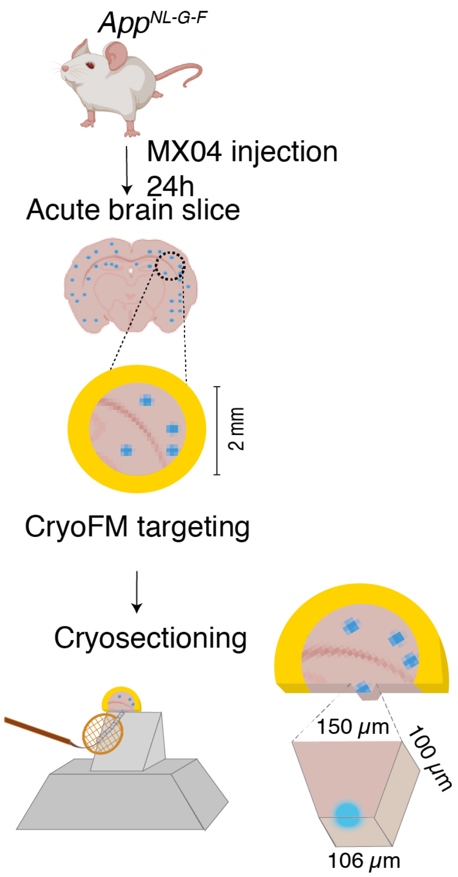

Figure 10: Workflow of sample preparation to determine native in-situ structure of amyloid β in brain tissue of *App*$^{NL-G-F}$ knock-in mice. 2 mm tissue biopsies of acute brain slices from mice that had been intraperitoneal injected with Methoxy-X04 24 h previously were high-pressure frozen. These frozen biopsies were then imaged with a cryo-FM to determine regions for cryo-sectioning. After trimming of the carriers, ultrathin cryo-sections were cut from high-pressure frozen tissue and attached to EM grids.

3.1.5. Optimising vitrification by high pressure freezing

Brain tissue has a relatively high water content (Wolthuis *et al.*, 2001). To prevent the formation of ice crystals during freezing, 2 mm tissue biopsies from acute slices were incubated in cryoprotectant and high-pressure frozen lower than 150° C at ~2,000 bar in <30 msec, then imaged by cryo-FM.

Overall, the 100 µm tissue biopsies inside metal carriers showed very high background fluorescence in knock-in and wild type samples, because the tissue is relatively thick and the gold of the carrier reflects the photons. Nonetheless, plaques inside HPF carriers had a clearly distinguishable fluorescent signal from the background (indicated by arrowheads in Figure 11 A, left), absent in wildtype tissue (Figure 11 A, right).

To validate that the signal was specific for amyloid, Methoxy-X04 stained Aβ fibrils prepared by recombinant expression were high-pressure frozen. These samples showed very similar fluorescent signals to high-pressure frozen $App^{NL\text{-}G\text{-}F}$ knock-in samples and were absent in buffer-only controls (Figure 11 B). This confirmed that Methoxy-X04 labelled amyloid can be detected by cryo-FM in vitrified tissue biopsies.

In order to optimise cryopreservation of the tissue and ensure the tissue remained as near to physiological conditions as possible, two different cryoprotectants were tested, namely 10% sucrose and 20% dextran (Figure 12 A, adapted from (Zuber *et al.*, 2005) or a cryoprotectant lacking sucrose (20% dextran Figure 12 B). Both cryoprotectants were prepared in the NMDG-HEPES solution. Therefore, 2 mm tissue biopsies were incubated in the cryoprotectant for 30-60 min, samples were high-pressure frozen, imaged with a cryo-FM to guide the cryo-sectioning and cryo-ET was performed.

Vitrification of samples was evaluated in cryo-tomographic tilt pairs after data collection by comparing multiple tilt increments from the same tilt series. Fibrils observed in tilt series were vitreous in cryoprotectants with or without sucrose as indicated by black arrowheads in Figure 12 A and B. This suggests that 20% dextran is sufficient to cryo-protect the tissue.

In contrast, partial devitrification is shown in Figure 12 C as indicated by white arrowheads. This tilt series also contained vitreous areas (black arrowheads). The devitrified area of the tilt series is identified by Bragg reflections of crystalline ice which appears as black spots because the electrons are reflected and scattered in different angles by the ice lattice (AL-Amoudi, Dubochet and Studer, 2002). The vitrified areas in the tilt pairs shown in Figure 12 C do not show the reflections of the crystalline ice, they are only seen in devitrified areas of the tilt series. The crystalline ice appears to ‘blink’ when different tilt increments are compared and thus structures look very different which introduces artefacts to the final tomogram reconstructions.

Cryo-protection of tissue with sucrose was chosen at first, because it did not show signs of devitrification. Moreover, tomograms taken from cryo-protected tissue in dextran without sucrose were vitrified. In conclusion, incubation of tissue biopsies in 20% dextran in NMDG-HEPES solution is sufficient to cryo-protect the tissue and thus was chosen for subsequent experiments to vitrify tissue samples containing Aβ plaques.

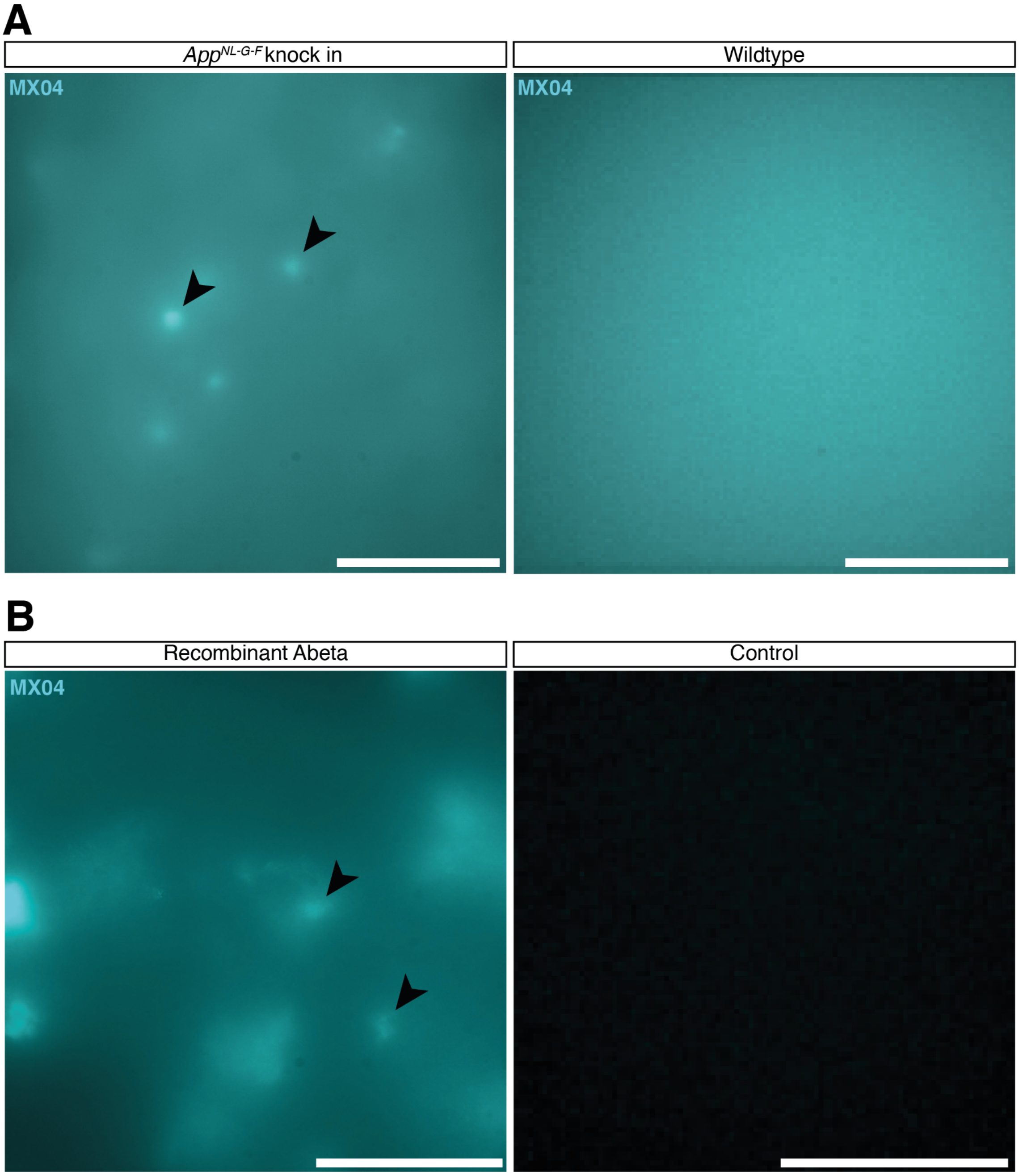

Figure 11: Cryo-FM images of high-pressure frozen tissue biopsies inside a gold carrier. Carriers show a very high background fluorescence in both, knock-in and wild type samples. Specific amyloid signals were observed in samples from *App*$^{NL\text{-}G\text{-}F}$ knock-in mice indicated by black arrowheads which could be clearly distinguished from background fluorescence (n=6), in contrast to wild type samples (n=1, A). As a positive control, Methoxy-X04 labelled recombinantly expressed Aβ fibrils were high-pressure

frozen and the high-pressure frozen buffer served as a negative control. Recombinantly expressed fibrils showed similar signals compared to samples from *App*$^{NL\text{-}G\text{-}F}$ knock-in mice whereas negative control had no fluorescent signal (n=1, B). All scale bars, 100 µm.

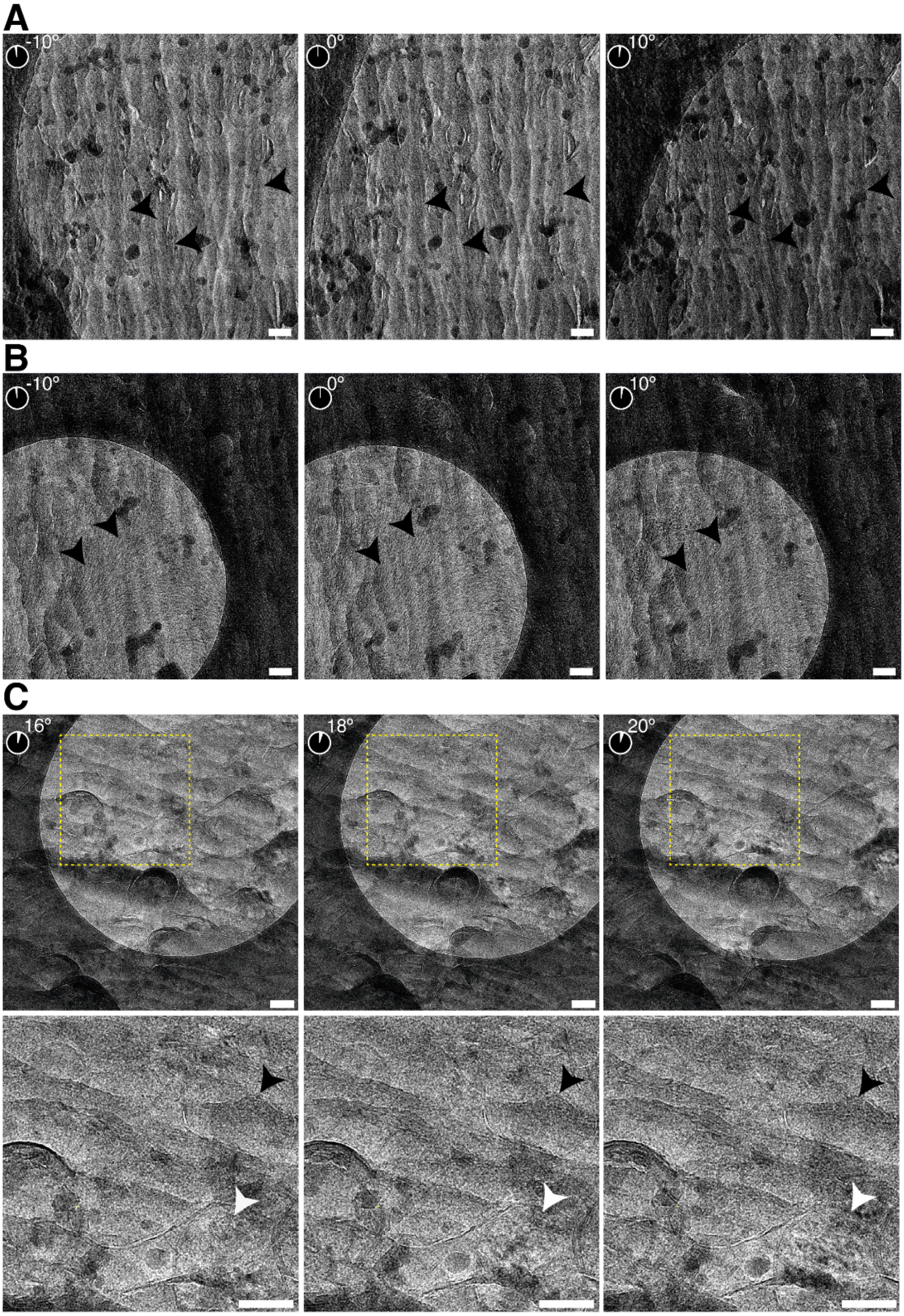
A
-10°
0°
10°
B
-10°
0°
10°
C
16°
18°
20°

Figure 12: Assessment of vitrification of Aβ fibrils with two different cryoprotectants in cryo-tomographic tilt series. Cryo-EM at -10º, 0º, +10º tilt (left to right) from samples that were high pressure frozen in NMDG-HEPES solution containing either 10% sucrose and 20 % dextran (A) or 20% dextran without sucrose (B). Fibrils were vitrified in both conditions as indicated by black arrowheads (A and B). Tilt increments from another micrograph are shown that had vitrified and devitrified regions. Micrographs at -16º, 18º and -20º tilt with black arrowheads indicating vitrified regions and white arrowheads devitrified regions of micrographs (C). All scale bars, 100 nm.

3.1.6. Localisation of fluorescence and cryo-sectioning

Next, a particular ‘needle in the haystack’ challenge was to locate the Aβ plaques (volume of ~ 14 μm^3) within the frozen tissue (~0.314 μm^3). To screen high pressure frozen samples for an amyloid signal, the cryo-FM stage was adapted to hold high-pressure frozen gold carriers. This allowed me to image the high-pressure frozen tissue within the gold carriers.

First, the carrier was examined under a stereomicroscope at room temperature (Figure 13 A) to compare the location of the tissue inside the carrier with the fluorescence image. The autofluorescence of the tissue revealed its orientation when imaged with a cryo-FM, because the tissue does not perfectly fill the carrier and the metal appears black in the background as seen in Figure 11 A and B. The metal appears black under the cryo-FM because the photons are absorbed and scattered. Thus the shape of the tissue within the carrier is compared between the stereomicroscope (Figure 13 A) and the fluorescent image (Figure 13 B).

Specific fluorescent signals of Methoxy-X04 were observed in these samples. Plaques were distinguished from ice and background fluorescence by imaging underneath the icy surface of the tissue inside carriers. As a control, high-pressure frozen tissue was imaged with a rhodamine filter cube (excitation 546/10, dichroic 560, emission 525/50). No signal can be seen in this channel, in contrast to the DAPI filter cube (excitation 365/50, dichroic 400, emission 460/50) which revealed the Methoxy-X04 labelled plaques (Figure 14).

As a next step, the nearest distance of the plaque of interest to the metal edge was measured in the cryo-FM image before the initial trimming step (Figure 13 B white line). The carrier containing the high-pressure frozen tissue sample was then oriented inside the specimen holder according to the tissue location within the well of the gold carrier. So that the plaque of interest was closest to the cutting edge.

The carriers were trimmed (Figure 13 C) and reimaged with a cryo-FM, so that the distances of the plaque of interest could be measured after trimming (Figure 13 D). Subsequently, a tissue pyramid was built for cryo-sectioning that contained the plaque of interest. Cryo-sections were cut (106 µm - 150 µm x 60 µm wide and 70 - 150 nm thick) and attached onto an EM grid using an electrostatic gun and micromanipulators.

As a quality control step, nsure cryosections were collected from a tissue pyramid containing an amyloid plaque, the gold carrier was re-imaged by cryo-FM. This confirmed that the tissue sections were collected from a Methoxy-X04 labelled amyloid plaque (Figure 13 E).

A schematic of the trimming steps and the dimensions of the tissue pyramid are shown in Figure 13 F.

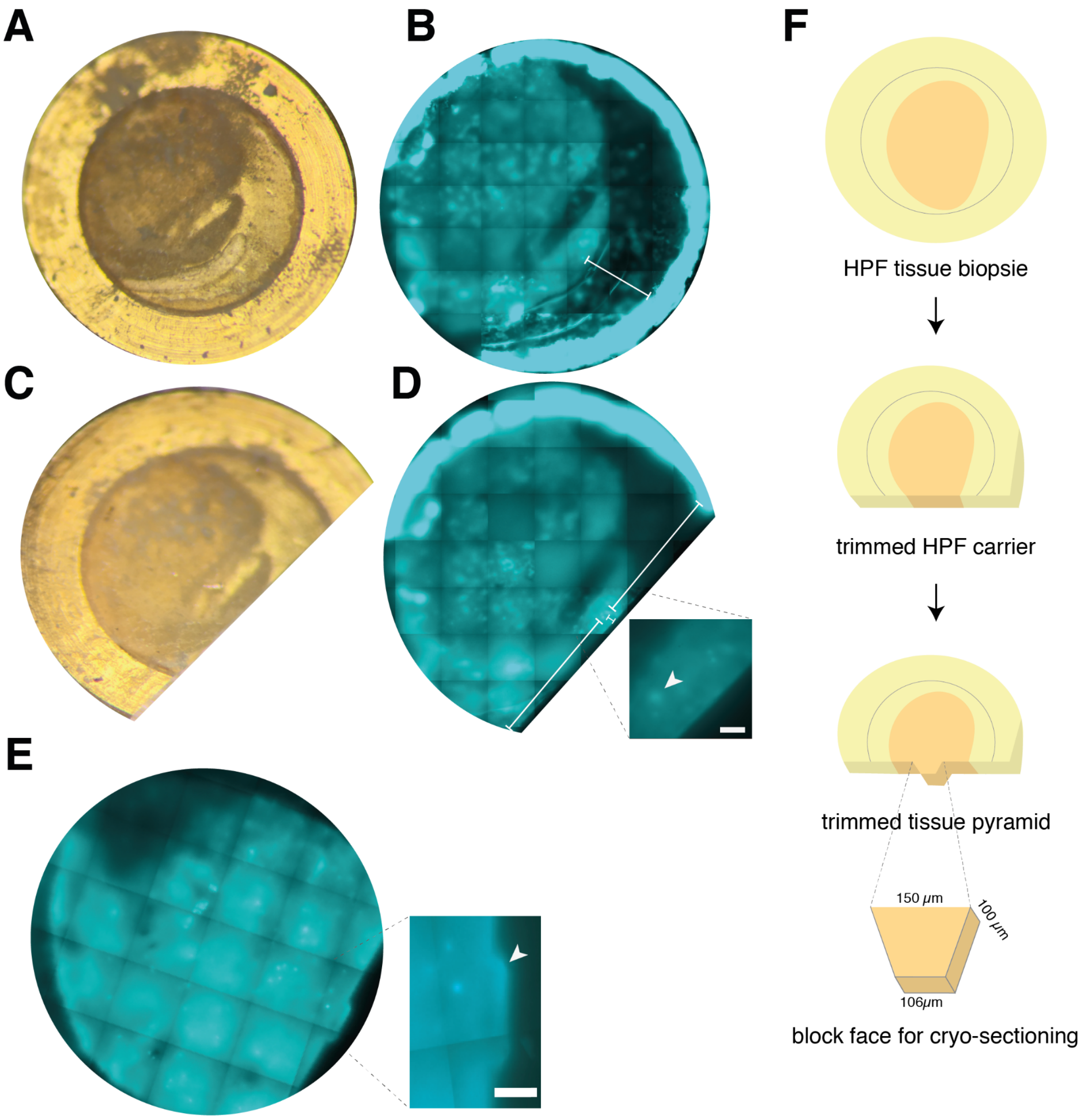

Figure 13: Targeting of fluorescent signal in HPF samples to solve the needle in a haystack problem. Carrier with HPF sample is shown under stereomicroscope of cryo-ultramicrotome which reveals the location of tissue inside the carrier (A). The same carrier was imaged with a cryo-FM. The line indicates the measurement from the edge of the carrier to one fluorescent plaque (B). Next, the carrier was trimmed (C) and reimaged with a cryo-FM (D) to measure distances from the plaque to the cutting edge and outside edges of the carrier, in order to build a pyramid (indicated by lines). Target is indicated by white arrowheads. After building a tissue pyramid the tissue was

cryo-sectioned and the carrier was reimaged under a cryo-FM to visualise the remainder of the tissue pyramid. A small portion of the plaque remained at the edge of the tissue pyramid which indicates that sections were cut from the targeted plaque (E). Schematic of individual trimming steps to build a pyramid for cryo-sectioning (F). All scale bars, 50 µm.

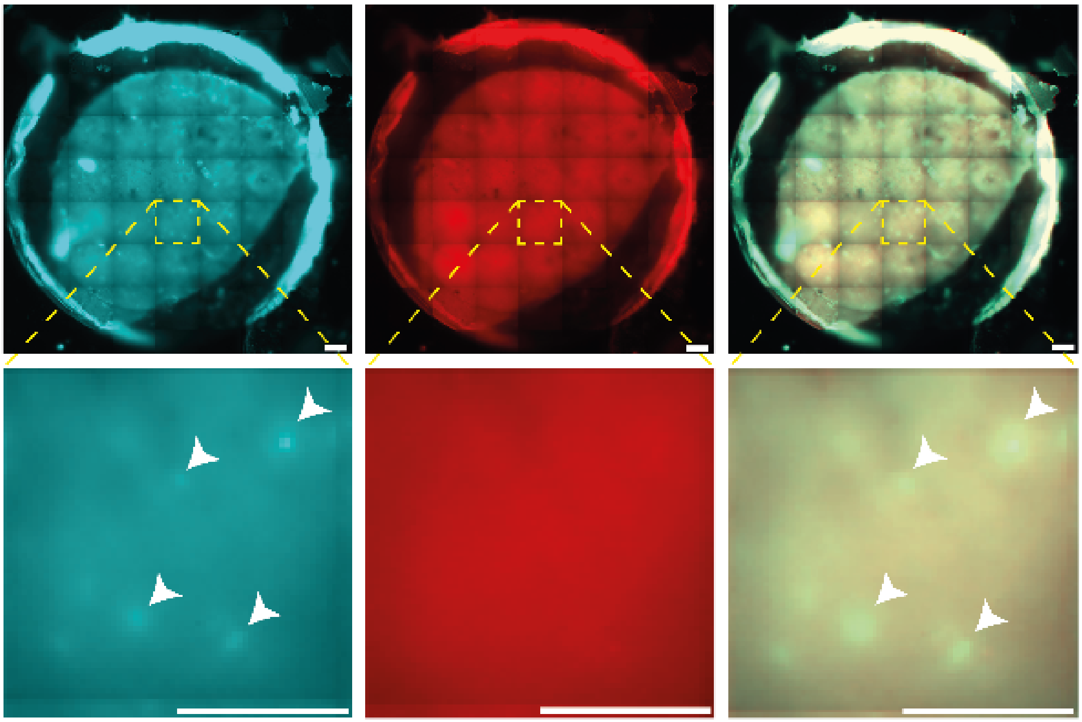

Figure 14: Test for specificity of amyloid signal in high-pressure frozen tissue. Cryo-FM tile scan of high-pressure frozen tissue from *App*$^{NL\text{-}G\text{-}F}$ knock-in mice inside gold carrier (top panel). The bottom panel shows one cryo-FM image. White arrowheads indicate Methoxy-X04 stained plaques (cyan, left). As a control, a rhodamine filter cube was used which shows no specific signal for plaques, only background fluorescence (red, middle). Overlay shows both channels. All scale bars, 200 µm.

3.1.7. Cryo-fluorescence microscopy and cryo-electron microscopy

To guide the collection of cryo-electron tomograms of Aβ plaques from *App*$^{NL\text{-}G\text{-}F}$ mice, cryo-EM grids containing ultrathin cryo-sections were imaged by cryo-FM to visualise the fluorescent signal of Methoxy-X04-stained amyloid. In addition, tissue attachment is a challenge in cryo-ultramicrotomy and cryo-FM revealed whether the sections were attached to the grid (Figure 15 A; this will be described in further detail in the next section).

Next, cryo-EM grids containing ultrathin cryo-sections were imaged on 300 keV Titan Krios at different magnifications. The fluorescent locations were mapped using the origin marker in the middle of the grid and the shape of cryosections as fiducial markers. Then, a cryo-EM atlas (tile scan of the whole EM square with 220x magnification, Figure 15 B, left) was taken to visualise the orientation of the origin marker and the cryo-sections in the electron micrograph and compare it to the cryo-FM image. Additionally, tissue attachment after the grid had been exposed to the vacuum of the cryo-EM was assessed on the atlas. Poorly attached tissue appeared to curl. This step is important to evaluate whether cryosections that contained a fluorescent signal were well attached to the grid and if the grid could be used for tomogram collection.

Then, the magnification was increased to 940x in order to screen individual grid squares (Figure 15 B, middle). This step is important to avoid areas with knife damage (Figure 15 B, right: compression from knife indicated by white arrowheads) in the tissue and ice contamination. Fluorescent signals in individual grid squares were mapped in cryo-FM images using the holes in the carbon foil, ice contaminations (Figure 15 B, middle, yellow arrows) and tissue damage (Figure 15 B, right, white arrows) as fiducial markers. These were then compared to the cryo-FM images. The 3.5 µm holes of the carbon film are shown in a 11,500 x magnified electron micrograph in Figure 15 B (right). Tomograms were collected within these holes. One to two tomograms were collected from each hole. Holes that contained Methoxy-X04-labelled amyloid plaque signals, had no ice contamination, and no or only minimal cutting damage were chosen for the collection of tomographic tilt series.

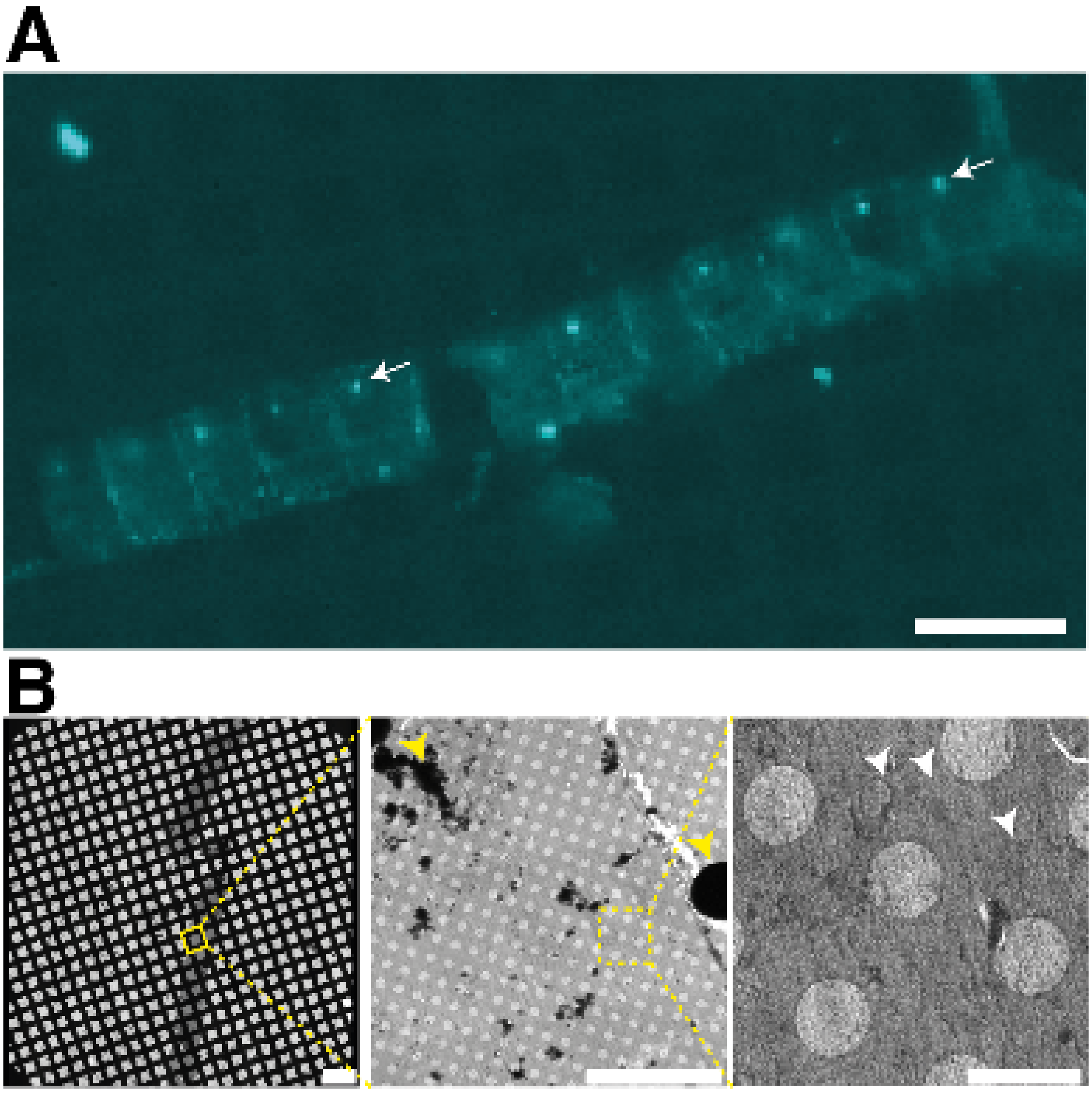

Figure 15: Mapping of cryo-FM and cryo-EM image for tomogram collection. Ribbon of cryo-sections from a Methoxy-X04 injected *App*$^{NL\text{-}G\text{-}F}$ knock-in mouse. White arrows indicate Aβ plaques. Scale bar, 20 µm (A). The left panel shows a cryo-EM atlas (low, 370 x magnification cryo-EM tile scan) of a grid with ribbons of tissue sections. Yellow box indicates one grid square which is shown in the middle panel (medium, 1200 x magnification). Yellow arrows indicate surface ice contamination. The right panel shows an electron micrograph of individual holes within grid squares (medium,

15000 x magnification). White arrows indicate compression damage from cryo-sectioning. Scale bars, 200 nm (B).

3.1.8. Improving the contrast in cryo-ET

Unlike negative stained and resin embedded EM, in cryo-EM biological specimens do not contain heavy metal stains. Instead, in cryo-EM, contrast is generated using defocus, energy filters, phase plates and objective apertures. The latter eliminate inelastically scattered electrons that otherwise would generate noise (Nakane *et al.*, 2020; Danev, Yanagisawa and Kikkawa, 2021). A defocus is applied because it preserves signals at low spatial frequencies by lowering the high frequency information. The objective aperture and energy filters remove inelastically scattered electrons that have lost energy, increasing the signal-to-noise ratio which improves the contrast. Here, all datasets were collected with a -20 keV energy filter to remove inelastically scattered electrons and increase signal-to-noise ratio. Different apertures and defocuses were used and results will be compared in this section.

First, a Volta Phase Plate (VPP) was used for data collection. The VPP has been shown to increase the signal-to-noise ratio in tomograms when imaging close to focus (Khoshouei *et al.*, 2017). Hence, alignment and conditioning of the VPP are time consuming and slow down tomogram collection and thus other strategies to improve the signal-to-noise ratio which results in better contrast were explored.

The VPP was positioned and aligned in the back focal plane so that the unscattered electrons can pass through. Next, the VPP was conditioned by exposing it to the electron beam for about 20-40 minutes to generate a phase shift of ~90°. For the first batch collection, the VPP position was changed and re-conditioned between each tilt series because the phase shift increases over time (Danev *et al.*, 2014). This was very time consuming and therefore, for the collection of dataset two, the VPP position was changed three times and reconditioned (position 1: tomograms 1 - 5, position 2: tomograms 6 - 13, position 3: tomograms 14 - 20).

The cryo-tomographic tilt series from 4 datasets had varying qualities. To determine why, defocus, phase shift and drift were estimated (Table 9). For tomogram collection without VPP using an objective aperture, nominal defocus was set to -5 to -6.5 μm. For VPP data collection nominal defocus was set to -0.8 to -1.3 μm. As shown in table 9, the average phase shifts were often below 90º and average defocuses were slightly higher than the nominal defocus. At high tilt increments, defocus estimation sometimes failed, giving images with very high or low defocus. These tilt increments were excluded from final tomographic reconstructions if the contrast was too low. Additionally, the high variability in tomogram quality was due to stage and sample drift. Therefore, drift between image frames was measured during motion correction. High drift (~ > 0.05 nm/s) was a potential source of misalignment during patch tracking and resulted in poor reconstructions.

Examples of defocus, phase shift and drift measurements are shown in Figure 12. Defocus from tomogram 1 in dataset 3 was 4.42 µm on average, which was close to nominal defocus. High tilt increments, around -60º tilt were below nominal defocus in this tilt series and around 60º tilt, measured defocus was higher than nominal defocus (Figure 16 A). The drift of tomogram 1 in dataset 3 was between 0 - 0.5 nm/s, tilt increments 0º to -20º showed no drift, very high drift was observed in a few tilt increments between +40 to +60º (Figure 16 B). Shifts in defocus and drift occurred in positive tilt increments at high tilts. During collection, a beam tilt is applied to image an adjacent area of the sample for autofocus and tracking which limits radiation damage of the collection area. At high tilt, large ice contaminants or the grid bar may have obscured imaging this adjacent area, which could also result in inaccurate auto focus and tracking. Some of these tilts were excluded if the resulting contrast was poor and therefore the signal-to-noise ratio was too low.

As another example, the phase shift from tomogram9 in dataset 2 is shown in (Figure 16 C). The phase shift estimated for this particular tilt series was 87.38º on average. The phase shift showed overall very high fluctuations in high tilt increments, i.e. -40 to -60º and +40 to +60º. Furthermore, Table 9 shows that phase shift in dataset two increases slightly in batch one (tomogram 1-6) and batch two (tomogram 7-13) for every tomogram. This shows that the phase plate is charged during collection as it is exposed to electrons. However, for the last batch (tomograms 14-20), the phase shift for these is around 70° on average which indicates that the VPP is very inconsistent. The VPP consists of a thin carbon film that varies in every position (Danev *et al.*, 2014). Dataset two in particular had a very low contrast and thus was only qualitatively analysed and excluded from quantifications.

Furthermore, in order to reconstruct the tomograms, some tilt increments had to be excluded. Each tilt series contained 61 increments of 2 degrees and the number of tilt increments used for reconstruction for each tomogram is shown in Table 9. Some views (especially at high tilt increments, near 60°) showed a poor contrast, resulting in a poor signal-to-noise ratio. This was often due to failure of autofocus and tracking on the microscope. Tilt series collected too close to the grid bars or surface ice contamination are more likely to have these problems.

Post-processing of tomograms, using deconvolution or nonlinear anisotropic diffusion (NAD) filtering can further improve the contrast of reconstructed tomograms. Here, different physical and computational approaches to improve the signal-to-noise ratio were compared. The first two datasets were collected with a volta phase plate (VPP; Fukuda *et al.*, 2015; Figure 17 A) and NAD filtered using a software called IMOD which has been shown to reduce the noise and preserve the signal (Frangakis and Hegerl, 2001). NAD filtering the VPP data improved the contrast and fibrils can be seen more clearly (Figure 17 B).

Dataset three and four were collected without a VPP and instead used a 100 µm objective aperture (Figure 17 C). Reconstructed tomograms were deconvoluted to remove noise with the tom_deconv matlab package that is part of the software Warp (Tegunov and Cramer, 2019, no date). This resulted in an increase in contrast and fibrils can be seen more clearly compared to the raw data (Figure 17 D).

In conclusion, deconvolution of tomograms resulted in a similar improvement in contrast compared to VPP and NAD filtering. Deconvolution enabled me to identify firbils in datasets 3 and 4, moreover this method was less time consuming than with a phase plate, enabling larger datasets to be collected on the Titan Krios electron microscope.

Data-set	Animal	Tomogram	Tilt increments	Defocus (µm)	Drift (nm/s)	Phase Shift (^{o})	Objective Aperture
1	1	1	57	-1.45	[4]	91.92	VPP
1	1	2	53	-1.52	[4]	72.30	VPP
1	1	3	54	-1.33	[4]	99.17	VPP
1	1	4	53	-1.42	[4]	95.00	VPP
1	1	5	51	-1.56	[4]	104.45	VPP
1	1	6	45	-2.35	0.23	85.52	VPP
1	1	7	44	-1.77	[4]	84.46	VPP
1	1	8	35	-1.24	[4]	92.92	VPP
1	1	9	[4]	[4]	[4]	[4]	VPP
1	1	10	59	-1.78	[4]	17.10	VPP
1	1	11	[4]	[4]	[4]	[4]	VPP
1	1	12	[4]	-1.65	[4]	92.68	VPP
2	1	1	52	-1.46	0.7	55.63	VPP
2	1	2	47	-5.65	1	57.01	VPP
2	1	3	49	-1.42	1	61.07	VPP

---

[4] tomograms 1-5 (dataset 1) were disregarded due to data loss

Data-set	Animal	Tomogram	Tilt increments	Defocus (µm)	Drift (nm/s)	Phase Shift (^{o})	Objective Aperture
2	1	4	49	-1.56	0.5	71.99	VPP
2	1	5	54	-1.015	1.01	68.21	VPP
2	1	6	52	-1.62	0.3	76.18	VPP
2	1	7	46	-1.66	0.5	75.39	VPP
2	1	8	55	-5.77	0.6	82.23	VPP
2	1	9	44	-1.35	0.7	87.38	VPP
2	1	10	50	-1.58	1	90.05	VPP
2	1	11	52	-5.74	0.7	93.92	VPP
2	1	12	51	-1.17	1	108.21	VPP
2	1	13	31	-6.76	0.25	114.25	VPP
2	1	14	54	-1.77	0.3	86.32	VPP
2	1	15	44	-6.88	0.3	72.80	VPP
2	1	16	53	-7.00	3	68.66	VPP
2	1	17	50	-7.10	0.75	68.62	VPP
2	1	18	53	-5.25	0.45	69.67	VPP
2	1	19	53	-6.70	1	48.51	VPP
2	1	20	40	-7.22	0.5	64.29	VPP
3	2	1	61	-4.42	0.264	-	C100
3	2	2	54	-4.63	0.228	-	C100
3	2	3	54	-4.71	0.217	-	C100
3	2	4	56	-5.08	0.219	-	C100
3	2	5	54	-3.70	0.219	-	C100

Data-set	Animal	Tomogram	Tilt increments	Defocus (µm)	Drift (nm/s)	Phase Shift (°)	Objective Aperture
3	2	6	58	-4.41	0.192	-	C100
3	2	7	42	-4.43	0.163	-	C100
3	2	8	48	-4.66	0.221	-	C100
3	2	9	47	-5.41	0.219	-	C100
3	2	10	52	-4.42	0.360	-	C100
4	2	1	48	-4.66	0.178	-	C100
4	2	2	48	-4.84	0.209	-	C100
4	2	3	46	-5.14	0.136	-	C100
4	2	4	41	-5.26	0.163	-	C100
4	2	5	45	-4.40	0.189	-	C100
4	2	6	43	-4.60	0.141	-	C100
4	2	7	33	-4.30	0.118	-	C100
4	2	8	48	-4.33	0.275	-	C100
4	2	9	44	-4.92	0.607	-	C100
4	2	10	44	-5.40	0.733	-	C100
4	2	11	55	-3.86	0.402	-	C100

Dataset	Animal	Tomogram	Tilt increments	Defocus (µm)	Drift (nm/s)	Phase Shift (°)	Objective Aperture
4	2	12	54	-4.39	0.285	-	C100
4	2	13	50	-4.92	0.400	-	C100

Table 9: Parameters estimated to assess the quality of tomograms. Number of tilt increments for each tomogram are shown. Defocus (µm), drift (nm) and phase shift (°) were measured for tomograms from all four datasets (n=4/2). The first two datasets were collected with a Volta phase plate (VPP), datasets three and four were collected with a 100 µm condenser lens (C100).

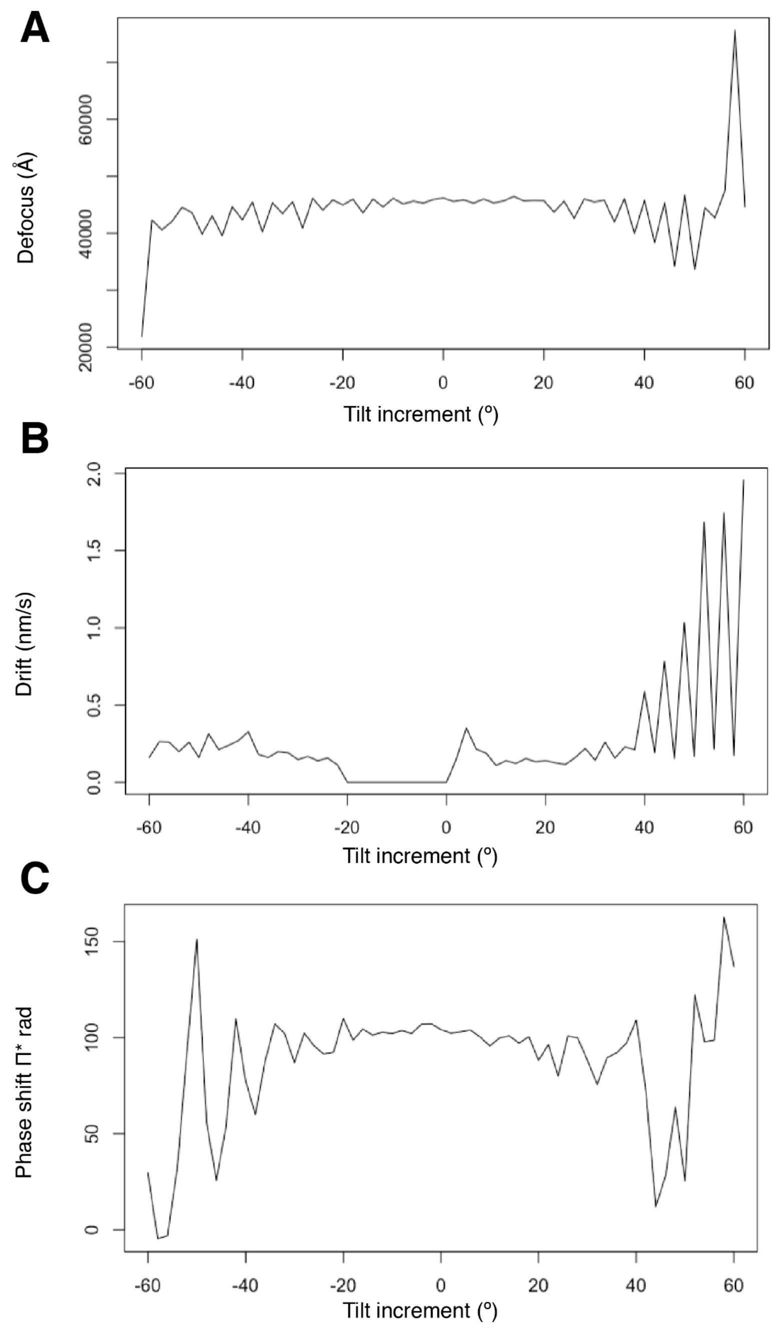

Figure 16: Examples of measurements for quality control after data collection. Measurements of defocus (dataset 3, tomogram 1, mean = -41300 Å = -4.13 µm, A), drift (dataset 3, tomogram 1, mean = 0.26 nm/s, B) and phase shift (dataset 2, tomogram 9, mean = 87.38, C). Defocus, drift and phase shift were stable in low tilt, whilst high tilt increments showed higher fluctuations.

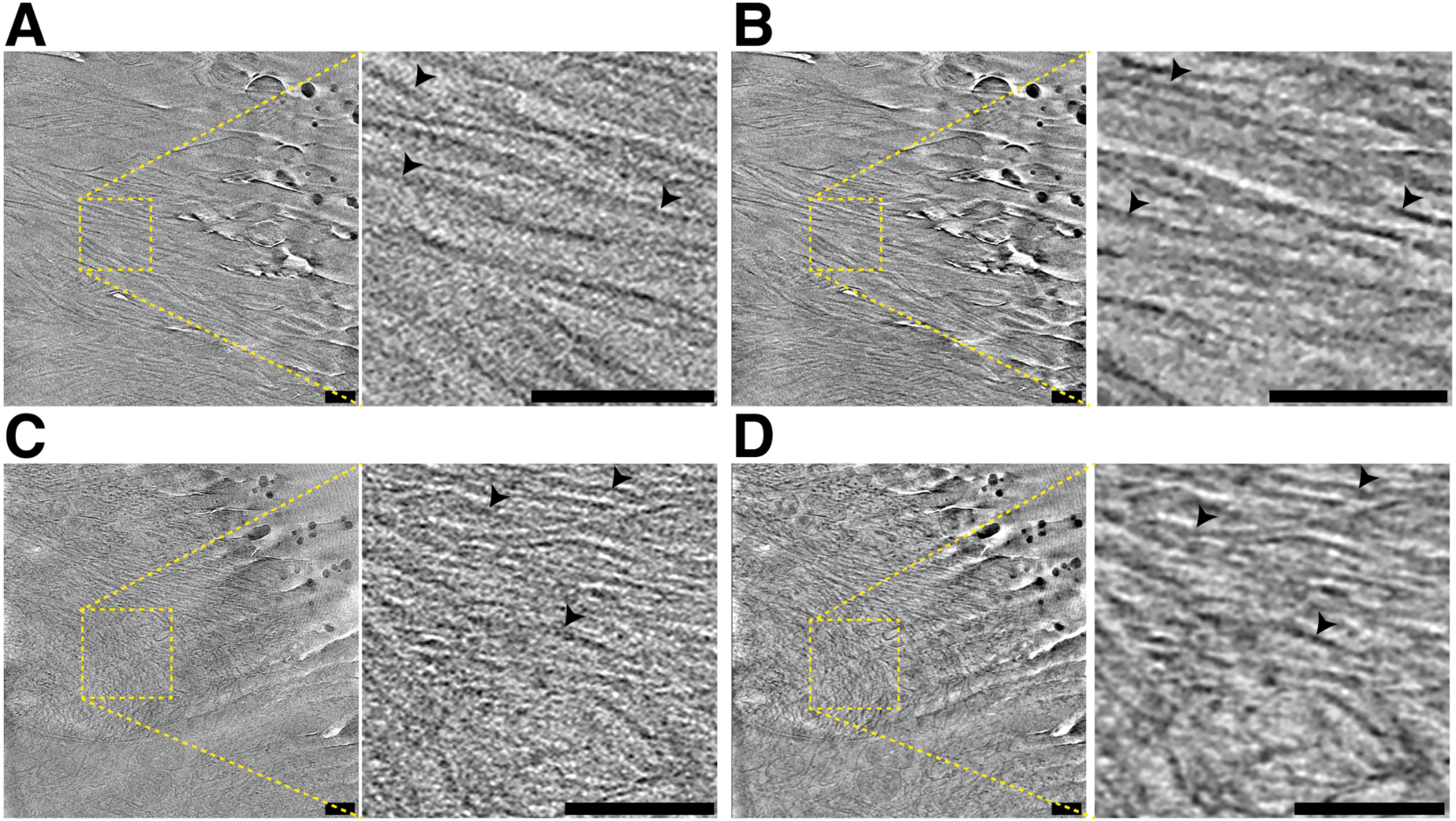
A
B
C
D

Figure 17: Comparison of different approaches to improve signal-to-noise ratio in tomograms. Virtual slice of a tomogram collected with a Volta Phase Plate (A) and filtered with Nonlinear Anisotropic Diffusion (B). Virtual slice of a tomogram collected with C100 aperture (C) and deconvoluted in warp (D). Fibrils were seen with both approaches, data collected with VPP and data collected with C100 aperture. Moreover, VPP combined with NAD filtering showed a similar improvement of contrast as deconvolution, thus both approaches enabled us to identify fibrils more clearly. However, VPP collection is more time consuming. All scale bars, 100 nm. Arrowheads denote fibrils.

Other challenges that arose during data collection included radiation damage, partial devitrification, poor attachment of the tissue to the EM grid, poor focus and tracking errors. Radiation damage is shown in Figure 18 A. Tissue attachment in cryo-EM can only be assessed in high tilt increments. Poorly attached parts of tissue sections seemed well attached at 0º tilt. However, in high tilt images tissue was detached from the grid (Figure 18 B). This led to poor tracking and poor focus, subsequently resulting in low signal-to-noise ratio and poor patch tracking. Hence, tissue attachment was evaluated in cryo-FM images to guide tomogram collection. Well attached tissue was on the same focal plane as the holes in the carbon (Figure 18 C).

Tomograms from poorly attached tissue could not be reconstructed, because too many tilt increments had to be excluded. Therefore, only tomograms from tissue that was in the same focal plane as the carbon in cryo-FM images were selected for data collection.

In total 55 tomographic tilt series were collected, 6 of which had to be included because the tomograms could not be reconstructed, too many views were excluded and the signal-to-noise ratio was poor. Moreover, 26 of the tomograms had a too low signal-to-noise and were therefore excluded from analysis.

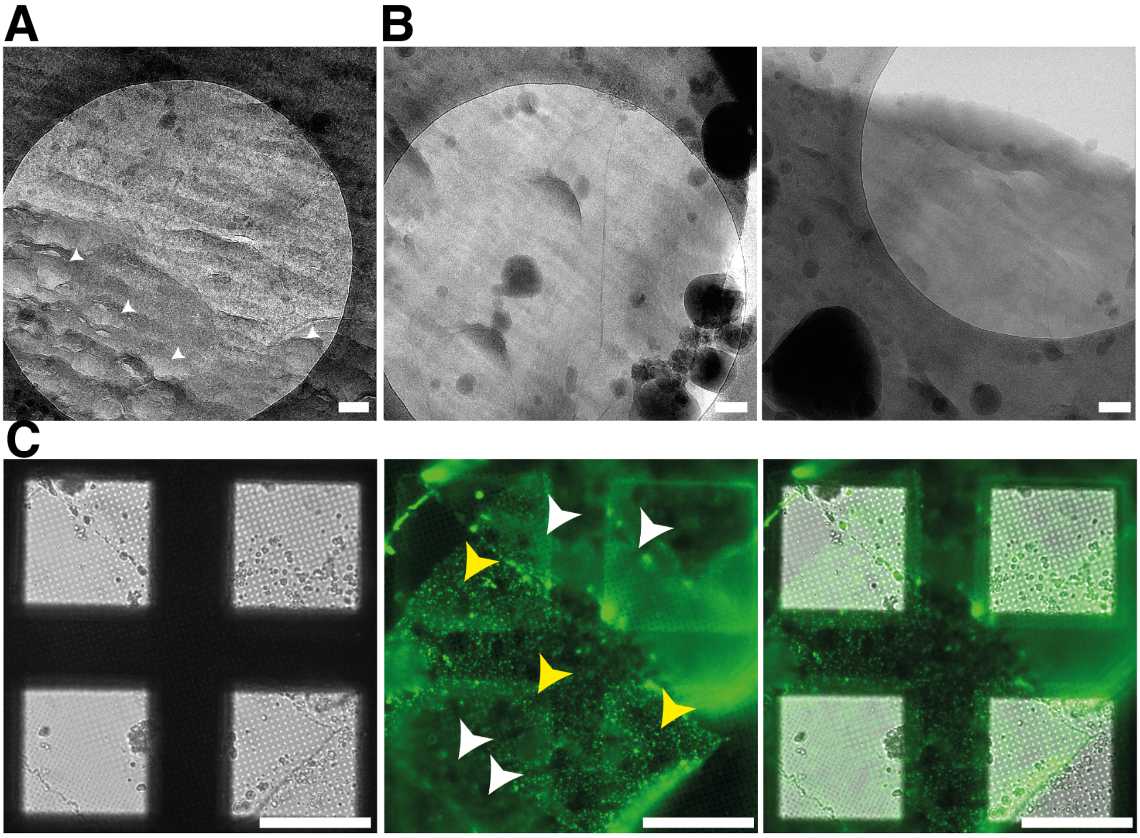

Figure 18: Challenges in cryo-ET. Electron micrographs from cryo-sections of *App*$^{NL\text{-}G\text{-}F}$ knock-in mice show radiation damage (white arrowheads, A). Poor tracking was observed in the tilt series of some tomograms, because tissue was not well attached. Tissue seemed attached at 0º, but detached at 10º tilt (B). Scale bars, 100 nm. Cryo-FM images of cryo-sections from *PSD95*$^{eGFP/eGFP}$ knock-in mouse imaged in a brightfield channel (left) show if tissue is in the same focal plane as holes in the carbon foil. The middle panel shows the eGFP channel, parts of the section with good tissue attachment (yellow arrowheads) compared to poor tissue attachment (white arrowheads). The right panel shows merge between brightfield and green channel. Areas where holes in the carbon and fluorescent signal are in focus are areas with good tissue attachments (C). Scale bars, 20 μm.

3.1.9. Cryo-CLEM

To confirm the location of amyloid pathology within tomograms after their collection, cryo-CLEM was performed. A matlab script was used to correlate cryo-EM (Figure 19 EM) and cryo-FM (Figure 15 Mx04) images (Kukulski *et al.*, 2011). All tomograms were collected from central and peripheral regions of the Aβ plaque, with high and low fluorescent intensities. Some of the tomograms were collected outside the plaque to test if fibrils could be observed outside of the regions that were labelled with Methoxy-X04. Collection was set up within the holes of the carbon. Correlation (Figure 19 merge) of cryo-EM (Figure 19 left) and cryo-FM (Figure 19 middle) images enabled me to validate if tomograms were collected within pathology of the plaque or in regions outside the Methoxy-X04 fluorescence. Fluorescent images of ultrathin cryo-sections showed the micro-architecture of Aβ plaques (Figure 19 middle). In comparison, ultrathin cryo-sections collected from wild type mice injected with Methoxy-X04 did not show fluorescence signals (Figure 19 right).

No fibrils were observed in three tomograms that had a Methoxy-X04 signal in the cryo-CLEM. Tomograms that showed Methoxy-X04 signal in the CLEM did not have fibrils.

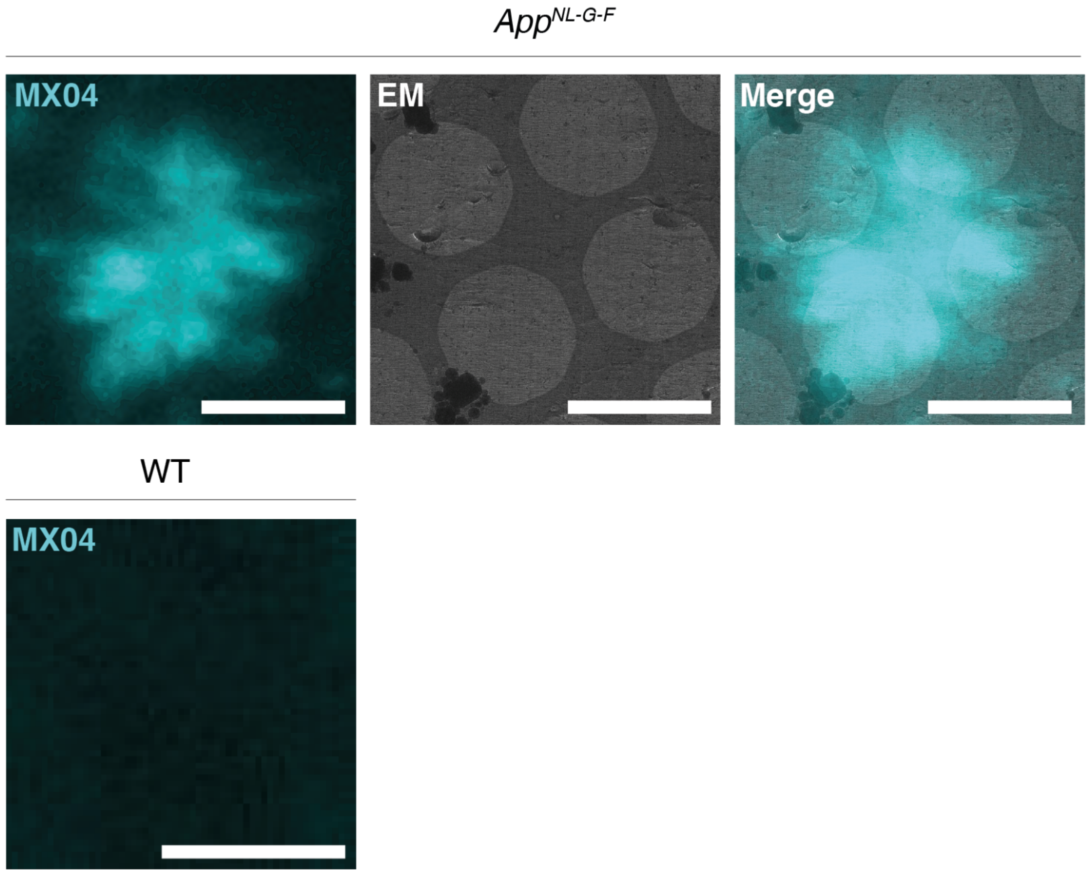

Figure 19: Correlation of cryo-EM and cryo-FM images after tomogram collection. Cryo-sections from Methoxy-X04 injected *App*$^{NL\text{-}G\text{-}F}$ mice imaged by cryo-FM (MX04) and cryo-EM (EM) were correlated (Merge) to determine regions where tomograms were collected. Cryo-sections from Methoxy-X04 injected wild-type (WT) mice show no specific fluorescence. All scale bars, 4 µm.

3.1.10. Multi colour cryo-CLEM

To enable to study structures of synapses in AD brains the workflow was further applied to *App*$^{NL\text{-}F}$ x *PSD95*$^{eGFP/ePFP}$ x *GluN1*$^{TAP/TAP}$ knock-in mice (Saito et al., 2014, (Frank *et al.*, 2016). Multiple labelling techniques were tested (Figure 20). Firstly, these mice were injected with Methoxy-X04. 24 h after injection, acute brain slices were prepared and incubated with a FLAG-Cy3 antibody to target the flag tag which is part of the genetically encoded 'TAP'-tag at the N-terminus of the GluN1 subunits of NMDA-Rs in App^{NL-F} x $PSD95^{eGFP/ePFP}$ x $GluN1^{TAP/TAP}$ knock-in mice. Consequently, Aβ plaques, PSD95 and NMDA-R were labelled in these samples by a small fluorescent molecule (Methoxy-X04), a genetically encoded fluorescent tag (GFP), and a fluorescent antibody (Flag), respectively. Tissue biopsies were taken from acute brain slices, incubated in cryoprotectant and high pressure frozen. These samples were processed as described above.

The cryo-CLEM shows a specific signal for Methoxy-X04 amyloid signal that is only detected in the cyan channel. A nonspecific signal (Figure 20 white arrowheads) can be seen which appears in all three channels and is therefore not an Aβ plaque, but could be ice contamination. The data suggests that synaptic signals (yellow, both PSD95 and NMDA-R) do not colocalise with Aβ plaques, but synapses are in the vicinity of plaques. Only a few of the PSD-95 (green) and NMDA-R (red) are colocalised (yellow), but the majority of PSD-95 signals do not colocalise with NMDA-R signals and vice versa (Figure 20 left, lower panel), as expected (Frank and Grant, 2017).

This provides a powerful tool to identify multiple distinct molecular targets for cryo-CLEM. Moreover, this enables further studies investigating how Aβ impacts the architecture of synapses and how it interacts with synapses.

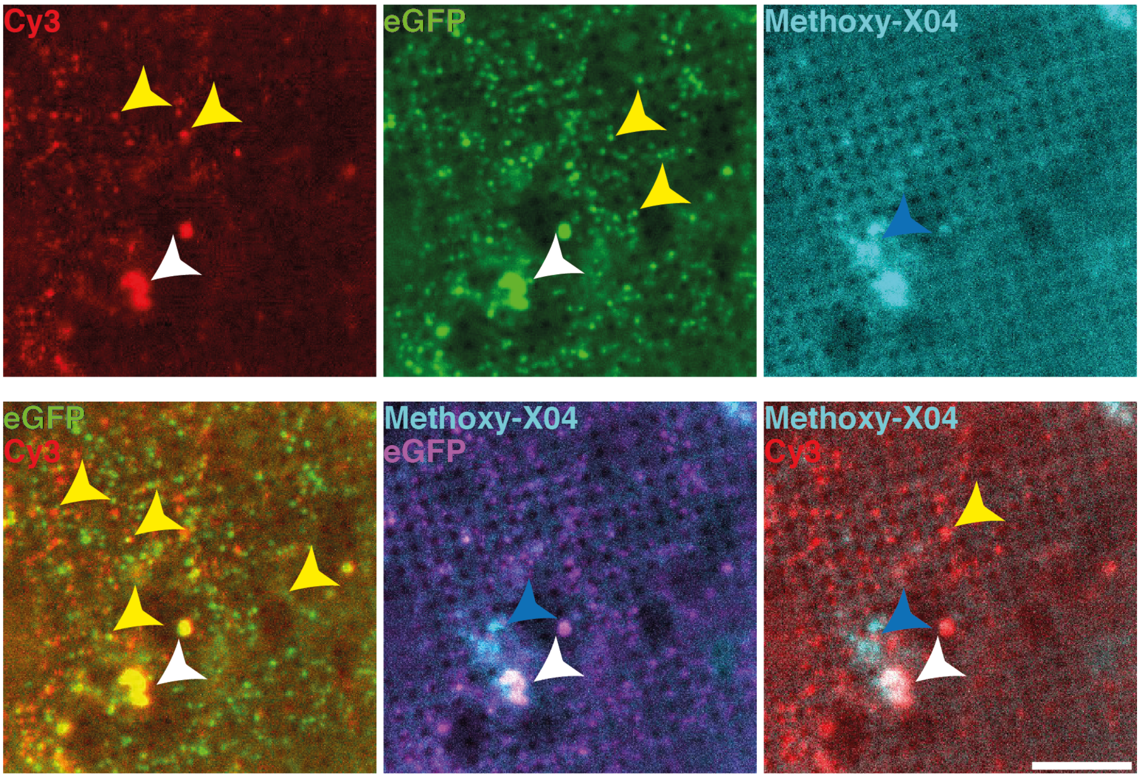

Figure 20: Labelling strategies for cryo-CLEM. Upper panel shows cryosections from *App*$^{NL-F}$ x *PSD95*$^{eGFP/eGFP}$ x *GluN1*$^{TAP/TAP}$ knock-in mice with different labelling approaches, including a FLAG-Cy3 antibody staining that binds to GluN1(red), a genetically encoded fluorophore, eGFP labelling PSD95, a synaptic marker (green) and a fluorescent dye, Methoxy-X04 labelling Aβ plaques (cyan). The lower panel shows merge of GFP (green) and FLAG-Cy3 (red), synapses which have a signal for PSD95 and GluN1 appear in yellow (left). Middle shows merge of eGFP (magenta) and Methoxy-X04 (cyan), overlay in white and the right panel shows FLAG-Cy3 (red) and Methoxy-X04 (cyan) signals, overlay appears white (yellow arrowheads - synapses, blue arrowheads - plaque, white arrowheads - nonspecific signal). Scale bar, 20 μm.

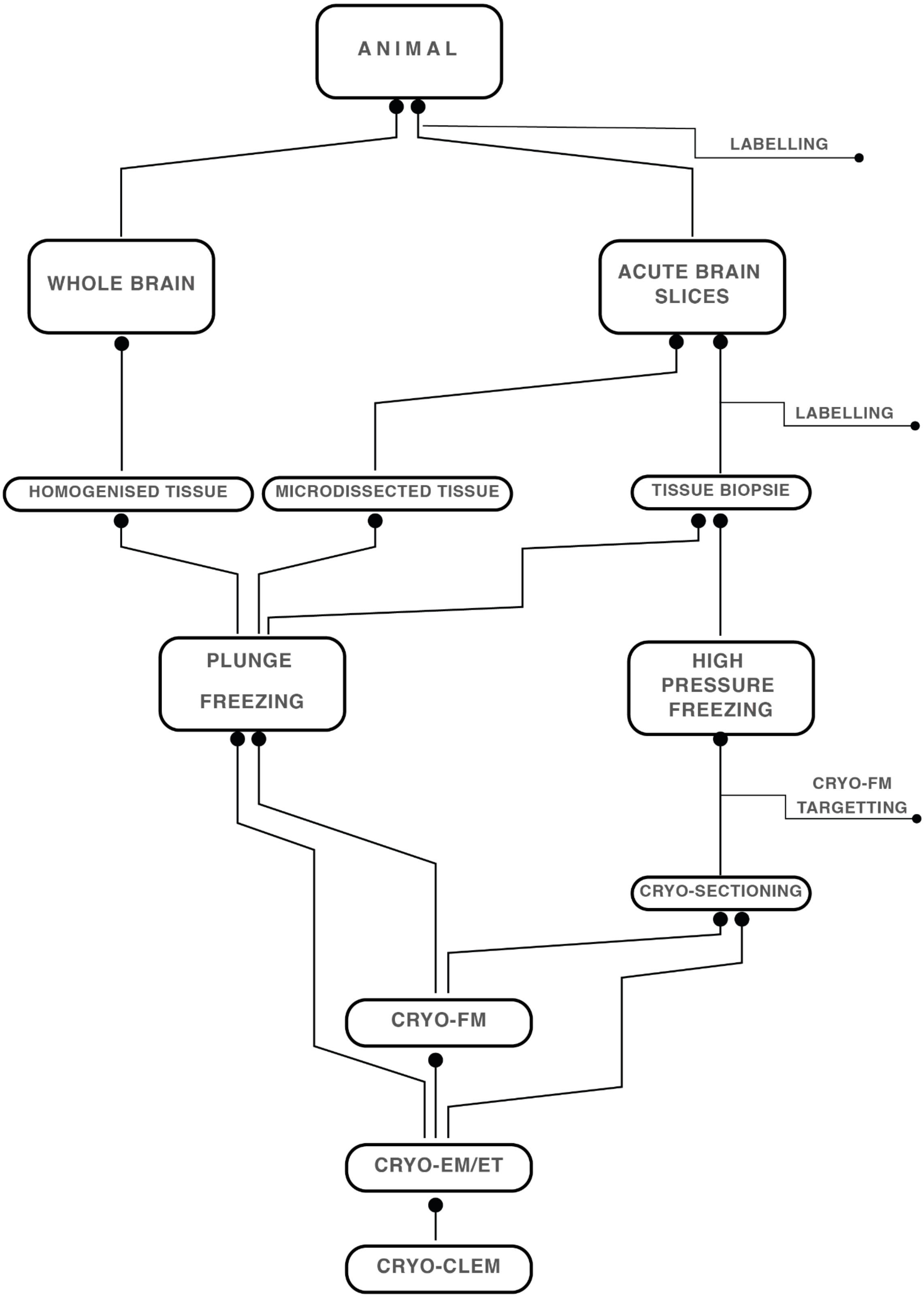

Figure 21: Scheme of sample preparation workflows for in-situ cryo-ET.

3.2. Discussion

I developed a novel workflow for cryogenic correlative light and electron tomography that enabled me to target Aβ plaques and study their native in-tissue architectures. Therefore, plaques were labelled, a buffer that limits excitotoxicity was used, brain tissue was vitrified, cryo-sectioned and cryo-CLEM was combined with cryo-ET. A schematic of possible workflows for sample preparation of in-tissue cryo-ET is shown in Figure 21. The sample preparation method for cryoEM strongly depends on the abundance and stability of the protein of interest, the structure that is studied and the tissue composition itself.

Here, $App^{NL\text{-}G\text{-}F}$ knock-in mice, a model of familial AD, were aged up to one year, because the plaque load in these mice is saturated after 9 months (Saito *et al.*, 2014b). Subsequently, mice were injected with a fluorophore, namely Methoxy-X04. This dye was shown to specifically label Aβ plaques specifically in live tissue (Klunk *et al.*, 2002).

For freezing, two different approaches were tested, plunge freezing and HPF. For plunge freezing, brains were homogenised. This method is more economical and has a much higher throughput compared to HPF and subsequent CEMOVIS. Moreover, for plunge freezing fiducial markers, such as immunogold can be introduced for later tomographic reconstructions. Cryo-sections have a lower signal-to-noise ratio, however the native in-tissue architecture remains relatively unperturbed. Unfortunately, plaques were not detected in plunge-frozen homogenates from $App^{NL\text{-}G\text{-}F}$ knock-in mice. A possible explanation is that plaques are unstable or the abundance of plaques is too low in brain homogenates to detect them. Thus, high pressure freezing and cryo-ultramicrotomy was performed which preserves the native state of the hydrated tissue (Al-Amoudi, Norlen and Dubochet, 2004). Improvements in CEMOVIS have made the technique more accessible in recent years. Electrostatic charge is used to attach tissue on a hydrophilic grid (Pierson *et al.*, 2010), so that the sample and the carbon of grids form interactions. Another major improvement was the development of micromanipulators which make this technique much more accessible (Studer *et al.*, 2014; Nakane *et al.*, 2020). Nevertheless, this technique is still very challenging and low throughput. Despite this, 4 datasets have been successfully collected and qualitatively as well as quantitatively analysed. The needle in the haystack problem that was encountered in samples due to relatively low plaque density added another difficult step to the workflow. I was able to perform cryogenic-fluorescent imaging of HPF carriers for the first time to guide the collections of ultrathin cryo-sections.

In the future, microdissection combined with plunge freezing can be established. Therefore, Methoxy-X04 stained plaques would be sucked out of ultrafresh brain slices under a fluorescence microscope into a pipette and immediately applied onto an EM followed by plunge freezing. This is more economical and faster than high pressure freezing and cryo-sectioning of tissue. Moreover, this technique has the potential to keep the tissue in its native state.

The data revealed that not all high-pressure frozen samples were vitreous. It still remains to be tested if vitrification depends on location cryo-sections were collected from within the carrier. Experiments on plunge freezing with copper tubes have revealed that vitreous ice is localised in the middle of the sample and crystalline ice on the outsides. Crystalline ice that forms on the outside applies additional pressure to the water molecules in the middle of the sample, which prevents the formation of crystalline ice in the centre of the tissue (Yakovlev and Downing, 2011). This has yet to be tested for high pressure freezing of tissue inside gold carriers. Therefore, multiple ribbons from the same carrier could be collected in different locations of the carrier to compare the vitrification of tissue between the edges and middle of tissue. To exclude that freezing is the source of devitrification, carriers from multiple batches of high pressure freezing have to be compared.

Cryo-FM images were collected in order to guid the tomogram collection. Location of fluorescence was determined and tissue attachment was assessed by imaging a z-stack and evaluating whether the fluorescent signal was in the same focal plane as the carbon on the grid.

Multiple tomograms that were collected could not be reconstructed due to various reasons, including poor tissue attachment, radiation damage, poor defocus, inadequate phase shift and stage drift during collection. Some tomograms were collected close to the edges so that the copper mesh of the grid was visible at high tilt.

Tissue attachment becomes particularly challenging in the vacuum of the cryo-EM and cutting damage cannot be fully eliminated during sectioning (Al-Amoudi, Norlen and Dubochet, 2004). The success rate of tissue attachment for cryo-sectioning was fairly low. Another problem is that the fluorescent signal of interest has to be in the holes of the carbon film resulting in regions that could not be targeted for tilt series collection. Lastly, sample preparation and transfer resulted in variable surface ice-contamination that appears black in cryo-EM, which also limited the number of available regions on the cryoEM grid that were suitable for tilt series collection. Overall, most grids with tissue sections that were prepared could not be used for cryo-ET. This makes the workflow really time consuming and challenging. Nevertheless, multiple datasets were collected from different grids which will be discussed in the next chapter.

To improve the contrast, different techniques were compared. First datasets were collected with a VPP which was very time consuming. Therefore, other physical and computational options were explored. Various software tools are available to deconvolute the data and perform missing wedge compensation to improve the contrast (Liu *et al.*, no date; Wagner and Raunser, 2020) which have to be explored further. Moreover, new cryoEM detectors and energy filters have been developed recently which may further improve signal-to-noise ratio (Nakane *et al.*, 2020); (Danev, Yanagisawa and Kikkawa, 2021).

Different labelling techniques for multicolour CLEM were explored, namely combining genetically encoded fluorophores, antibody live labelling and injection of fluorescent dyes. This provides another powerful tool to study different structures in tissue of AD surrounding the plaque in future.

4. Qualitative analysis to determine the in-tissue architecture of amyloid beta plaques and their surrounding environment

4.1. Results

4.1.1. Summary

Here, I applied the workflow to collect four datasets from two *App*$^{NL\text{-}G\text{-}F}$ mice (n = 4/2), for the reconstruction of six Aβ plaques. In total, 55 tomograms were collected from central and peripheral regions of the Aβ plaques, as well as regions adjacent to the plaques.

After correlating the FM to the EM, the Methoxy-X04 fluorescence for each tomogram was assessed. The centre of the plaque was defined by bright Methoxy-X04 fluorescent signals, the boundary as dim signals and the periphery was defined as regions containing fibrils but no Methoxy-X04 signal (Table 10). All cryo-CLEM data are shown in Appendix I: cryo-CLEM. The cryo-CLEM for 7 of the tomograms was too ambiguous.

24 tomograms were qualitatively analysed for putative extracellular (Table 11) and putative intracellular features (Table 12). Tomograms with poor signal-to-noise ratio or failed reconstruction were excluded from analysis (for more details see Chapter 3: Development of a sample preparation workflow for in-tissue correlated imaging-Improving the contrast in cryo-ET).

In this chapter, the in-tissue architecture of plaques and their surrounding tissue environment will be analysed. Fibrils in tomograms were located by cryo-CLEM, i.e. Methoxy-X04 signal revealed locations of fibrils in tomograms. Plaques were found to be heterogeneous, two different architectures of fibrils were classified as parallel bundles and meshwork. Plaques were located in the extracellular space and consisted of various macromolecular features. Cells were in close vicinity of plaques, which were identified by the presence of cellular organelles and a plasma membrane. Macromolecular and cellular constituents that were observed are classified or named based on their shape, size and structure.

Dataset	Animal	Tomogram	CLEM MX04	Centre	Boundary	Periphery
1	1	1	0	0	0	0
1	1	2	0	0	0	0
1	1	3	0	0	0	0
1	1	4	1	0	1	0
1	1	5	[5]	[5]	[5]	[5]
1	1	6	1	1	0	0
1	1	7	1	1	1	1
1	1	8	[5]	[5]	[5]	[5]
1	1	9	[5]	[5]	[5]	[5]
1	1	10	[5]	[5]	[5]	[5]
1	1	11	[5]	[5]	[5]	[5]
1	1	12	[5]	[5]	[5]	[5]

---

[5] CLEM was too difficult, region has not been found

Dataset	Animal	Tomogram	CLEM MX04	Centre	Boundary	Periphery
2	1	1	1	1	1	0
2	1	2	1	1	1	0
2	1	3	1	1	0	0
2	1	4	1	1	1	0
2	1	5	1	0	1	1
2	1	6	1	0	1	1
2	1	7	1	1	0	0
2	1	8	1	0	1	1
2	1	9	1	1	1	0
2	1	10	1	1	1	0
2	1	11	1	0	1	0
2	1	12	1	1	1	0
2	1	13	1	0	1	1
2	1	14	1	0	1	1
2	1	15	1	1	1	0

Dataset	Animal	Tomogram	CLEM MX04	Centre	Boundary	Periphery
2	**1**	16	[5]	[5]	[5]	[5]
2	1	17	1	1	0	0
2	1	18	1	1	1	0
2	1	19	1	1	0	0
2	1	20	1	1	0	0
3	2	1	1	0	1	0
3	2	2	1	1	0	0
3	2	3	1	1	1	0
3	2	4	1	1	0	0
3	2	5	0	0	1	1
3	2	6	1	1	1	0
3	2	7	1	0	1	0
3	2	8	1	0	1	0
3	2	9	1	0	1	0
3	2	10	0	0	0	0

Dataset	Animal	Tomogram	CLEM MX04	Centre	Boundary	Periphery
4	2	1	1	1	1	0
4	2	2	1	1	1	0
4	2	3	1	1	0	0
4	2	4	1	1	1	1
4	2	5	1	0	1	0
4	2	6	1	1	0	0
4	2	7	1	1	1	0
4	2	8	1	1	0	0
4	2	9	1	1	1	0
4	2	10	0	0	0	0
4	2	11	1	0	0	1
4	2	12	1	0	0	1
4	2	13	1	0	1	1

Table 10: Cryo-CLEM for all datasets. Tomograms from dataset 1 and 2 were collected from the same animal and dataset 3 and 4 were collected from a second animal. Tomograms were analysed for Methoxy X04 signals. Bright fluorescent signals were defined as central regions of plaque, dim signals as boundary and no fluorescence as periphery. Periphery of plaques contained fibrils. 1-observed, 0-not observed.

Dataset	Animal	Tomogram	Parallel bundles	Mesh work	Protein filled M	PM	C-shape M	Empty M	Dense-cored M	Nanopedia	Myelin	EV	Lipid-like droplets
1	1	6	1	1	1	0	1	0	1	1	0	1	1
2	1	2	1	1	0	0	0	0	0	0	1	0	0
2	1	8	1	0	1	0	0	1	1	0	1	1	0
2	1	9	1	1	0	0	0	1	0	0	0	0	0
3	2	1	1	1	1	0	1	0	1	1	0	1	1
3	2	2	1	0	1	1	1	0	1	1	0	1	1
3	2	3	1	0	0	1	0	0	1	0	0	1	1
3	2	4	1	0	1	0	0	1	1	1	1	1	1
3	2	5	0	0	0	0	0	0	0	0	0	1	0
3	2	6	0	1	0	1	0	1	0	0	0	1	0
3	2	7	1	1	0	1	0	1	0	0	0	1	0
3	2	8	0	0	0	1	0	0	0	0	0	0	0
3	2	9	0	0	0	1	0	0	0	0	0	0	0
3	2	10	0	0	0	0	0	0	0	0	1	0	0
4	2	1	0	1	1	1	0	0	1	0	1	0	0

Dataset	Animal	Tomo-gram	Parallel bundles	Mesh work	Protein filled M	PM	C-shape M	Empty M	Dense-cored M	Nano-pedia	Myelin	EV	Lipid-like droplets
4	2	2	1	1	0	1	0	0	0	0	0	0	0
4	2	3	0	1	1	0	1	1	1	1	0	1	0
4	2	4	0	1	1	0	0	1	1	0	1	1	0
4	2	5	0	0	0	0	0	0	0	0	1	0	0
4	2	6	1	1	0	1	0	0	1	0	0	0	0
4	2	7	1	1	1	0	0	1	0	0	0	1	1
4	2	10	0	0	0	0	0	0	0	0	0	0	0
4	2	10	0	0	0	0	0	0	0	0	0	0	0
4	2	12	0	0	1	0	1	0	0	0	0	0	0

Table 11: Putative extracellular features. Tomograms from dataset 1 and 2 collected from the same animal and dataset 3 and 4 were collected from a second animal were analysed for extracellular macromolecular constituents. Tomograms were analysed for presence of fibrils that were either organised in parallel bundles or meshwork. Protein filled membranes seemed to contain a network of higher-order proteins, lipid bilayers were labelled as plasma membrane (PM), c-shaped membranes contained c-shaped inclusions, empty membranes were ~50 nm small spherical membrane that had no electron dense content, dense cored membranes contained small electron dense spheres, thin tubular structures were

classified as nanopaedia. Myelinated axons were observed and extracellular vesicles were observed as spheres surrounded by membranes. Liquid-like droplets on the other hand, were not surrounded by membranes. (M - membrane) 0 features not observed, 1 feature observed.

Dataset	Animal	Tomogram	Ribosomes	ER	MTs	Actin	Mitochondria	MVB	other membrane bound organelles
1	1	6	0	0	0	0	0	0	0
2	1	2	0	0	0	0	0	0	0
2	1	8	0	0	0	0	0	0	0
2	1	9	0	0	0	0	0	0	0
3	2	1	0	0	0	0	0	0	0
3	2	2	1	0	0	0	0	1	0
3	2	3	1	0	1	1	0	1	0
3	2	4	0	0	0	0	0	0	0
3	2	5	1	1	0	0	0	1	0
3	2	6	1	0	0	0	0	0	1
3	2	7	1	1	1	0	0	0	1
3	2	8	1	0	0	0	1	0	0
3	2	9	1	1	1	0	1	1	1
3	2	10	0	0	0	0	0	0	0

Dataset	Animal	Tomogram	Ribosomes	ER	MTs	Actin	Mitochondria	MVB	other membrane bound organelles
4	2	1	0	0	1	1	1	0	0
4	2	2	1	1	1	0	1	1	1
4	2	3	0	0	0	0	0	0	0
4	2	4	1	0	1	0	0	0	0
4	2	5	1	1	1	0	1	1	0
4	2	6	1	0	0	0	0	0	0
4	2	7	0	0	0	0	0	0	0
4	2	10	0	0	1	1	1	0	1
4	2	12	0	0	0	1	0	0	0

Table 12: Putative intracellular features. Tomograms from dataset 1 and 2 collected from the same animal and dataset 3 and 4 were collected from a second animal were analysed for macromolecules and subcellular constituents. These include ribosomes which are small highly complex macromolecular structures, endoplasmic reticulum (ER) that has a highly complex tube-like structure and ribosomes are attached to it. Furthermore, ~25 nm thick microtubules (MT; Cooper 2000) and actin which forms on average 7 nm thick filaments (Cooper 2000). Mitochondria are double membrane bound with cristae. Multivesicular bodies (MVBs) are membrane bound organelles with multiple inclusions that are part of the endosomal

pathway. Other membrane bound organelles were found but could not be classified by their morphology. 0 features not observed, 1 features observed.

4.1.2. Architecture of Aβ plaques

Nanodomains with different architectures within an Aβ plaque were first observed in a tomogram collected in the centre of an Aβ plaque (tomogram 6 dataset 1, Figure 22 A). Interestingly, the plaque consisted not only of fibrils but also other macromolecular and subcellular constituents (Figure 22 B).

Using cryo-CLEM the location of fibrils was identified in tomograms. Interestingly, fibrils formed regions of varying densities and other macromolecular and subcellular constituents that interdigitated the fibrils were discovered. These were classified by their morphology based on what has been described in literature. These include subcellular compartments, extracellular vesicles, c-shaped membranes, nanopaedia and liquid-like droplets which will be described in greater detail in this chapter. Quantitative analysis of constituents found in plaques will be shown in Chapter5: Quantitative analysis of data.

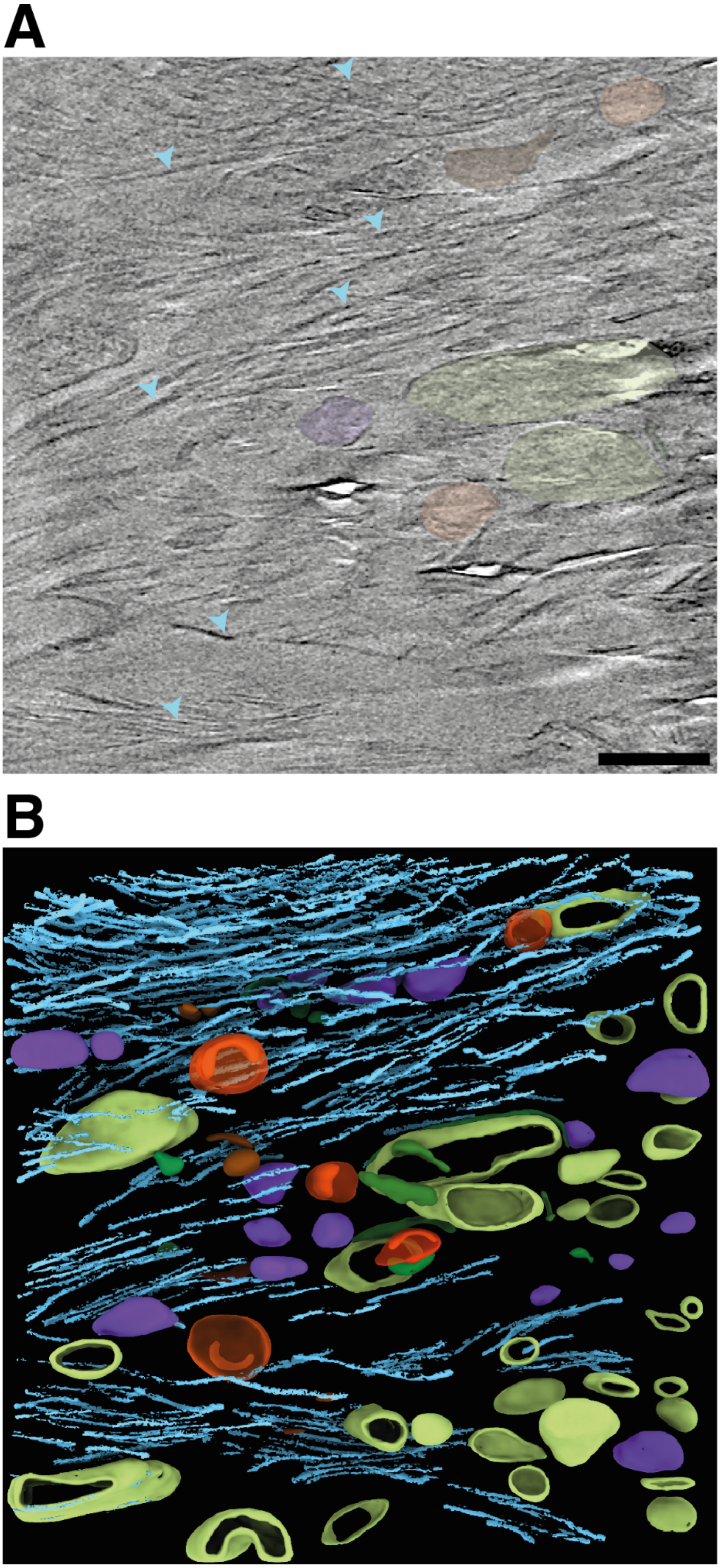
A
B

Figure 22: Virtual slice (2D image) from a tomogram of an Aβ plaque showing its native in-tissue architecture. Tomogram 6 in dataset 1 from *App*$^{NL\text{-}G\text{-}F}$ knock-in mice collected with a VPP and NAD filtered. Cryo-tomographic slice shows the heterogeneity of an Aβ plaque, macromolecular features are pseudo coloured, including Aβ fibrils (cyan arrowheads), subcellular compartments (light green), small tube like membranes we called ‘nanopaedia’ (dark green), extracellular vesicles (purple), liquid-like droplets (brown) and C-shaped membranes (orange, A). Scale bar, 100 nm. Segmentation of this tomogram visualises the architecture of the plaque and shows different areas of densities within the plaque. Moreover, subcellular compartments (light green), extracellular vesicles (purple), C-shaped membranes (orange), nanopaedia (green), and liquid-like droplets (brown) were found to interdigitate β-amyloid fibrils (cyan, B).

4.1.3. Aβ plaque fibrils and other macromolecular features within the plaque

Qualitative analysis of tomograms revealed that fibrils were organised into regions of different densities, including parallel bundles (Figure 23 A) and a tightly packed meshwork (Figure 23 B). These different fibril architectures were further investigated and quantitative data will be discussed in Chapter5:Quantitative analysis of data - Fibrils architecture. Most fibrils appeared to be very thin in the first dataset (Figure 22 A, Figure 23 A and B).

Additionally, the tomograms revealed some rather curious structures that all interdigitated amyloid fibrils (Figure 22). The subcellular compartments contained a higher order protein network that seemed to have a distinct organisation (Figure 23 C). Membranes were classified as subcellular compartments when their top and bottom were not visible in tomograms indicating that these membranes were processes from cells surrounding the plaques or very large exosomes. Interestingly, extracellular vesicles were found within the plaques (Figure 23 B, purple). They were classified as such when membranes were closed at top and bottom, in contrast to cellular processes. Some vesicles containing C-shaped membranes (Figure 23 D). Small tube-like structures were named membrane nanopaedia (Figure 23 E). Moreover, ~100 nm diameter smooth spherical constituents that were not surrounded by membranes were classified as liquid-like droplets (Figure 23 F). Fibrils seemed to emerge from one end of these liquid-like droplets.

Interestingly, fibrils appear thicker in dataset three and four (Figure 24), compared to those observed in dataset one (Figure 23 A and B). Therefore, the thickness of fibrils in all four datasets was measured and analysed in Chapter5: Quantification of fibrils - Measurements of Aβ fibril diameter.

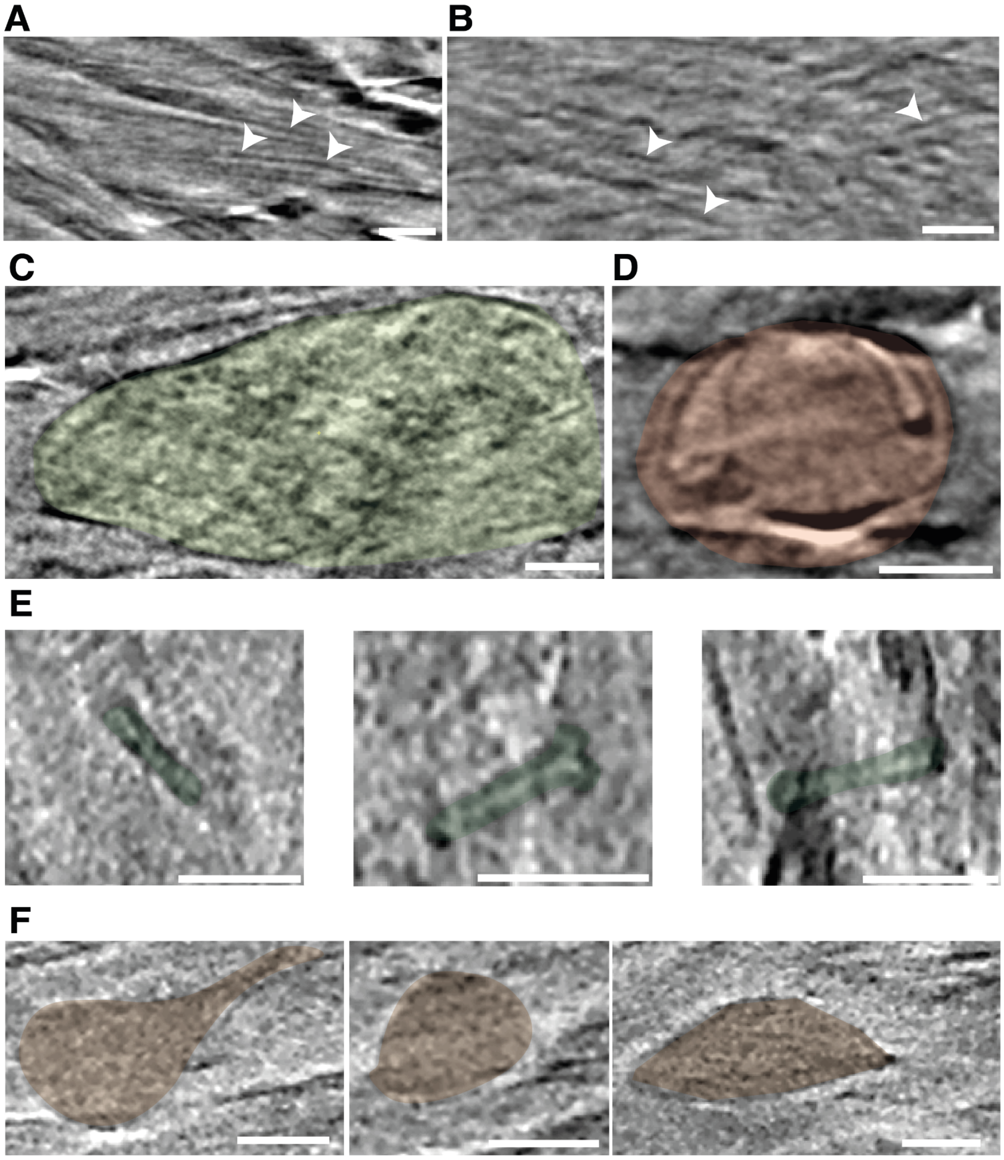

Figure 23: Various structures that were found within a plaque. Aβ plaque is composed of parallel bundles (A) and meshwork of fibrils (B). Indicated by white arrows. 2D images of numerous other macromolecular structures that interdigitated the fibrils were cropped from a tomogram and pseudocoloured, including subcellular structures containing a higher-order network of proteins (bright green, C), spherical membranes with c-shaped inclusions (orange, D), thin tube-like nanopaedia (dark green, E) and smooth liquid-like droplets indicated by black arrowheads (brown, F). All scale bars, 50 nm.

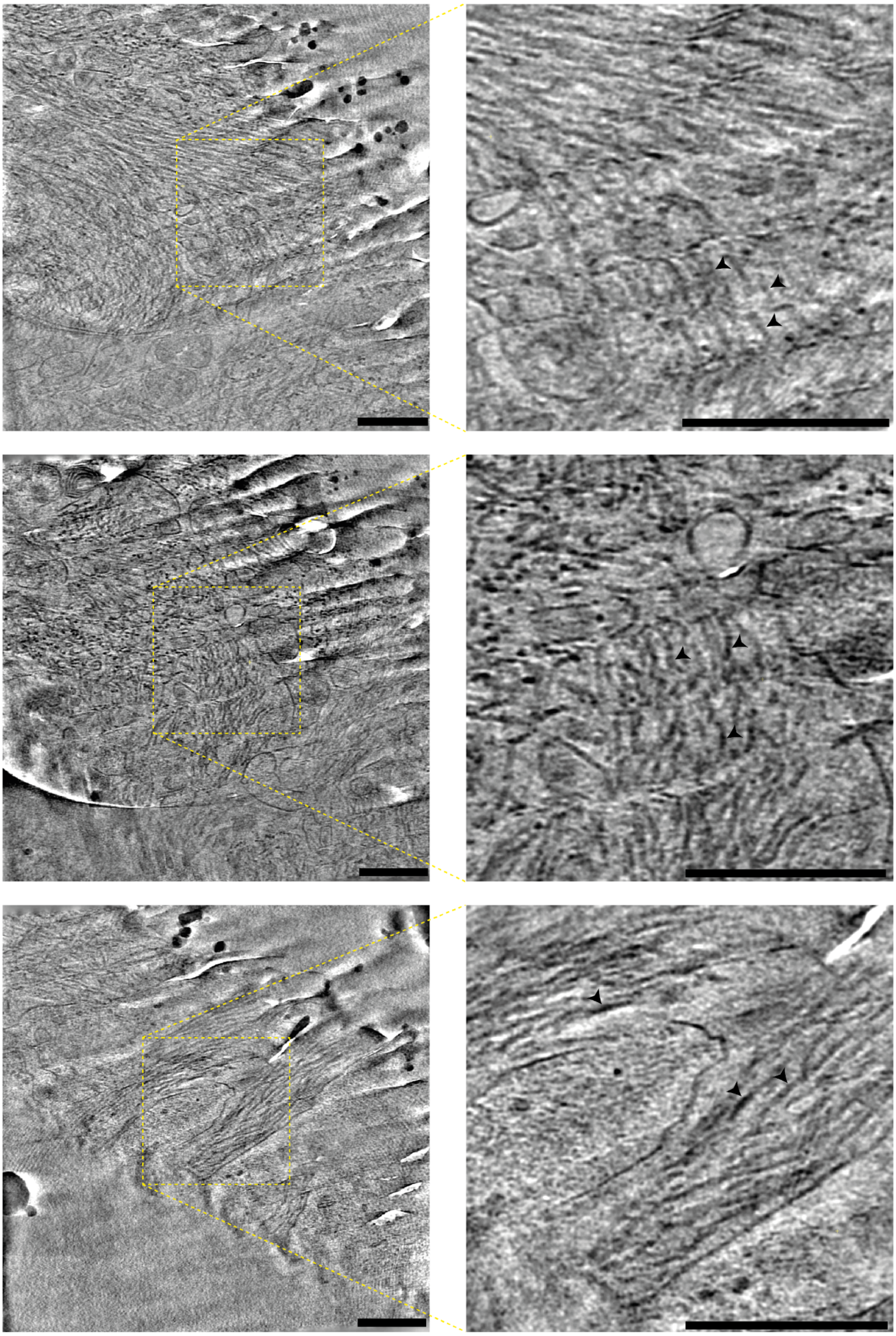

Figure 24: Different thicknesses of Aβ fibrils. Tomograms from different regions within the same plaque from dataset 3 are shown, tomogram 1 (top), tomogram 4

(middle), tomogram 7 (bottom). Three different examples show that some of the fibrils seem thicker than previously seen in dataset one. Black arrows indicate fibrils. Scale bars, 200 nm.

4.1.4. Measurements of putative exosomes and nanopaedia

Various macromolecular structures were found within the Aβ plaque. Two of them were classified as exosomes and nanopaedia according to their shapes. The diameters of these structures were measured to further classify them.

Therefore, three measurements were set across the structures in multiple z planes of each putative exosome. The variability of measurements taken was very high, reaching from 43.92 to 201.15 nm (mean= 81.97 ± 33.15 nm), measured from six tomograms (n=6/2, Figure 25 A). Furthermore, the diameter of nanpaedia which were small membranous tubes were 9.73 to 18.07 nm (mean=12.53 ± 2.39 nm) measured from one tomogram (n=1/1, Figure 25 B).

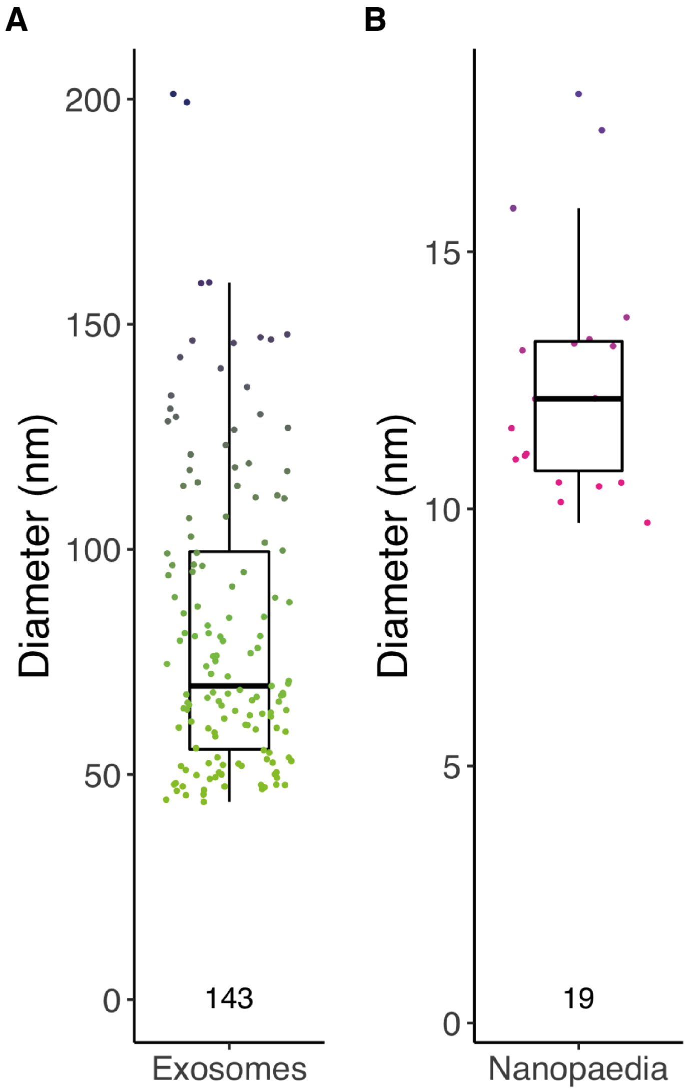

Figure 25: Diameter of putative exosomes and nanopaedia. Exosomes have a high variability in diameter between 43.92 and 201.15 nm (mean= 81.97 ± 33.15 nm, n=143, A). The diameter of nanopaedia reaches from 9.73 to 18.07 nm (mean=12.53 ± 2.39 nm, n=19, B).

4.1.5. Tissue surrounding plaques

The tomogram collection was guided by fluorescent Methoxy-X04 signals. Tomograms were not only collected from bright fluorescent signals inside the plaques (central region of the plaque), but also from dim signals adjacent to the core of the Aβ plaques (boundary). Some of the tomograms were collected in the periphery, in absence of Methoxy-X04 fluorescence (full list of where tomograms were collected is shown in Table 10).

Numerous cellular features were observed in close proximity of the plaque as well as between parallel bundles of fibrils. Some tomograms indicate that a population of fibrils was surrounded by lipid bilayers (Figure 26 A and B) but one could not deduce if these fibrils were intra-or extracellular because the amyloid and membranes extend beyond the thickness of the cryo-section. More data and lower magnification or a montage of tomograms is needed to determine this. Cellular processes were surrounding the fibrils in the tomographic slice shown in Figure 26 A. There were no cell organelles found within the compartment containing the amyloid, suggesting these amyloid fibrils were either extracellular or within an endosomal compartment, but not intracellular within the cytoplasm of the cell (Figure 26 C). Some subcellular processes were found within the plaque as described in Figure 22. An indication of cell cytoplasms were the presence of ribosomes, lipid bilayer and microtubules (Figure 27 A). One of the tomograms in our dataset contained a cell with actively translating ribosomes adjacent to the amyloid fibrils. Segmentation of this tomogram showed that fibrils are only in the extracellular space and not inside the cells (Figure 27 B).

Potential limitations of this technique are that it can be hard to determine extra- from intracellular space and the field of view in every single tomogram was limited. Therefore, multiple tomograms were collected from each plaque. All features that were discovered in one Aβ plaque are illustrated in Figure 28 A (legend in Figure 28 B). These suggested that the majority of fibrils arranged into a tightly packed meshwork were located at the very centre of the plaque. Parallel bundles were more often located towards the periphery of the plaque, although some meshwork was also found in peripheral regions of the plaque.

Furthermore, the core consisted of small c-shaped membranes and subcellular compartments, containing higher-order protein networks and dense cores. Subcellular compartments were also observed in the periphery interdigitating the fibrils. Myelinated axons, in contrast, were only localised at the periphery of the plaque. Lipid bilayers, mitochondrion, actin, microtubules, ribosomes and rough endoplasmic reticulum, suggest that metabolically active cells are in close proximity to the plaque (Figure 28 A).

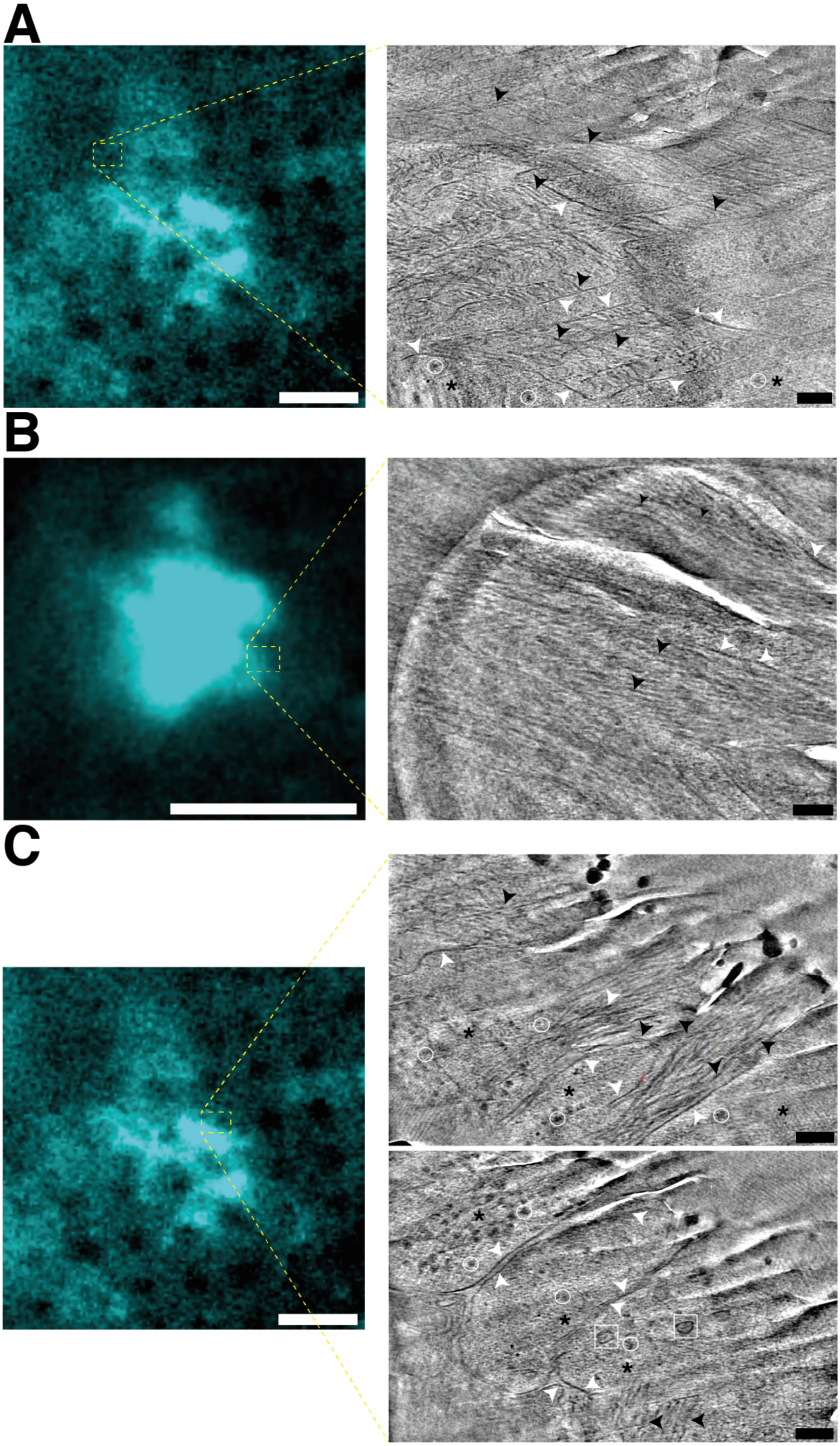
A
B
C

Figure 26: Plaques surrounded by lipid bilayers. Cryo-FM images (left) show regions where tomograms were collected. Scale bar, 4 µm. Cryo-tomographic slices (right) of Aβ fibrils surrounded by membranes of two different plaques from dataset 3 and 4 (A, B) and of cells that are interdigitating the pathology (C). Cell cytoplasms were identified by the presence of ribosomes and microtubules. White arrowheads - lipid bilayer, black arrowheads - fibrils, white circles - ribosomes, white boxes - microtubules. Scale bars, 100 nm.

A

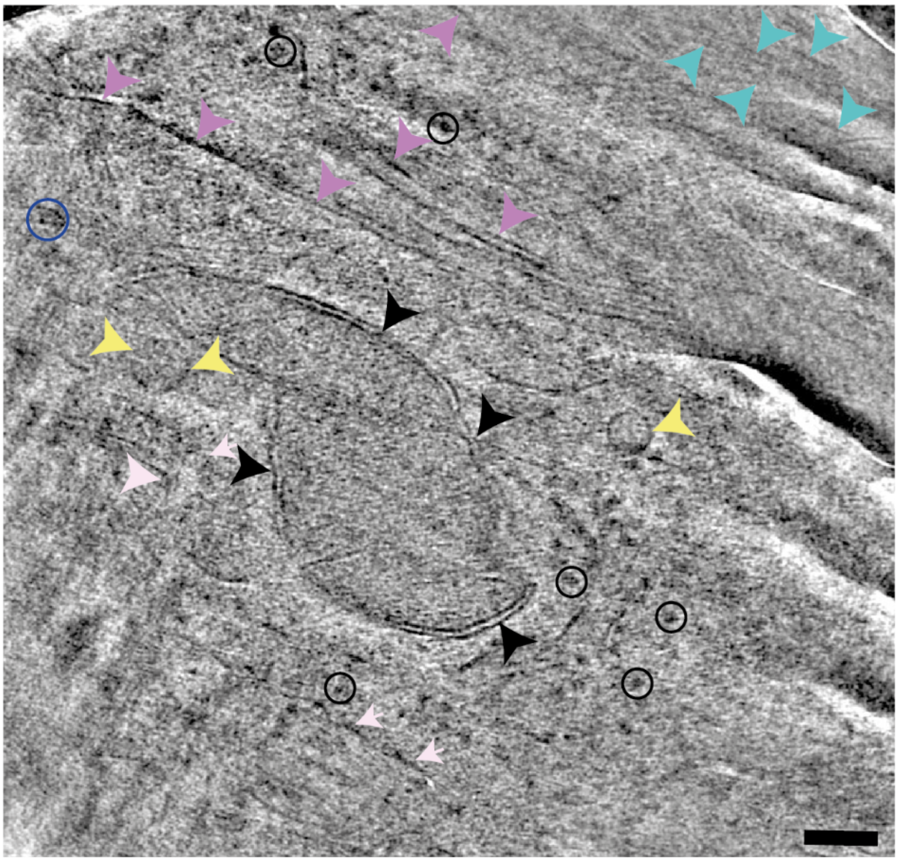

B

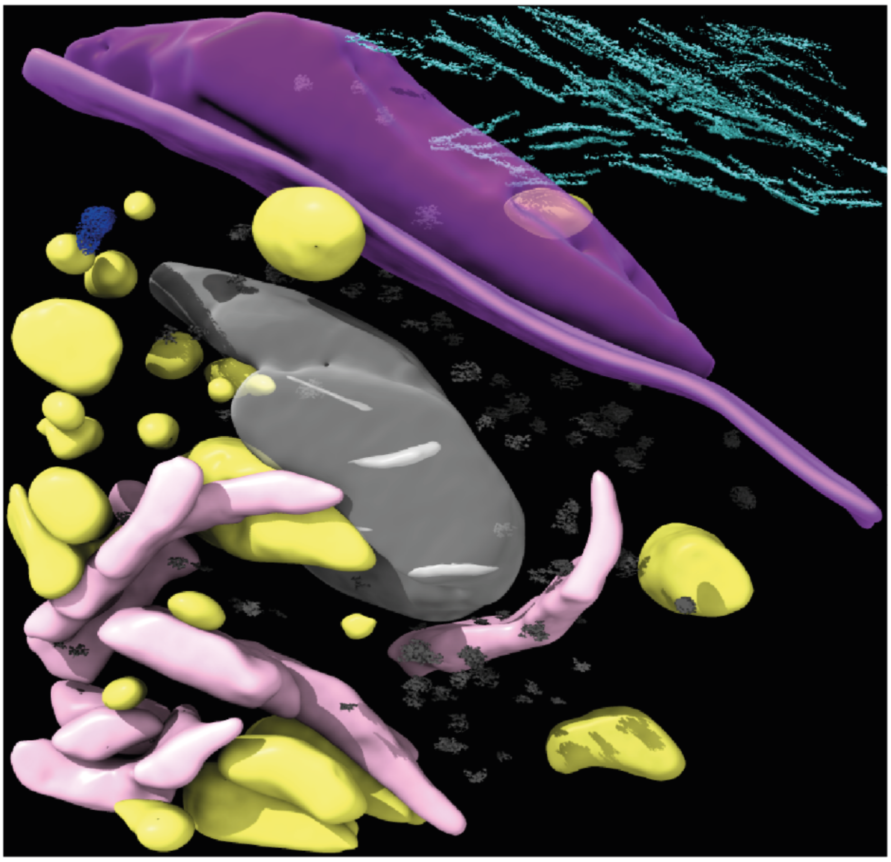

Figure 27: Cells were found in close vicinity of the plaques. Cryo-tomographic slice (dataset 4/tomogram 2) collected from ultrathin cryo-sections of *App*$^{NL\text{-}G\text{-}F}$ knock-in mice shows an actively translating cell close to the plaque. Fibrils, indicated by cyan arrowheads are in the upper right corner. Purple arrowheads indicate the plasma membrane of the cells which contain ribosomes (black circles), microtubules (blue circles), small membranes surrounded intracellular compartments (yellow arrowheads), mitochondrion (black arrowheads), endoplasmic reticulum (light pink arrows, scale bar 50 nm, A). Segmentation of tomogram shows cell organelles, including ribosomes (dark grey), endoplasmic reticulum (light pink), intracellular membranes (yellow), microtubules (dark blue) and plasma membrane (purple). Aβ fibrils (cyan) are in the right upper corner adjacent to the cell (B).

To assess if amyloid plaques were intracellular or extracellular, tissue biopsies used for dataset 4 were incubated with an extracellular marker, Dextran-AF-647. Fluorescent dextran was added to cryoprotectants before tissue biopsies were high-pressure frozen. The dextran fills the extracellular spaces and was imaged using a cryo-FM. Importantly, the Dextran-AF-647 signal (magenta) was absent in regions where cell cytoplasms were found (Figure 28 C).

The Dextran-AF-647 signal (magenta, Figure 29 middle) showed a very similar pattern to the Methoxy-X04 signal (cyan, Figure 29 left). Both channels were merged and the overlay between the Methoxy-X04 (cyan) and Dextran-AF-647 are shown in white (Figure 29 right). Most of the Methoxy-X04 amyloid signal was overlaid with the Dextran-AF-647, indicating that plaques are extracellular.

All tomograms from dataset 4 were collected from tissue that was incubated in Dextran-AF-647. Tomograms one, two, four, five and six contain intracellular features (Figure 28 A) and show no signal for Dextran-AF-647 in those regions (Figure 28 B). Thus, it was validated that parts of these tomograms were collected in the intracellular space. All tomograms from dataset 4 are listed in Table 13, Dextran-AF-647 signal, extra- and intracellular features are qualified. In conclusion, plaques were located in the extracellular space, in close proximity to cells. All cryo-CLEM data are shown in Appendix II: cryo-CLEM.

Dataset	Animal	Tomogram	Dextran-AF 647	Extra-cellular	Intra-cellular
4	2	1	1	1	1
4	2	2	0	1	1
4	2	3	1	1	0
4	2	4	1	1	1
4	2	5	0	0	1
4	2	6	1	1	1
4	2	7	1	1	0
4	2	8	1	1	1
4	2	9	1	1	0
4	2	10	0	0	1
4	2	11	0	0	1
4	2	12	1	1	1
4	2	13	1	1	0

Table 13: Tomograms from dataset 4 labelled with an extracellular marker. Tomograms were collected from extra- and intracellular space. Dextran-AF647 was used as a marker for the extracellular space. 1 - fluorescence, 0 - no fluorescence.

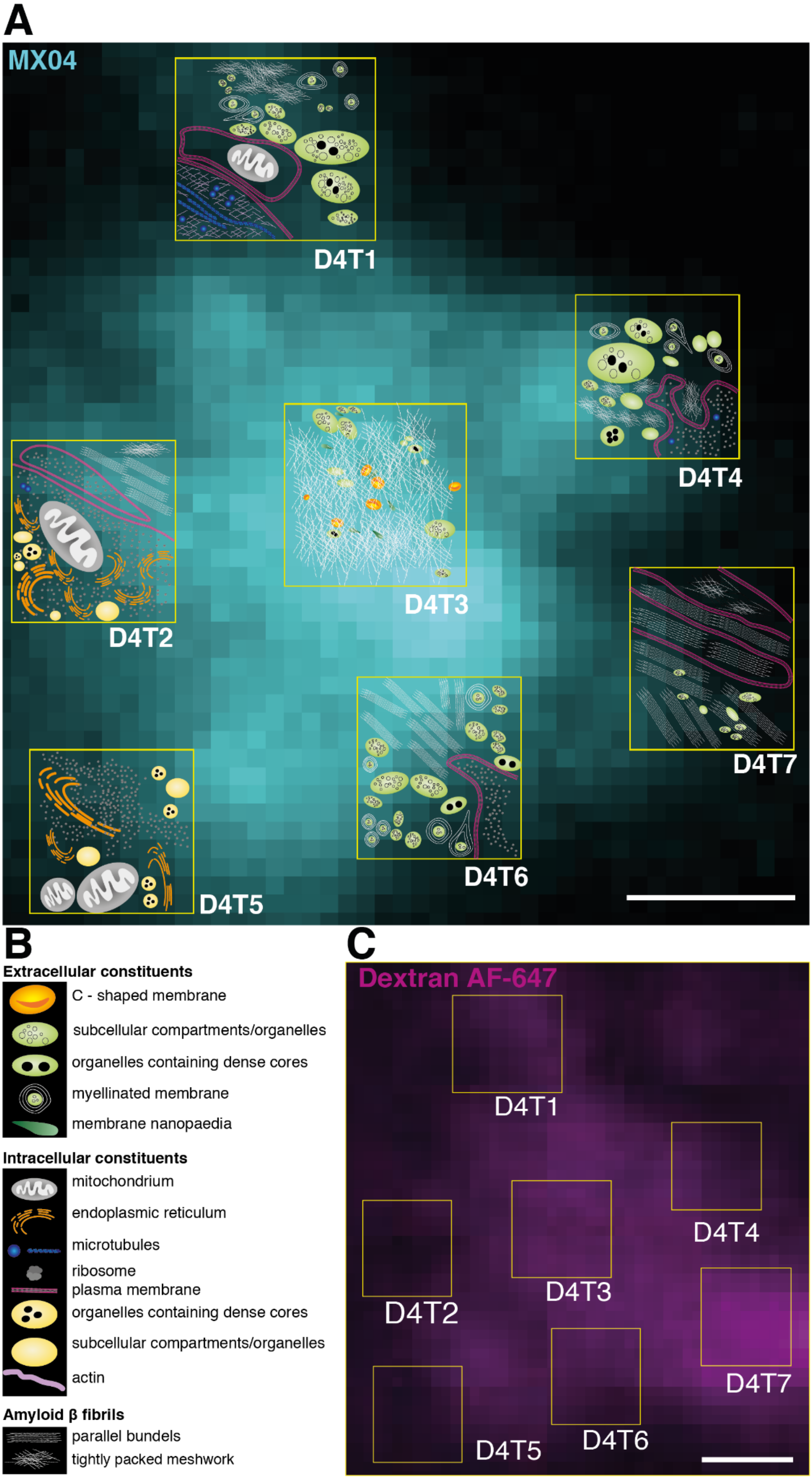
A
MX04
D4T1
D4T4
D4T3
D4T2
D4T7
D4T6
D4T5
B
Extracellular constituents
C - shaped membrane
subcellular compartments/organelles
organelles containing dense cores
myellinated membrane
membrane nanopaedia
Intracellular constituents
mitochondrium
endoplasmic reticulum
microtubules
ribosome
plasma membrane
organelles containing dense cores
subcellular compartments/organelles
actin
Amyloid β fibrils
parallel bundels
tightly packed meshwork
C
Dextran AF-647
D4T1
D4T4
D4T3
D4T2
D4T7
D4T5
D4T6

Figure 28: Cryo-FM image of a plaque stained with Methoxy-X04 and Dextran-AF647 with a schematic of macromolecular features seen in tomograms. Boxes show areas where tomograms from *App*$^{NL\text{-}G\text{-}F}$ knock-in mice were collected and schematic of fibril architectures, macromolecular and subcellular structures found within and around plaques (A) and figure legend (B). Tissue was labelled with Dextran-AF647, an extracellular marker and boxes show areas where tomograms were collected (C). All scale bars, 4 μm.

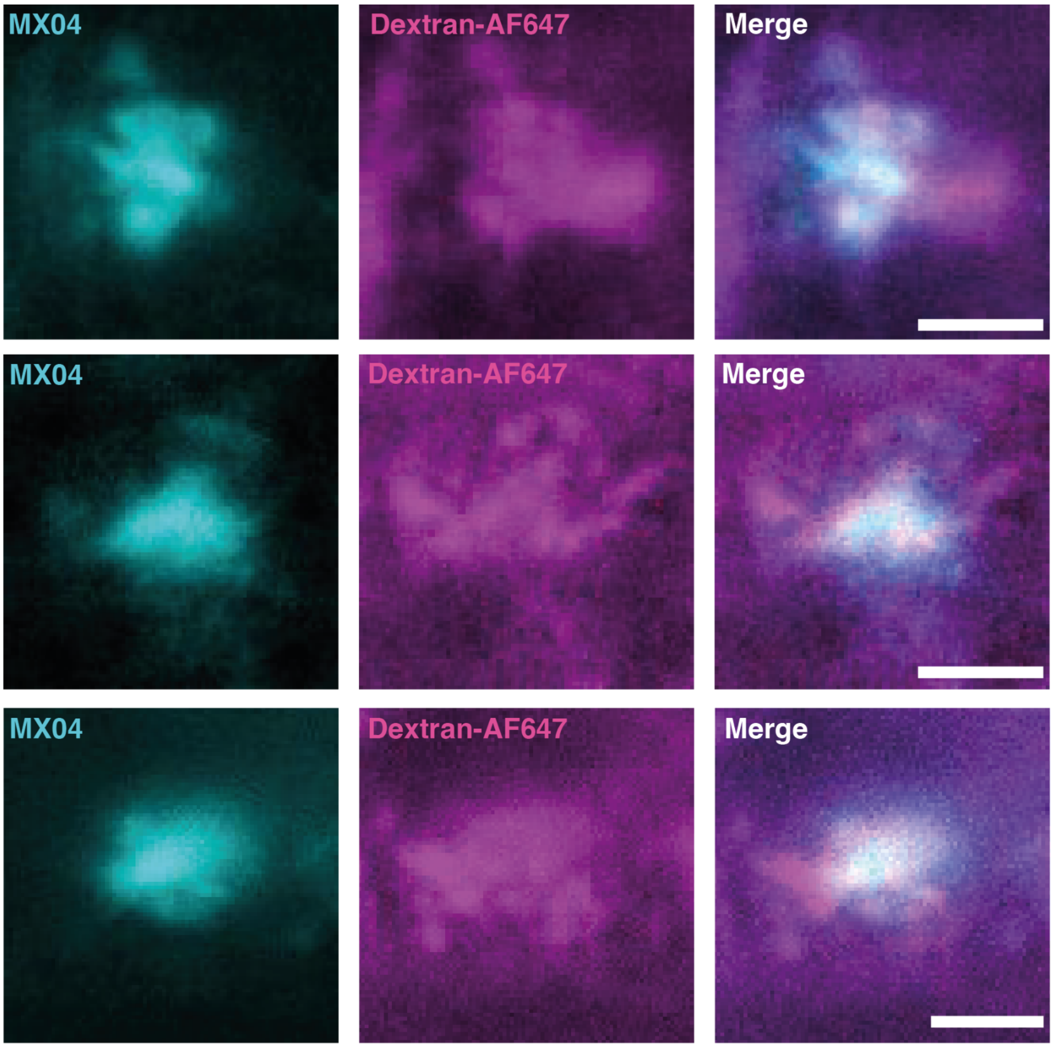

Figure 29: Methoxy-X04 labelled plaques were stained with Dextran-AF647 to visualise the extracellular space. Cryo-FM images of three different plaques labelled

with Dextran-AF647 from *App*$^{NL\text{-}G\text{-}F}$ knock-in mice injected with Methoxy-X04. Both signals (Methoxy-X04 - cyan, Dextran-AF-647 - magenta) were overlaid which confirmed that plaques were extracellular (merge, overlay in white). All scale bars, 4 μm.

4.2. Discussion

Methoxy-X04 was used to guide the collection of tomograms and define the region of the plaque tomograms were collected from. One limitation of Methoxy-X04 as a label is that it stains the dense core of plaques and thus fibrils outside of the plaques are not labelled (Bisht *et al.*, 2016). Furthermore, the 3D view of the entire plaque is limited by the thickness of the cryo-sections because the plaque is thicker than 70-150 nm. Thinner specimens on the other hand are required to achieve a better resolution in cryo-ET. To obtain the cryo-ET structure of cellular structures larger than the thickness of cryo-sections, cryo-ET of serial sectioning is theoretically possible and could give a reconstruction spanning the entire plaque. For this, multiple grids would have to be collected with tissue ribbons and the equivalent location in every tissue section would be imaged. However, no practical approach has been proposed or tested to apply this approach and this is expected to be very challenging not least because a fiducial marker would be needed to track the same region in every section and information is lost in regions of cutting damage.

In this study, the first in-tissue architecture of Aβ plaques in their native state was revealed. The plaques consisted of multiple regions of varying densities and fibril thicknesses. Moreover, fibril architectures within the plaques were found to be very heterogeneous, parallel bundles and a tightly packed meshwork of fibrils were observed. The plaques do not only consist of fibrils, but also numerous macromolecular features. In previous studies vacuoles and dense bodies were discovered within the plaques. Conventional EM indicated amyloid is arranged as a densely packed core and peripheral parallel bundles of fibrils resembling an amyloid star (Wegiel and Wisniewski, 1990; Frackowiak *et al.*, 1992; Kollmer *et al.*, 2016). However, for these studies, specimens were dehydrated and stained with heavy metals. Dehydration leads to shrinkage of tissue and heavy metal stainings can introduce artefacts (Korogod, Petersen and Knott, 2015).

In this study, a high diversity of subcellular structures was found within the plaques which was largely consistent with data from negative stained resin embedded specimens. However, the liquid-like droplets have not been reported previously by classical EM, which may be because they are lost or damaged during sample preparation for classical EM. Overall, the diversity of subcellular compartments and macromolecular constituents in a plaque is very different from healthy brain tissue (Peukes *et al.*, Biorxiv; Zuber *et al.*, 2005).

Tomograms from multiple regions of one plaque were reconstructed to compare the architecture of centre, boundaries, periphery and cells that are in close proximity to plaque. Plaques were surrounded by cells and membranes. Neurites and microglia processes have been seen to interdigitate the plaques (Walker, 2020). In future studies, different fluorescent markers, for instance to label microglia cells, could be established for multicolour cryo-CLEM to evaluate the in-tissue architecture of microglial cells with respect to the β-amyloid pathology and obtain a structural perspective on the cellular processes involving microglia and amyloid.

Furthermore, a marker that labelled the extracellular space revealed that the fibrils were indeed extracellular. The application of electron tomography (ET) to an *in-vitro* cell culture model of amyloid fibril formation showed that amyloid damages cells causing fragmentation and vesicular debris that was speculated to be lysosomal in origin, to become entangled within extracellular amyloid (Han *et al.*, 2017). Furthermore, microglia are recruited rapidly to newly-formed Aβ plaques for their uptake (Meyer-Luehmann *et al.*, 2008a) subsequently leading to the death of such microglia and the release of plaques into the extracellular space (Baik *et al.*, 2016; Huang *et al.*, 2021). These findings suggest that Aβ aggregates have an intracellular origin before extracellular deposition and that microglia promote plaque growth. Future studies could apply the approach I have developed to examine the biogenesis of amyloid plaques with younger $App^{NL\text{-}G\text{-}F}$ mice to study plaque development over several months.

5. Quantitative analysis of amyloid architecture

5.1. Results

5.1.1. Fibrils architecture

The plaque architecture showed multiple regions of fibrils with different densities. Here, the heterogeneity observed in fibril architecture was quantitatively analysed in reciprocal space by fast fourier transformation (FFT). Fast fourier transform plots the spatial frequencies of the reconstructed tomograms to quantify repeating or ordered arrangements of amyloid fibrils. The FFT contains information of every single pixel in a 2D image. For FFT, 32x32 pixel large boxes from different regions of tomograms from two *App*$^{NL\text{-}G\text{-}F}$ mice were cropped and analysed using Fiji ImageJ. Features with a consistent spacing result in peaks in the FFT plot.

This analysis revealed regions of the amyloid containing parallel bundles of Aβ fibrils, revealed by peaks in the FFT plot (19 regions in total, Figure 30 B) and a meshwork of fibrils in eight tomograms (24 regions in total, Figure 30 A). The FFTs measured from meshwork only showed either no peaks or only a broad gaussian peak at the origin, suggesting that the architecture in that region had no higher order (Figure 30 A). Distances between parallel fibrils from eight tomograms were measured which demonstrated that variations in interfibril distance were relatively high, namely 2-14 nm (Figure 30 C). This implies that parallel bundles were not crystalline. The FFT measurements from all tomograms are shown in the Appendix II: Fast Fourier Transformation.

A

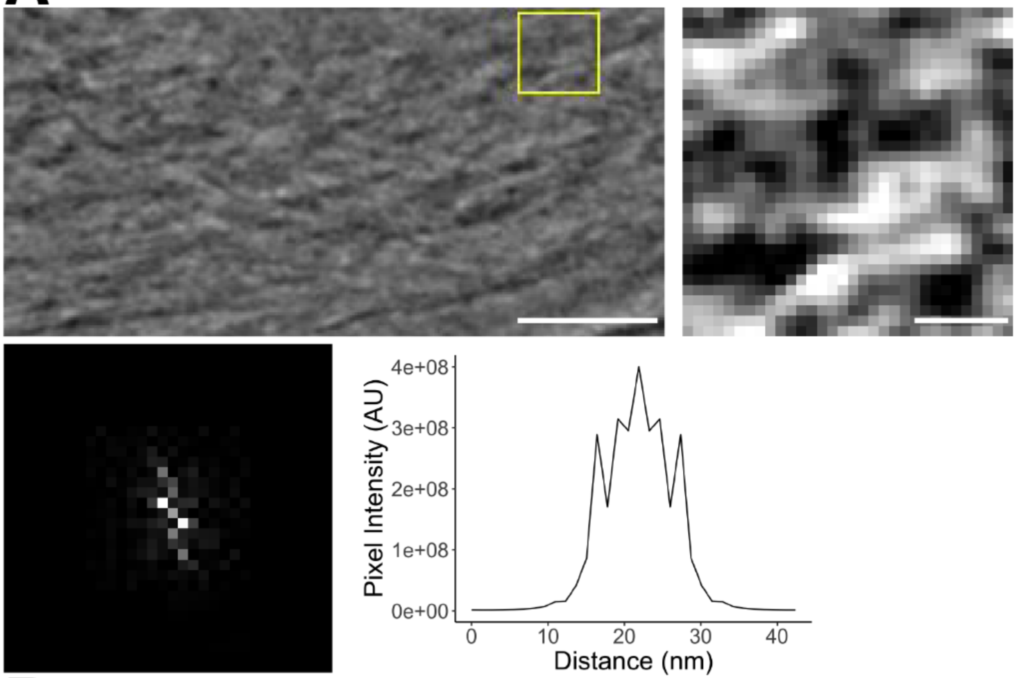
4e+08
3e+08
2e+08
1e+08
0e+00
Pixel Intensity (AU)
0
10
20
30
40
Distance (nm)

B

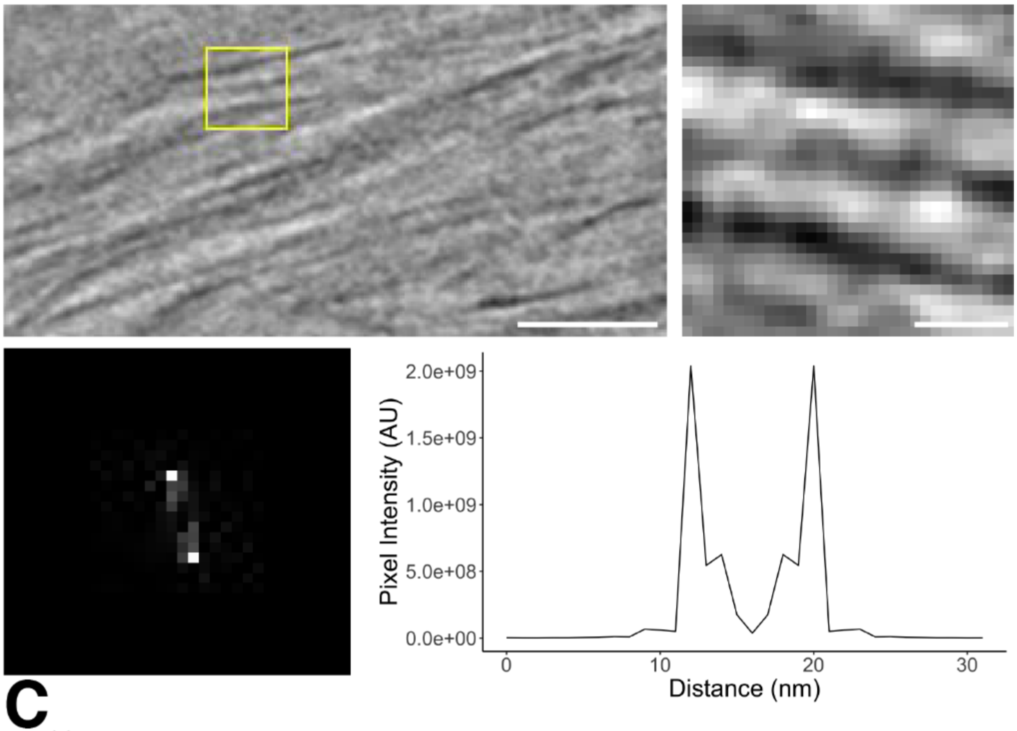
2.0e+09
1.5e+09
1.0e+09
5.0e+08
0.0e+00
Pixel Intensity (AU)
0
10
20
30
Distance (nm)

C

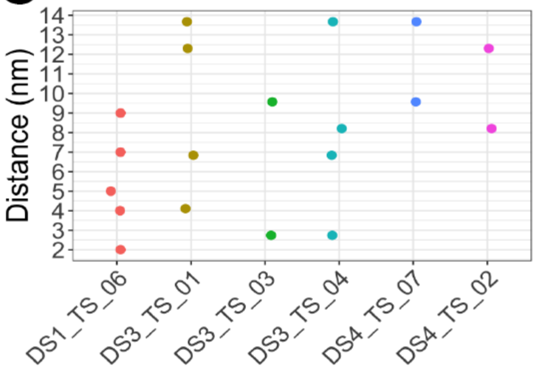
Distance (nm)
14
13
12
11
10
9
8
7
6
5
4
3
2
DS1_TS_06
DS3_TS_01
DS3_TS_03
DS3_TS_04
DS4_TS_07
DS4_TS_02

Figure 30: Fast fourier transforms from regions of different densities within the Aβ plaques. Examples of FFTs shown from dataset one, tomogram six. Boxes indicate regions of tomographic slices that were cropped for analysis. FFTs are shown and distances between fibrils are plotted. The FFT of the meshwork shows that fibrils were not parallel. The graph does not show individual peaks for fibrils within the meshwork (n=8/2, A). In contrast, FFT from parallel bundles showed two peaks clearly distinguishable (n=8/2, B). Distances between fibrils within parallel bundles were plotted and displayed a high variation reaching from 2 nm to 14 nm (C). All scale bars, 10 nm.

I next tested if the parallel versus meshwork arrangement of fibrils correlated with the relative cryo-CLEM Methoxy-X04 fluorescence intensity (Figure 31 A and B). Both tomographic slices shown in Figure 31 A and B (middle) were collected in regions of high fluorescent intensities (Figure 31 A and B top).

In total 28 measurements were taken from meshwork of fibrils and 20 measurements from parallel bundles of fibrils. Total pixel intensities in boxes were measured. The total fluorescent intensities measured from parallel bundles compared to meshworks of fibrils did not show a significant difference (p-value = 0.237, Methoxy-X04 mean fluorescence intensity of mesh and parallel bundles, respectively: 92.64 and 90.66 arbitrary units). Indeed, a high variability of Methoxy-X04 intensities within parallel bundles and within meshwork was observed, thus Methoxy-X04 seems to bind both equally (Figure 31 C).

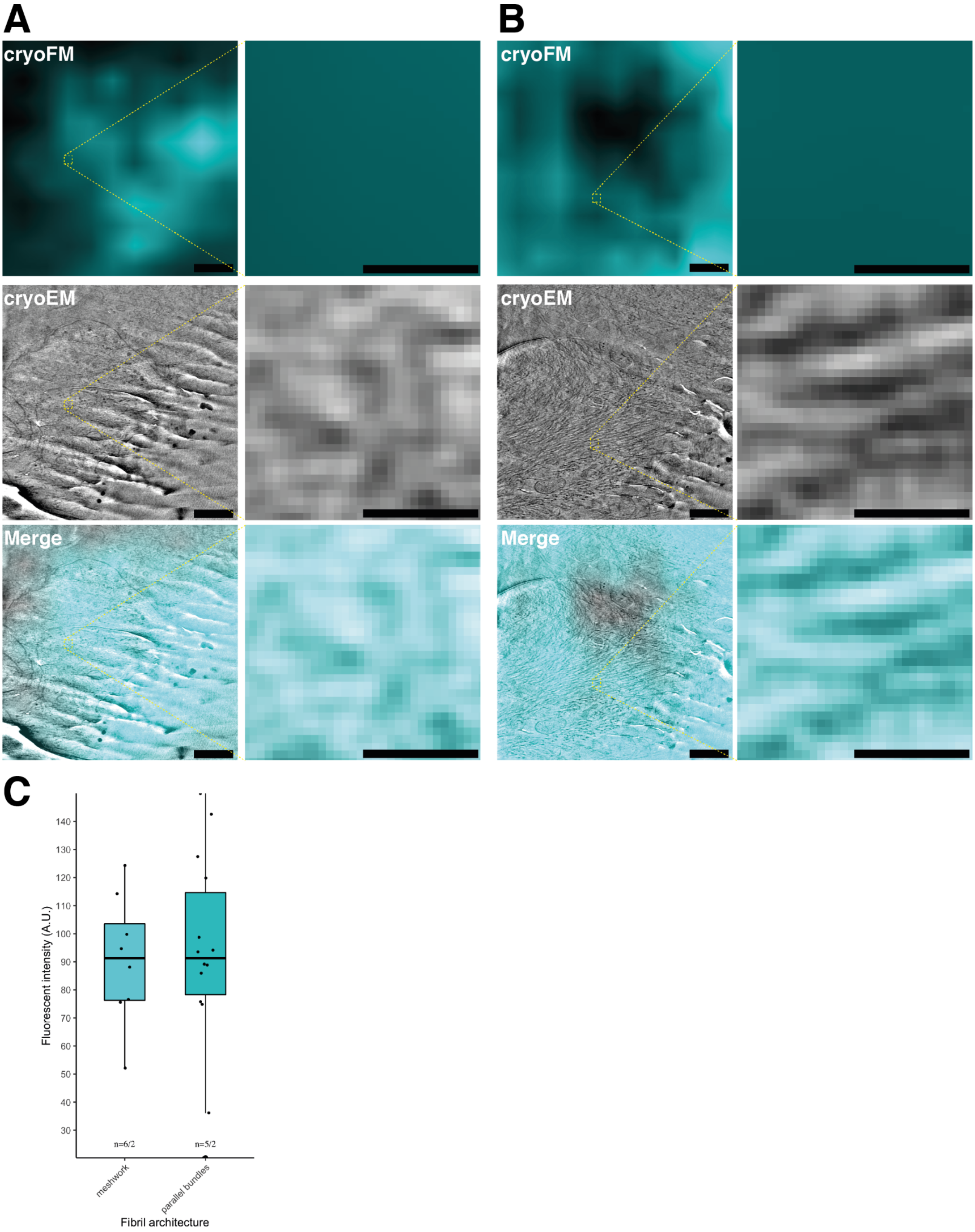

Figure 31: Measurements of fluorescent intensities from cryo-FM images of parallel bundles and meshwork. Regions of cryo-EM images used for FFT were cropped from cryo-FM images to evaluate differences in fluorescent intensities between

regions with different fibril densities. Fluorescent signals from cryo-FM were overlaid with cryo-EM images from meshwork (n=6/2, A) and parallel bundles (n=5/2, B). There was no significant difference between fluorescent intensities of parallel bundles and meshwork (p-value = 0.237, C). Scale bars left, 200 nm. Scale bars right, 10 nm.

5.1.2. Measurements of Aβ fibril diameter

Different Aβ fibril thicknesses were observed in tomograms from *App*$^{NL\text{-}G\text{-}F}$ knock-in mice (shown in Chapter 3 - 3.1.2 Architecture of Aβ plaques). To quantify the thickness of Aβ fibrils within plaques, diameters of 1834 fibrils (~50 fibrils per tomogram, three measurements per fibril) were manually measured from 12 in-tissue tomograms from four datasets (two *App*$^{NL\text{-}G\text{-}F}$ mice) in IMOD. Fibril edges were marked with points on either side of fibrils using IMOD. Then, nearest neighbour analysis was performed using matlab. Membranes of in-tissue tomograms were measured as an internal standard. They were found to be 5.01 ± 0.34 nm as expected (Tian *et al.*, 2021).

Additionally, three tomograms were collected from *ex-vivo* sarkosyl-extracted fibrils purified from *App*$^{NL\text{-}G\text{-}F}$ knock-in mice (kindly provided by Stanley Goodbody). These samples were used for single particle analysis (SPA). 451 measurements were taken from tomograms (~50 measurements per tomogram, three measurements per fibril). Measurements were performed in the exact same way for in-tissue and *ex-vivo* tomograms. Results of both in-tissue and *ex-vivo* structures were compared.

The diameters measured from fibrils in-tissue was between 2.47 and 11.58 nm, (mean=5.01 ± 1.37 nm, Figure 32 A). In contrast, the diameter of *ex-vivo* fibrils was between 5.06 and 16.62 nm (mean=6.49 ± 1.54 nm, Figure 28 B). Thus, fibrils in-tissue appeared to be on average thinner than *ex-vivo*, sarkosyl-extracted and purified fibrils (p = 2.2e-16 < alpha 0.05, Figure 28 C).

However, objects that moved together up and down in z were measured as one fibril. The third panel in Figure 32 A suggests that some fibrils could potentially be parallel bundles of fibrils rather than one thicker fibril.

The different in-tissue fibril widths could indicate a variety of different fibril conformers or may be a consequence of measurement error. In the latter case, one would expect to find a similar distribution of fibril widths in all tomograms. I therefore tested if variable widths were evenly distributed across different regions of multiple amyloid plaques. Cryo-FM images of regions in plaque where tomograms were collected are shown in Figure 33 A together with the mean of fibril diameter from each region. The graph shows the distribution of fibril diameters in each tomogram. There was a high variety of fibril diameters within each tomogram. The tomograms were collected from five different plaques. The data suggests that there is no relation of fibril diameter and plaque region, i.e. core, boundary, periphery. Colours used in the plot match the colours of the boxes and means in the cryo-FM image (Figure 33 B). Overall the mean diameters are between 4.73 - 6.88 nm (Table 14). Significant differences between groups were measured using a one-way ANOVA with p=<2e-16, (F(11,1822)=39.13,p<0.01). P-values of the *post hoc* test are shown in Table 15 for each group. Overall 64 % of data showed significant differences and 36 % of data had the same mean diameter. These data suggest that the variability of fibril diameter could not be attributed to measurement error and suggest that the fibrillar material within amyloid plaques is not composed of a single conformer.

However, the pixel size in the in-tissue and *ex-vivo* tomograms was relatively large with 13.68 and 11.60 Å, respectively. Moreover all of these measurements were performed manually and thus, measurement errors can arise which could explain the high variation of the diameter.

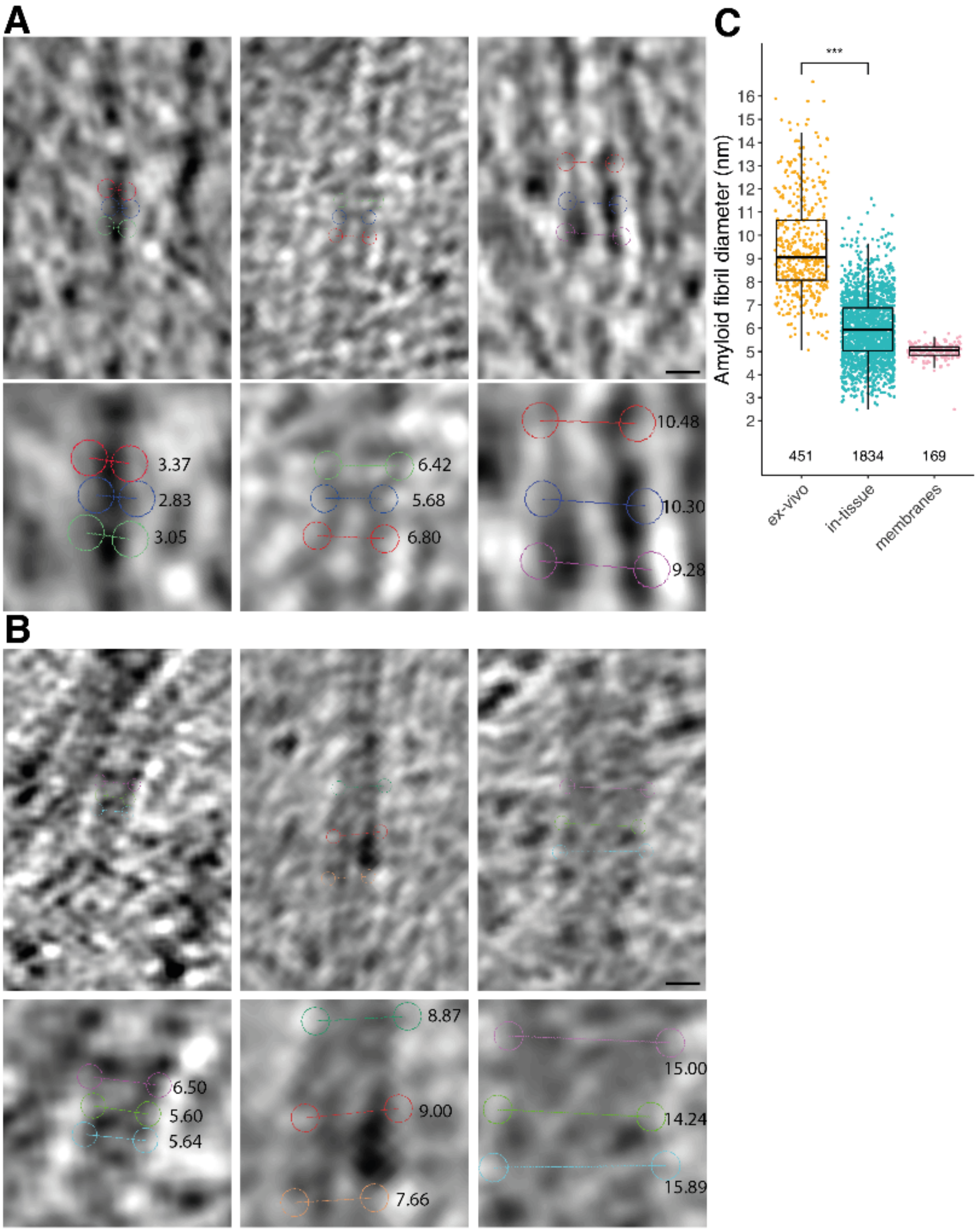

Figure 32: Fibril diameters measured from in-tissue and *ex-vivo* tomograms measured from *App*$^{NL\text{-}G\text{-}F}$ knock-in mice. In total fibril thickness 12 tomograms, 1834 marker points (150 per tomogram) from in-tissue tomograms collected from two *App*$^{NL\text{-}G\text{-}F}$ knock-in mice (A) were measured. Three tomograms from purified fibrils with

451 marker points were analysed (B). Thickness of in-tissue (2.47 - 11.58 nm, mean 5.01 ± 1.37 nm) and purified (5.06 - 16.62 nm, mean 6.49 ± 1.54 nm) is significantly different with p = 2.2e-16 < (alpha 0.05, C). Diameters of membranes from in-tissue tomograms were measured as internal controls (5.01 ± 0.34 nm). All scale bars, 50 nm.

To attempt to obtain a better measurement of fibril diameter, subtomogram averaging was performed. For subtomogram averaging, subvolumes of fibril segments, i.e. multiple 2D images of macromolecules, were extracted from 3D tomography reconstruction. Initially, a reference is generated and subvolumes are iteratively aligned to this reference. The resulting averages are expected to have increased signal-to-noise ratio and allow us to resolve structures in greater detail, compared to tomograms (Briggs, 2013).

Tomograms were collected from samples of *ex-vivo* fibrils purified from *App*$^{NL\text{-}G\text{-}F}$ knock-in mice. Peet was used to perform subtomogram averaging (Nicastro *et al.*, 2006; Heumann, 2011). Averages were generated from 125 *ex-vivo* particles, picked in IMOD with a pixel size of 11.60 Å. Particles were aligned to the tomogram Y-axis and reference was refined in every iteration. The averages obtained from these samples were used as an initial reference to align particles from in-tissue tomograms.

187 particles from in-tissue tomograms (pixel size 13.68 Å) were picked in IMOD from a tomogram for subtomogram averaging. Particles were aligned to initial reference in every iteration.

The resolution for tomograms from *ex-vivo* fibrils (measured at 0.5 FSC) was 4.25 nm (Figure 34 A) and fibrils from in-tissue samples had a resolution of 7.89

nm (Figure 34 B). However, the resolution limit for subtomogram averaging is the Nyquist frequency (2 x pixel size) which was 6.84 Å for this data. This is insufficient to resolve the structure of fibrils beyond the information that these fibrils are rod shaped. Given that signal to noise increases by the square root of the number of subvolumes, the low resolution of the averaged map could be a consequence of the relatively low number of subvolumes used for this analysis. I considered increasing the number of subvolumes, however due to the resolution limit, the averaging of fibrils cannot align on the basis of the distance between individual β strands in the fibril. There are not expected to be any features to align other than the potential twist of the fibril. Moreover, if there is fibril heterogeneity, as suggested by our fibril width measurements, this will also contribute to a lower resolution in subtomogram averaging.

In comparison, the cryo-EM model generated by SPA had a resolution of 3.0 Å. Individual features can be clearly seen in the model compared to subtomogram averaging data (Figure 34 C). SPA revealed the fold of individual amino acids and the stereochemical arrangement of amino acid side chains.

Subtomogram averaging on structures in-tissue is therefore exceptionally challenging due to the high signal-to-noise ratio in tissue sections. Future data collection could employ a smaller pixel size to collect data for subtomogram averaging. It is worth noting that tomograms with a small pixel size would not be suitable for examining the architecture of amyloid plaques because a small pixel size reduces the field of view. Moreover, reducing the pixel size alone is unlikely to generate a high resolution structure because in comparison to purified, plunge frozen samples, tissue cryo-sections have a crowded environment that is likely to further lower the signal-to-noise ratio. Tissue cryo-sections are approximately 2-fold thicker than SPA cryo-EM plunge-frozen samples (70-150 nm and 30-80 nm, respectively). This also has a profound effect on the obtainable resolution because thicker samples increase the inelastic scattering of electrons that reduces the signal-to-noise.

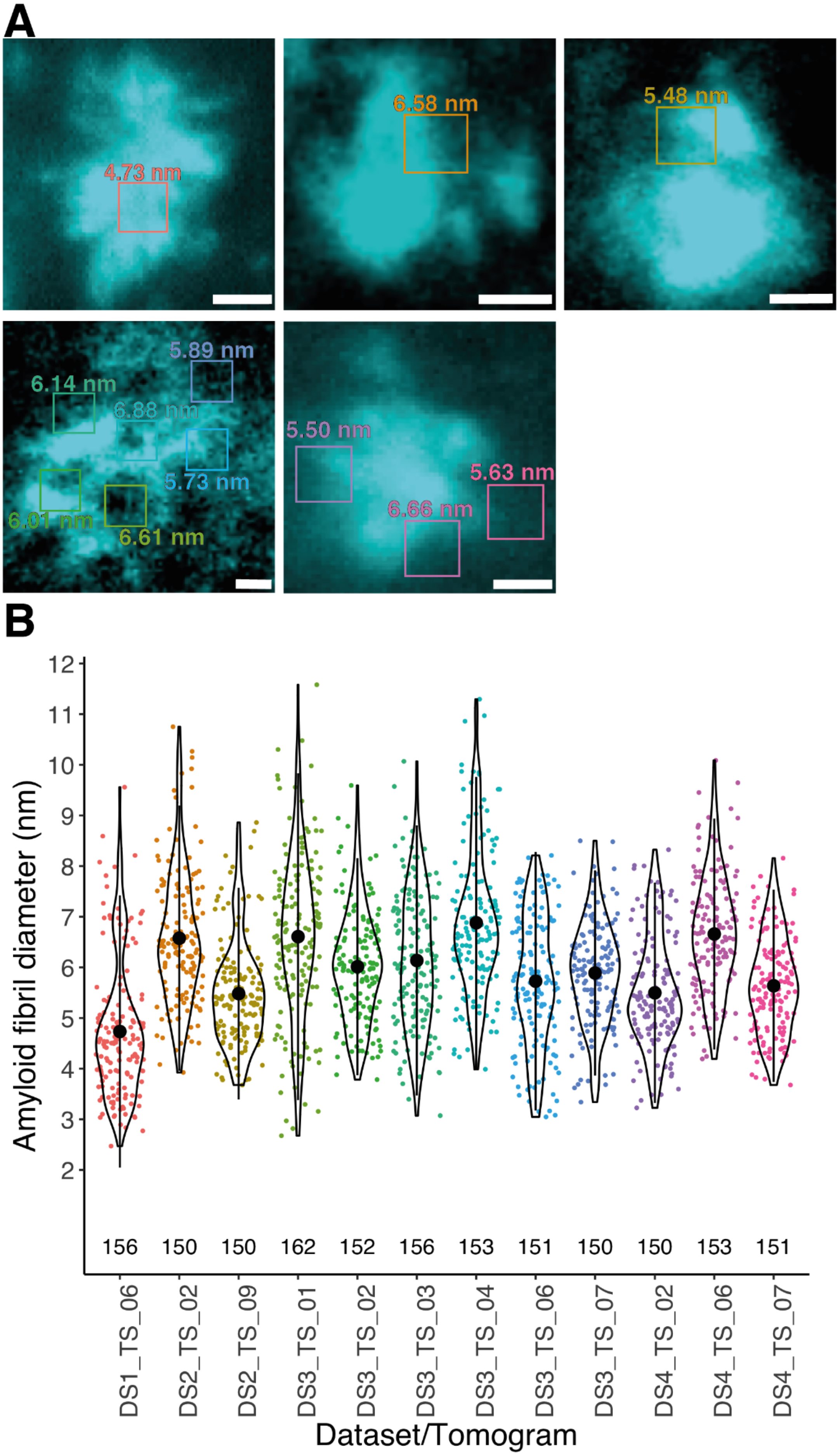
A
4.73 nm
6.58 nm
5.48 nm
5.89 nm
6.14 nm
6.88 nm
5.73 nm
6.01 nm
6.61 nm
5.50 nm
5.63 nm
6.66 nm
B
Amyloid fibril diameter (nm)
12
11
10
9
8
7
6
5
4
3
2
156
150
150
162
152
156
153
151
150
150
153
151
DS1_TS_06
DS2_TS_02
DS2_TS_09
DS3_TS_01
DS3_TS_02
DS3_TS_03
DS3_TS_04
DS3_TS_06
DS3_TS_07
DS4_TS_02
DS4_TS_06
DS4_TS_07
Dataset/Tomogram

Figure 33: Diameter measurements for each in-tissue tomogram. Cryo-CLEM data is shown and the areas where tomograms were taken are indicated, mean of fibril diameters are shown (A) Fibril diameter measured from two mice (two datasets each). In total 12 tomograms, 1834 marker points (~ 150 per tomogram) in-tissue were measured in IMOD. The variances of fibril diameter from each tomogram are very high, reaching from 2.47 to 11.58 nm. All scale bars, 4 µm.

Dataset	Animal	Tomogram	Mean (nm)	Min (nm)	Max (nm)
1	1	6	4.73	2.47	9.56
2	1	2	6.58	3.93	10.75
2	1	9	5.48	3.68	8.86
3	2	1	6.61	2.68	11.58
3	2	2	6.01	3.78	9.59
3	2	3	6.14	3.07	10.07
3	2	4	6.88	3.99	11.30
3	2	6	5.73	3.05	8.21
3	2	7	5.89	3.34	8.50
4	2	2	5.50	3.23	8.32
4	2	6	6.66	4.19	10.09
4	2	7	5.64	3.68	8.16

Table 14: Fibril diameter from each tomogram. Mean, minimum and maximum diameter in nm are shown.

Comparison	Adjusted p-value	Significance
DS2_TS_02-DS1_TS_06	1.33704158855608E-11	***
DS2_TS_09-DS1_TS_06	8.89367992873424E-06	***
DS3_TS_01-DS1_TS_06	1.33704158855608E-11	***
DS3_TS_02-DS1_TS_06	1.34907640614301E-11	***

Comparison	Adjusted p-value	Significance
DS3_TS_03-DS1_TS_06	1.34834365894676E-11	***
DS3_TS_04-DS1_TS_06	1.33704158855608E-11	***
DS3_TS_06-DS1_TS_06	1.95656824075741E-10	***
DS3_TS_07-DS1_TS_06	1.35522704169944E-11	***
DS4_TS_02-DS1_TS_06	4.90379299766808E-06	***
DS4_TS_06-DS1_TS_06	1.33704158855608E-11	***
DS4_TS_07-DS1_TS_06	1.36947295725776E-08	***
DS2_TS_09-DS2_TS_02	1.54269930163764E-11	***
DS3_TS_01-DS2_TS_02	0.999999999658836	n.s.
DS3_TS_02-DS2_TS_02	0.00470429639758352	*
DS3_TS_03-DS2_TS_02	0.0795435192632271	n.s.
DS3_TS_04-DS2_TS_02	0.591283192625936	n.s.
DS3_TS_06-DS2_TS_02	2.08721441241622E-07	n.s.
DS3_TS_07-DS2_TS_02	0.000102388479451432	***
DS4_TS_02-DS2_TS_02	1.7910339877858E-11	***
DS4_TS_06-DS2_TS_02	0.99998836304003	n.s.
DS4_TS_07-DS2_TS_02	3.77453890365587E-09	***
DS3_TS_01-DS2_TS_09	1.3633316697792E-11	***
DS3_TS_02-DS2_TS_09	0.0102806454819587	**
DS3_TS_03-DS2_TS_09	0.000256789394279422	***
DS3_TS_04-DS2_TS_09	1.34875444146587E-11	***
DS3_TS_06-DS2_TS_09	0.85837156840454	n.s.
DS3_TS_07-DS2_TS_09	0.161056186725386	n.s.
DS4_TS_02-DS2_TS_09	1	n.s.
DS4_TS_06-DS2_TS_09	1.35188527039531E-11	***
DS4_TS_07-DS2_TS_09	0.99540492667724	n.s.
DS3_TS_02-DS3_TS_01	0.00140083645242584	**
DS3_TS_03-DS3_TS_01	0.0337581404485341	*
DS3_TS_04-DS3_TS_01	0.71755596518943	n.s.
DS3_TS_06-DS3_TS_01	2.70071012220541E-08	***
DS3_TS_07-DS3_TS_01	2.14306764005912E-05	***
DS4_TS_02-DS3_TS_01	1.37934108579429E-11	***
DS4_TS_06-DS3_TS_01	0.999999892438821	n.s.

Comparison	Adjusted p-value	Significance
DS4_TS_07-DS3_TS_01	3.81013665062824E-10	***
DS3_TS_03-DS3_TS_02	0.999441454156297	n.s.
DS3_TS_04-DS3_TS_02	7.71439911950722E-08	***
DS3_TS_06-DS3_TS_02	0.680347104697238	n.s.
DS3_TS_07-DS3_TS_02	0.999274225238325	n.s.
DS4_TS_02-DS3_TS_02	0.015264815117134	*
DS4_TS_06-DS3_TS_02	0.000357510440811448	***
DS4_TS_07-DS3_TS_02	0.247070872958629	n.s.
DS3_TS_04-DS3_TS_03	8.63883666579746E-06	***
DS3_TS_06-DS3_TS_03	0.145411035865029	n.s.
DS3_TS_07-DS3_TS_03	0.847328670802671	n.s.
DS4_TS_02-DS3_TS_03	0.000427061199468337	***
DS4_TS_06-DS3_TS_03	0.0111458814099	**
DS4_TS_07-DS3_TS_03	0.0213119033009297	*
DS3_TS_06-DS3_TS_04	1.35693678515736E-11	***
DS3_TS_07-DS3_TS_04	2.85665713306571E-10	***
DS4_TS_02-DS3_TS_04	1.34839917009799E-11	***
DS4_TS_06-DS3_TS_04	0.919865412615137	n.s
DS4_TS_07-DS3_TS_04	1.34678934671228E-11	***
DS3_TS_07-DS3_TS_06	0.993293678282348	n.s.
DS4_TS_02-DS3_TS_06	0.904770441231191	n.s.
DS4_TS_06-DS3_TS_06	4.51169368531623E-09	***
DS4_TS_07-DS3_TS_06	0.999968873402044	n.s.
DS4_TS_02-DS3_TS_07	0.208031767653818	n.s.
DS4_TS_06-DS3_TS_07	4.44866226612106E-06	***
DS4_TS_07-DS3_TS_07	0.83401457270162	n.s.
DS4_TS_06-DS4_TS_02	1.35500499709451E-11	***
DS4_TS_07-DS4_TS_02	0.99821409676697	n.s.
DS4_TS_07-DS4_TS_06	6.88038515050948E-11	***

Table 15: Comparison of average fibril diameters from all tomograms. One way ANOVA and post hoc (Tukey HSD) tests were performed between data from all tomograms. The adjusted p-values after performing the post hoc test are shown here

and the significance between every single group. Significance codes: 0 '***' 0.001 '**' 0.01 '*' 0.05 n.s. (not significant) >0.05.

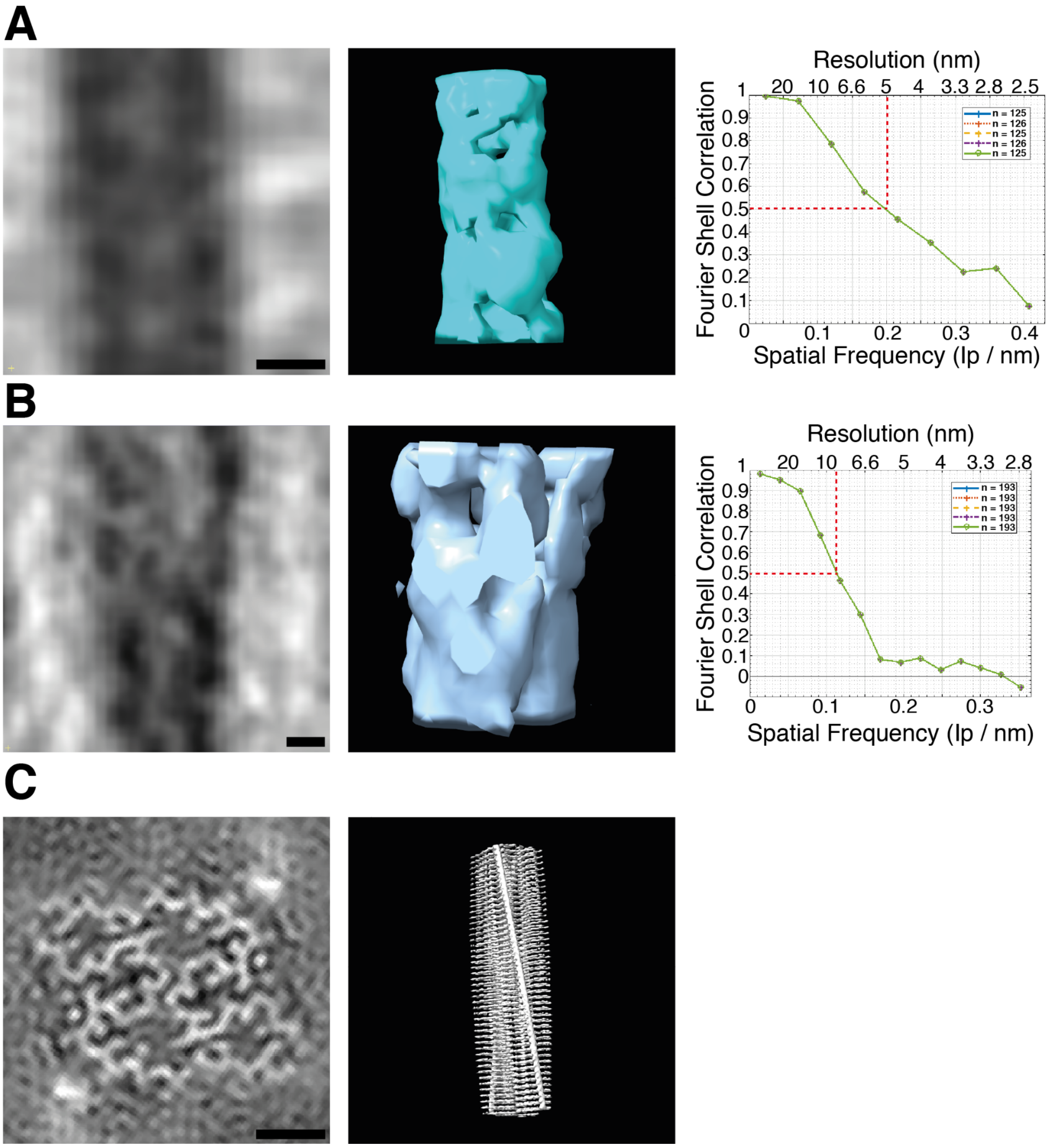

Figure 34: Cryo-EM structures of *ex-vivo*, in-tissue tomograms and SPA data from *App*$^{NL\text{-}G\text{-}F}$ knock-in mice. Subtomogram averages of tomograms from purified fibrils (A) and in-tissue tomograms (B) are shown in the left panel, middle panel shows models of averages. Scale bars, 5 nm. The resolutions were measured by fourier shell correlation at 0.5 in IMOD and plotted: 4.25 nm for purified fibrils and 7.89 nm for fibrils

in tissue (right). Cryo-EM map and model fibril structure from sakosyl-extracted Aβ(42) from *App*$^{NL\text{-}G\text{-}F}$ knock-in mice at 3.0 Å resolution (C). Scale bar, 2.5 nm.

5.1.3. The atomic structure of fibrils from *App*$^{NL\text{-}G\text{-}F}$ knock-in mice

A recent report of the structure of *ex-vivo* sarkosyl-extracted β-amyloid from postmortem brain indicated two different fibril forms (Yang *et al.*, 2022). Fibrils from *App*$^{NL\text{-}F}$ mice form one of these two Aβ conformers. However, the *App*$^{NL\text{-}G\text{-}F}$ knock-in strain contains the D22G Arctic familial AD mutation within the Aβ(1-42) peptide, which may give rise to a different fibril structure.

Therefore, the cryo-EM structure of sarkosyl-extracted fibrils from *App*$^{NL\text{-}G\text{-}F}$ knock-in mice was compared to the structures obtained by (Yang *et al.*, 2022). Structure obtained from *App*$^{NL\text{-}G\text{-}F}$ mice has a pseudo-2_1 screw symmetry with a helical twist of 179.352° (Figure 31 A) and a disordered C-terminus (Figure 35 D). Overall, *ex-vivo* fibrils from these mice show differences in conformation compared to type I and type II human structures (Figure 35 B and C, respectively), but the fold between residues Phe20-Met35 is conserved. The superposition shows the differences in N-termini. Moreover, structures from sarkosyl extracted fibrils from *App*$^{NL\text{-}F}$ mice (Yang *et al.*, 2022) are identical to human type II structures (not shown). Thus, structural differences are observed between *App*$^{NL\text{-}G\text{-}F}$ and *App*$^{NL\text{-}F}$ knock-in mice (Figure 35 D).

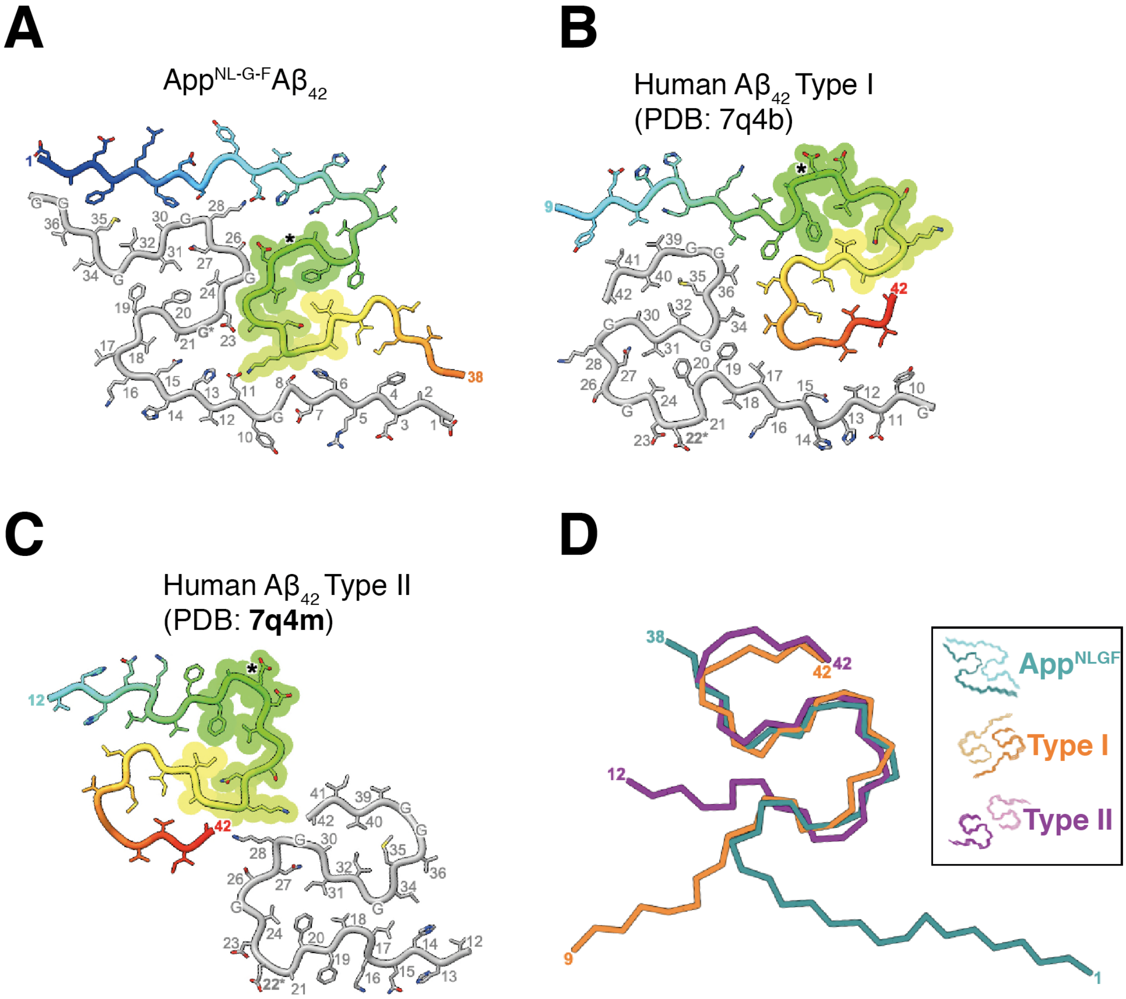

Figure 35: Sarkosyl extracted cryo-EM structures (modified from Martin Wilkinson). Structure of Aβ(42) from *App^{NL-G-F}* knock-in mice (obtained by Martin Wilkinson, A) compared to human type I (Yang et al. 2022, B) and type II (Yang et al. 2022, C) cryo-EM structures. Asterisk indicates regions that have identical AA sequences in all three structures. S shape is conserved in all three structures, the N-terminal tail differs (D).

5.2. Discussion

In order to gain a better insight into the microarchitecture of the plaques, Aβ fibrils were quantitatively analysed.

The heterogeneity of fibril densities within the plaques were validated by fast Fourier analysis. The resulting fast fourier transforms suggested that there is a clear distinction between parallel bundles and meshwork. However, fluorescent intensities of CLEM data cannot be correlated to those differences. The accuracy of the matlab script used for CLEM has been shown to be between 33 and 89 nm in samples with fiducial markers (Kukulski *et al.*, 2011). Here, the samples do not have fiducial markers, thus the CLEM is expected to be less precise.

Furthermore, the thickness of fibrils from in-tissue and *ex-vivo* tomograms was very diverse. SPA implies that fibrils are about 7 nm thick and a more recent study has shown 12 nm thick fibrils with a width of 5 nm at their crossover point (Gremer *et al.*, 2017; Kollmer *et al.*, 2019; Ghosh *et al.*, 2021). All these different measurements described in the literature were found in this study together with very thin fibrils. This indicates that thicker fibrils might be more stable and therefore withstand the process of purification. The fibril diameters did not seem to be related to their location within the plaque. However there appeared to be a higher concentration of fibrils with a particular width in one region of a plaque versus another, which is consistent with the concept of templated growth, secondary nucleation and prionogenic spread that have been suggested for amyloids (Goedert and Spillantini, 2006).

Fibril rotations were seen to be left-handed in samples from human AD brains and right handed in meninges from CAA patients. For this study, AFM is required to determine whether fibrils from *App*$^{NL\text{-}G\text{-}F}$ knock-in mice are left or right handed.

Unfortunately, the resolution limit for cryo-ET of tissue sections is still on a nanometer scale at about 5 nm, compared to subnanometer resolution in SPA (Nakane *et al.*, 2020). Cryo-sections are relatively thick whereas purified fibrils are plunge-frozen in a very thin layer of ice. SPA and *in-situ* tomography are both relevant and thus data was combined to get insights into the architecture of Aβ plaque.

Subtomogram averaging has yet to be improved. Challenges are that biological specimens are relatively thick compared to SPA which lowers the signal-to-noise ratio and tissue samples are very heterogeneous. Sample preparation remains to be improved. Subtomogram averaging on ribosomes in vitrified cells has achieved a resolution of 5.6 Å which shows the potential of this method in ideal samples (Tegunov *et al.*, 2021).

For subtomogram averaging, the pixel size of tomograms has to be lower which means data is collected at a higher magnification, but this limits the field of view and the in-tissue architecture could not be studied. This could be a potential future plan to collect data at very high magnification and perform subtomogram averaging on in-tissue Aβ fibrils and get the first subnanometer resolution of a fibril in its native tissue environment. An additional challenge is the alignment of the tomograms, to get a better reconstruction for subtomogram averaging, a fiducial marker could be introduced.

6. General Discussion

6.1. Summary of key findings and discussion

Highlights

1) A workflow for the sample preparation and cryogenic electron tomography on a mouse model for Alzheimer’s disease was established: samples were vitrified by high pressure freezing and plaques were targeted for cryo-sectioning.

2) Novel insights into the native architecture of amyloid β plaques in their native tissue environment were gained: diversities within the fibril architectures and subcellular and macromolecular constituents interdigitating the fibrils were observed.

3) Regions of different densities and organisations of fibrils within the plaque were quantified, namely a meshwork of fibrils and parallel bundles of fibrils.

The workflow I established was applied to study the in-tissue structure of Aβ plaques in AD, but could be utilised to study a variety of neurodegenerative diseases and also healthy brain tissue.

In previous studies, Aβ plaques were extensively studied on a near atomic resolution scale by SPA of synthetic Aβ fibrils (Schmidt *et al.*, 2015) and *in-vitro* seeded Aβ fibrils collected from human AD brain tissue by electron microscopy (Lu *et al.*, 2013); (Yang *et al.*, 2022); (Kollmer *et al.*, 2019)(Lu *et al.*, 2013). Cryo-EM is important for drug discovery and design (Van Drie and Tong, 2020), however, our understanding of the pathophysiological mechanisms in AD brains are very poor. SPA is unlikely to contribute to our understanding of fibrils outside their native environments. In contrast, the approach I established here allows us to study plaques unperturbed and can be used for hypothesis generation and to design new experiments, such as time resolved or functional studies. These have the potential to answer key questions: How does this pathology develop? What is the origin of plaques? Therefore, the workflow developed in this study was utilised to investigate the native architecture of Aβ plaques and their surrounding tissue environments in *App*$^{NL\text{-}G\text{-}F}$ knock-in mice.

Aβ plaques were found to be very heterogeneous with different regions of varying densities and organisation. In negative stained resin embedded samples Aβ plaques have a star shape consisting of a densely packed core with parallel fibrils, a transition region containing vacuoles and dense bodies as well as a periphery with bundles of Aβ fibrils. Moreover, the plaques are enclosed by multiple microglia cells (Wegiel and Wisniewski, 1990; Frackowiak *et al.*, 1992); Figure 36).

Interestingly, in cell cultures with seeded Serum amyloid A1 (SAA1), 3 different architectures were found, namely fibril meshwork, fibril bundle and amyloid star suggesting that not only Aβ plaques have this characteristic macroarchitecture (Kollmer *et al.*, 2016). Here, I found the plaque architecture was studied in its native state for the first time and some of these characteristic architectures were found. However, only parts of each plaque were reconstructed and analysed in each tomogram. The macroarchitecture of the plaques encompassing the whole molecular architecture of a single plaque by cryo-ET still remains to be determined.

Moreover, a great variety of macromolecular constituents were found within the plaques. Cryo-ET on a monocyte cell culture found 50 - 100 nm vesicular structures within the plaques formed by seeded Aβ(40) (Han *et al.*, 2017) which correlates to size of exosomes 40 - 100 nm (Raposo and Stoorvogel, 2013). Structures found in this study were 40 - 200 nm in size, suggesting that exosomes were interdigitating the Aβ fibrils within plaques. Here, this feature was evident for the first time in brain tissue of an AD model in its native state.

To date, little is known about the toxicity of the varying structures of Aβ itself. The role of microglia and astrocytes in plaque formation and clearance is not well understood. Mouse models with dense cored plaques were depleted from microglia which resulted in a decrease of parenchymal dense core plaques, although plaques were formed around vasculature (Spangenberg *et al.*, 2019;

Shabestari *et al.*, 2022). However, the role of microglia and astrocytes is not well understood. It is likely that microglial cells trigger a cascade of events that promote neuroinflammation, which is a hallmark of AD.

It has been proposed that dense core plaques do not form spontaneously, but are formed by microglia (Baik *et al.*, 2016). Studies showed that neurites and microglia interdigitate the plaque and astrocytes are in the periphery of the plaque, surrounding and encapsulating it (Walker, 2020). This indicates that microglia are in close proximity to plaques in this study. Moreover, Triggering Receptor Expressed in Myeloid cells 2 (TREM2), which is a marker for reactive microglia, has been observed to be a genetic risk factor for AD (Gratuze, Leyns and Holtzman, 2018). It has been shown that microglia are recruited to the plaques and clears them via phagocytosis, local inflammation is caused by microglia which triggers neurotoxic effects (Duckett and de la Torre, 2001). This suggests that microglia are in close contact with the plaque. A microglial marker has yet to be established for cryo-ET on AD tissue but would enable a structural understanding of the interaction of microglia with amyloid pathology.

The application of electron tomography (ET) of cells showed that plaques form intracellularly, leading to cell death (Han *et al.*, 2017). The plaques are then released into the extracellular space (Meyer-Luehmann *et al.*, 2008b). Furthermore, microglia are recruited rapidly to newly-formed Aβ plaques for their uptake (Meyer-Luehmann *et al.*, 2008a) subsequently leading to the death of such microglia and the release of plaques into the extracellular space (Baik *et al.*, 2016; Huang *et al.*, 2021). These findings suggest that Aβ can be located intra- or extracellularly and that microglia promote plaque growth. Here, we found the plaques to be extracellular, although the labelling experiment with fluorescent dextran has to be repeated to test whether a certain percentage of fibrils can be found to be intracellular. Cell death of microglia and release of the plaque could indicate that the organelles found to be interdigitating the disease could be cell debri and organelles for cell clearance, such as phagosomes. The ‘empty membranes’ found here could be the remnants of dead or damaged cells, they are very small and do not seem to have any content. This could indicate that cells died and fragments of these dead cells are found within the plaques or damage that was introduced during tissue preparation for cryo-ET.

ApoE is another genetic risk factor associated with AD, the APOE e4 gene increases the risk of developing AD (Corder *et al.*, 1993; Strittmatter *et al.*, 1993; Harold *et al.*, 2009). ApoE is primarily synthesised by astrocytes and microglia, it binds to Aβ and facilitates Aβ uptake through cell surface receptors to clear it (Kim *et al.*, 2009; Kanekiyo *et al.*, 2011). Here, liquid-like droplets were found that seemed to be connected to fibrils. These could contain ApoE which would indicate that ApoE forms interactions with the fibrils. Further experiments using a cryo-CLEM label for ApoE could test this hypothesis.

The majority of these previous studies investigating amyloid and microglia were performed in mice or cell models, but not in human tissue. Microglia behaves differently in mice (Zhang *et al.*, 2016), AD mouse models do not resemble the same phenotypes compared to AD patients and very isolated features of the disease are studied. For example, $App^{NL\text{-}G\text{-}F}$ mice do not develop tauopathy or neurodegeneration (Saito *et al.*, 2014a)), yet the amyloid hypothesis proposes that Aβ triggers the aggregation of tau. Moreover, numerous studies of tau tangles find that these correlate strongly to neuronal loss and clinical symptoms, in contrast to Aβ plaques (Villegas *et al.*, 2022). The cryo-ET data presented here can give us a first insight into all the relevant features that are involved in disease mechanisms in mouse models and could be applied to post mortem AD human tissue to compare the microarchitecture of the plaque to those in mice.

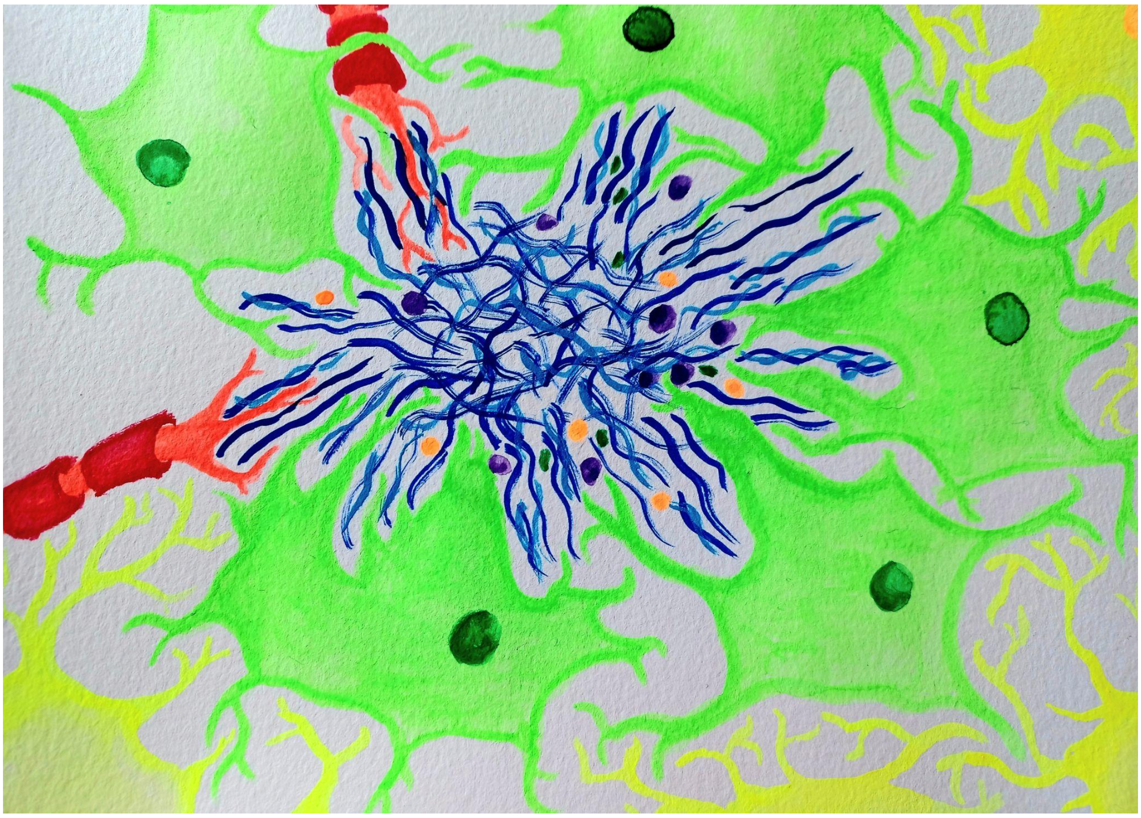

Figure 36: My watercolour painting of a plaque. Fibrils (blue) are interdigitated by subcellular processes and macromolecular features such as c-shaped membranes (orange) and exosomes (purple). They are surrounded and interdigitated by neurites (red, myelinated axons) and microglia (green). Astrocytes encapsulate microglia cells that surround plaque (green).

AD is a progressive disease that is thought to start more than a decade before symptoms are first diagnosed (Dubois *et al.*, 2016). It is speculated that therapeutic targeting amyloids may be ineffective if given too late, when plaques are already detected in brains and patients have already developed symptoms (Emery, 2011). Therefore, early detection and prevention is needed. In this study, the *App*$^{NL\text{-}G\text{-}F}$ mice used were 9 months old with a saturated plaque load. Thus, understanding the architecture of the plaques is only the first step on the way to understanding disease mechanisms and understanding the earliest stages of amyloid biogenesis represent a future challenge. Therefore, all the different features that make up the plaques have to be identified to study the mechanisms that trigger plaque formation and promote clearance. These must be placed in a temporal context applying the methods I developed here on younger *App*$^{NL\text{-}G\text{-}F}$ mice, to understand how β-amyloidosis progresses over time.

Fibrils were found to be very heterogeneous and a significant subpopulation of the fibrils were found to be much thinner than those determined from *ex-vivo* and *in-vitro* sources. A possible explanation for this could be that plaques do not only consist of fibrils, but also protofilaments. *Ex-vivo* and in-tissue tomography were combined with SPA to study fibril structures. In addition, microdissection (as described in Chapter 3: Development of a sample preparation workflow for in-tissue correlated imaging - Discussion) could be a powerful tool to study different fibril polymorphs and other organelles within the plaque using subtomogram averaging. For this, samples are dissected out of the tissue into a pipette and immediately plunge-frozen. Additionally, a fiducial marker, namely immunogold is added for patch tracking before freezing, to improve the tomographic reconstruction. Moreover, thin plunge-frozen samples typically have a much better contrast compared to thick tissue sections which means the signal-to-noise ratio is better. This approach could provide samples suitable for high-resolution SPA cryo-EM without the need for extraction and purification using harsh detergents.

There are a lot of questions that remain unanswered: How does the plaque assemble? What role do microglia cells play in the assembly of the plaques? Do glial cells trigger toxicity and degeneration or clearance of plaques and regeneration? What is the balance of plaque clearance vs. inflammatory damage triggered by microglia? Which is the toxic species of Aβ?

6.2. Future plans

Much still remains to be done to (1) improve the novel sample preparation workflow, (2) study plaque architecture in human tissue, (3) introduce labels to study organelles interdigitating fibrils as well as cells in periphery and (4) study progression of the disease in mice.

6.2.1. Workflow development

The workflow developed has to be optimised further to improve the resolution. Firstly, vitrification can be studied without adding any cryoprotectant to the tissue. It still remains unknown if the high sugar content in the NMDG HEPES solution is sufficient to cryo-protect the tissue. Therefore, samples prepared in NMDG HEPES solution will be compared to those prepared in HACSF.

For this study patch tracking was used to align all tilt increments (Mastronarde, no date), however implementing fiducial markers for patch tracking into the workflow can improve the quality of the tomographic reconstructions. Therefore, tissue can be incubated in immunogold or quantum dots. Moreover, fluorescent markers such as quantum dots have the advantage that they can be used to improve the precision of cryo-CLEM.

To improve the quality of tomograms, FIB-SEM and cryo-liftout can be performed. FIB-SEM has an implemented fluorescence microscope and thus can be used to target the plaques during milling (Schaffer *et al.*, 2019). This technique has the advantage that it does not show any cutting damage like CEMOVIS and it has been shown by (Schaffer *et al.*, 2019) that a thickness of 100 nm sections can be achieved which is similar to the 70-150 nm sections prepared in this study.

In order to test whether thinner fibrils are lost in the process of purification, microdissection and plunge freezing can be performed. In contrast to purification of fibrils, no detergents will be added and therefore tissue is kept in its native state. The advantage over cryo-sectioning is that the contrast and thus the signal-to-noise ratio is better in a thin film of ice.

Another possibility is laser-capture microdissection of the plaques from tissue. For this, the plaques are cut out of the tissue with a laser. This method has been developed for fixed tissue sections and has yet to be established for fresh sections.

6.2.2. In-tissue architecture of human AD tissue

Furthermore, this workflow can be applied to human tissue. The cryoprotectant might have to be optimised for that. Tissue will be sectioned on a vibratome and incubated in Methoxy-X04 for 1 h, then high-pressure frozen. First, this would be performed on flush frozen post-mortem human tissue. Once the workflow is optimised, it would be applied to post mortem human tissue in collaboration with a pathologist. To validate that plaques are high pressure frozen some sections will be stained with toluidine blue (Morikawa, Sato and Ezaki, 2018). Toluidine blue allows us to see the location of amyloid plaques in the tissue sections with a stereomicroscope. If plaque load is high enough tissue biopsies will be collected and high pressure frozen.

6.2.3. Labels to study vicinity of plaques

Other experiments to study the native architecture of amyloid plaques and surrounding tissue environment are for example multiple labelling approaches to classify organelles and macromolecular features within the plaque. These include TREM2 to label active microglia, ApoE antibodies, markers for exosomes such as ESCRT proteins (Doyle and Wang, 2019).

To test whether cells surrounding plaques are viable, marker can be introduced, such as Acridine orange (living cells), Hoechst 33342 (apoptotic cells) and propidium iodide (late apoptotic/necrotic cells; (Foglieni, Meoni and Davalli, 2001; Buskila *et al.*, 2014).

The plaque consists not only of fibrils, but also other macromolecules and has been shown to be surrounded by neurites and microglia which interdigitate the pathology and is surrounded by astrocytes. Thus more markers are needed to characterise different parts of the plaque and locate where in the plaque all of them are. Therefore, multicolour cryo-CLEM is needed which has been established (Chapter3: Multi colour cryo-CLEM).

Moreover, in the long term new mouse models can be cross bred. Tomograms from multi-labelled *PSD95*$^{eGFP/eGFP}$ *x App*$^{NL\text{-}G\text{-}F}$ *x GluN1*$^{TAP/TAP}$ have to be collected to analyse the native in-tissue architecture of synapses in AD. Additionally, *App*$^{NL\text{-}G\text{-}F}$ mice can be crossbred with a mouse model that has a fluorescent tag in microglia cells.

6.2.4. Progression of AD in mouse model

This study can give new insights into mechanisms that cause the disease by designing follow up experiments to identify structures within the plaque. For example functional studies to see disease mechanisms and time resolved approaches to visualise the formation of plaques and other structures. These can be performed in cell cultures with markers for the different structures found. 2PM is a powerful tool to study disease progression *in-vivo* (Chen *et al.*, 2018), this can be combined with cryo-CLEM and cryo-ET to see different stages of plaque formation *in-vivo*. Therefore, the plaque labelled with Methoxy-X04 observed by 2PM through an intracranial window, mice can be sacrificed at various time points. Then the brain is taken out and a tissue biopsy is high-pressure frozen (Karreman et *al.*,, 2016). Methoxy-X04 can be used for

2PM and also imaged in high-pressure frozen samples. Landmarks in tissue serve as fiducial markers to identify regions of interest for cryo-CLEM such as blood vessel patterns (Luckner *et al.*, 2018). Vasculature can be labelled by cardiac perfusion of mice with 1,1′-dioctadecyl-3,3,3′,3′-tetramethylindocarbocyanine perchlorate (Li *et al.*, 2008).

7. Appendix I: Processing

7.1. Etomo

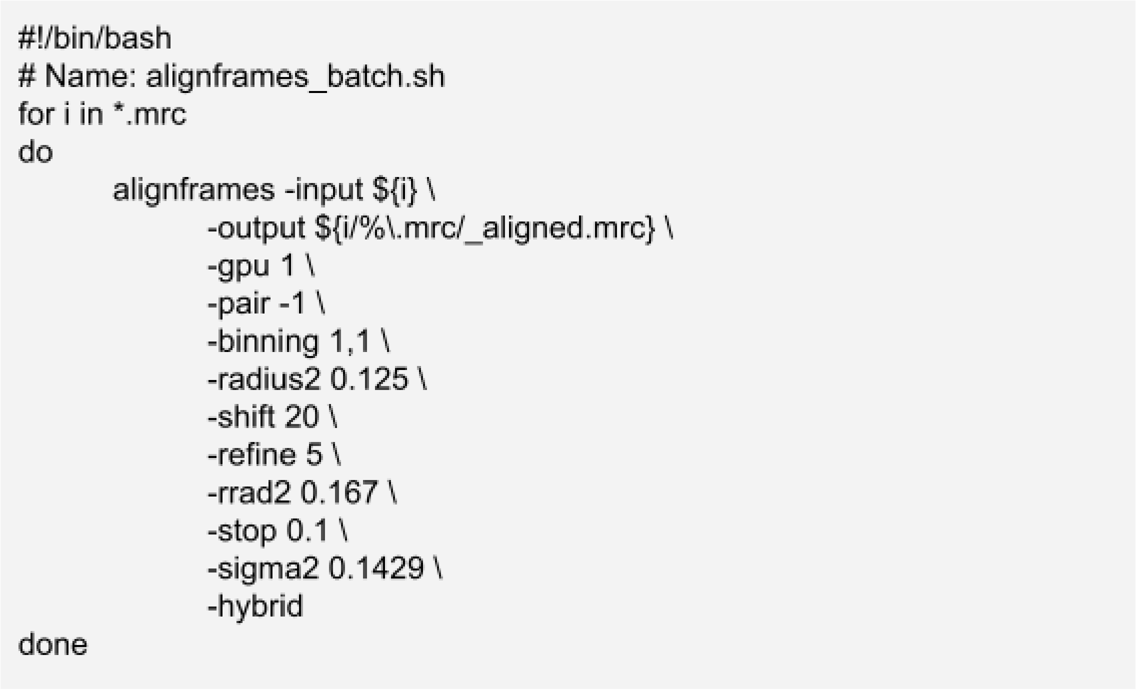

```
#!/bin/bash
# Name: alignframes_batch.sh
for i in *.mrc
do
        alignframes -input ${i} \
                -output ${i/%\.mrc/_aligned.mrc} \
                -gpu 1 \
                -pair -1 \
                -binning 1,1 \
                -radius2 0.125 \
                -shift 20 \
                -refine 5 \
                -rrad2 0.167 \
                -stop 0.1 \
                -sigma2 0.1429 \
                -hybrid
done
```

Figure 37: Script for motion correction in imod.

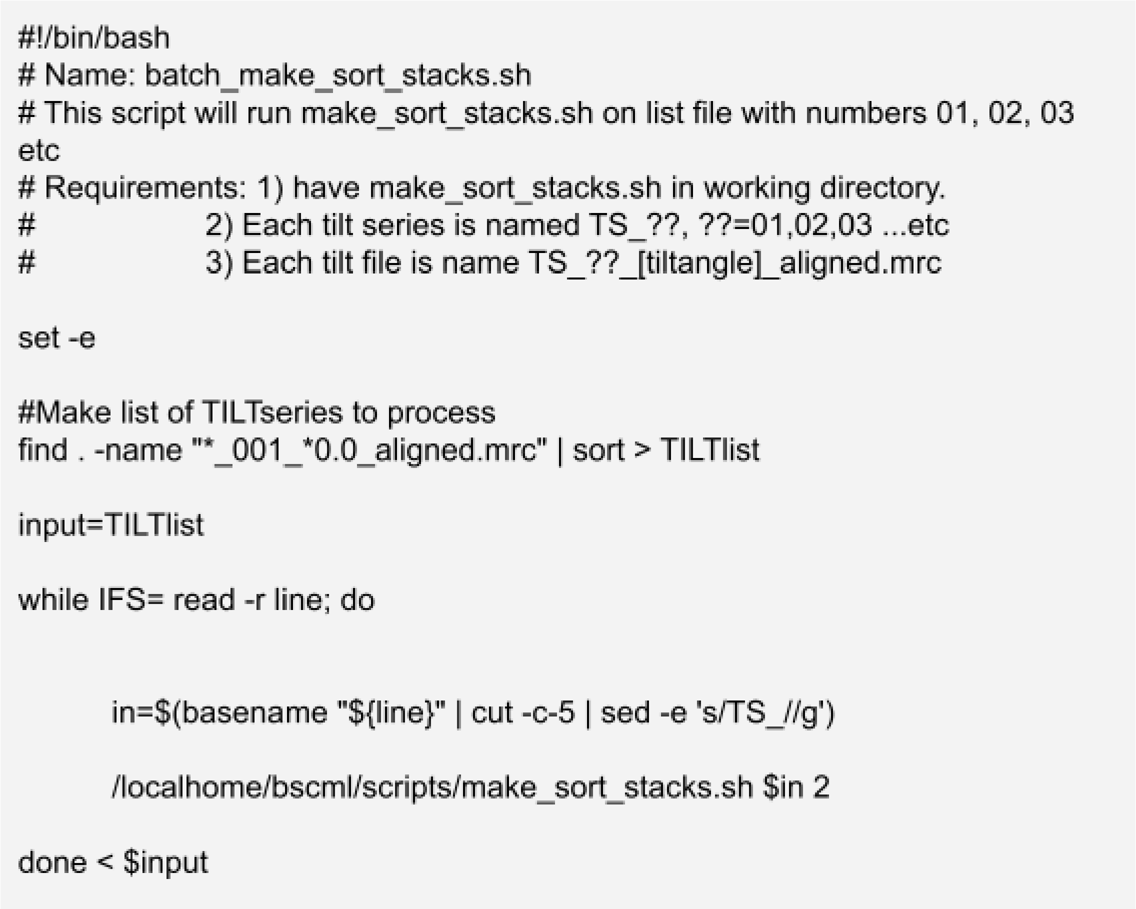

```
#!/bin/bash
# Name: batch_make_sort_stacks.sh
# This script will run make_sort_stacks.sh on list file with numbers 01, 02, 03
etc
# Requirements: 1) have make_sort_stacks.sh in working directory.
#               2) Each tilt series is named TS_??, ??=01,02,03 ...etc
#               3) Each tilt file is name TS_??_[tiltangle]_aligned.mrc

set -e

#Make list of TILTseries to process
find . -name "*_001_*0.0_aligned.mrc" | sort > TILTlist

input=TILTlist

while IFS= read -r line; do


        in=$(basename "${line}" | cut -c-5 | sed -e 's/TS_//g')

        /localhome/bscml/scripts/make_sort_stacks.sh $in 2

done < $input
```

Figure 38: Script to create a list of tomograms and execute another script that stacks tilt series in imod.

```
#!/bin/bash
# Name: make_sort_stacks.sh
if [[ $# -lt 2 || $1 == "-h" || $1 == "--help" ]]
then
	cat <<USE
	USAGE: make_sort_stacks.sh <tiltseries index> <dose rate>
	EXAMPLE: make_sort_stacks.sh 1 3.5
	Which will process TS_01_*_aligned.mrc with dose of 3.5e/A2
USE
	exit 0
fi
# INPUTS
idx=${1} # Which tilt series to work on e.g. 1 for TS_01
dose_rate=${2}
# VARIABLES
fmt_idx=$(printf "%02d" ${idx})
nimg=$(find . -name "TS_${fmt_idx}*_aligned.mrc" | wc -l)
# MAKE SORTED TILTSERIES
find . -name "TS_${fmt_idx}*_aligned.mrc" |\sort -t_ -n -k 4,4 |\awk -v
nimg=${nimg} '
BEGIN {print nimg;}
	{printf("%s\n0\n", $0);}
' > TS_${fmt_idx}_filelistin.txt;
newstack -q -filein TS_${fmt_idx}_filelistin.txt \
	-output TS_${fmt_idx}_aligned.st
#rm TS_${fmt_idx}_filelistin.txt
# MAKE RAWTLT FILE
find . -name "TS_${fmt_idx}*_aligned.mrc" |\
sort -t_ -n -k 4,4 |\
awk -F_ '
	{
	tilt_angle = $4 + 0.0;
	printf("%f\n", tilt_angle);
	}
' > TS_${fmt_idx}.rawtlt
# MAKE DOSE LIST
find . -name "TS_${fmt_idx}*_aligned.mrc" |\
sort -t_ -n -k 3,3 |\
awk -F_ -v dose_rate=${dose_rate} '
	BEGIN {
	dose = 0.0;}
	{printf("%d\t%f\n", $4 + 0, dose);
	dose += dose_rate;}
' |\
sort -n -k1,1 |\cut -f 2 > TS_${fmt_idx}_dose_list.csv
```

Figure 39: Script that is used to stack tilt series in imod. This script was executed by batch_make_sort_stacks.sh.

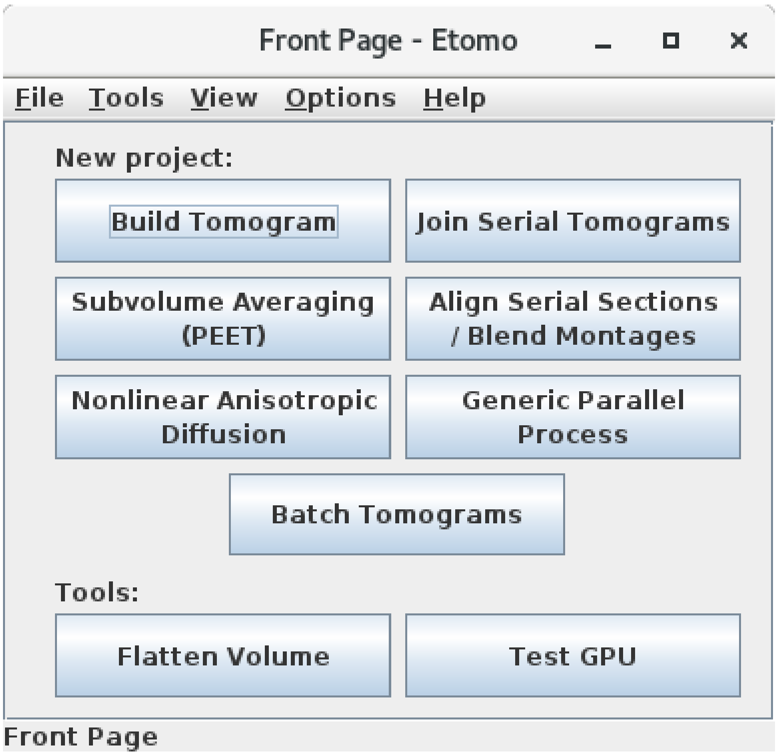

Figure 40: Etomo was used for tomogram reconstruction from the motion corrected, aligned stacks by selecting 'build tomogram'.

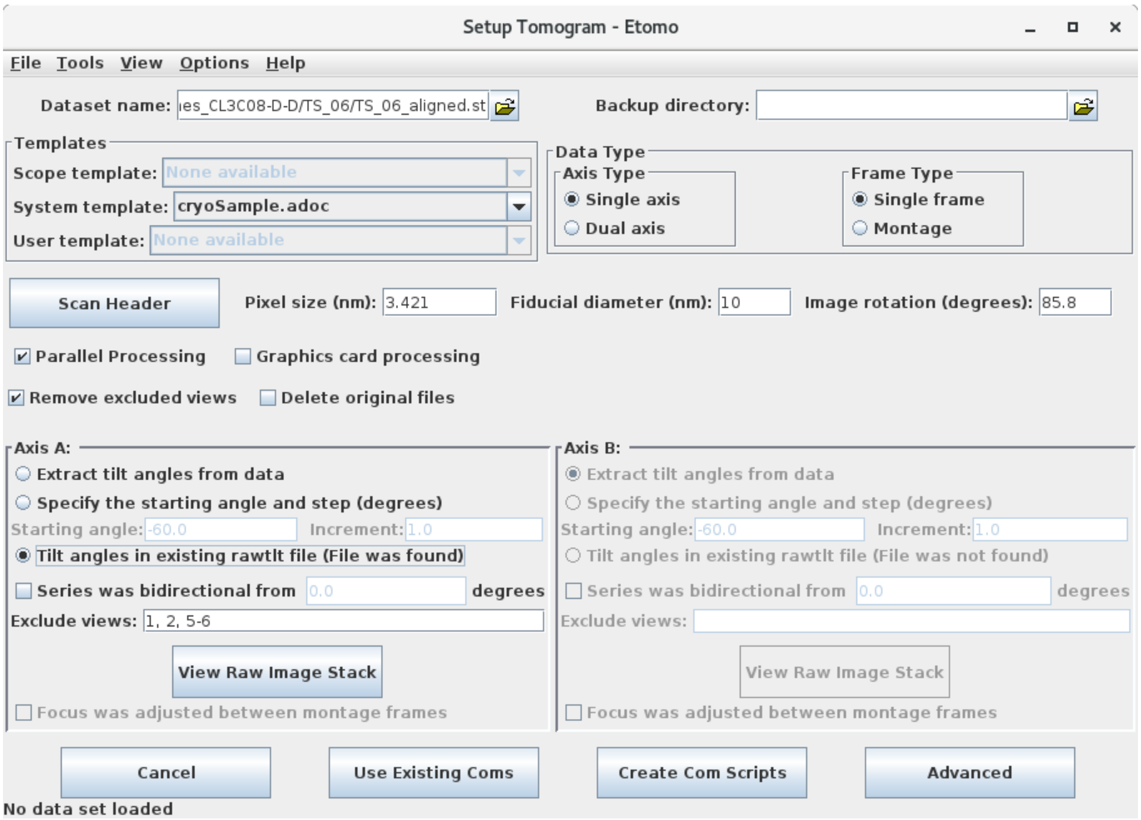

Dataset name: ıes_CL3C08-D-D/TS_06/TS_06_aligned.st

Backup directory:

Templates

Scope template: None available

System template: cryoSample.adoc

User template: None available

Data Type

Axis Type: ● Single axis ○ Dual axis

Frame Type: ● Single frame ○ Montage

Pixel size (nm): 3.421

Fiducial diameter (nm): 10

Image rotation (degrees): 85.8

☑ Parallel Processing ☐ Graphics card processing

☑ Remove excluded views ☐ Delete original files

Axis A:

○ Extract tilt angles from data

○ Specify the starting angle and step (degrees)

Starting angle: -60.0 Increment: 1.0

● Tilt angles in existing rawtlt file (File was found)

☐ Series was bidirectional from 0.0 degrees

Exclude views: 1, 2, 5-6

☐ Focus was adjusted between montage frames

Axis B:

● Extract tilt angles from data

○ Specify the starting angle and step (degrees)

Starting angle: -60.0 Increment: 1.0

○ Tilt angles in existing rawtlt file (File was not found)

☐ Series was bidirectional from 0.0 degrees

Exclude views:

☐ Focus was adjusted between montage frames

No data set loaded

Figure 41: Etomo Setup to create command scripts for tomogram reconstruction. The stack (.st file) was used for tomogram reconstruction. CryoSample.adoc was selected as a template with single axis and single frame image. The pixel size was determined from the header and the image rotation depends on the microscope. Tilt series was carefully inspected before reconstruction and views to exclude were listed. Views that were collected on a grid bar or on ice and views that had a very poor signal-to-noise ratio were excluded. The rawtlt file was created by imod using the batch_make_sort_stacks.sh script. ‘Create Com Scripts’.

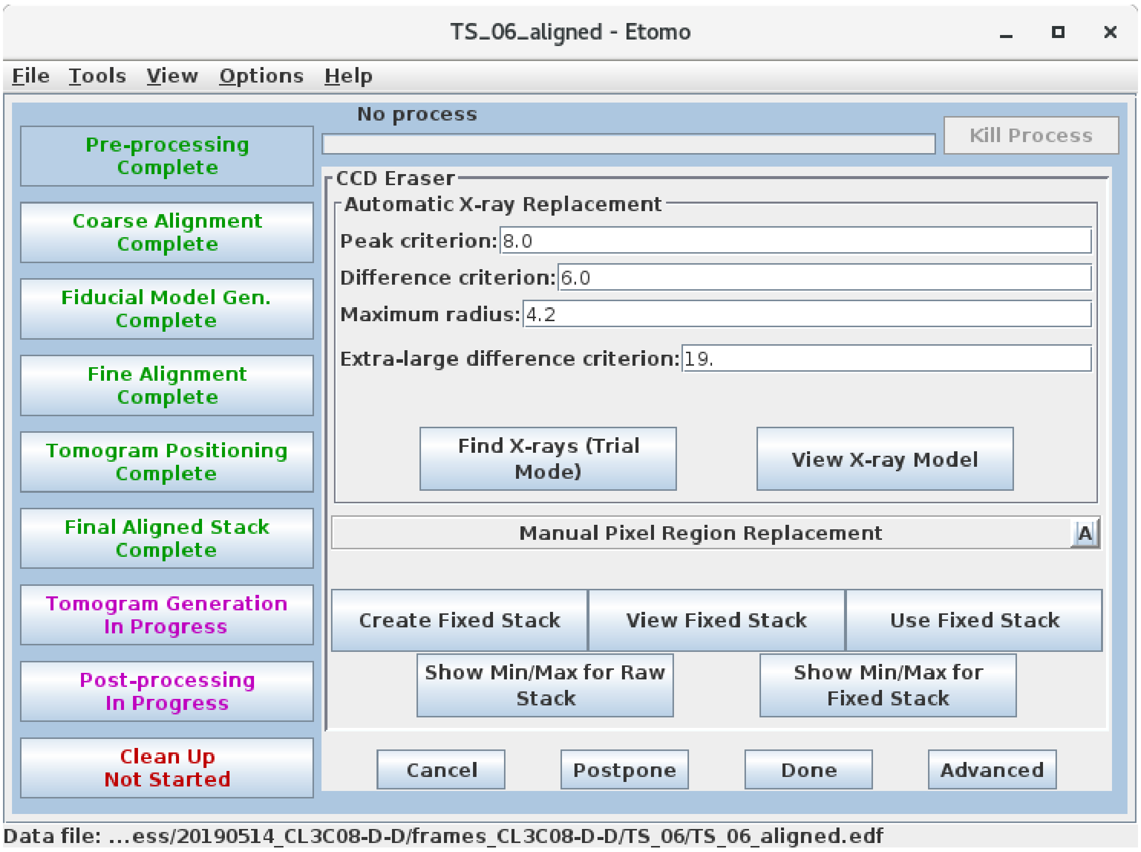

Peak criterion: 8.0

Difference criterion: 6.0

Maximum radius: 4.2

Extra-large difference criterion: 19.

Data file: ...ess/20190514_CL3C08-D-D/frames_CL3C08-D-D/TS_06/TS_06_aligned.edf

Figure 42: Pre-processing. X-rays and other artefacts were removed ('Find X-rays'). Fixed stack was created ('Create Fixed Stack') and used ('Use Fixed Stack').

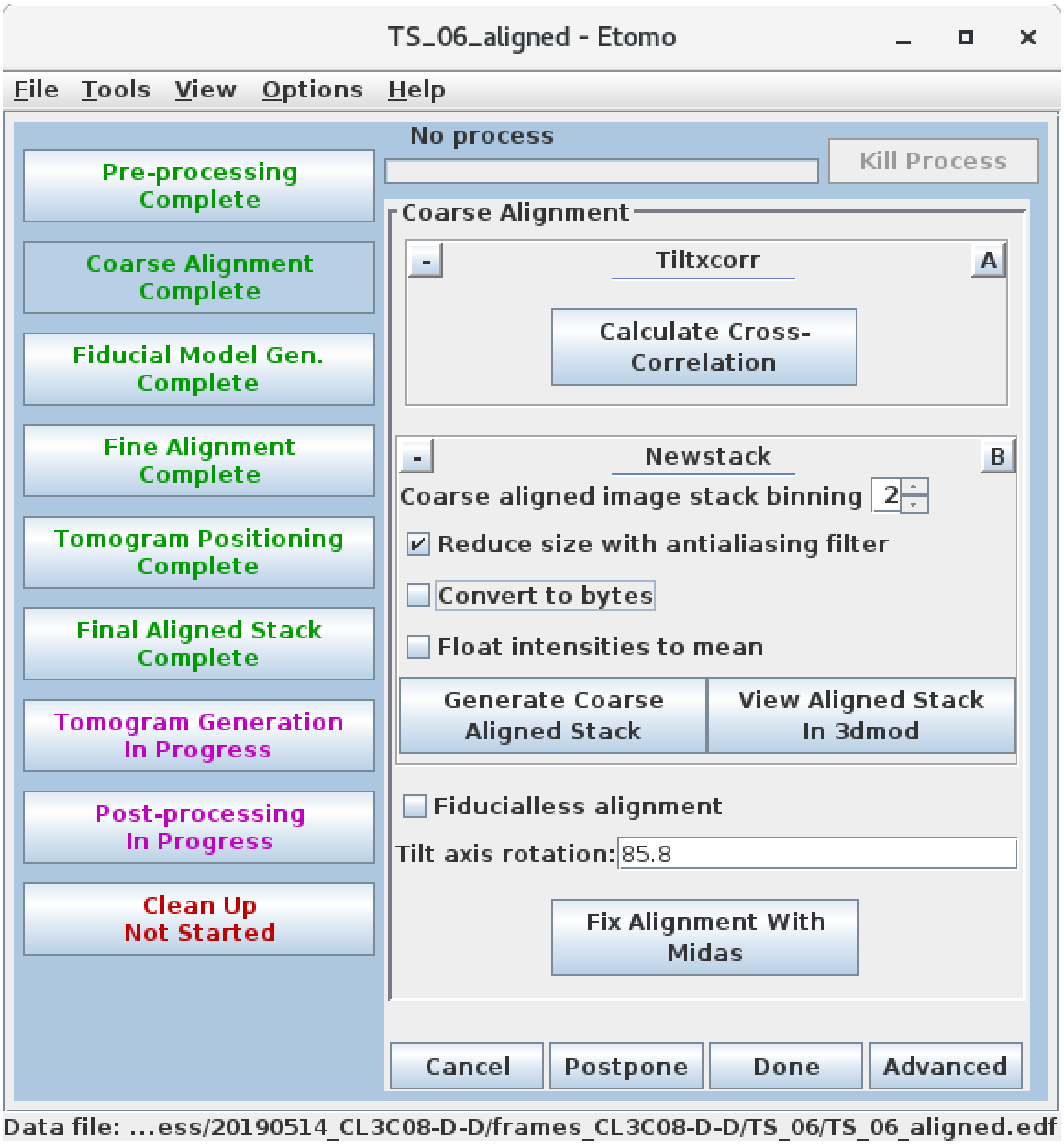

Coarse aligned image stack binning 2

☑ Reduce size with antialiasing filter

☐ Convert to bytes

☐ Float intensities to mean

☐ Fiducialless alignment

Tilt axis rotation: 85.8

Data file: ...ess/20190514_CL3C08-D-D/frames_CL3C08-D-D/TS_06/TS_06_aligned.edf

Figure 43: Coarse Alignment. Cross correlation was needed to align each image with the previous one (‘Calculate Cross Correlation’). The coarse aligned stack was generated with binning 2 or 4 and the size was reduced with an antialiasing filter which reduces some of the noise (‘Generate Coarse Aligned Stack’).

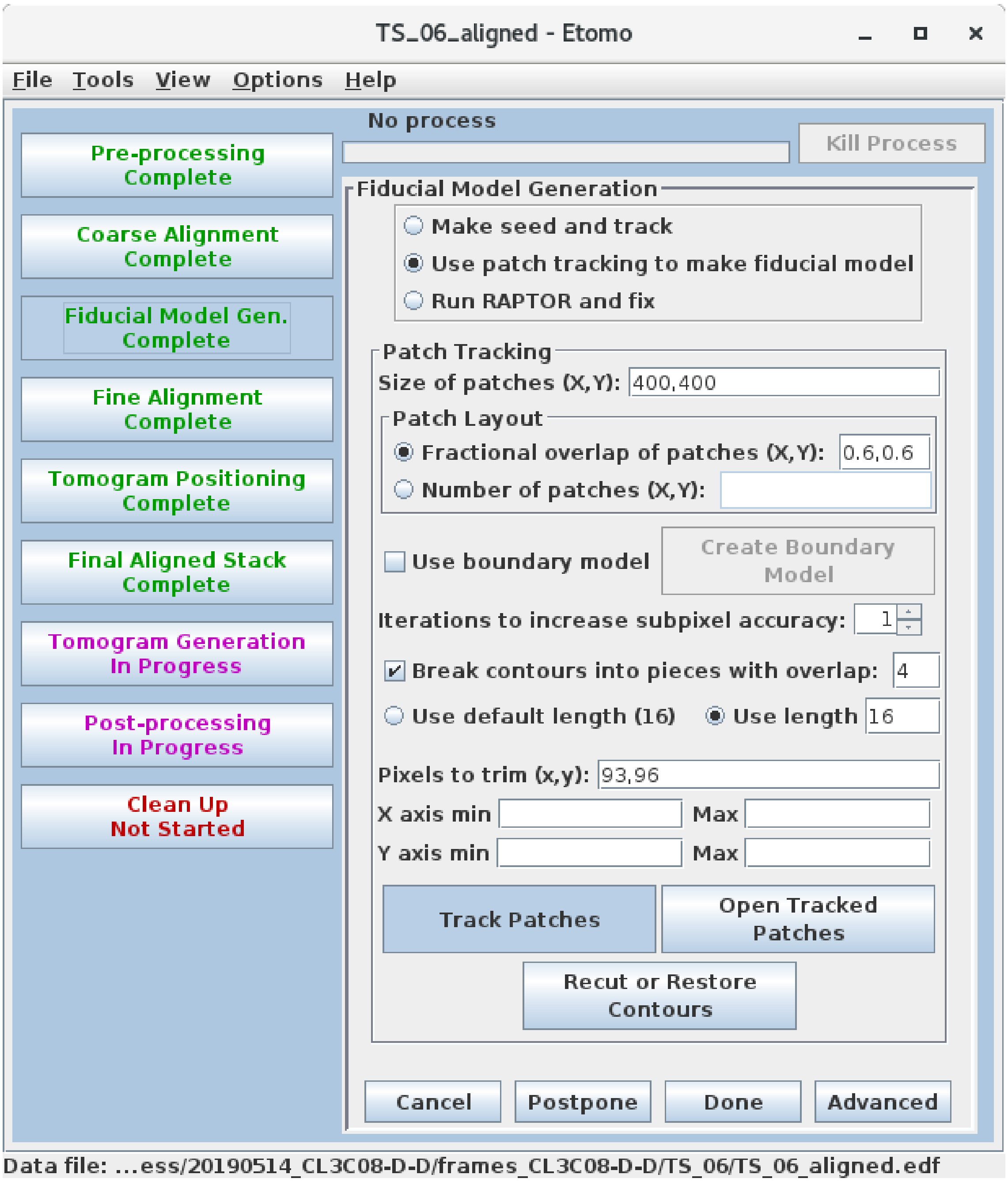

No process

Fiducial Model Generation

○ Make seed and track
● Use patch tracking to make fiducial model
○ Run RAPTOR and fix

Patch Tracking

Size of patches (X,Y): 400,400

Patch Layout

● Fractional overlap of patches (X,Y): 0.6,0.6
○ Number of patches (X,Y):

☐ Use boundary model

Iterations to increase subpixel accuracy: 1

☑ Break contours into pieces with overlap: 4

○ Use default length (16) ● Use length 16

Pixels to trim (x,y): 93,96

X axis min Max

Y axis min Max

Data file: ...ess/20190514_CL3C08-D-D/frames_CL3C08-D-D/TS_06/TS_06_aligned.edf

Figure 44: Fiducial Model Generation. Patch tracking was used, because the samples did not have any fiducial markers.

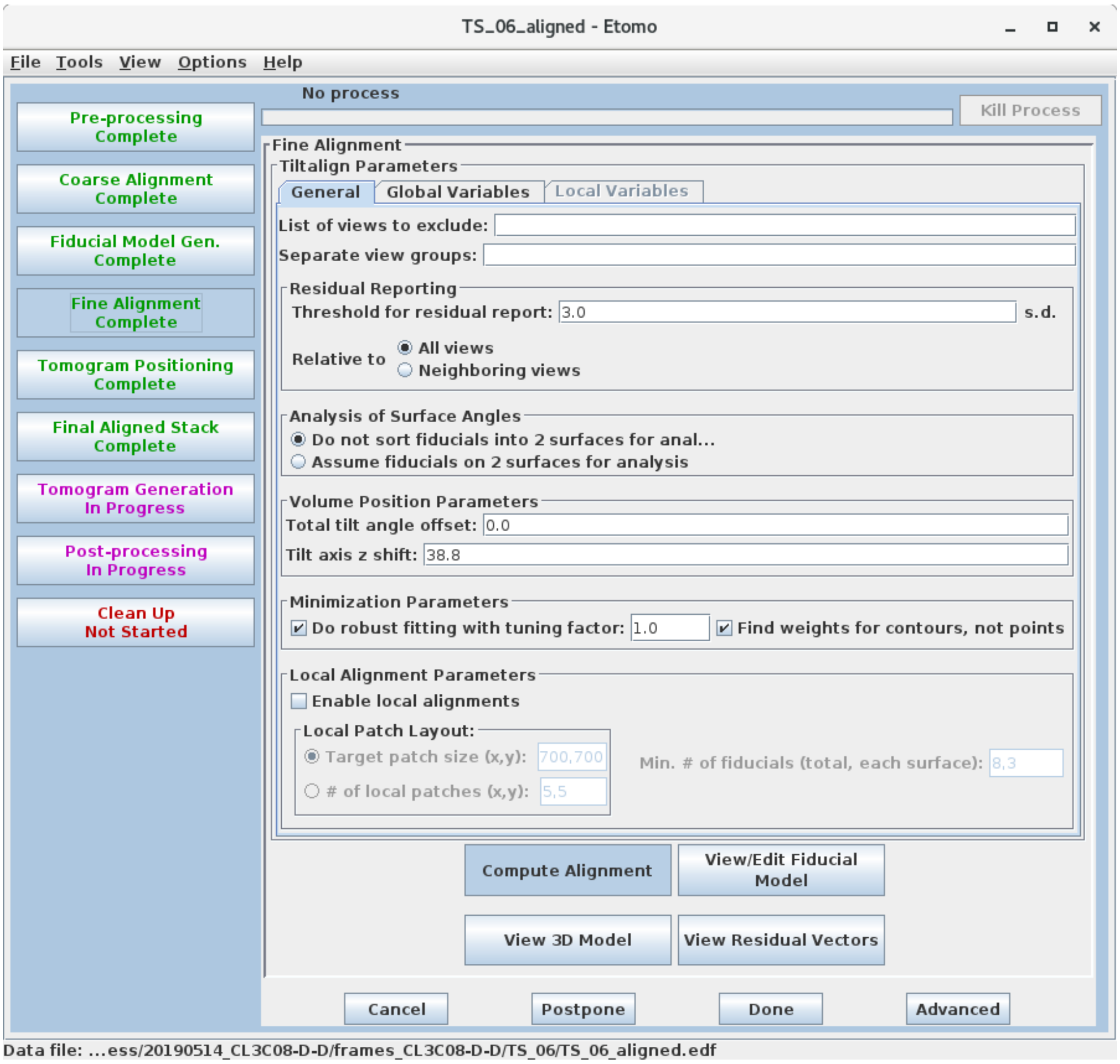

List of views to exclude:

Separate view groups:

Residual Reporting

Threshold for residual report: 3.0 s.d.

Relative to ● All views ○ Neighboring views

Analysis of Surface Angles

● Do not sort fiducials into 2 surfaces for anal...

○ Assume fiducials on 2 surfaces for analysis

Volume Position Parameters

Total tilt angle offset: 0.0

Tilt axis z shift: 38.8

Minimization Parameters

☑ Do robust fitting with tuning factor: 1.0 ☑ Find weights for contours, not points

Local Alignment Parameters

☐ Enable local alignments

Local Patch Layout:

● Target patch size (x,y): 700,700

○ # of local patches (x,y): 5,5

Min. # of fiducials (total, each surface): 8,3

Data file: ...ess/20190514_CL3C08-D-D/frames_CL3C08-D-D/TS_06/TS_06_aligned.edf

Figure 45: Fine Alignment. The threshold for residual report is 3.0. Global variables that were chosen can be seen in the next figure.

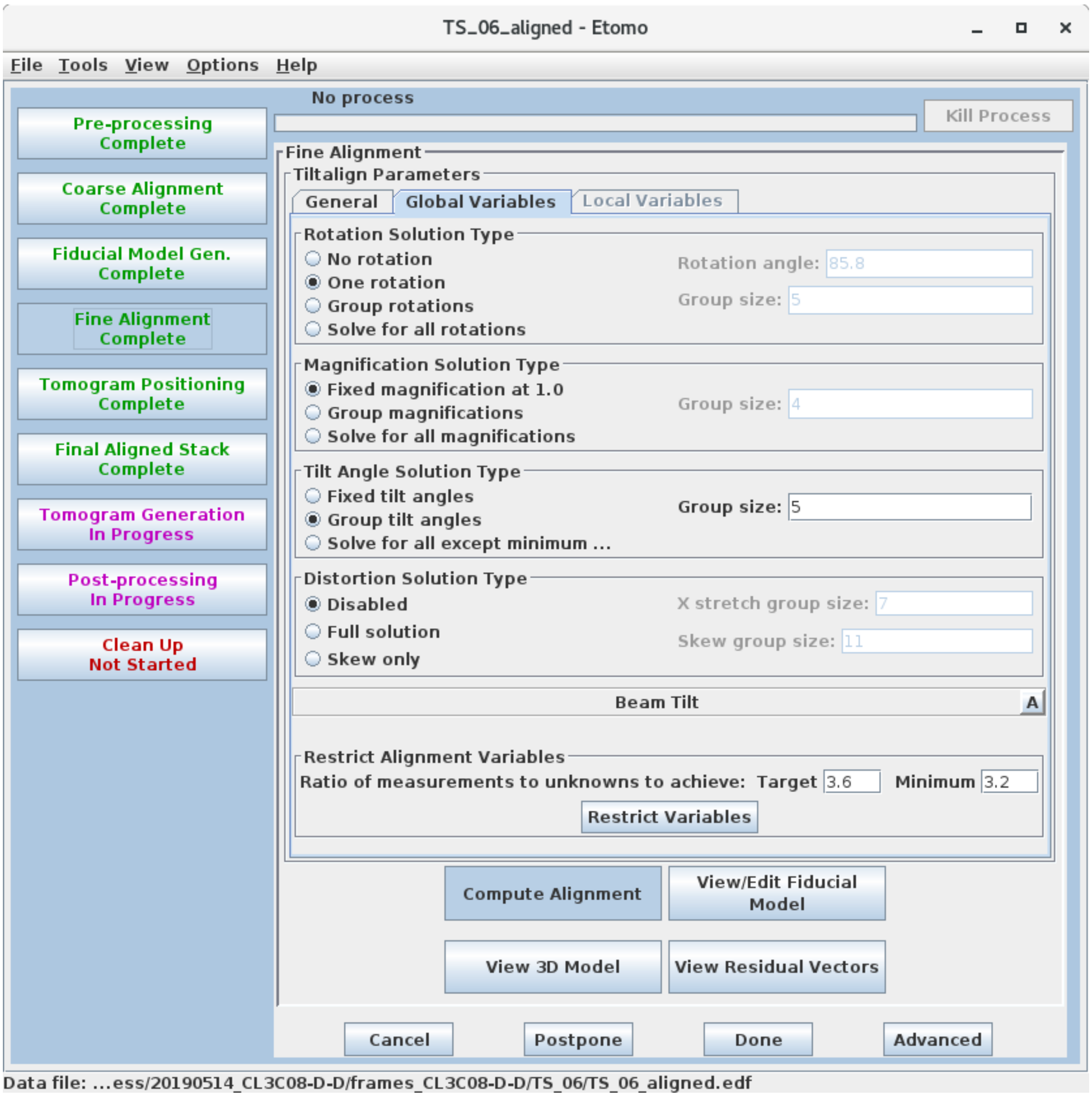

Rotation Solution Type
○ No rotation
● One rotation
○ Group rotations
○ Solve for all rotations
Rotation angle: 85.8
Group size: 5

Magnification Solution Type
● Fixed magnification at 1.0
○ Group magnifications
○ Solve for all magnifications
Group size: 4

Tilt Angle Solution Type
○ Fixed tilt angles
● Group tilt angles
○ Solve for all except minimum ...
Group size: 5

Distortion Solution Type
● Disabled
○ Full solution
○ Skew only
X stretch group size: 7
Skew group size: 11

Restrict Alignment Variables
Ratio of measurements to unknowns to achieve: Target 3.6 Minimum 3.2

Data file: ...ess/20190514_CL3C08-D-D/frames_CL3C08-D-D/TS_06/TS_06_aligned.edf

Figure 46: Fine Alignment. Parameters that were selected are shown. The alignment was calculated (‘Compute Alignment’) and could be improved manually by deleting individual points or an entire contour, see next figure.

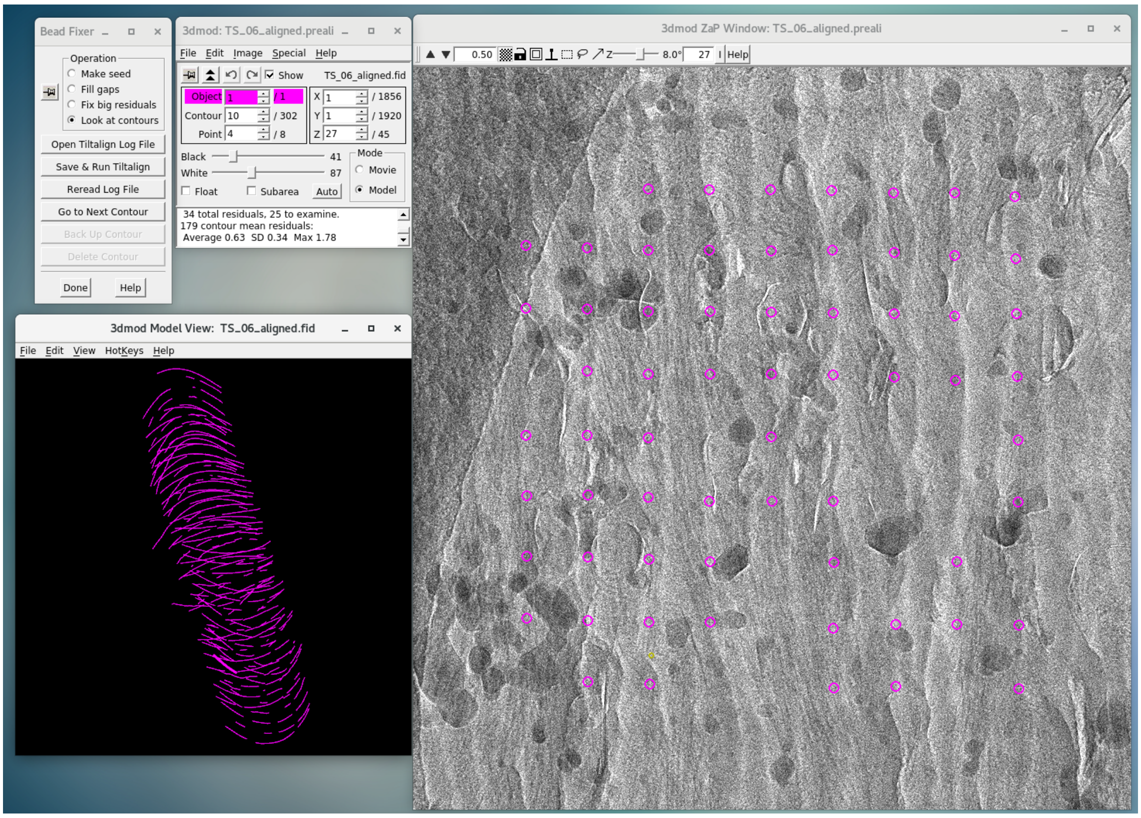

Operation
○ Make seed
○ Fill gaps
○ Fix big residuals
● Look at contours

Open Tiltalign Log File
Save & Run Tiltalign
Reread Log File
Go to Next Contour
Back Up Contour
Delete Contour

☑ Show
Object 1 / 1
Contour 10 / 302
Point 4 / 8
X 1 / 1856
Y 1 / 1920
Z 27 / 45
Black 41
White 87
☐ Float ☐ Subarea
○ Movie
● Model

0.50 8.0° 27

```
 34 total residuals, 25 to examine.
179 contour mean residuals:
 Average 0.63  SD 0.34  Max 1.78
```

Figure 47: Fine Alignment. The fiducial model was opened in 3dmod ('View/Edit Fiducial Model'). The average mean residual should be as low as possible. Multiple contours were deleted. Contours with highest mean residual were shown in the bead fixer window ('Go to Next Contour') and deleted manually ('Ctrl+Shift+D'), then the average mean residual was calculated ('Save & Run Tilt Align'). This step was repeated until the average mean residual was below 1 nm. However, every z position of the tilt series had to have at least 1 point, if there were too few points left in the tilt series no more points of the contours were deleted.

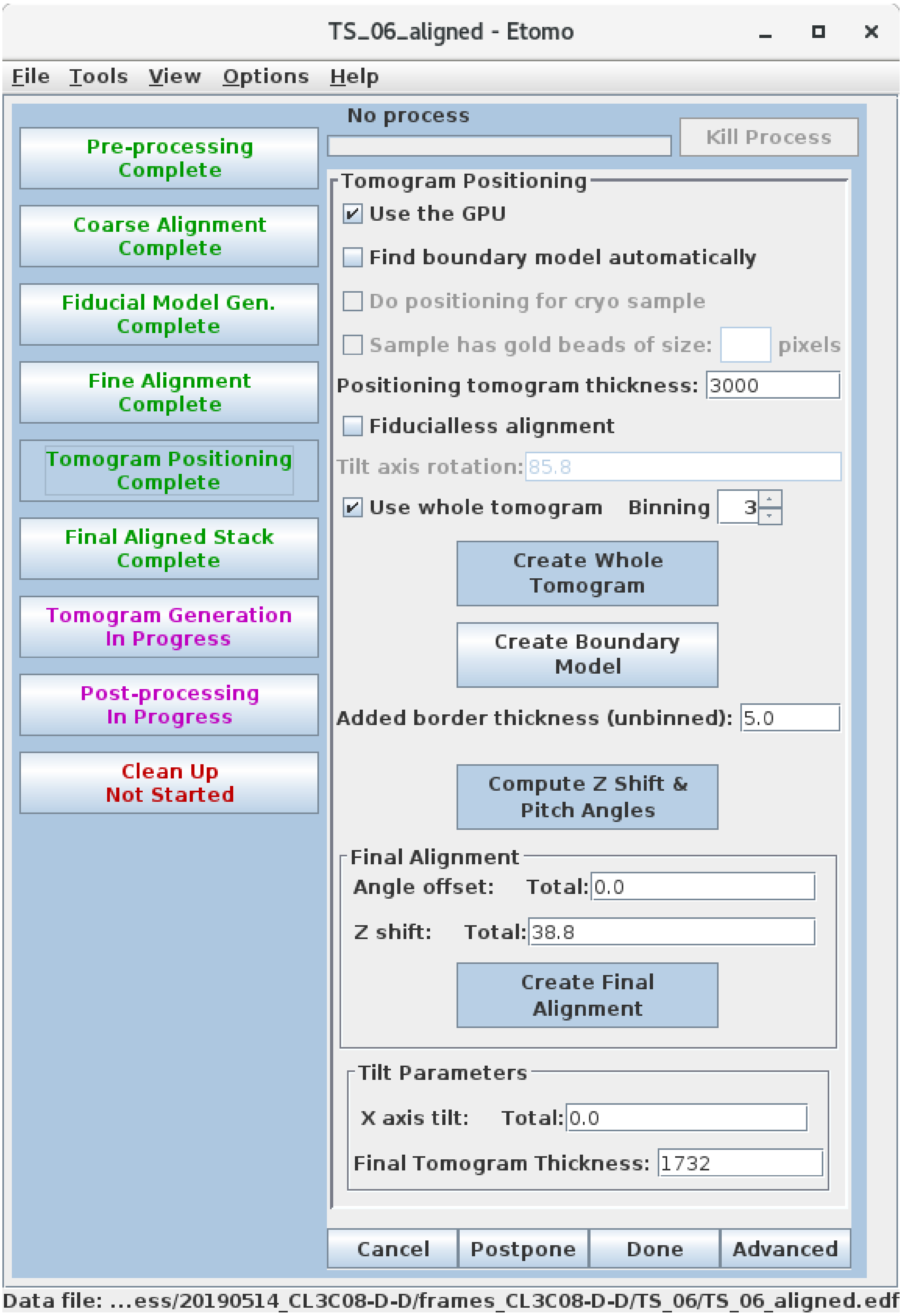

Tomogram Positioning

☑ Use the GPU

☐ Find boundary model automatically

☐ Do positioning for cryo sample

☐ Sample has gold beads of size: pixels

Positioning tomogram thickness: 3000

☐ Fiducialless alignment

Tilt axis rotation: 85.8

☑ Use whole tomogram Binning 3

Added border thickness (unbinned): 5.0

Final Alignment

Angle offset: Total: 0.0

Z shift: Total: 38.8

Tilt Parameters

X axis tilt: Total: 0.0

Final Tomogram Thickness: 1732

Data file: ...ess/20190514_CL3C08-D-D/frames_CL3C08-D-D/TS_06/TS_06_aligned.edf

Figure 48: Tomogram positioning. The z height of the tomogram was determined by creating the tomogram (‘Create Whole Tomogram’) and opening the slicer window (‘Create Boundary Model’, shown in next figure). Z shift was computed (‘Compute Z shift and Pitch Angles’), values for Angle offset and X axis tilt were deleted for final alignment (‘Create Final Alignment’) to determine the thickness of the tomogram.

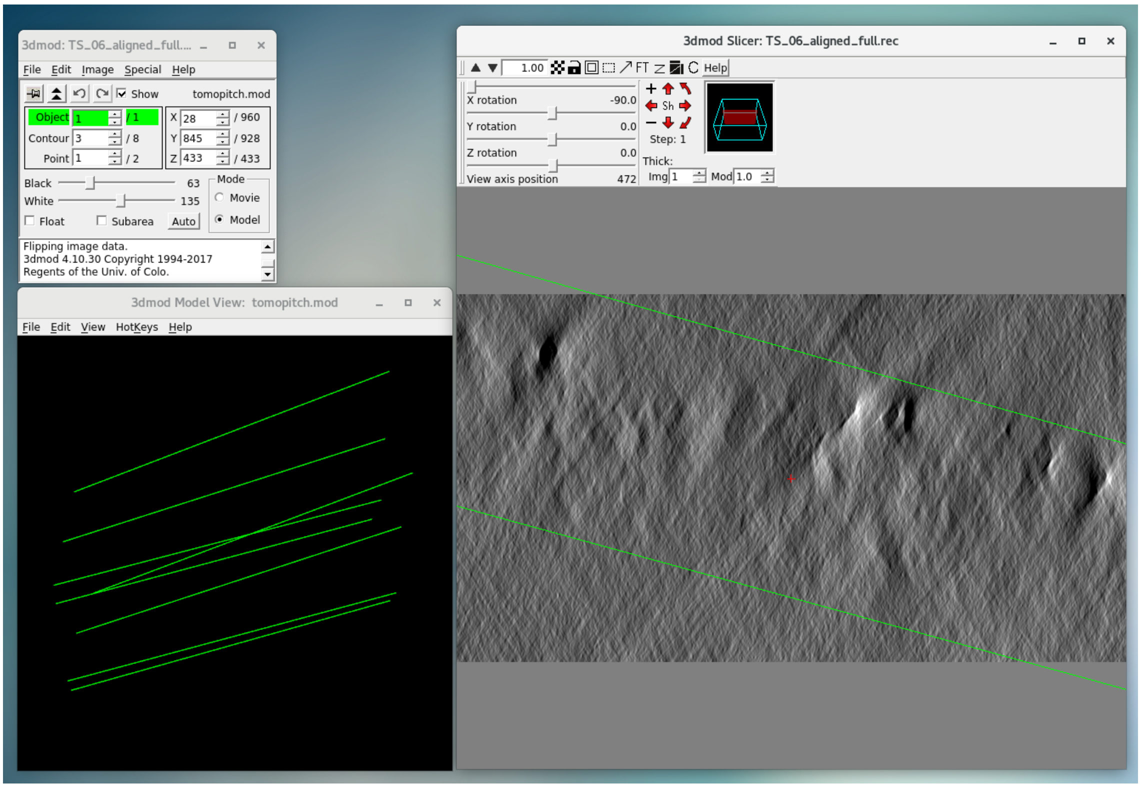

☑ Show
Object 1 / 1
Contour 3 / 8
Point 1 / 2
X 28 / 960
Y 845 / 928
Z 433 / 433
Black 63
White 135
☐ Float
☐ Subarea
○ Movie
● Model

Flipping image data.
3dmod 4.10.30 Copyright 1994-2017
Regents of the Univ. of Colo.

1.00
X rotation -90.0
Y rotation 0.0
Z rotation 0.0
View axis position 472
Img 1
Mod 1.0

Figure 49: Tomogram Positioning. After opening the tomogram in 3dmod (‘Create Boundary Model’), the slicer window was opened by pressing ‘/’ and the X rotation was set to -90. 6 contours were added in 3 different axis positions (bottom, middle, top) using the middle mouse button. Therefore, a contour was set so that the material in the tomogram was in the middle. ‘S’ to save model.

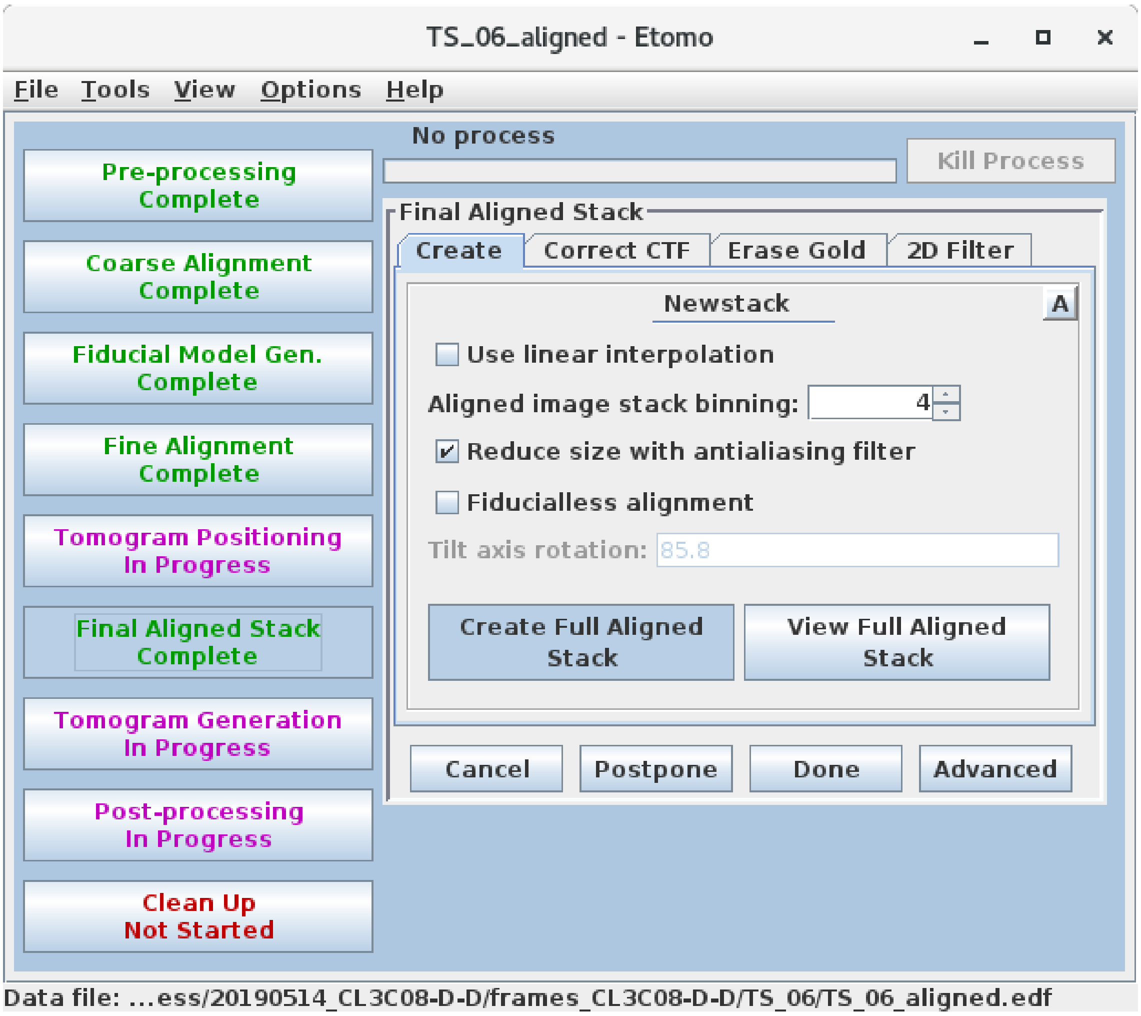

☐ Use linear interpolation

Aligned image stack binning: 4

☑ Reduce size with antialiasing filter

☐ Fiducialless alignment

Tilt axis rotation: 85.8

Data file: ...ess/20190514_CL3C08-D-D/frames_CL3C08-D-D/TS_06/TS_06_aligned.edf

Figure 50: Final aligned Stack. A new stack was created with binning 4 (‘Create Full Aligned Stack’).

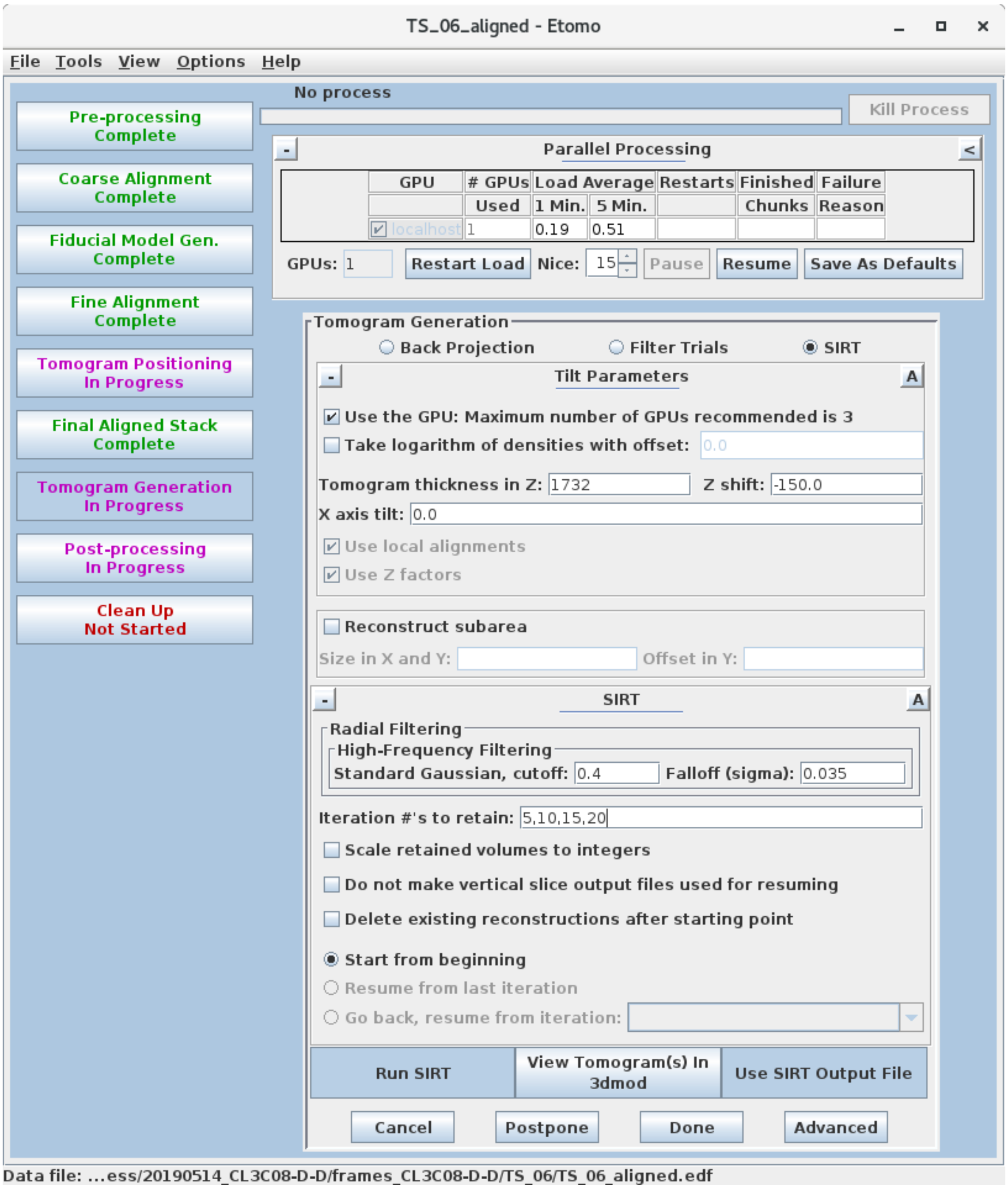

TS_06_aligned - Etomo

GPU	# GPUs Used	Load Average 1 Min.	5 Min.	Restarts	Finished Chunks	Failure Reason
☑ localhost	1	0.19	0.51			

GPUs: 1 Nice: 15

Tomogram Generation

○ Back Projection ○ Filter Trials ● SIRT

☑ Use the GPU: Maximum number of GPUs recommended is 3

☐ Take logarithm of densities with offset: 0.0

Tomogram thickness in Z: 1732 Z shift: -150.0

X axis tilt: 0.0

☑ Use local alignments

☑ Use Z factors

☐ Reconstruct subarea

Size in X and Y: Offset in Y:

Radial Filtering

High-Frequency Filtering

Standard Gaussian, cutoff: 0.4 Falloff (sigma): 0.035

Iteration #'s to retain: 5,10,15,20

☐ Scale retained volumes to integers

☐ Do not make vertical slice output files used for resuming

☐ Delete existing reconstructions after starting point

● Start from beginning

○ Resume from last iteration

○ Go back, resume from iteration:

Data file: ...ess/20190514_CL3C08-D-D/frames_CL3C08-D-D/TS_06/TS_06_aligned.edf

Figure 51: Tomogram Generation. Simultaneous Iterative Reconstruction (SIRT) technique was used to create the tomograms. 5, 10, 15 and 20 iterations were selected (‘Run SIRT’). After opening the tomograms in 3dmod (‘View Tomograms in 3dmod’) one of the iterations was used as SIRT output file (for most tomograms sirt 5 had the best signal to noise ratio, ‘Use SIRT Output File’).

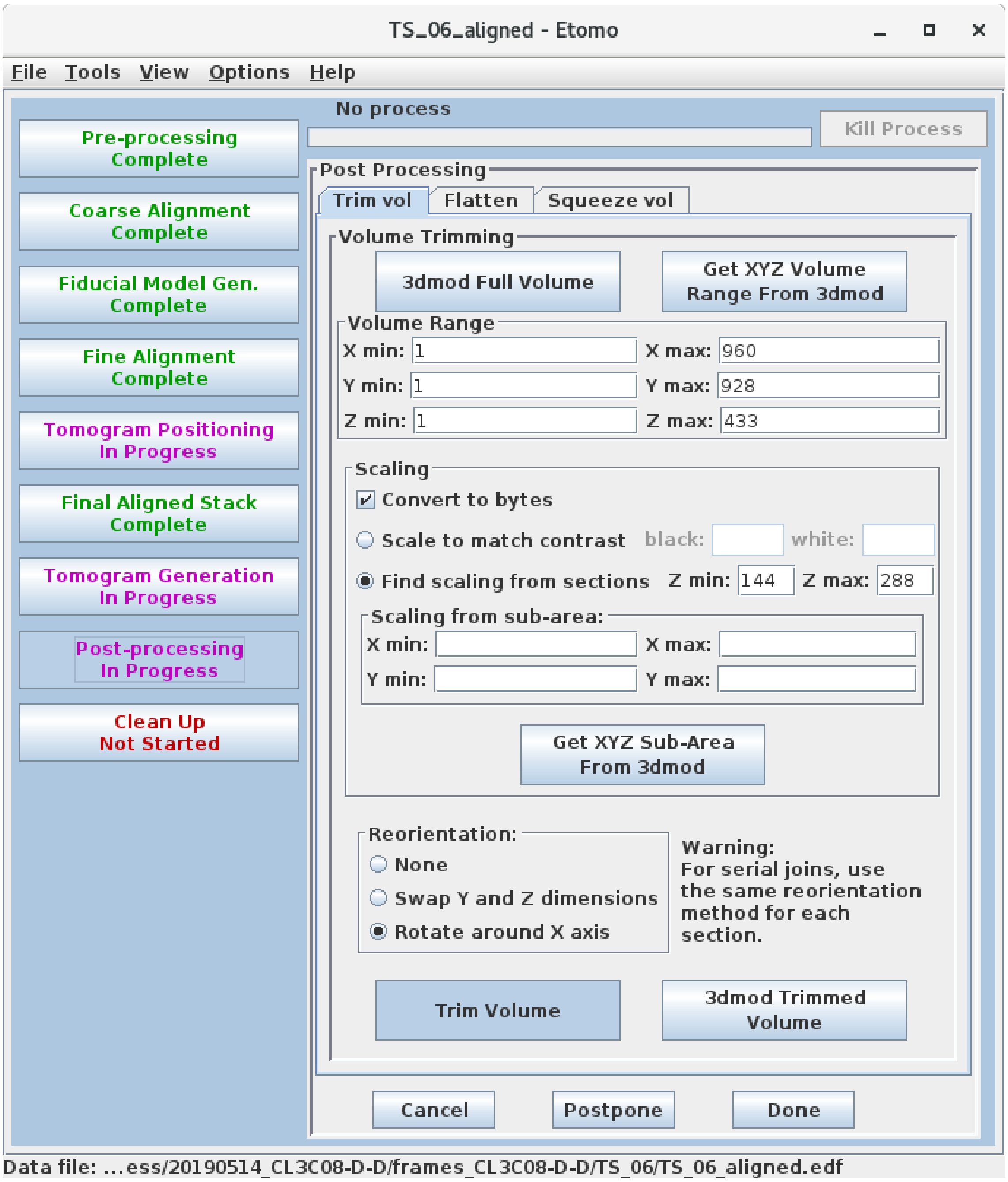

Volume Range

X min: 1 X max: 960

Y min: 1 Y max: 928

Z min: 1 Z max: 433

Scaling

☑ Convert to bytes

○ Scale to match contrast black: white:

● Find scaling from sections Z min: 144 Z max: 288

Scaling from sub-area:

X min: X max:

Y min: Y max:

Reorientation:

○ None

○ Swap Y and Z dimensions

● Rotate around X axis

Warning:
For serial joins, use the same reorientation method for each section.

Data file: ...ess/20190514_CL3C08-D-D/frames_CL3C08-D-D/TS_06/TS_06_aligned.edf

Figure 52: Post-processing. The tomogram was rotated around the X axis (‘Trim Volume’).

7.2. Nonlinear Anisotropic Diffusion Filtering

A

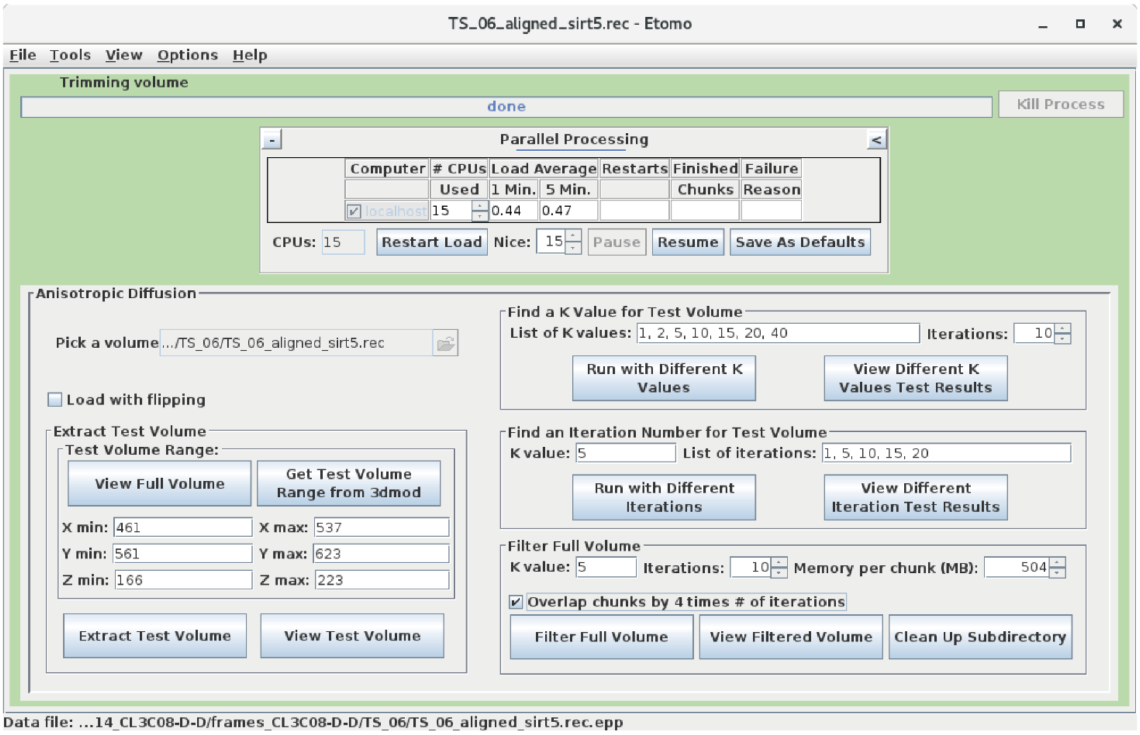

Trimming volume

done

Computer	# CPUs Used	Load Average 1 Min.	Load Average 5 Min.	Restarts	Finished Chunks	Failure Reason
☑ localhost	15	0.44	0.47			

CPUs: 15

Nice: 15

Pick a volume .../TS_06/TS_06_aligned_sirt5.rec

☐ Load with flipping

List of K values: 1, 2, 5, 10, 15, 20, 40

Iterations: 10

K value: 5

List of iterations: 1, 5, 10, 15, 20

X min: 461

X max: 537

Y min: 561

Y max: 623

Z min: 166

Z max: 223

K value: 5

Iterations: 10

Memory per chunk (MB): 504

☑ Overlap chunks by 4 times # of iterations

Data file: ...14_CL3C08-D-D/frames_CL3C08-D-D/TS_06/TS_06_aligned_sirt5.rec.epp

B

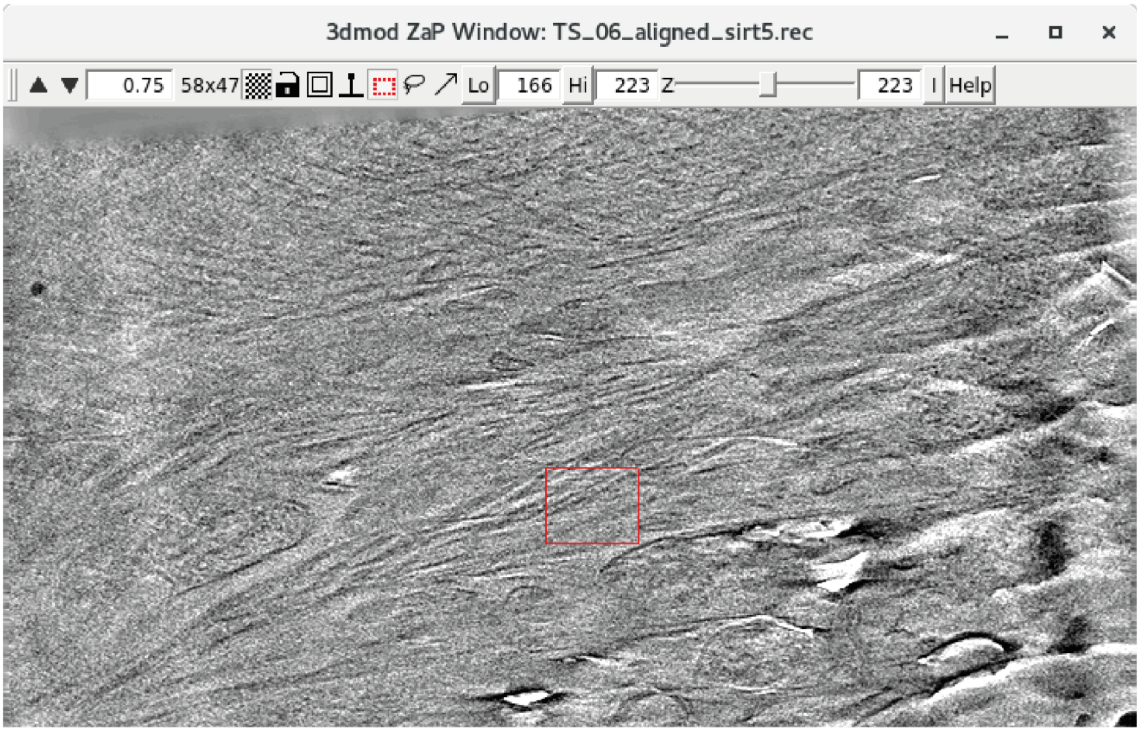

0.75

58x47

Lo 166

Hi 223

Z 223

Figure 53: Nonlinear Anisotropic Diffusion (NAD) filtering. Tomogram was imported and opened in 3dmod (A). Box was drawn around features of interest and by pressing 'Hi' and 'Lo' z positions were set (B). Then the range was extracted ('Get Test Volume Range from 3dmod', 'Extract Test Volume', A). First different K-values were tested and the one with the best signal-to-noise ratio was manually determined. Second, different iterations were tested, inspected by eye and the best signal-to-noise was chosen to do the final NAD for the whole tomogram.

7.3. Deconvolution

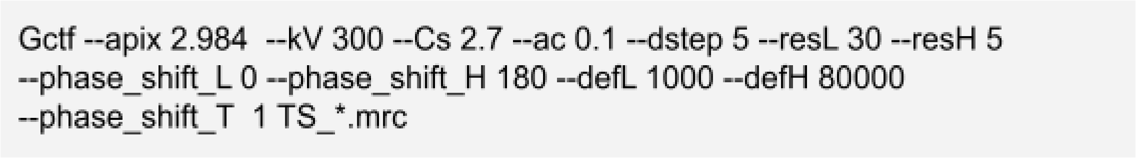

```
Gctf --apix 2.984  --kV 300 --Cs 2.7 --ac 0.1 --dstep 5 --resL 30 --resH 5
--phase_shift_L 0 --phase_shift_H 180 --defL 1000 --defH 80000
--phase_shift_T  1 TS_*.mrc
```

Figure 54: Gctf to estimate the defocus and phase shift. The estimated defocus values were needed for deconvolution in matlab.

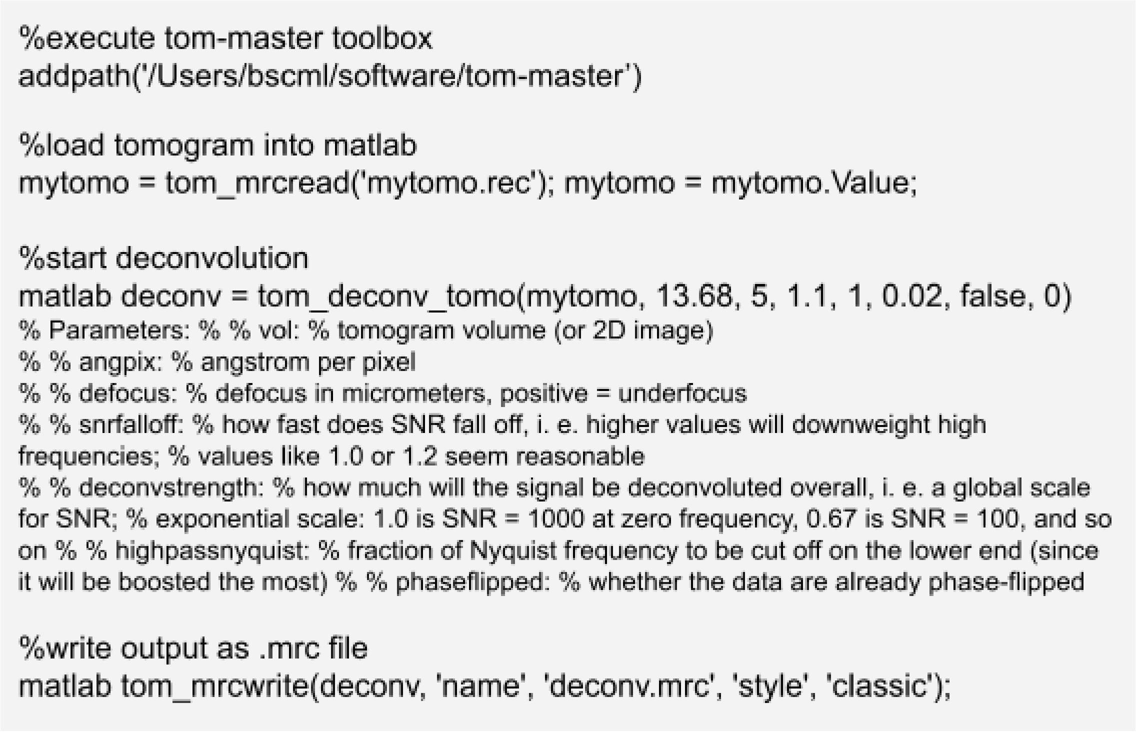

```
%execute tom-master toolbox
addpath('/Users/bscml/software/tom-master')

%load tomogram into matlab
mytomo = tom_mrcread('mytomo.rec'); mytomo = mytomo.Value;

%start deconvolution
matlab deconv = tom_deconv_tomo(mytomo, 13.68, 5, 1.1, 1, 0.02, false, 0)
% Parameters: % % vol: % tomogram volume (or 2D image)
% % angpix: % angstrom per pixel
% % defocus: % defocus in micrometers, positive = underfocus
% % snrfalloff: % how fast does SNR fall off, i. e. higher values will downweight high
frequencies; % values like 1.0 or 1.2 seem reasonable
% % deconvstrength: % how much will the signal be deconvoluted overall, i. e. a global scale
for SNR; % exponential scale: 1.0 is SNR = 1000 at zero frequency, 0.67 is SNR = 100, and so
on % % highpassnyquist: % fraction of Nyquist frequency to be cut off on the lower end (since
it will be boosted the most) % % phaseflipped: % whether the data are already phase-flipped

%write output as .mrc file
matlab tom_mrcwrite(deconv, 'name', 'deconv.mrc', 'style', 'classic');
```

Figure 55: Deconvolution. Tomo-master was downloaded from github: https://github.com/dtegunov/tom and added to matlab. The tomogram was loaded into matlab ‘mytomo.rec’ was replaced with the name of the tomogram. The deconvolution was performed with the command ‘matlab_deconv’ and the values shown were used. Lastly, the output file was written.

7.4. Subtomogram Averaging

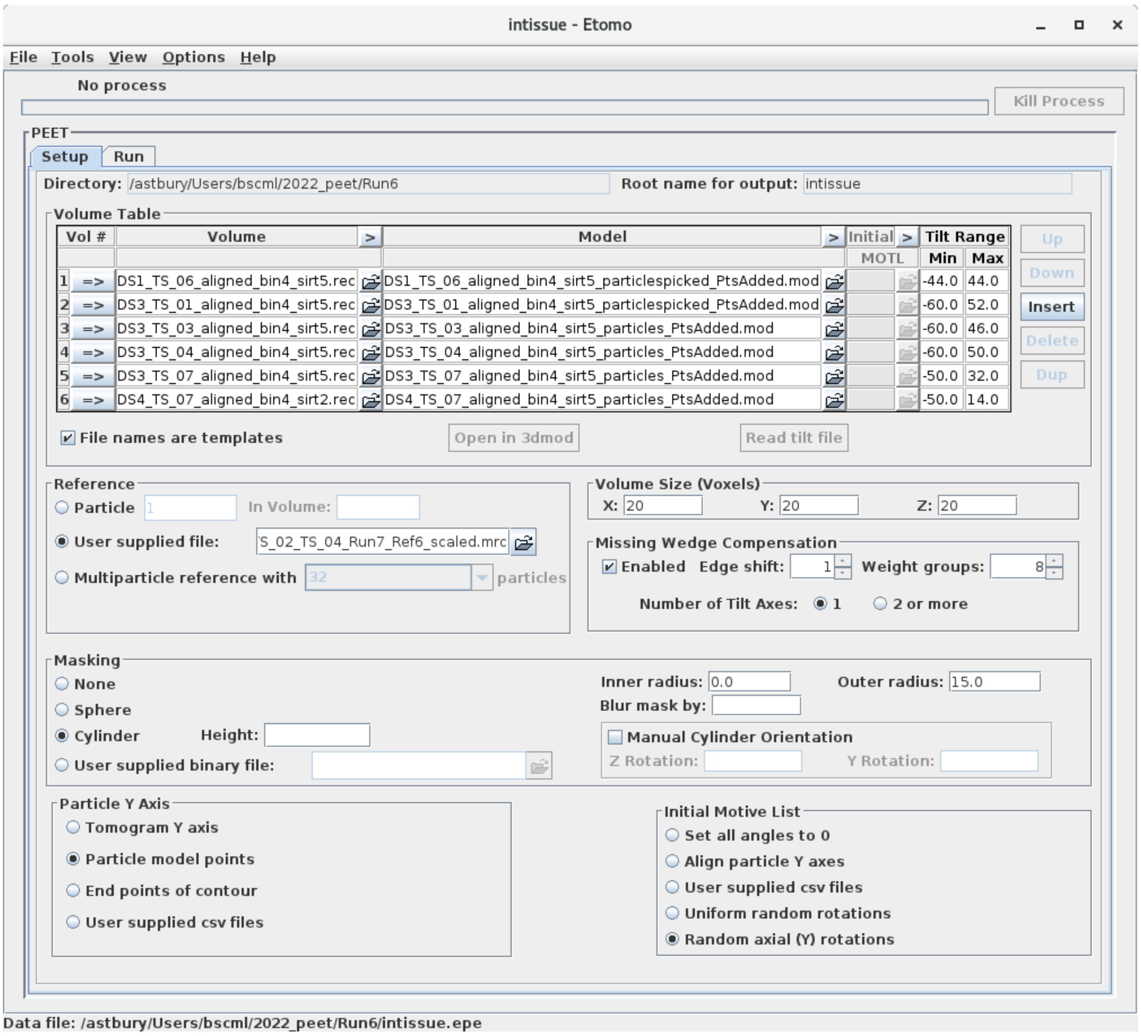

Directory: /astbury/Users/bscml/2022_peet/Run6   Root name for output: intissue

Volume Table

Vol #		Volume	Model	Initial MOTL	Tilt Range Min	Tilt Range Max
1	=>	DS1_TS_06_aligned_bin4_sirt5.rec	DS1_TS_06_aligned_bin4_sirt5_particlespicked_PtsAdded.mod		-44.0	44.0
2	=>	DS3_TS_01_aligned_bin4_sirt5.rec	DS3_TS_01_aligned_bin4_sirt5_particlespicked_PtsAdded.mod		-60.0	52.0
3	=>	DS3_TS_03_aligned_bin4_sirt5.rec	DS3_TS_03_aligned_bin4_sirt5_particles_PtsAdded.mod		-60.0	46.0
4	=>	DS3_TS_04_aligned_bin4_sirt5.rec	DS3_TS_04_aligned_bin4_sirt5_particles_PtsAdded.mod		-60.0	50.0
5	=>	DS3_TS_07_aligned_bin4_sirt5.rec	DS3_TS_07_aligned_bin4_sirt5_particles_PtsAdded.mod		-50.0	32.0
6	=>	DS4_TS_07_aligned_bin4_sirt2.rec	DS4_TS_07_aligned_bin4_sirt5_particles_PtsAdded.mod		-50.0	14.0

☑ File names are templates

Reference
○ Particle 1 In Volume:
● User supplied file: S_02_TS_04_Run7_Ref6_scaled.mrc
○ Multiparticle reference with 32 particles

Volume Size (Voxels)
X: 20 Y: 20 Z: 20

Missing Wedge Compensation
☑ Enabled Edge shift: 1 Weight groups: 8
Number of Tilt Axes: ● 1 ○ 2 or more

Masking
○ None
○ Sphere
● Cylinder Height:
○ User supplied binary file:
Inner radius: 0.0 Outer radius: 15.0
Blur mask by:
☐ Manual Cylinder Orientation
Z Rotation: Y Rotation:

Particle Y Axis
○ Tomogram Y axis
● Particle model points
○ End points of contour
○ User supplied csv files

Initial Motive List
○ Set all angles to 0
○ Align particle Y axes
○ User supplied csv files
○ Uniform random rotations
● Random axial (Y) rotations

Data file: /astbury/Users/bscml/2022_peet/Run6/intissue.epe

Figure 56: Subtomogram Averaging using peet. Tomograms and model files which were prepared by particle picking in imod and addModPts to add points with spacing of 1 pixel (run in command line: 'addModPts DS1_TS_06_aligned_bin4_sirt5.mod DS1_TS_06_aligned_bin4_sirt5.mod 1') were imported into peet. The tilt range was extracted from the individual .rawtlt files from etomo (see 7.1 Etomo). As a reference for the in-tissue tomograms, the reference file from tomograms of *ex-vivo* prepared fibrils was used ('User supplied file'). For *ex-vivo* tomograms, particle 1 was used as reference. Boxe sizes were 20 voxels using a cylindrical mask with an outer radius of

15 pixels and missing wedge compensation. The particle Y axis was selected as particle model points and the initial motif list was created from random axial (Y) rotations. The setup for the Run tab is shown in the next figure.

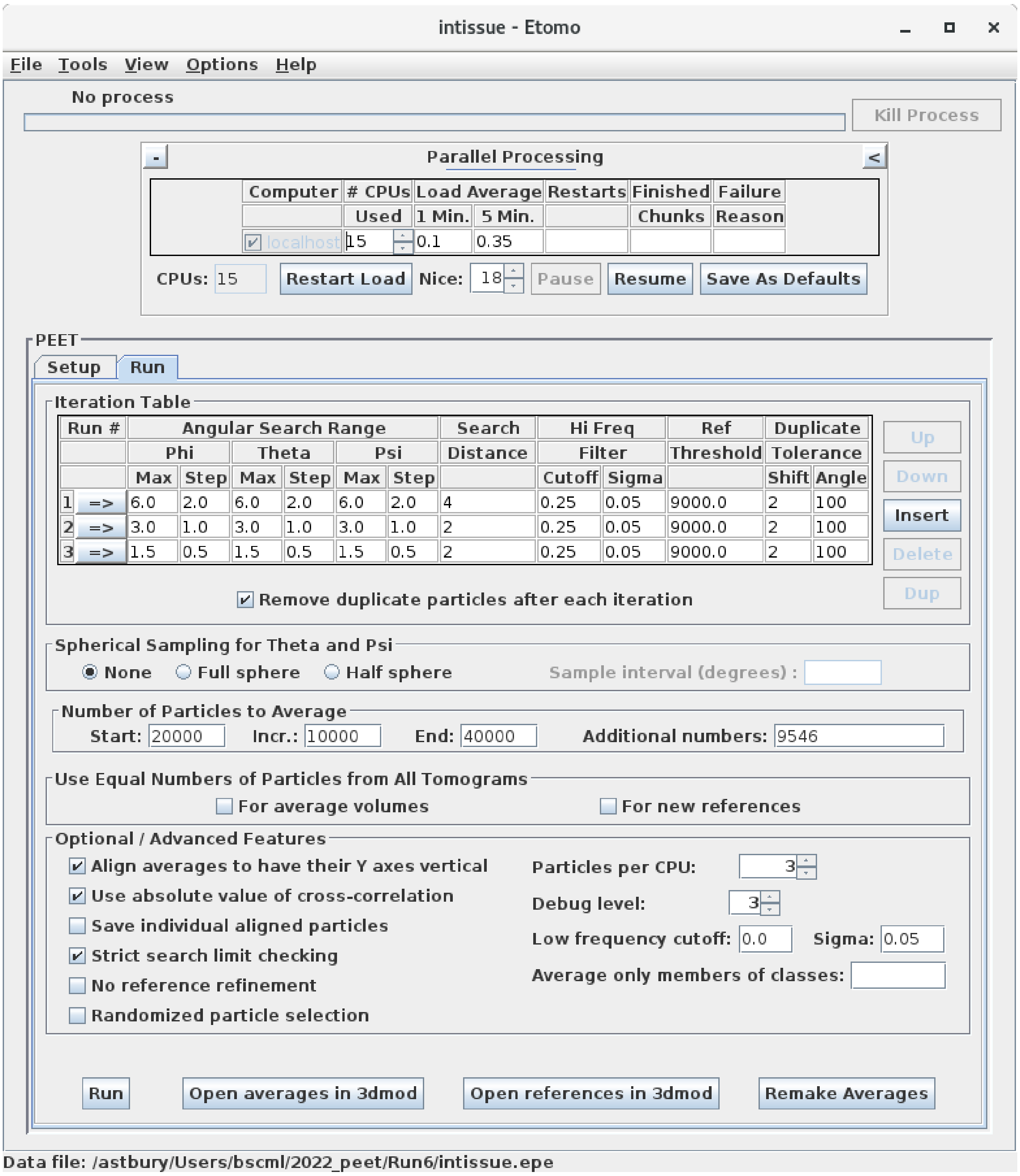

Computer	# CPUs	Load Average		Restarts	Finished	Failure
	Used	1 Min.	5 Min.		Chunks	Reason
☑ localhost	15	0.1	0.35			

CPUs: 15 Nice: 18

Iteration Table

Run #		Angular Search Range						Search	Hi Freq		Ref	Duplicate	
		Phi		Theta		Psi		Distance	Filter		Threshold	Tolerance	
		Max	Step	Max	Step	Max	Step		Cutoff	Sigma		Shift	Angle
1	=>	6.0	2.0	6.0	2.0	6.0	2.0	4	0.25	0.05	9000.0	2	100
2	=>	3.0	1.0	3.0	1.0	3.0	1.0	2	0.25	0.05	9000.0	2	100
3	=>	1.5	0.5	1.5	0.5	1.5	0.5	2	0.25	0.05	9000.0	2	100

☑ Remove duplicate particles after each iteration

Spherical Sampling for Theta and Psi

● None ○ Full sphere ○ Half sphere Sample interval (degrees) :

Number of Particles to Average

Start: 20000 Incr.: 10000 End: 40000 Additional numbers: 9546

Use Equal Numbers of Particles from All Tomograms

☐ For average volumes ☐ For new references

Optional / Advanced Features

☑ Align averages to have their Y axes vertical

☑ Use absolute value of cross-correlation

☐ Save individual aligned particles

☑ Strict search limit checking

☐ No reference refinement

☐ Randomized particle selection

Particles per CPU: 3

Debug level: 3

Low frequency cutoff: 0.0 Sigma: 0.05

Average only members of classes:

Data file: /astbury/Users/bscml/2022_peet/Run6/intissue.epe

Figure 57: Subtomogram Averaging using peet. The iteration table for angular search ranges can be seen in this figure. In total, 49546 particles were averaged and duplicated particles were removed. Peet was run on 15 CPUs.

8. Appendix II: cryo-CLEM

8.1. Methoxy-X04

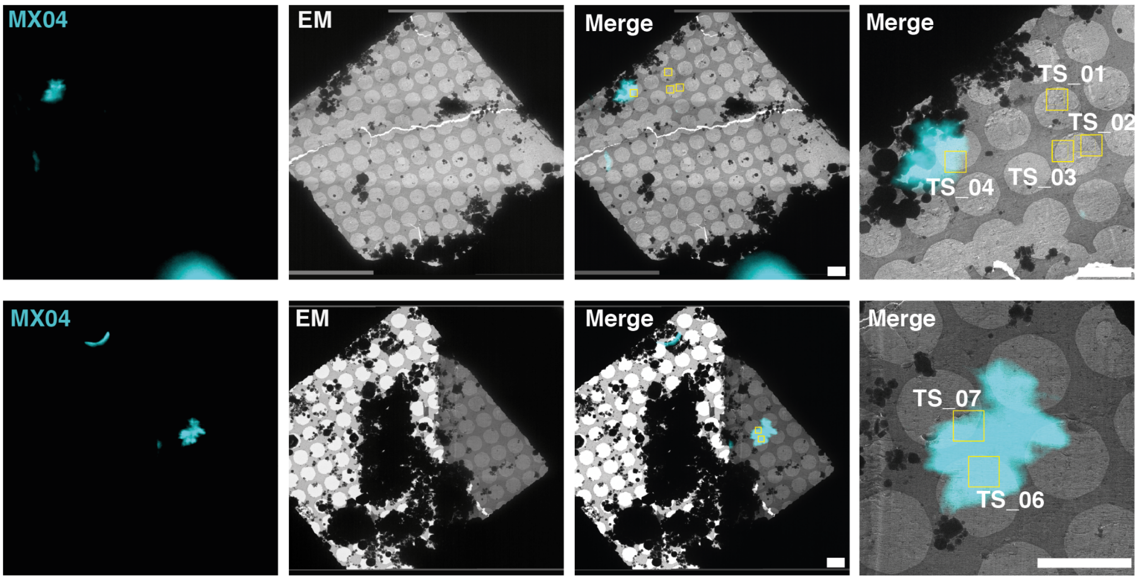

Figure 58: Methoxy-X04 cryo-CLEM for dataset 1. Methoxy-X04 (MX04) signal (cyan) is shown on the left. The second panel shows the electron micrographs, the third panel shows the merged images for the entire grid square and close-up of regions where tomograms were collected are shown on the right. Yellow boxes indicate areas where tomograms were collected. Cryo-CLEM for tomograms TS_05, TS_08-TS_12 could not be done because of missing data or CLEM was too difficult and regions were not found. All scale bars, 4µm.

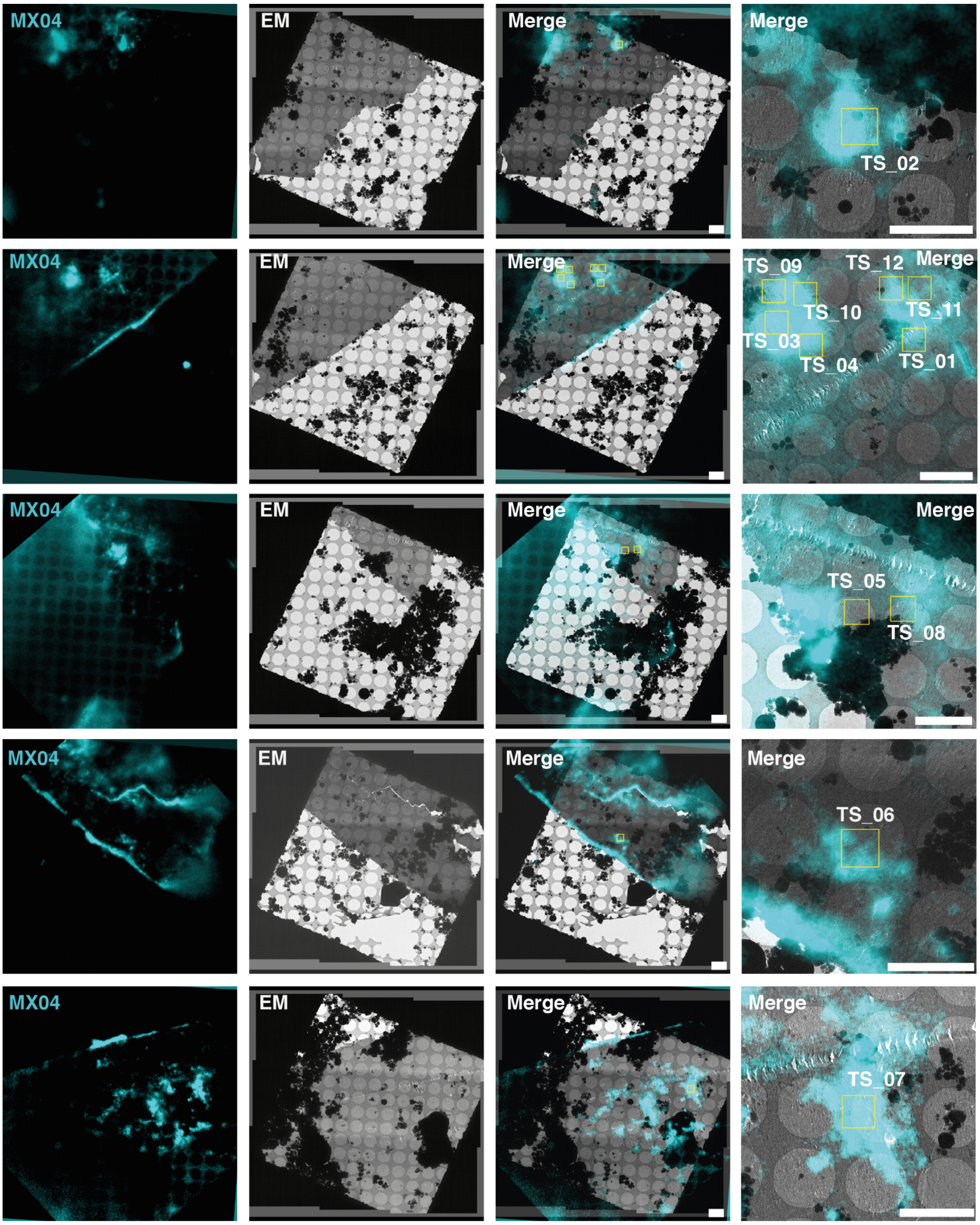
MX04
EM
Merge
Merge
TS_02
MX04
EM
Merge
TS_09
TS_12
Merge
TS_10
TS_11
TS_03
TS_04
TS_01
MX04
EM
Merge
Merge
TS_05
TS_08
MX04
EM
Merge
Merge
TS_06
MX04
EM
Merge
Merge
TS_07

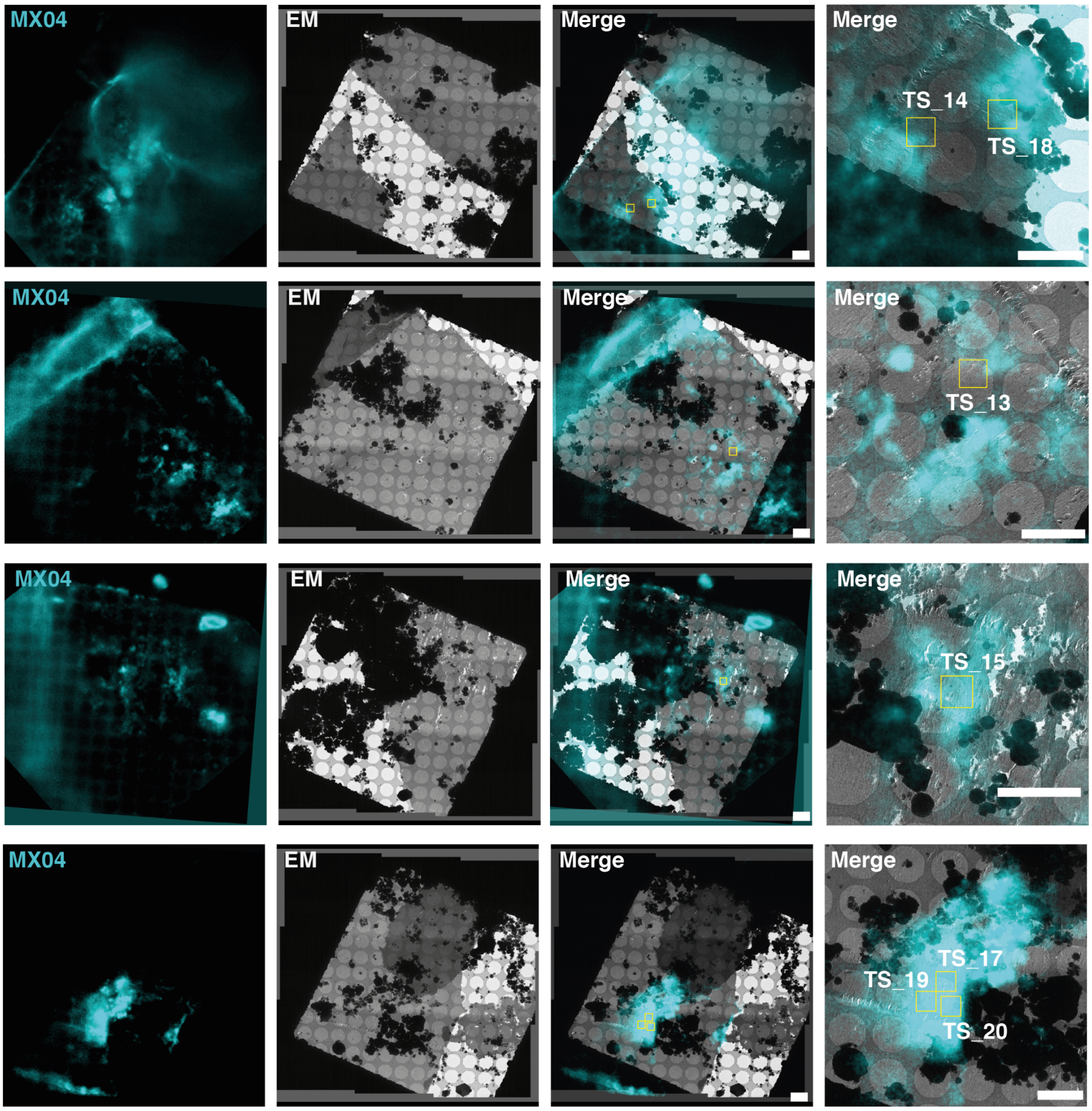

Figure 59: Methoxy-X04 cryo-CLEM for dataset 2. Methoxy-X04 (MX04) signal (cyan) is shown on the left. The second panel shows the electron micrographs, the third panel shows the merged images for the entire grid square and close-up of regions where tomograms were collected are shown on the right. Yellow boxes indicate areas where tomograms were collected. Cryo-CLEM for tomogram TS_16 could not be done because CLEM was too difficult and the region was not found. All scale bars, 4µm.

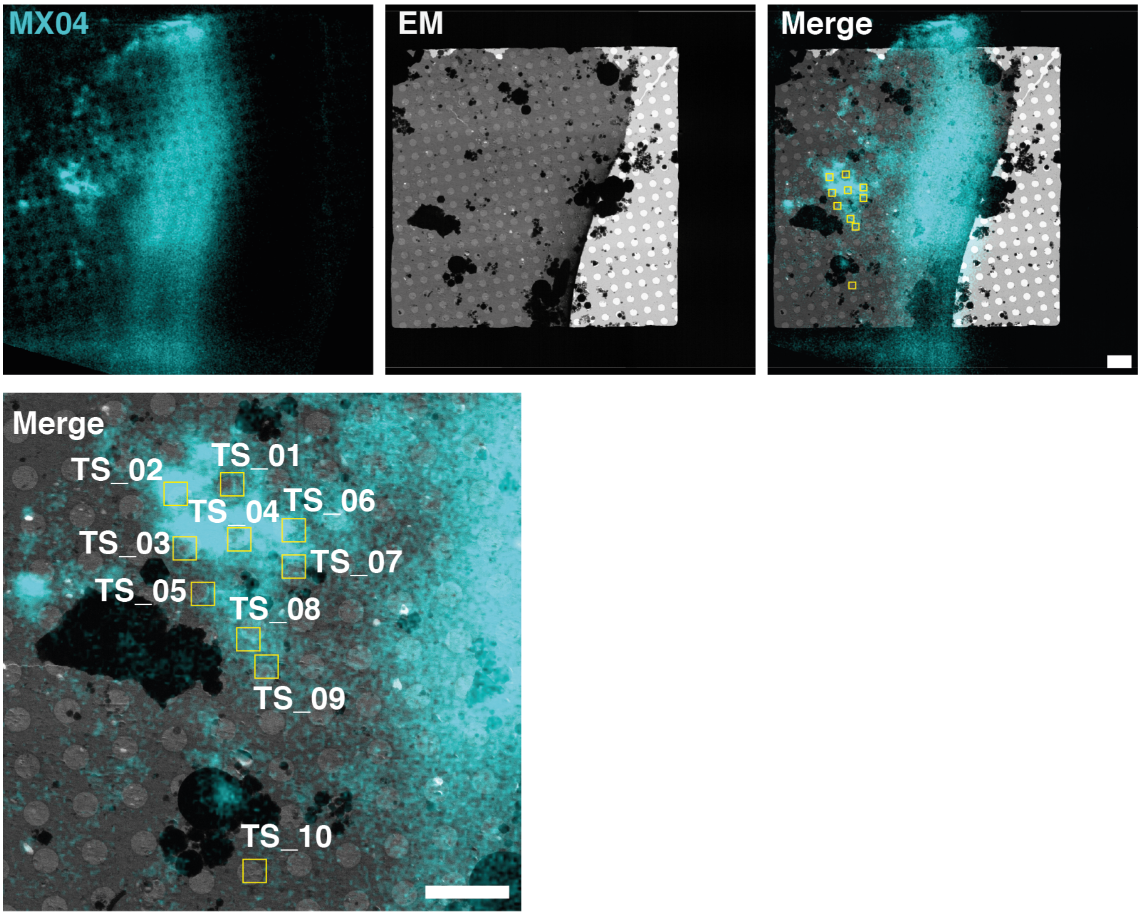

Figure 60: Methoxy-X04 cryo-CLEM for dataset 3. Methoxy-X04 (MX04) signal (cyan) is shown on the left. The second panel shows the electron micrographs, the right panel shows the merged images for the entire grid square and close-up of regions where tomograms were collected are shown in the bottom panel. Yellow boxes indicate areas where tomograms were collected. All scale bars, 4μm.

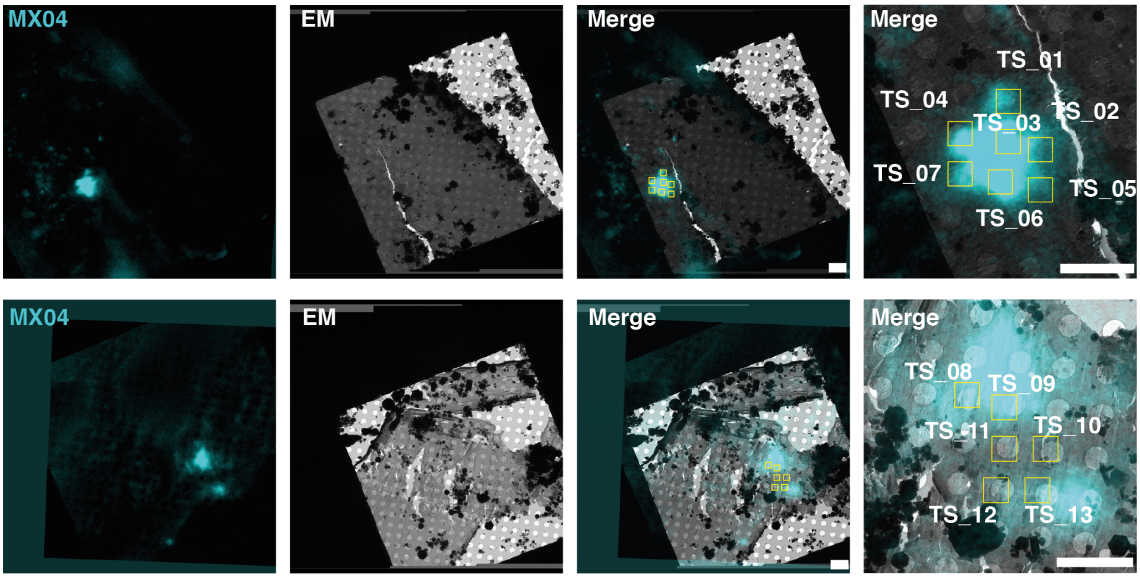

Figure 61: Methoxy-X04 cryo-CLEM for dataset 4. Methoxy-X04 (MX04) signal (cyan) is shown on the left. The second panel shows the electron micrographs, the third panel shows the merged images for the entire grid square and close-up of regions where tomograms were collected are shown in the right panel. Yellow boxes indicate areas where tomograms were collected. All scale bars, 4μm.

8.2. Dextran-AF647

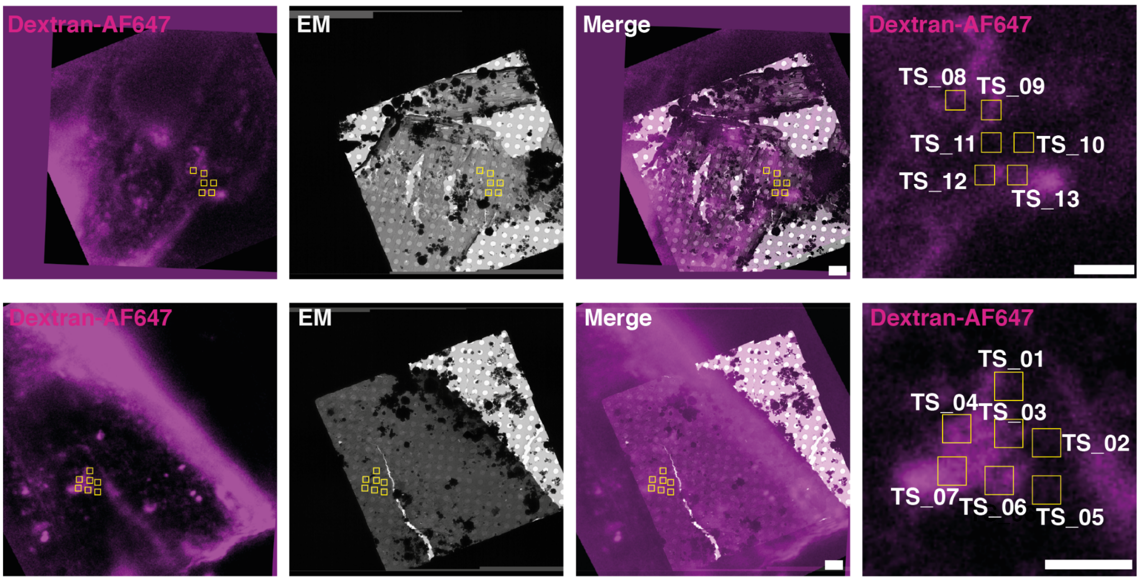

Figure 62: Dextran-AF647 cryo-CLEM for dataset 4. Dextran-AF647 signal (magenta) is shown on the left. The second panel shows the electron micrographs, the third panel shows the merged images for the entire grid square and close-up of regions where tomograms were collected are shown in the right panel. Yellow boxes indicate areas where tomograms were collected. Fluorescent dextran is used as an extracellular marker. All scale bars, 4μm.

9. Appendix III: Fast Fourier Transformation

DS1_TS_06

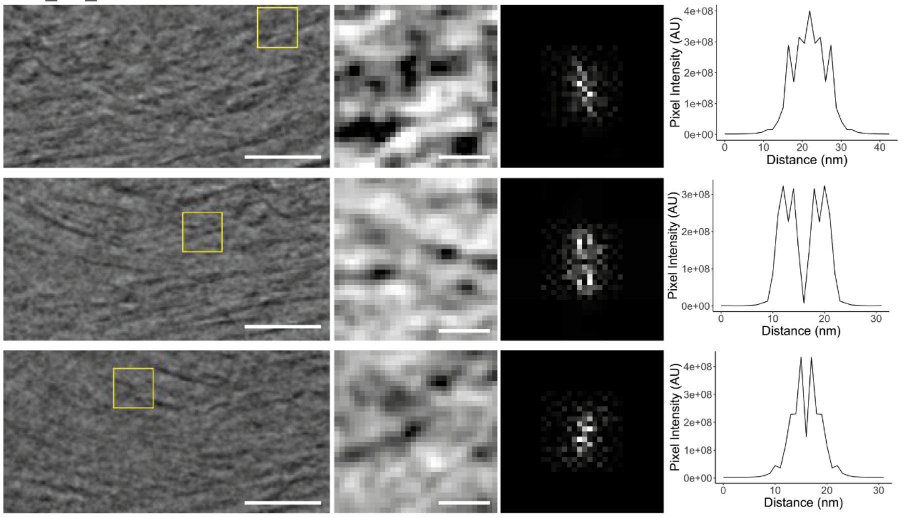

DS3_TS01

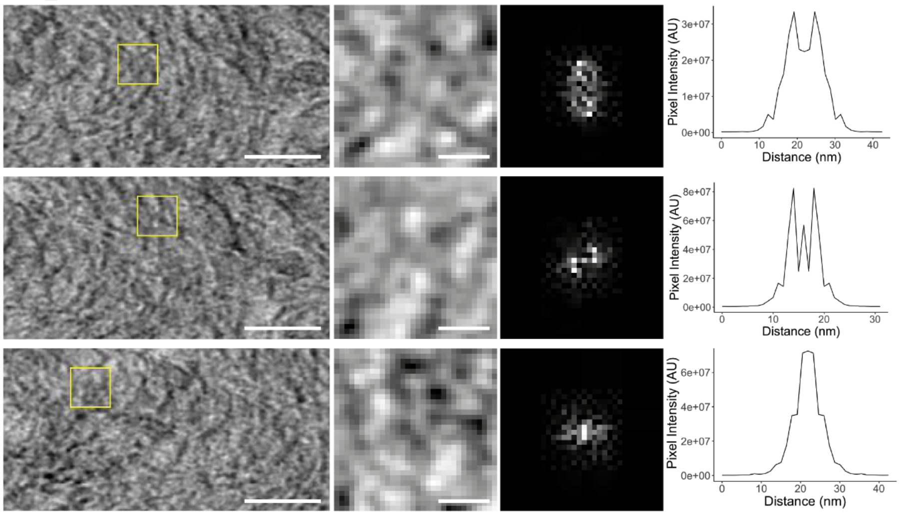

DS3_TS06

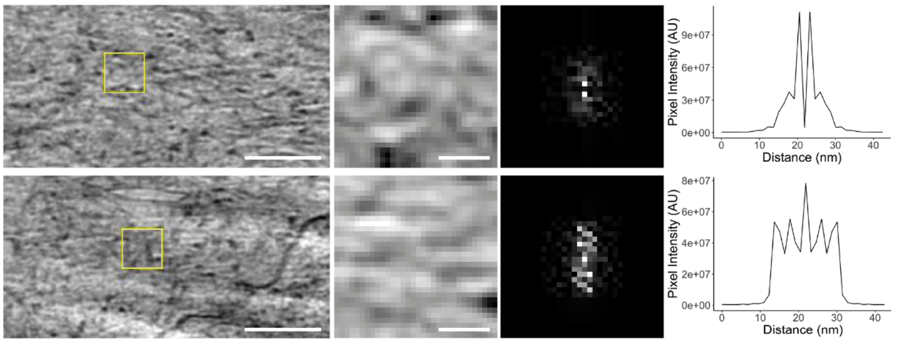

DS3_TS06

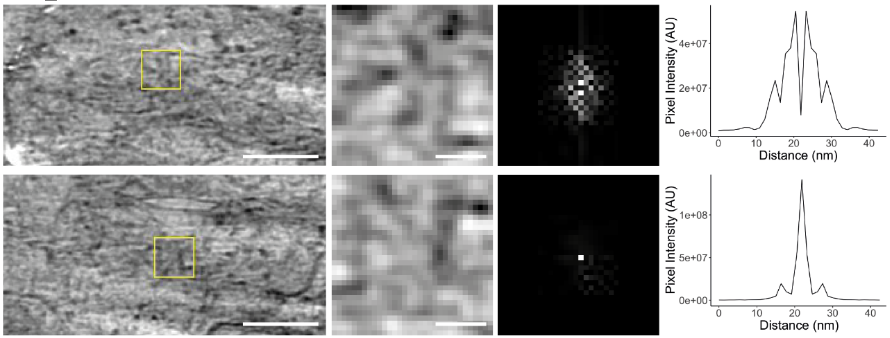

DS4_TS_07

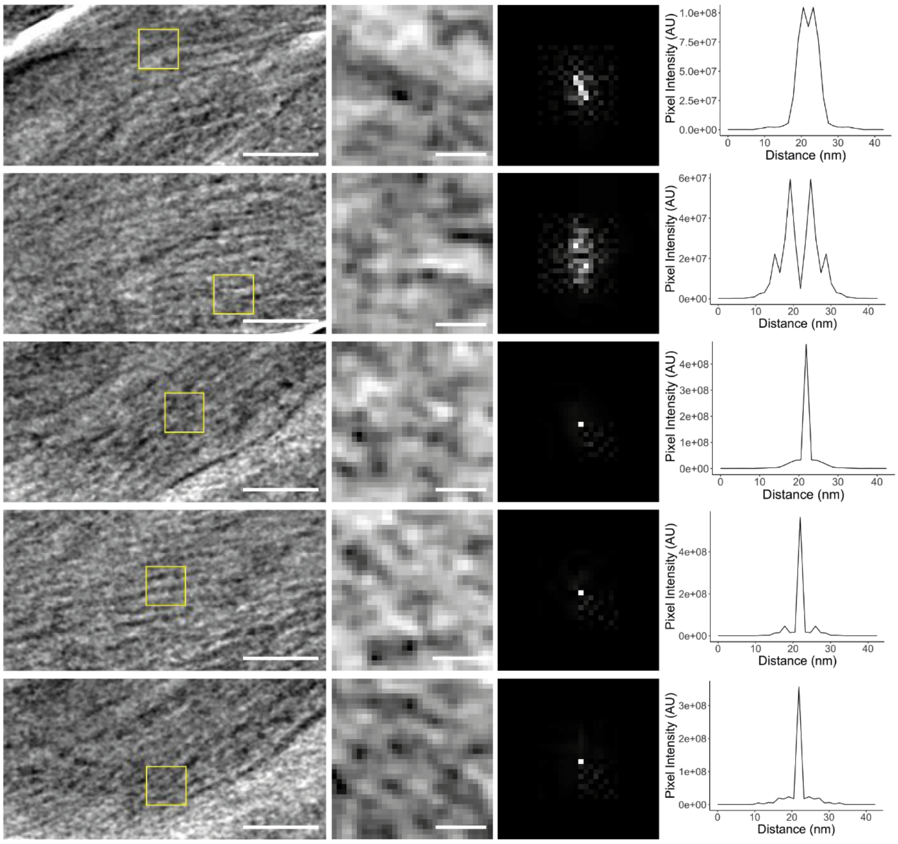

DS4_TS02

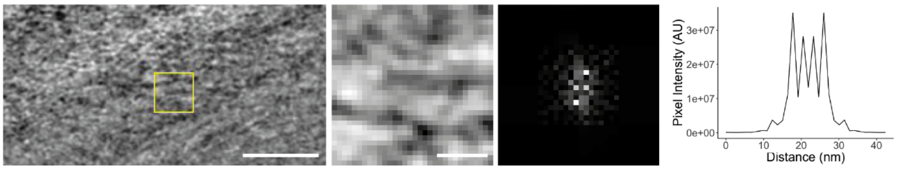

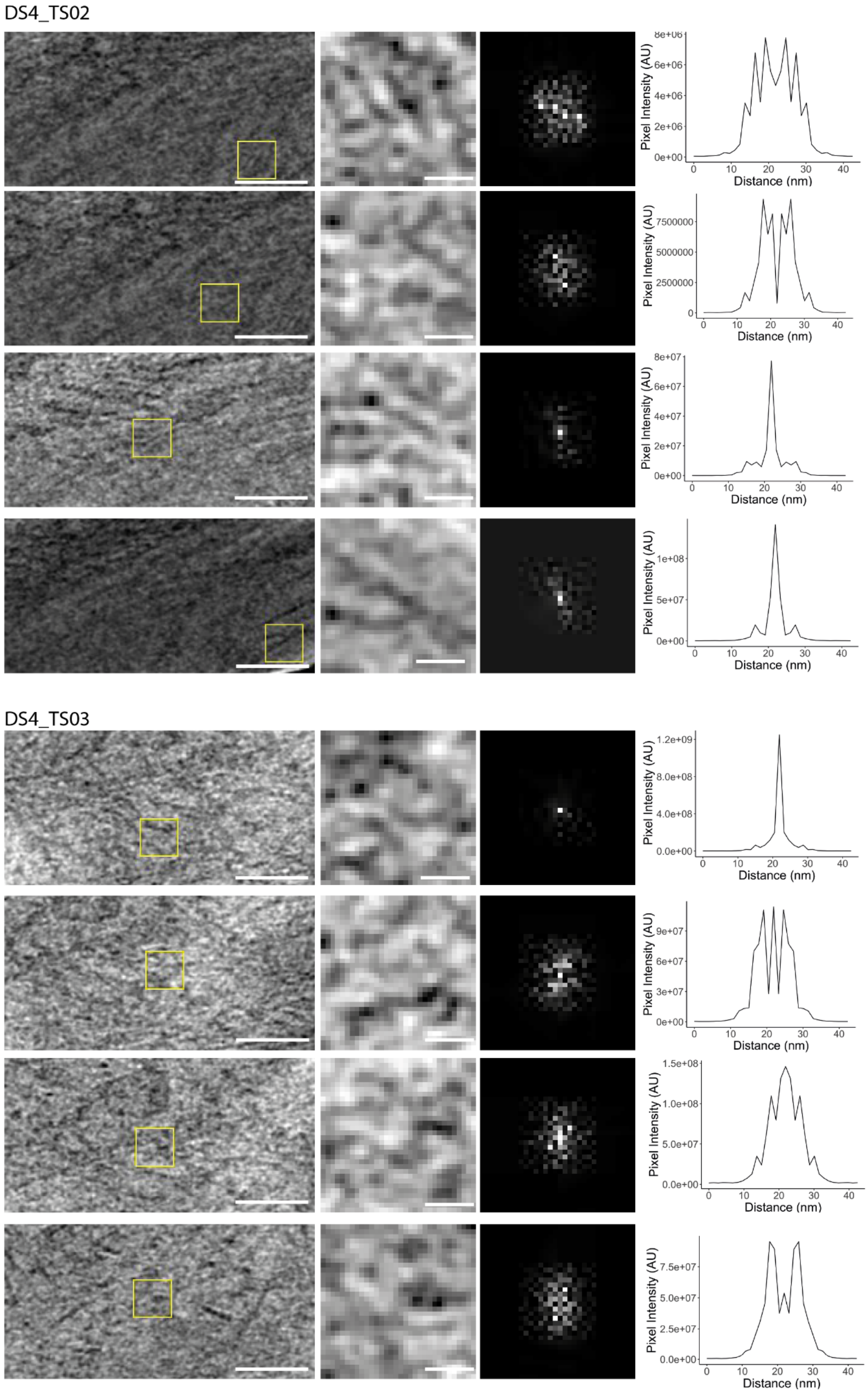

Figure 63: Fourier transformation of mesh of fibrils from all tomograms. Overview of Meshwork is shown on the left (scale bar 100 nm), boxes have been cropped for

FFT (middle) and FFT is shown in the 3rd panel. Graph of distances shows multiple peaks (right).

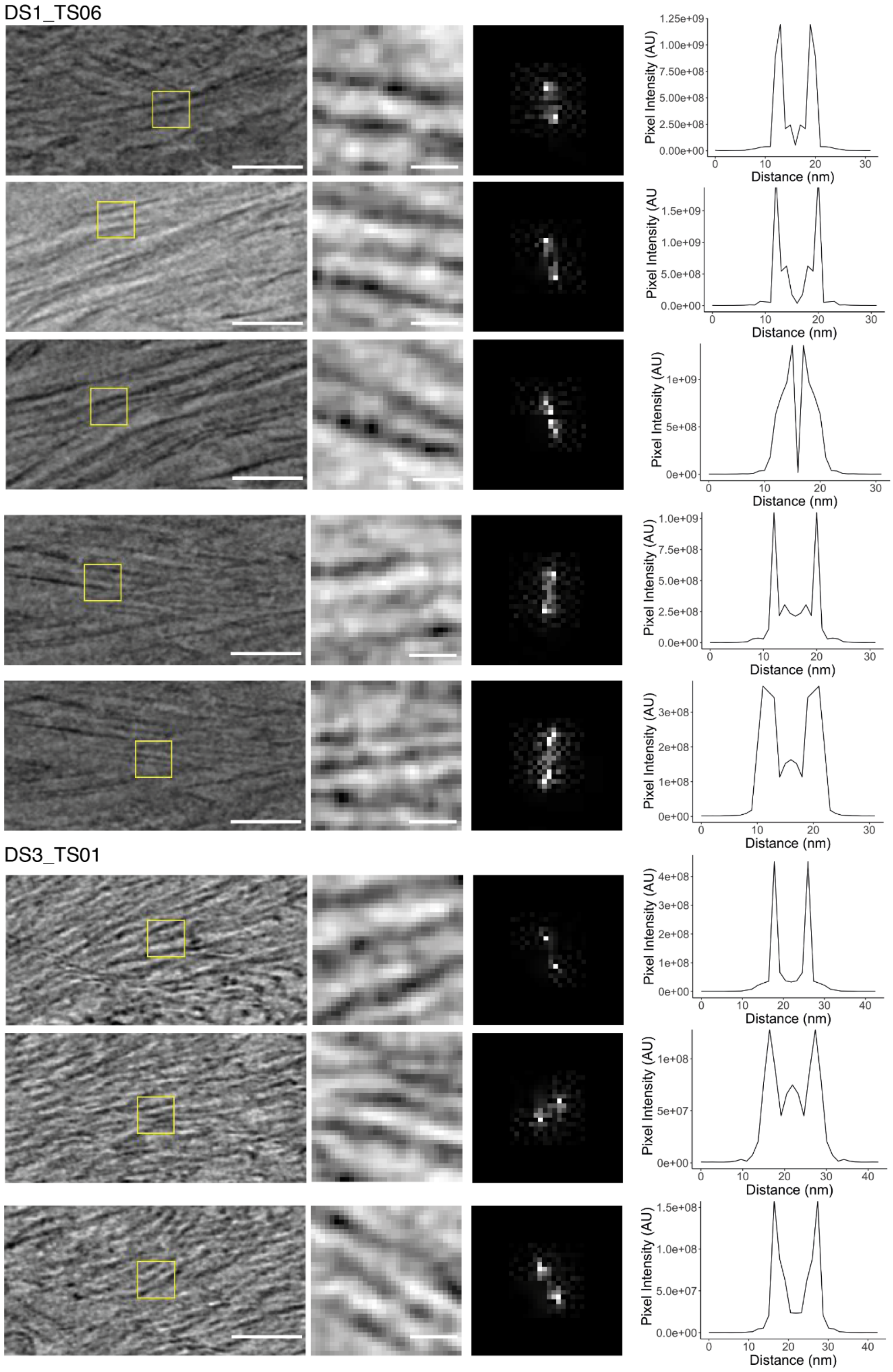
DS1_TS06
Pixel Intensity (AU)
1.25e+09
1.00e+09
7.50e+08
5.00e+08
2.50e+08
0.00e+00
Distance (nm)
1.5e+09
1.0e+09
5.0e+08
0.0e+00
1e+09
5e+08
0e+00
1.0e+09
7.5e+08
5.0e+08
2.5e+08
0.0e+00
3e+08
2e+08
1e+08
0e+00
0
10
20
30
DS3_TS01
4e+08
3e+08
2e+08
1e+08
0e+00
1e+08
5e+07
0e+00
1.5e+08
1.0e+08
5.0e+07
0.0e+00
40

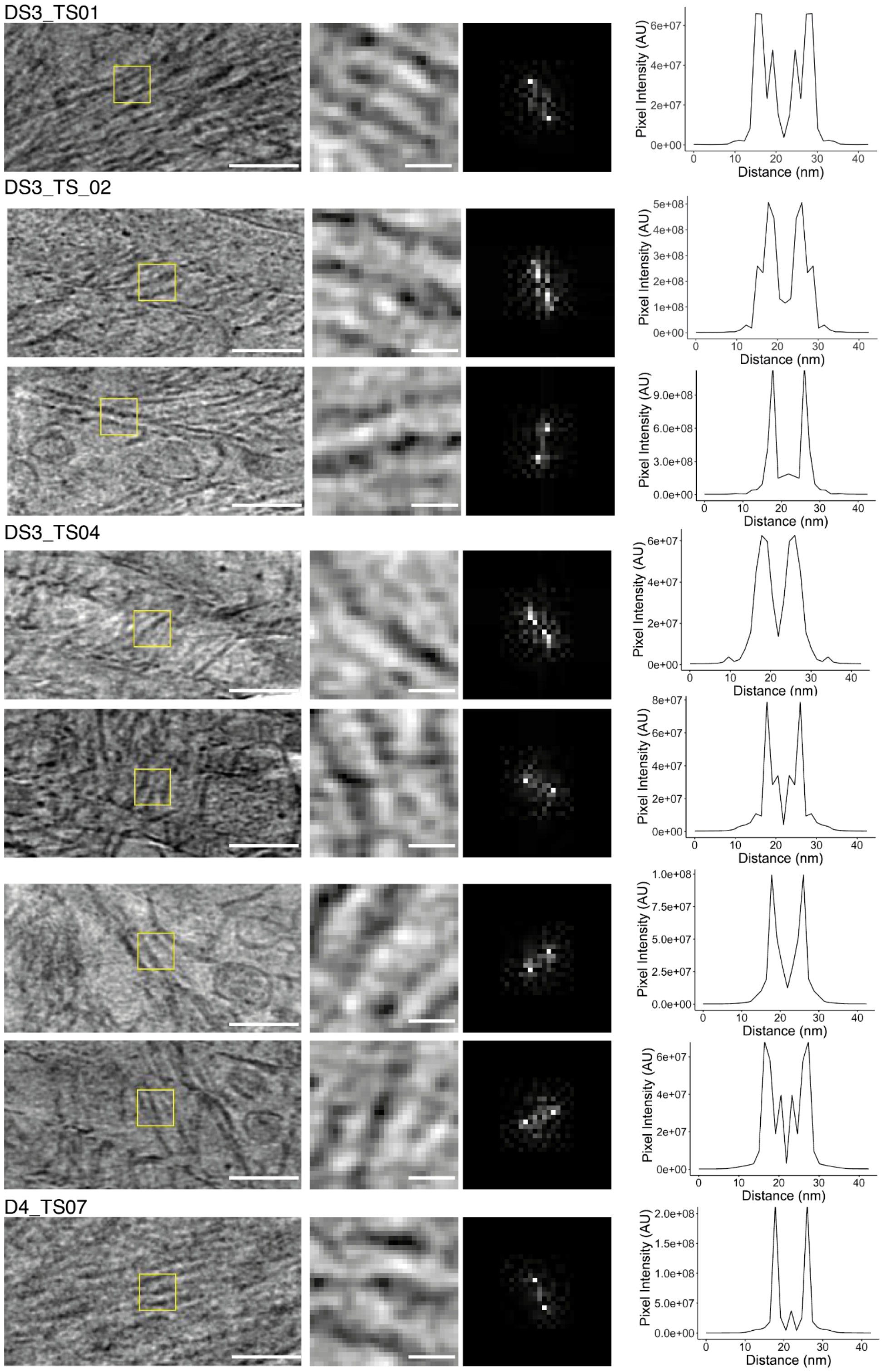
DS3_TS01
DS3_TS_02
DS3_TS04
D4_TS07
Pixel Intensity (AU)
Distance (nm)
0
10
20
30
40
0e+00
2e+07
4e+07
6e+07
1e+08
2e+08
3e+08
4e+08
5e+08
0.0e+00
3.0e+08
6.0e+08
9.0e+08
8e+07
2.5e+07
5.0e+07
7.5e+07
1.0e+08
5.0e+07
1.5e+08
2.0e+08

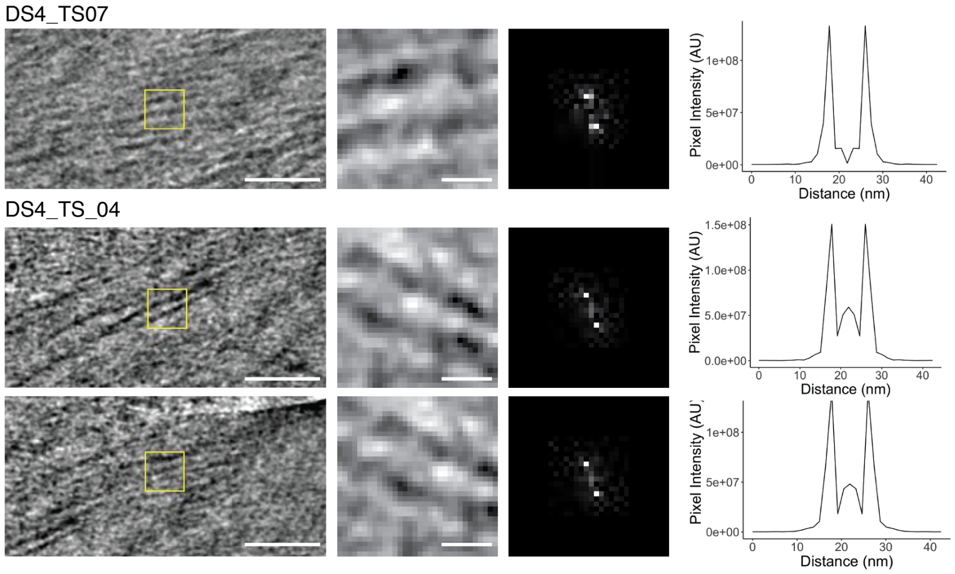

Figure 64: Fourier transformation of parallel bundles of fibrils from all tomograms. Overview of bundles is shown on the left (scale bar 100 nm), boxes have been cropped for FFT (middle) and FFT is shown in the 3rd panel. Graph of distances shows two distinct peaks (right).

10. Acknowledgments

First of all I would like to thank my friend Danielle Charles, for all the BBQs, camping trips and all the hiking adventures we went on together. It made my time here in the UK an absolute pleasure! Thank you for being so easy-going, taking my mind off the thesis stress and spending the lockdowns with me playing cards and sneaking around the Aldi middle aisle for hours!

Thank you to my supervisor team Dr. Rene Frank and Dr. Susan Deuchers for giving me the chance to do this wonderful project, giving me lots of feedback, good advice on my project and my future career.

Vielen Dank Corinna, für Kaffeepausen an stressigen Tagen, für all die Wanderausflüge und Städtetrips, wenn wir mal etwas Abwechslung brauchten! Thank you to all my lovely lab colleagues and friends for all the lunch and coffee breaks: Ailidh Burgess, Megan Lovatt, Maddie Gilbert, Catherine Hodgson and Barbara Altenhuber.

Thanks to Tim Passchier for all his bad dad jokes and adventures we shared! Especially for being an amazing tour guide on the west highland way!

Thanks also to the ABSL facility Dr. Rebecca Thompson, Dr. Emma Hesketh, Dr. Daniel Maskell, Dr. Charlotte Scarff, Dr. Yehuda Halfon, Louie Aspinall, Josh White, Tom O’Sullivan and Martin Fuller. All of you have been great helping me trouble shooting and being always open for a chat whenever I needed a break from science.

Finally, I would like to acknowledge the University of Leeds for funding my project, the FEI Titan Krios microscopes were funded by the University of Leeds, Academy of Medical Sciences Springboard Award (SBF005/1046), and the Wellcome Trust (108466/Z/15/Z).

11. References

Adrian, M. *et al.* (1984) ‘Cryo-electron microscopy of viruses’, *Nature*, pp. 32–36. doi:10.1038/308032a0.

AL-Amoudi, A., Dubochet, J. and Studer, D. (2002) ‘Amorphous solid water produced by cryosectioning of crystalline ice at 113 K’, *Journal of microscopy*, 207(Pt 2), pp. 146–153.

Al-Amoudi, A., Norlen, L.P.O. and Dubochet, J. (2004) ‘Cryo-electron microscopy of vitreous sections of native biological cells and tissues’, *Journal of structural biology*, 148(1), pp. 131–135.

Alzheimer’s Association (2016) *2016 Alzheimer’s Disease Facts and Figures: Includes a Special Report on the Personal Financial Impact of Alzheimer on Families*.

Alzhelmer, A. (1907) ‘Uber eine eigenartige Erkrankung der Hirnrinde’, *Allg. Z. Psychiatr.*, 64, pp. 146–148.

Baghallab, I. *et al.* (2018) ‘Epitomic Characterization of the Specificity of the Anti-Amyloid Aβ Monoclonal Antibodies 6E10 and 4G8’, *Journal of Alzheimer’s disease: JAD*, 66(3), p. 1235.

Baik, S.H. *et al.* (2016) ‘Microglia contributes to plaque growth by cell death due to uptake of amyloid β in the brain of Alzheimer’s disease mouse model’, *Glia*, 64(12), pp. 2274–2290.

Baldwin, A.J. *et al.* (2011) ‘Metastability of native proteins and the phenomenon of amyloid formation’, *Journal of the American Chemical Society*, 133(36), pp. 14160–14163.

Ballanyi, K. and Ruangkittisakul, A. (2008) ‘Brain Slices’, in *Encyclopedia of Neuroscience*. Springer, Berlin, Heidelberg, pp. 483–490.

Baumeister, W., Grimm, R. and Walz, J. (1999) ‘Electron tomography of molecules and cells’, *Trends in cell biology*, 9(2), pp. 81–85.

Benson, M.D. *et al.* (2020) ‘Amyloid nomenclature 2020: update and recommendations by the International Society of Amyloidosis (ISA) nomenclature committee’, *Amyloid: the international journal of experimental and clinical investigation: the official journal of the International Society of Amyloidosis*, 27(4), pp. 217–222.

Betzig, E. *et al.* (2006) ‘Imaging Intracellular Fluorescent Proteins at Nanometer Resolution’, *Science*, pp. 1642–1645. doi:10.1126/science.1127344.

Bisht, K. *et al.* (2016) ‘Correlative Light and Electron Microscopy to Study Microglial Interactions with β-Amyloid Plaques’, *Journal of visualized experiments: JoVE* [Preprint], (112). doi:10.3791/54060.

Boassa, D. *et al.* (2013) ‘Mapping the Subcellular Distribution of -Synuclein in Neurons using Genetically Encoded Probes for Correlated Light and Electron Microscopy:

Implications for Parkinson’s Disease Pathogenesis’, *Journal of Neuroscience*, pp. 2605–2615. doi:10.1523/jneurosci.2898-12.2013.

Briggs, J.A.G. (2013) ‘Structural biology in situ--the potential of subtomogram averaging’, *Current opinion in structural biology*, 23(2), pp. 261–267.

Buskila, Y. *et al.* (2014) ‘Extending the viability of acute brain slices’, *Scientific reports*, 4, p. 5309.

Castaño-Díez, D. *et al.* (2012) ‘Dynamo: A flexible, user-friendly development tool for subtomogram averaging of cryo-EM data in high-performance computing environments’, *Journal of Structural Biology*, pp. 139–151. doi:10.1016/j.jsb.2011.12.017.

Chang, J.-J. *et al.* (1983) ‘Freezing, sectioning and observation artefacts of frozen hydrated sections for electron microscopy’, *Journal of Microscopy*, pp. 109–123. doi:10.1111/j.1365-2818.1983.tb04714.x.

Chen, C. *et al.* (2018) ‘In Vivo Near-Infrared Two-Photon Imaging of Amyloid Plaques in Deep Brain of Alzheimer’s Disease Mouse Model’, *ACS Chemical Neuroscience*, pp. 3128–3136. doi:10.1021/acschemneuro.8b00306.

Chen, G.-F. *et al.* (2017) ‘Amyloid beta: structure, biology and structure-based therapeutic development’, *Acta pharmacologica Sinica*, 38(9), pp. 1205–1235.

‘Clustering and variance maps for cryo-electron tomography using wedge-masked differences’ (2011) *Journal of structural biology*, 175(3), pp. 288–299.

Cognet, L., Lounis, B. and Choquet, D. (2014) ‘Tracking receptors using individual fluorescent and nonfluorescent nanolabels’, *Cold Spring Harbor protocols*, 2014(2), pp. 207–213.

Cole, R.W., Jinadasa, T. and Brown, C.M. (2011) ‘Measuring and interpreting point spread functions to determine confocal microscope resolution and ensure quality control’, *Nature protocols*, 6(12), pp. 1929–1941.

Cole, S.L. and Vassar, R. (2007) ‘The Alzheimer’s disease Beta-secretase enzyme, BACE1’, *Molecular Neurodegeneration*, p. 22. doi:10.1186/1750-1326-2-22.

Computer Visualization of Three-Dimensional Image Data Using IMOD (no date). Available at: https://bio3d.colorado.edu/imod/paper/ (Accessed: 30 August 2022).

Corder, E.H. *et al.* (1993) ‘Gene dose of apolipoprotein E type 4 allele and the risk of Alzheimer’s disease in late onset families’, *Science*, 261(5123), pp. 921–923.

‘Cryo-EM in molecular and cellular biology’ (2022) *Molecular cell*, 82(2), pp. 274–284.

Danev, R. *et al.* (2014) ‘Volta potential phase plate for in-focus phase contrast transmission electron microscopy’, *Proceedings of the National Academy of Sciences of the United States of America*, 111(44), pp. 15635–15640.

Danev, R., Yanagisawa, H. and Kikkawa, M. (2021) ‘Cryo-EM performance testing of hardware and data acquisition strategies’, *Microscopy* , 70(6), pp. 487–497.

Dickson, T.C. and Vickers, J.C. (2001) ‘The morphological phenotype of beta-amyloid plaques and associated neuritic changes in Alzheimer’s disease’, *Neuroscience*, 105(1), pp. 99–107.

Downing, K.H. and Nogales, E. (2010) ‘Cryoelectron Microscopy Applications in the Study of Tubulin Structure, Microtubule Architecture, Dynamics and Assemblies, and Interaction of Microtubules with Motors’, *Cryo-EM, Part C: Analyses, Interpretation, and Case studies*, pp. 121–142. doi:10.1016/s0076-6879(10)83006-x.

Doyle, L.M. and Wang, M.Z. (2019) ‘Overview of Extracellular Vesicles, Their Origin, Composition, Purpose, and Methods for Exosome Isolation and Analysis’, *Cells* , 8(7). doi:10.3390/cells8070727.

Dubochet, J. *et al.* (1982) ‘Electron microscopy of frozen water and aqueous solutions’, *Journal of Microscopy*, pp. 219–237. doi:10.1111/j.1365-2818.1982.tb04625.x.

Dubochet, J. (2012) ‘Cryo-EM-the first thirty years’, *Journal of Microscopy*, pp. 221–224. doi:10.1111/j.1365-2818.2011.03569.x.

Dubochet, J. and McDowall, A.W. (1981) ‘VITRIFICATION OF PURE WATER FOR ELECTRON MICROSCOPY’, *Journal of Microscopy*, pp. 3–4. doi:10.1111/j.1365-2818.1981.tb02483.x.

Dubois, B. *et al.* (2016) ‘Preclinical Alzheimer’s disease: Definition, natural history, and diagnostic criteria’, *Alzheimer’s & dementia: the journal of the Alzheimer's Association*, 12(3), p. 292.

Duckett, S. and de la Torre, J.C. (2001) *Pathology of the Aging Human Nervous System*. Oxford University Press.

Duff, K. *et al.* (1996) ‘Increased amyloid-beta42(43) in brains of mice expressing mutant presenilin 1’, *Nature*, 383(6602), pp. 710–713.

Emery, V.O.B. (2011) ‘Alzheimer disease: are we intervening too late? Pro’, *Journal of neural transmission* , 118(9), pp. 1361–1378.

Fitzpatrick, A.W. *et al.* (2011) ‘Inversion of the Balance between Hydrophobic and Hydrogen Bonding Interactions in Protein Folding and Aggregation’, *PLoS Computational Biology*, p. e1002169. doi:10.1371/journal.pcbi.1002169.

Fitzpatrick, A.W.P. *et al.* (2017) ‘Cryo-EM structures of tau filaments from Alzheimer’s disease’, *Nature*, 547(7662), pp. 185–190.

Foglieni, C., Meoni, C. and Davalli, A.M. (2001) ‘Fluorescent dyes for cell viability: an application on prefixed conditions’, *Histochemistry and cell biology*, 115(3), pp. 223–229.

Frackowiak, J. *et al.* (1992) ‘Ultrastructure of the microglia that phagocytose amyloid and the microglia that produce beta-amyloid fibrils’, *Acta neuropathologica*, 84(3), pp. 225–233.

Frangakis, A.S. and Hegerl, R. (2001) ‘Noise reduction in electron tomographic reconstructions using nonlinear anisotropic diffusion’, *Journal of structural biology*, 135(3), pp. 239–250.

Frank, R.A. and Grant, S.G. (2017) 'Supramolecular organization of NMDA receptors and the postsynaptic density', *Current opinion in neurobiology*, 45, pp. 139–147.

Frank, R.A.W. *et al.* (2016) 'NMDA receptors are selectively partitioned into complexes and supercomplexes during synapse maturation', *Nature communications*, 7, p. 11264.

Fukuda, Y. *et al.* (2015) 'In situ studies of cellular architecture by Electron Cryo-Tomography with Volta Phase Plate', *Microscopy and Microanalysis*, pp. 1835–1836. doi:10.1017/s1431927615009952.

Gao, Y. *et al.* (2016) 'TRPV1 structures in nanodiscs reveal mechanisms of ligand and lipid action', *Nature*, 534(7607), pp. 347–351.

Garwood, C.J. *et al.* (2017) 'Review: Astrocytes in Alzheimer's disease and other age-associated dementias: a supporting player with a central role', *Neuropathology and applied neurobiology*, 43(4), pp. 281–298.

Ghosh, U. *et al.* (2021) 'Molecular structure of a prevalent amyloid-β fibril polymorph from Alzheimer's disease brain tissue', *Proceedings of the National Academy of Sciences of the United States of America*, 118(4). doi:10.1073/pnas.2023089118.

Glauert, A.M., Rogers, G.E. and Glauert, R.H. (1956) 'A New Embedding Medium for Electron Microscopy', *Nature*, pp. 803–803. doi:10.1038/178803a0.

Goedert, M. and Spillantini, M.G. (2006) 'A century of Alzheimer's disease', *Science* , 314(5800). doi:10.1126/science.1132814.

Gonen, T. *et al.* (2005) 'Lipid-protein interactions in double-layered two-dimensional AQP0 crystals', *Nature*, 438(7068), pp. 633–638.

Gratuze, M., Leyns, C.E.G. and Holtzman, D.M. (2018) 'New insights into the role of TREM2 in Alzheimer's disease', *Molecular Neurodegeneration*. doi:10.1186/s13024-018-0298-9.

Gray, E.G. (1959) 'Axo-somatic and axo-dendritic synapses of the cerebral cortex: an electron microscope study', *Journal of anatomy*, 93, pp. 420–433.

Gremer, L. *et al.* (2017) 'Fibril structure of amyloid-β(1–42) by cryo–electron microscopy', *Science*, pp. 116–119. doi:10.1126/science.aao2825.

Guerrero-Ferreira, R.C. and Wright, E.R. (2014) 'Zernike phase contrast cryo-electron tomography of whole bacterial cells', *Journal of structural biology*, 185(1), pp. 129–133.

Hagen, W.J.H., Wan, W. and Briggs, J.A.G. (2017) 'Implementation of a cryo-electron tomography tilt-scheme optimized for high resolution subtomogram averaging', *Journal of structural biology*, 197(2), pp. 191–198.

Han, S. *et al.* (2017) 'Amyloid plaque structure and cell surface interactions of β-amyloid fibrils revealed by electron tomography', *Scientific reports*, 7, p. 43577.

Harold, D. *et al.* (2009) 'Genome-wide association study identifies variants at CLU and PICALM associated with Alzheimer's disease', *Nature genetics*, 41(10), pp. 1088–1093.

Hatta, T. (1987) ‘Le Chatelier Principle’, *The New Palgrave Dictionary of Economics*, pp. 1–5. doi:10.1057/978-1-349-95121-5_917-1.

Hell, S. and Stelzer, E.H.K. (1992) ‘Properties of a 4Pi confocal fluorescence microscope’, *Journal of the Optical Society of America A*, p. 2159. doi:10.1364/josaa.9.002159.

Hell, S.W. and Wichmann, J. (1994) ‘Breaking the diffraction resolution limit by stimulated emission: stimulated-emission-depletion fluorescence microscopy’, *Optics letters*, 19(11), pp. 780–782.

Henderson, R. *et al.* (1990) ‘Model for the structure of bacteriorhodopsin based on high-resolution electron cryo-microscopy’, *Journal of molecular biology*, 213(4), pp. 899–929.

Henderson, R. and Unwin, P.N. (1975) ‘Three-dimensional model of purple membrane obtained by electron microscopy’, *Nature*, 257(5521), pp. 28–32.

Hermann, R., Walther, P. and Müller, M. (1996) ‘Immunogold labeling in scanning electron microscopy’, *Histochemistry and Cell Biology*, pp. 31–39. doi:10.1007/bf02473200.

Hopwood, D. (1969) ‘Fixatives and fixation: a review’, *The Histochemical Journal*, pp. 323–360. doi:10.1007/bf01003278.

Horisberger, M. (1981) ‘Colloidal gold : a cytochemical marker for light and fluorescent microscopy and for transmission and scanning electron microscopy’, *Scanning electron microscopy*, (Pt 2), pp. 9–31.

Huang, Y. *et al.* (2021) ‘Microglia use TAM receptors to detect and engulf amyloid β plaques’, *Nature immunology*, 22(5), pp. 586–594.

H�ndgen, M. (1968) ‘Der Einflu� verschiedener Aldehyde auf die Strukturerhaltung gez�chteter Zellen und auf die Darstellbarkeit von vier Phosphatasen’, *Histochemie*, pp. 46–61. doi:10.1007/bf00304573.

‘Intravital Correlative Microscopy: Imaging Life at the Nanoscale’ (2016) *Trends in cell biology*, 26(11), pp. 848–863.

Jing, Y. *et al.* (2021) ‘Super-Resolution Microscopy: Shedding New Light on In Vivo Imaging’, *Frontiers in Chemistry*, 0. doi:10.3389/fchem.2021.746900.

Kanekiyo, T. *et al.* (2011) ‘Heparan sulphate proteoglycan and the low-density lipoprotein receptor-related protein 1 constitute major pathways for neuronal amyloid-beta uptake’, *The Journal of neuroscience: the official journal of the Society for Neuroscience*, 31(5), pp. 1644–1651.

Kato, T. *et al.* (2019) ‘CryoTEM with a Cold Field Emission Gun That Moves Structural Biology into a New Stage’, *Microscopy and Microanalysis*, pp. 998–999. doi:10.1017/s1431927619005725.

Khoshouei, M. *et al.* (2017) ‘Subtomogram analysis using the Volta phase plate’, *Journal of structural biology*, 197(2), pp. 94–101.

Kiernan, J.A. (2000) ‘Formaldehyde, Formalin, Paraformaldehyde And Glutaraldehyde: What They Are And What They Do’, *Microscopy Today*, pp. 8–13. doi:10.1017/s1551929500057060.

Kim, J. *et al.* (2009) ‘Overexpression of low-density lipoprotein receptor in the brain markedly inhibits amyloid deposition and increases extracellular A beta clearance’, *Neuron*, 64(5), pp. 632–644.

Klug, A. and Finch, J.T. (1968) ‘Structure of viruses of the papilloma-polyoma type. IV. Analysis of tilting experiments in the electron microscope’, *Journal of molecular biology*, 31(1), pp. 1–12.

Klunk, W.E. *et al.* (2002) ‘Imaging Abeta plaques in living transgenic mice with multiphoton microscopy and methoxy-X04, a systemically administered Congo red derivative’, *Journal of neuropathology and experimental neurology*, 61(9), pp. 797–805.

Knoll, M. and Ruska, E. (1932) ‘Das Elektronenmikroskop’, *Zeitschrift f�r Physik*, pp. 699–699. doi:10.1007/bf01330526.

Knowles, T.P.J., Vendruscolo, M. and Dobson, C.M. (2014) ‘The amyloid state and its association with protein misfolding diseases’, *Nature reviews. Molecular cell biology*, 15(6), pp. 384–396.

Koffie, R.M. *et al.* (2009) ‘Oligomeric amyloid beta associates with postsynaptic densities and correlates with excitatory synapse loss near senile plaques’, *Proceedings of the National Academy of Sciences of the United States of America*, 106(10), pp. 4012–4017.

Kollmer, M. *et al.* (2016) ‘Electron tomography reveals the fibril structure and lipid interactions in amyloid deposits’, *Proceedings of the National Academy of Sciences*, pp. 5604–5609. doi:10.1073/pnas.1523496113.

Kollmer, M. *et al.* (2019) ‘Cryo-EM structure and polymorphism of Aβ amyloid fibrils purified from Alzheimer’s brain tissue’, *Nature Communications*. doi:10.1038/s41467-019-12683-8.

Korogod, N., Petersen, C.C.H. and Knott, G.W. (2015) ‘Ultrastructural analysis of adult mouse neocortex comparing aldehyde perfusion with cryo fixation’, *eLife*, 4. doi:10.7554/eLife.05793.

Kremer, J.R., Mastronarde, D.N. and McIntosh, J.R. (1996) ‘Computer visualization of three-dimensional image data using IMOD’, *Journal of structural biology*, 116(1), pp. 71–76.

Kukulski, W. *et al.* (2011) ‘Correlated fluorescence and 3D electron microscopy with high sensitivity and spatial precision’, *The Journal of cell biology*, 192(1), pp. 111–119.

Kyle, R.A. (2001) ‘Amyloidosis: a convoluted story’, *British Journal of Haematology*, pp. 529–538. doi:10.1046/j.1365-2141.2001.02999.x.

Lambert, M.P. *et al.* (1998) ‘Diffusible, nonfibrillar ligands derived from $A\beta_{1–42}$ are potent central nervous system neurotoxins’, *Proceedings of the National Academy of Sciences*, pp. 6448–6453. doi:10.1073/pnas.95.11.6448.

Laverty, D. *et al.* (2019) ‘Cryo-EM structure of the human α1β3γ2 GABAA receptor in a lipid bilayer’, *Nature*, 565(7740), pp. 516–520.

Liu, J. *et al.* (2019) ‘The Role of NMDA Receptors in Alzheimer’s Disease’, *Frontiers in Neuroscience*. doi:10.3389/fnins.2019.00043.

Liu, Y.-T. *et al.* (no date) ‘Isotropic Reconstruction of Electron Tomograms with Deep Learning’. doi:10.1101/2021.07.17.452128.

Li, Y. *et al.* (2008) ‘Direct labeling and visualization of blood vessels with lipophilic carbocyanine dye DiI’, *Nature protocols*, 3(11), pp. 1703–1708.

Lockwood, W.R. (1964) ‘A RELIABLE AND EASILY SECTIONED EPOXY EMBEDDING MEDIUM’, *The Anatomical record*, 150, pp. 129–139.

Lovatt, M., Leistner, C. and Frank, R.A.W. (2022) ‘Bridging length scales from molecules to the whole organism by cryoCLEM and cryoET’, *Faraday discussions* [Preprint]. doi:10.1039/D2FD00081D.

Lucˇic´, V. *et al.* (2005) ‘Morphological Characterization of Molecular Complexes Present in the Synaptic Cleft’, *Structure*, pp. 423–434. doi:10.1016/j.str.2005.02.005.

Luckner, M. *et al.* (2018) ‘Label-free 3D-CLEM Using Endogenous Tissue Landmarks’, *iScience*, 6, pp. 92–101.

Lu, J.-X. *et al.* (2013) ‘Molecular structure of β-amyloid fibrils in Alzheimer’s disease brain tissue’, *Cell*, 154(6). doi:10.1016/j.cell.2013.08.035.

Mastronarde, D.N. (2005) ‘Automated electron microscope tomography using robust prediction of specimen movements’, *Journal of structural biology*, 152(1), pp. 36–51.

Mastronarde, D.N. (no date) ‘Fiducial Marker and Hybrid Alignment Methods for Single- and Double-axis Tomography’, *Electron Tomography*, pp. 163–185. doi:10.1007/978-0-387-69008-7_6.

Medalia, O. *et al.* (2002) ‘Macromolecular architecture in eukaryotic cells visualized by cryoelectron tomography’, *Science*, 298(5596), pp. 1209–1213.

Meyer-Luehmann, M. *et al.* (2008a) ‘Rapid appearance and local toxicity of amyloid-beta plaques in a mouse model of Alzheimer’s disease’, *Nature*, 451(7179), pp. 720–724.

Meyer-Luehmann, M. *et al.* (2008b) ‘Rapid appearance and local toxicity of amyloid-beta plaques in a mouse model of Alzheimer’s disease’, *Nature*, 451(7179), pp. 720–724.

Morikawa, S., Sato, A. and Ezaki, T. (2018) ‘A simple, one-step polychromatic staining method for epoxy-embedded semithin tissue sections’, *Microscopy: the journal of the Quekett Microscopical Club*, 67(6), p. 331.

Mucke, L. *et al.* (2000) ‘High-Level Neuronal Expression of A$\beta_{1–42}$in Wild-Type Human Amyloid Protein Precursor Transgenic Mice: Synaptotoxicity without Plaque Formation’, *The Journal of Neuroscience*, pp. 4050–4058. doi:10.1523/jneurosci.20-11-04050.2000.

Nägerl, U.V. *et al.* (2008) 'Live-cell imaging of dendritic spines by STED microscopy', *Proceedings of the National Academy of Sciences of the United States of America*, 105(48), pp. 18982–18987.

Nakane, T. *et al.* (2020) 'Single-particle cryo-EM at atomic resolution', *Nature*, 587(7832), pp. 152–156.

Nicastro, D. *et al.* (2006) 'The Molecular Architecture of Axonemes Revealed by Cryoelectron Tomography', *Science*, 313(5789), pp. 944–948.

Nogales, E. (2016) 'The development of cryo-EM into a mainstream structural biology technique', *Nature methods*, 13(1), pp. 24–27.

O'Reilly, F.J. *et al.* (2020) 'In-cell architecture of an actively transcribing-translating expressome', *Science*, 369(6503), pp. 554–557.

Palay, S.L. *et al.* (1962) 'Fixation of neural tissues for electron microscopy by perfusion with solutions of osmium tetroxide', *The Journal of cell biology*, 12, pp. 385–410.

Peukes, J. *et al.* (no date) 'The molecular infrastructure of glutamatergic synapses in the mammalian forebrain'. doi:10.1101/2021.02.19.432002.

Pierson, J. *et al.* (2010) 'Improving the technique of vitreous cryo-sectioning for cryo-electron tomography: electrostatic charging for section attachment and implementation of an anti-contamination glove box', *Journal of structural biology*, 169(2), pp. 219–225.

Rall, W. *et al.* (1966) 'Dendrodendritic synaptic pathway for inhibition in the olfactory bulb', *Experimental neurology*, 14(1), pp. 44–56.

Raposo, G. and Stoorvogel, W. (2013) 'Extracellular vesicles: exosomes, microvesicles, and friends', *The Journal of cell biology*, 200(4), pp. 373–383.

Reitz, C. and Mayeux, R. (2014) 'Alzheimer disease: epidemiology, diagnostic criteria, risk factors and biomarkers', *Biochemical pharmacology*, 88(4), pp. 640–651.

Reynolds, E.S. (1963) 'The use of lead citrate at high pH as an electron-opaque stain in electron microscopy', *The Journal of cell biology*, 17, pp. 208–212.

Ries, J. *et al.* (2012) 'A simple, versatile method for GFP-based super-resolution microscopy via nanobodies', *Nature methods*, 9(6), pp. 582–584.

Rosier, D.J.D.E., de Rosier, D.J. and Klug, A. (1968) 'Reconstruction of Three Dimensional Structures from Electron Micrographs', *Nature*, pp. 130–134. doi:10.1038/217130a0.

Rust, M.J., Bates, M. and Zhuang, X. (2006) 'Stochastic optical reconstruction microscopy (STORM) provides sub-diffraction-limit image resolution', *Nature methods*, 3(10), p. 793.

Saito, T. *et al.* (2014a) 'Single App knock-in mouse models of Alzheimer's disease', *Nature neuroscience*, 17(5), pp. 661–663.

Saito, T. *et al.* (2014b) 'Single App knock-in mouse models of Alzheimer's disease', *Nature neuroscience*, 17(5), pp. 661–663.

Sasaguri, H. *et al.* (2017) ‘APP mouse models for Alzheimer’s disease preclinical studies’, *The EMBO Journal*, pp. 2473–2487. doi:10.15252/embj.201797397.

Scarff, C.A. *et al.* (2018) ‘Variations on Negative Stain Electron Microscopy Methods: Tools for Tackling Challenging Systems’, *Journal of visualized experiments: JoVE* [Preprint], (132). doi:10.3791/57199.

Schaffer, M. *et al.* (2015) ‘Cryo-focused Ion Beam Sample Preparation for Imaging Vitreous Cells by Cryo-electron Tomography’, *Bio-protocol*, 5(17). doi:10.21769/bioprotoc.1575.

Schaffer, M. *et al.* (2019) ‘A cryo-FIB lift-out technique enables molecular-resolution cryo-ET within native Caenorhabditis elegans tissue’, *Nature methods*, 16(8), pp. 757–762.

Schertel, A. *et al.* (2013) ‘Cryo FIB-SEM: volume imaging of cellular ultrastructure in native frozen specimens’, *Journal of structural biology*, 184(2), pp. 355–360.

Schindelin, J. *et al.* (2012) ‘Fiji: an open-source platform for biological-image analysis’, *Nature methods*, 9(7), pp. 676–682.

Schmidt, A. *et al.* (2011) ‘Crystal structure of small protein crambin at 0.48 Å resolution’, *Acta Crystallographica Section F Structural Biology and Crystallization Communications*, pp. 424–428. doi:10.1107/s1744309110052607.

Schmidt, M. *et al.* (2015) ‘Peptide dimer structure in an Aβ(1–42) fibril visualized with cryo-EM’, *Proceedings of the National Academy of Sciences*, pp. 11858–11863. doi:10.1073/pnas.1503455112.

Schorb, M. and Briggs, J.A.G. (2014) ‘Correlated cryo-fluorescence and cryo-electron microscopy with high spatial precision and improved sensitivity’, *Ultramicroscopy*, 143, pp. 24–32.

Schröder, R.R., Hofmann, W. and Ménétret, J.-F. (1990) ‘Zero-loss energy filtering as improved imaging mode in cryoelectronmicroscopy of frozen-hydrated specimens’, *Journal of Structural Biology*, pp. 28–34. doi:10.1016/1047-8477(90)90095-t.

Schwabe, T., Srinivasan, K. and Rhinn, H. (2020) ‘Shifting paradigms: The central role of microglia in Alzheimer’s disease’, *Neurobiology of disease*, 143, p. 104962.

Serrano-Pozo, A. *et al.* (2011) ‘Neuropathological Alterations in Alzheimer Disease’, *Cold Spring Harbor Perspectives in Medicine*, pp. a006189–a006189. doi:10.1101/cshperspect.a006189.

Shabestari, S.K. *et al.* (2022) ‘Absence of microglia promotes diverse pathologies and early lethality in Alzheimer’s disease mice’, *Cell Reports*, p. 110961. doi:10.1016/j.celrep.2022.110961.

Shao, C.Y. *et al.* (2011) ‘Postsynaptic degeneration as revealed by PSD-95 reduction occurs after advanced Aβ and tau pathology in transgenic mouse models of Alzheimer’s disease’, *Acta Neuropathologica*, pp. 285–292. doi:10.1007/s00401-011-0843-x.

Simpson, W.L. (1941) ‘An experimental analysis of the Altmann technic of freezing-drying’, *The Anatomical Record*, pp. 173–189. doi:10.1002/ar.1090800204.

Spangenberg, E. *et al.* (2019) ‘Sustained microglial depletion with CSF1R inhibitor impairs parenchymal plaque development in an Alzheimer’s disease model’, *Nature Communications*. doi:10.1038/s41467-019-11674-z.

Spires-Jones, T.L. *et al.* (2007) ‘Impaired Spine Stability Underlies Plaque-Related Spine Loss in an Alzheimer’s Disease Mouse Model’, *The American Journal of Pathology*, pp. 1304–1311. doi:10.2353/ajpath.2007.070055.

Spires, T.L. *et al.* (2005) ‘Dendritic spine abnormalities in amyloid precursor protein transgenic mice demonstrated by gene transfer and intravital multiphoton microscopy’, *The Journal of neuroscience: the official journal of the Society for Neuroscience*, 25(31), pp. 7278–7287.

Stelzmann, R.A., Norman Schnitzlein, H. and Reed Murtagh, F. (1995) ‘An english translation of alzheimer’s 1907 paper, ?�ber eine eigenartige erkankung der hirnrinde?’, *Clinical Anatomy*, pp. 429–431. doi:10.1002/ca.980080612.

Strittmatter, W.J. *et al.* (1993) ‘Apolipoprotein E: high-avidity binding to beta-amyloid and increased frequency of type 4 allele in late-onset familial Alzheimer disease’, *Proceedings of the National Academy of Sciences of the United States of America*, 90(5), pp. 1977–1981.

Studer, D. *et al.* (2014) ‘A new tool based on two micromanipulators facilitates the handling of ultrathin cryosection ribbons’, *Journal of structural biology*, 185(1), pp. 125–128.

Tang, G. *et al.* (2007) ‘EMAN2: An extensible image processing suite for electron microscopy’, *Journal of Structural Biology*, pp. 38–46. doi:10.1016/j.jsb.2006.05.009.

Taylor, A.I.P. and Staniforth, R.A. (2022) ‘General Principles Underpinning Amyloid Structure’, *Frontiers in neuroscience*, 16, p. 878869.

Tegunov, D. *et al.* (2021) ‘Multi-particle cryo-EM refinement with M visualizes ribosome-antibiotic complex at 3.5 Å in cells’, *Nature methods*, 18(2). doi:10.1038/s41592-020-01054-7.

Tegunov, D. and Cramer, P. (2019) ‘Real-time cryo-electron microscopy data preprocessing with Warp’, *Nature methods*, 16(11), pp. 1146–1152.

Tegunov, D. and Cramer, P. (no date) ‘Real-time cryo-EM data pre-processing with *Warp*’. doi:10.1101/338558.

‘The dimensions of DNA in solution’ (1981) *Journal of molecular biology*, 152(1), pp. 153–161.

Theer, P., Hasan, M.T. and Denk, W. (2003) ‘Two-photon imaging to a depth of 1000 μm in living brains by use of a Ti:Al_2O_3 regenerative amplifier’, *Optics Letters*, p. 1022. doi:10.1364/ol.28.001022.

Thorn, K. (2016) ‘A quick guide to light microscopy in cell biology’, *Molecular biology of the cell*, 27(2), pp. 219–222.

Tian, Y. *et al.* (2021) ‘3D-visualization of amyloid-β oligomer interactions with lipid membranes by cryo-electron tomography’, *Chemical science* , 12(20), pp. 6896–6907.

Ting, J.T. *et al.* (2018) ‘Preparation of Acute Brain Slices Using an Optimized N-Methyl-D-glucamine Protective Recovery Method’, *Journal of visualized experiments: JoVE* [Preprint], (132). doi:10.3791/53825.

Tokuyasu, K.T. (1973) ‘A technique for ultracryotomy of cell suspensions and tissues’, *The Journal of cell biology*, 57(2), pp. 551–565.

Twomey, E.C. *et al.* (2016) ‘Elucidation of AMPA receptor-stargazin complexes by cryo-electron microscopy’, *Science*, 353(6294), pp. 83–86.

Urban, N.T. *et al.* (2011) ‘STED nanoscopy of actin dynamics in synapses deep inside living brain slices’, *Biophysical journal*, 101(5), pp. 1277–1284.

Van Drie, J.H. and Tong, L. (2020) ‘Cryo-EM as a powerful tool for drug discovery’, *Bioorganic & medicinal chemistry letters*, 30(22), p. 127524.

Vassar, R. *et al.* (1999) ‘Beta-secretase cleavage of Alzheimer’s amyloid precursor protein by the transmembrane aspartic protease BACE’, *Science*, 286(5440), pp. 735–741.

Vassar, R. (2013) ‘BACE1, the Alzheimer’s beta-secretase enzyme, in health and disease’, *Molecular Neurodegeneration*. doi:10.1186/1750-1326-8-s1-o7.

Villegas, S. *et al.* (2022) ‘Amyloid-beta peptide and tau protein crosstalk in Alzheimer’s disease’, *Neural Regeneration Research*, p. 1666. doi:10.4103/1673-5374.332127.

Wagner, T. and Raunser, S. (2020) ‘The evolution of SPHIRE-crYOLO particle picking and its application in automated cryo-EM processing workflows’, *Communications biology*, 3(1), p. 61.

Walker, L.C. (2020) ‘Aβ Plaques’, *Free neuropathology*, 1. doi:10.17879/freeneuropathology-2020-3025.

Wälti, M.A. *et al.* (2016) ‘Atomic-resolution structure of a disease-relevant Aβ(1–42) amyloid fibril’, *Proceedings of the National Academy of Sciences*. doi:10.1073/pnas.1600749113.

Webb, R.H. (1996) ‘Confocal optical microscopy’, *Reports on Progress in Physics*, pp. 427–471. doi:10.1088/0034-4885/59/3/003.

Wegiel, J. and Wisniewski, H.M. (1990) ‘The complex of microglial cells and amyloid star in three-dimensional reconstruction’, *Acta neuropathologica*, 81(2), pp. 116–124.

Wisniewski, H.M. *et al.* (1989) ‘Spectrum of morphological appearance of amyloid deposits in Alzheimer’s disease’, *Acta neuropathologica*, 78(4), pp. 337–347.

Wolthuis, R. *et al.* (2001) ‘Determination of water concentration in brain tissue by Raman spectroscopy’, *Analytical chemistry*, 73(16), pp. 3915–3920.

Yakovlev, S. and Downing, K.H. (2011) ‘Freezing in sealed capillaries for preparation of frozen hydratedsections’, *Journal of microscopy*, 244(3), pp. 235–247.

Yang *et al.* (no date) ‘Cryo-EM Structures of Amyloid-β 42 Filaments from Human Brain’. doi:10.1101/2021.10.19.464936.

Yang, Y. *et al.* (2022) ‘Cryo-EM structures of amyloid-β 42 filaments from human brains’, *Science*, 375(6577), pp. 167–172.

Yiannopoulou, K.G. and Papageorgiou, S.G. (2020) ‘Current and Future Treatments in Alzheimer Disease: An Update’, *Journal of Central Nervous System Disease*, p. 117957352090739. doi:10.1177/1179573520907397.

Younkin, S.G. (1995) ‘Evidence that A?42 is the real culprit in alzheimer’s disease’, *Annals of Neurology*, pp. 287–288. doi:10.1002/ana.410370303.

Zhang, K. (2016) ‘Gctf: Real-time CTF determination and correction’, *Journal of structural biology*, 193(1), pp. 1–12.

Zhang, Y. *et al.* (2016) ‘Purification and Characterization of Progenitor and Mature Human Astrocytes Reveals Transcriptional and Functional Differences with Mouse’, *Neuron*, 89(1), pp. 37–53.

Zuber, B. *et al.* (2005) ‘The mammalian central nervous synaptic cleft contains a high density of periodically organized complexes’, *Proceedings of the National Academy of Sciences of the United States of America*, 102(52), pp. 19192–19197.